Development of a computational framework coupling the non-Newtonian lattice Boltzmann method and the discrete element method with application to block caving.

Leonardi, Christopher Ross

Leonardi, Christopher Ross (2009) *Development of a computational framework coupling the non-Newtonian lattice Boltzmann method and the discrete element method with application to block caving..* thesis, Swansea University.
http://cronfa.swan.ac.uk/Record/cronfa42882

Swansea University
School of Engineering

Development of a Computational Framework Coupling the Non-Newtonian Lattice Boltzmann Method and the Discrete Element Method with Application to Block Caving

Christopher Ross Leonardi
B.E. (Hons)

THESIS SUBMITTED TO THE UNIVERSITY OF WALES IN CANDIDATURE
FOR THE DEGREE OF DOCTOR OF PHILOSOPHY

August 2009

DECLARATION AND STATEMENTS

DECLARATION

This work has not previously been accepted in substance for any degree and is not being concurrently submitted in candidature for any degree.

Candidate:

Date: 04/12/09

STATEMENT 1

This thesis is the result of my own investigations, except where otherwise stated. Other sources are acknowledged by footnotes giving explicit references. A bibliography is appended.

Candidate:

Date: 04/12/09

STATEMENT 2

I am hereby consent for my thesis, if accepted, to be available for photocopying and for inter-library loan, and for the title and summary to be made available to outside organisations.

Candidate:

Date: 04/12/09

ACKNOWLEDGEMENTS

I am indebted to many people, without whom this work would not have commenced let alone been completed.

I would like to first gratefully acknowledge Rio Tinto Technology and Innovation including Dr Alan Moss, Dr Chris Cross and Dr Andre van As, for their generous support of this research. In particular, I would like to thank Dr Gert van Hout for his effort and enthusiasm as my industrial mentor.

I would like to sincerely thank my supervisors, Prof Roger Owen and Prof Djordje Perić, not only for their tremendous academic guidance but also their ongoing and invaluable friendship. I am especially grateful to Prof Owen for arranging the opportunity for me to study abroad and for the extra effort he made to make Dianna and I feel at home in our new surroundings.

My research associates at Swansea University, Prof Yuntian Feng and Dr Kuanjin Han, offered me great assistance throughout the course of my research and for this I am deeply appreciative. From institutions around the world I would also like to acknowledge Prof Li-Shi Luo, Prof John Williams, Prof Irina Ginzburg, Dr Ben Cook, Dr Eric Strack, Dr Joshua Boyd and Dr Alexander Vikhansky for answering my many questions.

I am grateful to Dr Jon Rance and Dr Henry Anderson and the staff at Rockfield Software Ltd for their unending assistance throughout the course of my study. I would particularly like to thank Dr Jian Yu, Dr Mark Cottrell, Dr Martin Dutko, Dr Tony Crook, Mr James Armstrong, Mr Mike Hudson and Dr Attila Garai for their invaluable technical support and their enthusiastic conversations on all things research-related and otherwise. I would also like to thank Mr Jonathon Cain and Dr Adam Bere for helping me maintain calm and perspective when I was feeling particularly stressed.

I would like to thank my fellow researchers, Dr Francisco Pires, Dr Mauricio Lobão, Dr Kato Jun and Dr Josep Segura Serra for sharing the experience of being a PhD candidate with me. The time we spent working together, re-

gardless of which office nook we were located in, was always enjoyable.

I would like to express my gratitude to Rockfield Technologies Australia for accommodating me during the final months spent compiling this thesis. I would also like to thank Prof Jeffrey Loughran for motivating me to make the step to postgraduate study, and Mr Scott Anderson, who over the past seven years has been an incredible friend and engineering mentor to me.

On behalf of Dianna and myself, I would like to thank all of our wonderful friends throughout Swansea and South Wales, for sharing so may incredible experiences with us and giving us a second home that will be a part of the rest of our lives.

For their love, support and hard work I would like to thank my family, especially my parents Joe and Angie. Without them, none of what I have achieved to date would have been possible.

Finally, I would like to declare my greatest and most heartfelt thanks to my beautiful fiancée, Dianna. Four years ago she relentlessly encouraged me to pursue further study and in the time since she has reassured me in times doubt, comforted me when I was feeling overwhelmed, and afforded me infinite patience when work has consumed my time. During the course of my study her support has been incredible and for this I hope that one day I can repay her.

For Dianna

SUMMARY

In this thesis, a novel computational framework is presented that couples the lattice Boltzmann method (LBM) in a nonlinear form to the discrete element method (DEM) for the simulation of fines migration in block cave mines. Fines migration is characterised by the faster movement of fine material towards the mine draw points in comparison to larger, blocky material. This can result in the percolation of waste material into the fragmented ore body and, consequently, the reduction of the operational efficiency of the mine. By employing computational techniques a greater understanding of the kinematic behaviour of fines and ore within the cave can be developed, which can in turn aid the solution of this problem.

To simulate the fines migration phenomenon using solely discrete elements with a wide size range would require in the order of 10^8 (or greater) particles and subsequently be intractable. Therefore, in this research the DEM is employed to model the dynamics of large blocks and the LBM is used to model the interstitial fines phase. This gives rise to a fully coupled LBM-DEM computational framework capable of simulating dense phase particle suspensions with application in a wide range of problems outside the scope of this work.

In the last 20 years the LBM has emerged as an alternative to conventional computational fluid dynamics (CFD) methods, with advantages over the more traditional approaches including the ability to use a regular grid, high space-time resolution, full scalability on parallel computers, as well as efficient and robust implementation in complex fluid domains. In the context of this research the most significant strength of the LBM is its ability to be efficiently and robustly coupled to a large number of densely packed discrete elements.

It is proposed that the fines particles in the cave can be modelled as a non-Newtonian fluid and thus the standard LBM formulation is extended to capture the constitutive behaviour of a bulk material. A range of constitutive models is investigated including the viscoelastic power law model and the viscoplastic Bingham model and a numerical rheometry technique is developed that allows the calibration of the material model to experimental data for different soils.

This thesis presents the issues relevant to this novel approach to fines migration modelling, such as fluid-solid interaction, the coupling of explicit schemes, and the characterisation of a bulk material as a non-Newtonian fluid. Extensive validation of the non-Newtonian LBM-DEM framework is presented for aspects of fluid flow, structural coupling and material characterisation. The developed framework is then applied in both two-dimensional and three-dimensional problems and the phenomenon of fines migration is investigated.

CONTENTS

LIST OF FIGURES

LIST OF TABLES

NOMENCLATURE

B_n	IMB cell coverage weighting function
c	lattice speed
c_n, c_t	discrete element normal and tangential damping coefficient
$\mathbf{c_i}$	particle distribution function velocities
c_s	lattice speed of sound
C_D	fluid drag coefficient
e	fluid energy
$e_{\alpha\beta}$	fluid rate of strain tensor
$\dot{e}$	characteristic rate of strain
f_i	particle distribution functions of the lattice Boltzmann method
f_i^{eq}	equilibrium particle distribution functions
f_i^{+}	post-collision particle distribution functions
f_i^{++}	post-body force particle distribution functions
g	single-particle distribution function of the Boltzmann equation
g^{eq}	Maxwell-Boltzmann equilibrium distribution function
$\mathbf{G}$	gravitational force
$\mathbf{j}$	fluid momentum

k_n, k_t	discrete element normal and tangential contact penalty
m	regularised Bingham model parameter
M	multiple relaxation time transformation matrix
$\bar{M}$	equivalent mass of contacting discrete elements
M_{ij}	linearised collision matrix
n	viscoelastic power law index
n_i	Boolean particle occupation variables in lattice gas automata
N_{SUB}	LBM-DEM sub-cycling number
p	fluid pressure
$p_{\alpha\beta}$	fluid stress tensor
$\mathbf{q}$	fluid heat flux
$\hat{\mathsf{S}}$	multiple relaxation time collision matrix
$\mathbf{u}$	fluid velocity
$\mathbf{U_p}$	discrete element translational velocity
$\mathbf{v_b}$	discrete element boundary velocity
w	equilibrium distribution function weights
$\mathbf{x}$	lattice coordinates
$\mathbf{X_p}$	discrete element centroid coordinates
Δt	time step
Δx	lattice spacing
δ	smallness parameter of the Chapman-Enskog analysis
$\delta_{\alpha\beta}$	Kroneckor delta
δ_n	discrete element contact penetration
ε_n	IMB cell coverage ratio
ϵ	Knudsen number

η	instantaneous viscosity in the cylindrical Couette rheometer
λ	DEM critical time step factor
μ	dynamic viscosity
ν	kinematic viscosity
ν_0	viscoelastic power law consistency constant
ξ	Boltzmann equation particle velocity
$\Pi_{\alpha\beta}$	momentum flux tensor
ρ	fluid density
τ	Bhatnagar-Gross-Krook single relaxation time
τ_y	Bingham plastic yield stress
$\tau_{\alpha\beta}$	fluid shear stress tensor
ϕ	Mohr-Coulomb friction angle
ω_n	resonant frequency of discrete element contact
Ω_i	generalised LGA/LBM collision operator
Ω_i^s	IMB method collision operator
$\mathbf{\Omega_p}$	discrete element angular velocity

CHAPTER 1

INTRODUCTION

Block caving is an underground mining method in which ore is allowed to collapse due to its own weight, in a controlled fashion, into chutes or draw points. This technique is usually applied to mine large orebodies that are too deep to extract economically using an open pit and also exhibit suitable rock mass properties. Such material properties will result in sufficient fragmentation and consequently caved material that can be handled and transported effectively. Generally, the block cave method allows for the bulk mining of large, relatively lower grade, orebodies. Examples of block cave mines include Northparkes copper-gold mine (Australia), Questa molybdenum mine (New Mexico, USA), Henderson molybdenum mine (Colorado, USA), Grasberg copper-gold-silver mine (Indonesia) and the Palabora copper deposit (South Africa), which operated formerly as an open pit.

One of the major advantages of block caving is the minimisation of the mining footprint incurred in the process of extracting minerals from the ground. An open cast pit is not necessary and stockpiles of waste material on the surface are consequently not required. Block caving can also be employed to extend the life of open pit mines that have become economically nonviable with surface extraction methods by continuing operations with a cave below the pit floor.

One of the disadvantages associated with block caving is the potential for surface subsidence. As ore is removed from the cave, support for the overhead waste is relaxed which can lead to subsidence and rupturing of the surface above the mine. Other problems and disadvantages include potentially prohibitive mine development costs, unpredictable caving of the orebody, and

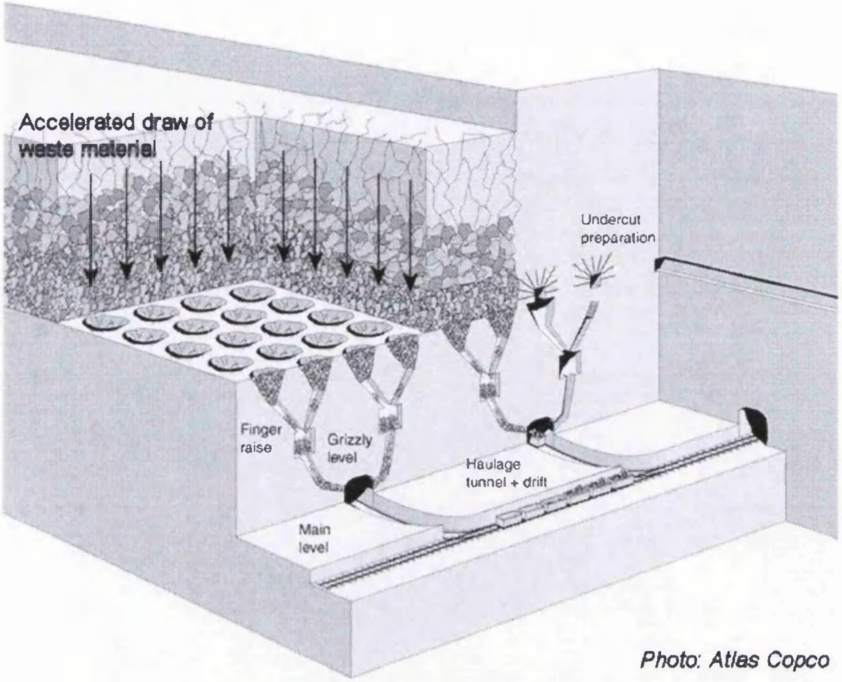

Figure 1.1: Schematic diagram of a block cave mine highlighting the migration of waste fines into the orebody. Photo: Atlas Copco

difficulties in observing the mine performance due its size and location underground.

Figure 1.1 is a schematic representation of a typical block cave mine. The development of the mine involves the drilling of the undercut level and production level tunnels followed by undercut blasting to initiate fragmentation in the orebody rock above. The draw bells are then blasted from the production level upwards into the undercut muck pile, thereby allowing the extraction of ore from draw points at the bottom of the draw bells. As fragmented material is drawn from the block cave the support of the intact cave back[1] is reduced until the stresses induced by gravity overcome the ultimate strength of the material. The fractured material is added to the top of the muck pile and the cave back propagates upwards. In this fashion, the rate and sequencing of draw is used to control the speed and location of caving. The drawn ore is transported to an underground comminution plant and then hauled to the surface for transport or further processing.

---

[1] The cave back is the lower boundary of the intact rock above the muck pile in the cave.

1.1 Description of the Industrial Problem

Aside from the constant challenge of maintaining stable and predictable caving, one of the primary issues that affects the performance of block caves is dilution. This occurs when material from the waste zones adjacent to the orebody mixes with the ore during caving and or draw, as discussed in more detail below. Other operational issues include air blast, water seepage and mud rush.

Air blast can occur when an air gap is allowed to grow between the cave back and the top of the muck pile. This is usually caused by resistance to fracturing of the cave back as draw removes the muck pile support. Sudden failure of the cave back over a large air gap can then blast air through the muck pile to the production level tunnels. Air blast potential is minimised by monitoring the location of the cave back and the amount of ore drawn from the cave to ensure no significant air gap is formed.

The presence of water in a cave in small amounts is acceptable, and can sometimes be advantageous, however large quantities of water can present problems such as poor working environment, risk of mud rush, washing out of potentially rich fines, and operational and handling problems in orepasses and chutes [82].

Mud rush in a block cave mine is a significant hazard to mine crews, equipment and production. Potential sources of mud in the region of a block cave need to be well understood so that appropriate measures can be taken to manage potential risks. Important factors that need to be considered are surface topography (i.e. presence of water reservoirs), ambient rainfall, erosion potential of material in and above the cave, geological structures and joints which can act as channels for directing mud into the cave region, effects of surface subsidence, permeability of the caved mass, and the viscosity of generated mud [82]. One important tool used for managing mud rushes is a water balance of the cave. If all water entering the cave from its surroundings is accounted for at the development level, it can be channelled and pumped out of the mine and the operators can be confident that no 'damming' of water and or mud is occurring in the caved material. Such accumulation can result in pressure build-up and increased chance of a mud rush.

Dilution, or more specifically the unexpected early onset of dilution, is a major obstacle to the profitability of a block cave. Dilution is realised when low grade waste material reports at the draw point along with or in extreme cases instead of ore. This reduces the concentration of mineralisation in the extracted material and thus reduces operational efficiency. Further, a cut-off grade is defined for the draw points of a block cave below which it is no longer economically viable to draw from them. Therefore, not only can high

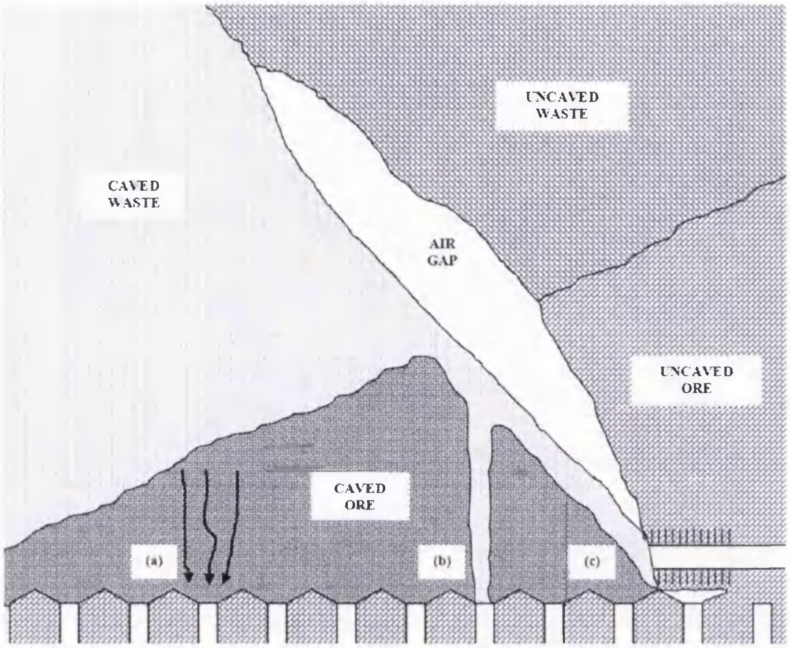

Figure 1.2: The three primary mechanisms of dilution in a block cave marked as (a) fines migration, (b) isolated draw and (c) rilling.

and unexpected levels of dilution reduce the mine efficiency it can also cause the unplanned closure of draw points which in turn affects the draw strategy of surrounding areas of the mine.

The three primary mechanisms of dilution are isolated draw (also known as rat-holing), rilling and fines migration. These are shown schematically in Figure 1.2. Isolated draw occurs when a narrow zone of the fragmented orebody moves towards the draw point without interacting with the surrounding material. This phenomenon, which is dependent on the draw point spacing and range of fragmentation size creates an accelerated path for waste above the muck pile to travel to the draw point as marked at (b) in Figure 1.2. Rilling, marked (c) in Figure 1.2, can occur when the attitude of the orebody-waste interface deviates from vertical. This creates the opportunity for waste to travel along the free surface of the muck pile and present unexpectedly at draw points. Finally, fines migration is the percolation of small particulate material through large blocks in the muck pile, as marked at (a) in Figure 1.2.

The phenomenon of fines migration during block cave operation is the focus of this research. As draw is undertaken the fragmented material in the draw zone moves towards the draw point and the voids between large blocks evolve. This continual changing of the void space allows smaller material (i.e.

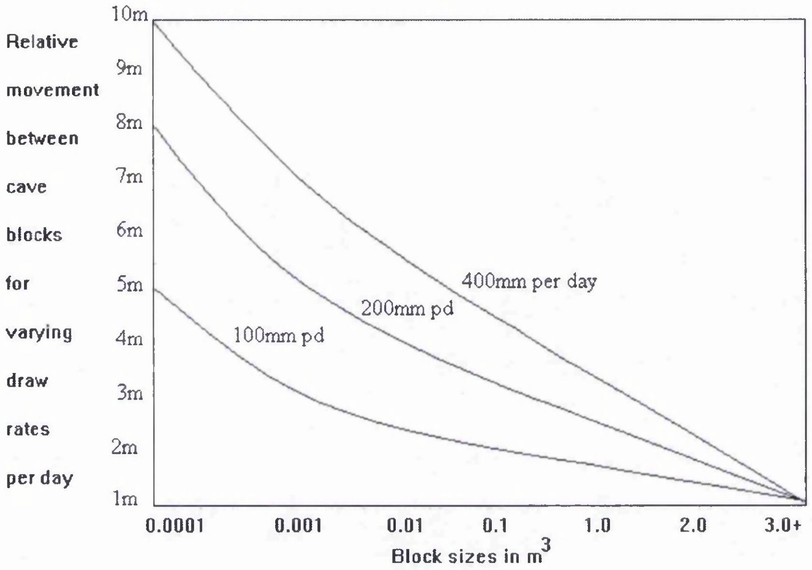

Figure 1.3: Graph of the relative speed of material in a block cave depending on the particle size and the rate of draw reproduced from *A Practical Manual on Block Caving* by Dennis Laubscher [82].

fines) to percolate into adjacent free space and subsequently move towards the draw point faster than its neighbouring blocks. A chart of the relative speed of blocks and fines for varying draw rates from *A Practical Manual on Block Caving* by Dennis Laubscher [82] is reproduced in Figure 1.3. This graph indicates that fines may travel as much as $10m$ further than blocks of $3m^3$ for an average draw of $400mm$ per day. Percolation rates of this magnitude go some way to explaining the early onset of dilution.

Fines migration allows the ingress of waste into the fragmented ore, which is obviously undesirable due to the resultant grade reduction. A rare exception to this rule is when the mineralisation in the waste zone occurs as fines which, upon migrating into the fractured ore, actually increase the grade of drawn material. However, typical mine operation attempts to minimise fines migration and dilution by maintaining even, interactive draw in the muck pile. This is in turn dependent on the use of the correct correct draw point spacing and draw strategy, resulting in a height of interaction zone (HIZ) above which the muck pile moves uniformly downward to the production level. Another common fines migration mitigation procedure is the breaking of mechanical arches of coarse blocks at draw points as soon as they are discovered. The reasoning for this procedure is that it is often possible to continue drawing fines from a draw point long after an arch of coarse blocks has formed at the same location [82].

1.2 Current Approaches to the Problem

A review of the literature reveals very little scientific effort targeted at the block cave phenomenon of fines migration. Typically, the broader problem of dilution is discussed within the even broader context of gravity flow. On this topic, the handbook by Rudolf Kvapil [77] is a good reference on the characterisation and prediction of flow behaviour in block, sub-level and panel caving.

Early investigations into the gravity flow of material in cave mines utilised scaled physical models [77]. These experiments observed the flow behaviour of sand through a transparent, scaled apparatus representative of a section of the mine geometry. Monitoring of the flow was aided by dying the initial configuration into layers or cells of different colours and observing the configuration as it was deformed by draw. These experiments offered insight into the geometry of the isolated draw zone (IDZ) above a single draw point as well as the interaction between neighbouring draw zones for different draw sequencing. One of the significant shortcomings of these physical models is the limitation to effectively two-dimensional (i.e. thin three-dimensional slices) experiments. In turn, these two-dimensional physical models suffer from the fact that they are not strictly two-dimensional due to the interaction of the sand and the glass faces of the apparatus.

In a complete 3D experiment the cross-sectional geometry of the draw zone obviously cannot be properly observed. However, despite the visibility problems three-dimensional scale models have been employed to investigate gravity flow. In these tests the undeformed sand is seeded with markers which are collected at the outlet as draw proceeds. Using the known amount of drawn material at the instant a marker is retrieved its path through the draw zone is approximated. Another significant issue with scaled physical modelling is the difficulty in extrapolating the behaviour of fine granular material such as river sand to blocks of $3m^3$ or larger as found in a cave mine. In addition, the use of a material such as river sand does not easily permit the inclusion of smaller material that would represent the real scale fines. To address the latter issue Power [107] undertook moderate-scale physical modelling using crushed rock with a distribution from $3\,mm$ to $45mm$, however some recent opinion is that the additional insight that can be offered by physical modelling is on the decline [51].

Another early technique for investigating the gravity flow inside a block cave is the use of infield markers. This approach involves placing a number of robust coded markers, such as reinforced concrete blocks or car tyres, in the orebody and then recording when and where (e.g. which draw point) they appear at the production level. Field marker monitoring eliminates the problem of scaling dynamic bulk material behaviour observed in physical models to that at the field scale. As an example, field scale draw trials were undertaken at Ridgeway gold mine between 2001 and 2004 to improve understanding of the granular flow kinematics that influence dilution entry, assess the effectiveness of interactive draw procedures, and to quantify recovery and dilution to improve future grade predictions [106].

More recently, Susaeta [124, 125] reported on the development of a mathematical model for gravity flow in cave mines based on the results of scaled physical modelling and infield experiments from three different sites. The model is defined as a function of extraction, material properties and layout geometry, and is able to reproduce characteristic behaviours such as isolated, isolated-interactive, and full interactive draw. By quantifying the level of interactivity in a proposed layout and draw strategy an assessment on the anticipated level of dilution could then be made. This is founded on the widely held belief that dilution is minimised by even, interactive draw [124].

An attempt at modelling gravity flow during block caving was made by Verduga and Ubilla [135] using numerical methods and a Mohr-Coulomb critical state model in cave geometries $100m$ wide and between $50m$ and $150m$ high. This work was based on a number of assumptions, the first being that the muck pile can be modelled as a continuous medium and the change in particle size due to secondary fragmentation can be ignored. The gravity flow was also assumed to be quasi-static based on the fact that only six to eight tonnes of material is removed from the draw point at approximately 10 minute intervals. Lastly, the Mohr-Coulomb model was assumed cohesionless and the modulus of deformation was defined as a function of the minor principal stress and the stress path. Draw was replicated numerically by relaxing the support of material at the draw point until deformations became too large for the solution to converge. The results highlighted the influence that the internal friction of the material has on the draw zone diameter (decreasing with increasing friction angle) and the abutment stresses adjacent the draw point (increasing with increasing friction angle). The effect of draw point spacing on interactivity of flow was also investigated with a spacing of 1.2 times the isolated draw zone diameter found to result in interactive draw. Within the context of fines migration the use of a single continuous medium to model the muck pile renders this approach inappropriate.

Another popular computational approach to modelling gravity flow in block caves is the use of cellular automata. This simple technique involves the discretisation of the cave into a number of cells each of which hosts a single binary variable. In gravity flow applications this variable defines the absence or presence of caved material at that location. Alfaro and Saavedra [3] presented an automaton that is based on the propagation of voids from the draw point to the free surface of the muck pile. A void is introduced at the draw point by emptying a cell which is then filled by material from one of the cells directly above it using a probabilistic function. In this fashion, the void randomly 'bubbles' to the top of the cave at which time a new void is introduced at the draw point. The shape of the resulting draw zone is tuned by altering the probability distribution for material dropping into the void below.

The attraction of cellular automata is that they are computationally inexpensive, allowing large geometries to be analysed for long time scales. This simplicity is at the expense of real physical features such as gravity, friction, stress and particle size which are not modelled directly but replicated using probabilistic rules. Therefore the prediction of a complex physical process is governed by the tuning of a small number of model parameters. CAVE-SIM [116] is a commercial code based on a parallel implementation of cellular automata that can be applied to full cave geometries over their anticipated life. This allows parametric studies to be undertaken on the operation of the mine with the results compared in dollar value. On the issue of dilution cellular automata can be used to predict dilution via rilling or isolated draw however the removal of a real particle size distribution means that fines migration cannot be captured.

The discrete element method (DEM) [27] is a numerical scheme that simulates the interaction of large assemblies of distinct particles and as such it is well suited to gravity flow problems. The details of the method are discussed in more detail in Section 3.1 but at its core is the interaction of non-deformable particles using a soft contact model. The strength of DEM is that it incorporates the physics and kinematics of bulk material flows including friction, stress from contact force, particle size and shape variation. Unfortunately the inclusion of this physical detail is expensive, and stability requirements for discrete element contact limit the length of the explicit scheme's time step. When implemented on contemporary computational hardware these factors mean that the number of particles and the length of time that can be simulated using DEM is subject to practical limits. Despite computational limits the discrete element method has been employed in the field of block caving to investigate caving and fragmentation, [111], swell in a draw column [32], dilution by rilling in a sub-level cave [115], and percolation in caved rock under draw [105]. More examples of DEM application in block caving, particularly in draw zone interaction, can be found in [68].

The work of Selldén and Pierce [115] used the discrete element method to simulate dilution in a sub-level cave by rilling at the brow of a draw point. The approximate dimensions of the cave were $27.5\,m$ high, $24.75m$ wide and $7m$ deep. The fine ore, coarse ore and waste material was simulated using two-ball clumps with equivalent radii of $0.25m$, $0.5m$ and $0.4m$, respectively. The model results were able to provide dilution entry points[2] that were similar to those observed in the field but quite different to those in the literature. Whilst this study did utilise a distribution of particle size, it's focus was on dilution by mass rilling rather than the migration of fines through large blocks.

Pierce [105] is currently the only known scientific work that focuses on the phenomenon of fines migration in block caves, which in this case is referred to as inter-particle percolation. This study used the discrete element method to investigate the percolation of small elements through large elements in both small scale shear tests and large scale cave draw simulations. The objective of the research was to determine the significant factors that influence percolation and to develop equations based on these trends for implementation in REBOP (discussed below). Of particular interest was the hypothesis that regions of high shear in bulk material flows induce greater levels of percolation. This work is of direct relevance to the present study, in which simulation of fines migration is the focus, and as such it is discussed in more detail in Chapters 5 and 6.

From this brief review of approaches to investigating gravity flow, and particularly fines migration, in cave mines it can be surmised that physical modelling has reached the limit of insight it can provide, simplistic models based on cellular automata ignore many important physical features, and DEM is still computationally intractable for field scale simulations. As an attempt to compromise between the relative strengths and weaknesses of CA and DEM, a *Rapid Emulator Based on PFC* (REBOP) was created [84]. REBOP is a numerical tool that uses a set of gravity flow rules to simulate the development and interaction of draw zones in a block cave. These particle interaction rules are a simplification of the behaviour that is observed in discrete element models of block cave draw including collapse, erosion and free-surface slumping. In a REBOP analysis, the muck pile is discretised into a number of horizontal layers and a mass balance is used to determine how much material moves from a layer to voids created in the layer below. The growth and interaction of isolated draw zones, both with other IDZs and the free surface of the muck pile, is predicted. By simplifying the contact mechanics of DEM into a set of rules the computational requirements are greatly reduced. This, like cellular automata, allows large geometries to be simulated over the anticipated life of the mine in acceptable computational time frames. Also, additional rules can be incorporated into REBOP to predict physical phenomena such as dilution, mixing, and grade extraction. This

---

[2] The dilution entry point is the percentage of total draw at which dilution first appears.

feature was exploited in the inter-particle percolation investigation of Pierce [105] through the generation of migration rules based on DEM simulations that could be added to REBOP.

The work of Carlson et al. [16] is an example of the application of REBOP in an industrial setting, in this case at Henderson Mine.

1.3 The Approach to this Work

A greater understanding of the kinematic behaviour of fines and ore within a cave during draw is integral to the solution of problems associated with fines migration. Other pertinent issues include the origin of the fines and its location within or near the muck pile, the size and shape of the fines, and the mathematical characterisation of the fines. Section 1.2 discussed the current approaches to the problem including field marker monitoring, laboratory scale experiments, and computational techniques such as cellular automata (CA), the discrete element method (DEM) and REBOP.

As has already been mentioned, DEM has been successfully employed to simulate the dynamics of large blocks in a cave during draw and to simulate small scale migration problems. However, the extension of this approach to modelling large scale migration of fines would require the simultaneous solution of elements larger than $2m$ (blocks) and smaller than $20mm$ (fines). In an industrial size, three-dimensional model this method would require in the order of 10^8 particles and subsequently be intractable. This issue is elucidated schematically in Figure 1.4a. It should be noted that the computational load associated with this number of particles does not present the only challenge to the DEM approach. The mass ratio of fines and blocks would also make stable contact difficult to achieve in regions of high contact force in the cave.

Considering the challenges associated with modelling fines using DEM, the approach of the present study is to model large cave blocks as discrete elements and the fines phase as an interstitial continuum. A novel computational approach is presented that incorporates the lattice Boltzmann method (LBM) in a nonlinear form for the simulation of the fines with the DEM for the simulation of large blocks in a fully coupled framework. The is shown schematically in Figure 1.4b where the spatial grid of the LBM is overlain on the discrete elements.

The LBM [90, 19] has emerged as an alternative to conventional computational fluid dynamics (CFD) methods that employ spatial and temporal discretisations of the Navier-Stokes equations. A key advantage of the LBM over traditional CFD (see [131] for a review) is its ability to be efficiently and robustly coupled to a large number of densely packed discrete elements.

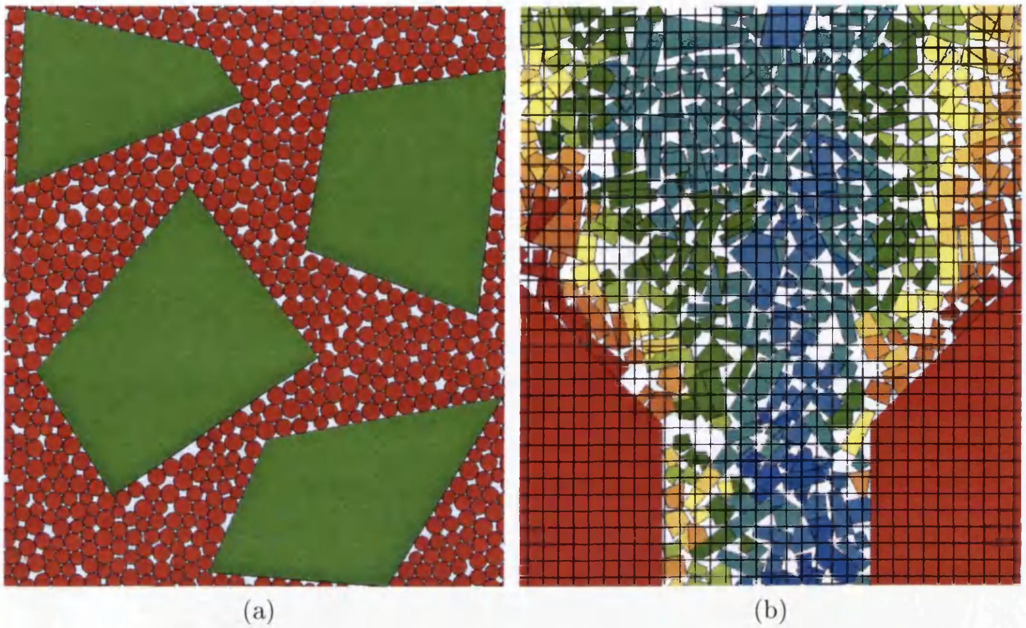

(a) (b)

Figure 1.4: Issues related to the application of the DEM and LBM in fines migration including (a) schematic representation of the large number of small elements required to represent the fines and (b) the coupling of the LBM grid to the DEM.

The main computational obstacles in Lagrangian CFD approaches are the need for continuous mesh geometry adaptation to circumvent severe mesh distortion, and the generation of a valid mesh for dense particle flows where intermittent discrete element contact is a dominant physical phenomenon. Since the work of Ladd [78, 79], a number of LBM fluid-solid interaction techniques have been developed including the immersed moving boundary technique by Noble and Torczynski [97]. Employing the discrete element method to account for particle-particle interactions gives rise to a fully coupled LBM-DEM computational framework capable of simulating dense phase particle suspensions. The explicit time stepping scheme of both LBM and DEM, when coupled using a dynamic time step update algorithm, makes this strategy a competitive numerical tool for the simulation of particle-fluid systems. Such a coupled methodology was first proposed by Cook et al. [25] in simulating particle-fluid systems dominated by particle-fluid and particle-particle interactions.

The block cave environment exhibits a binary mixture of both large blocks and fine powder type particulates. It is proposed that the motion of the fine particles will be modelled as a non-Newtonian fluid and thus the standard LB

Soil Particle Sizes	Fraction	Sieve Size	Diameter (mm)
Boulders		12" plus	≥ 300
Cobbles		3" - 12"	75 - 300
Gravels	- Coarse	0.75" - 3"	19 - 75
	- Fine	No. 4 - 0.75"	4.76 - 19
Sands	- Coarse	No. 10 - No. 4	2 - 4.76
	- Medium	No. 40 - No. 10	0.42 - 2
	- Fine	No. 200 - No. 40	0.074 - 0.42
Fines (silts and clays)		Passing No. 200	< 0.074

Table 1.1: The classification of soil particles as proposed by ASTM (Unified Soil Classification System), reproduced from McMinn [89].

formulation for Newtonian fluids must be extended to capture the constitutive behaviour of a granular medium or bulk material. In the relatively small volume of work dedicated to nonlinear fluids in the LBM, the power law model is the most popular choice for describing non-Newtonian behaviour. For example, the implementation of power law fluids within the LBM has been undertaken [1, 122] to investigate both pseudoplasticity (shear-thinning) and dilatancy (shear-thickening) behaviour. A similar approach is adopted in this work along with investigations of the adaptation of other constitutive models such as the Bingham plastic in the LBM.

The use of the term *fines* in this work is primarily governed by the relative distribution of oversize and undersize in a cave, and thus not necessarily quantified by one specific size grade. The American Society for Testing and Materials (ASTM) has proposed a system for the classification of soil particles based on size, which has been widely adopted. It is reproduced from [89] in Table 1.1. According to this system the term fines refers to particles with diameter less than $0.074mm$. However, in the context of this project the term *fines* is used to refer to material within the cave which is significantly smaller than the dominant blocks, which have characteristic lengths in the order of a metre. This would incorporate at least the particle classes of gravels, sands and fines and any future use of the term *fines* in this project should give consideration to this fact.

1.4 Scope of Research

The aim of this research is to develop a fully coupled LBM-DEM computational framework that is modified to include non-Newtonian constitutive models for fines. This framework is to then be applied to small and large scale percolation problems relevant to the phenomenon of fines migration in block cave mining. Both two-dimensional and three-dimensional simulations are considered.

This scope can be decomposed into four distinct components as follows.

1. Implement the lattice Boltzmann method for fluid flows in a commercial finite element-discrete element (FEM-DEM) code, *Elfen*, and validate its performance against a small number of benchmark tests.

2. Couple the newly-implemented LBM to the discrete element modelling features of the FEM-DEM code to facilitate hydrodynamic interaction, and validate the fluid-structure interaction against benchmarks and analytical solutions.

3. Research and implement non-Newtonian constitutive models suitable for the representation of granular material in the LBM-DEM framework. Then, investigate the modification and calibration of these constitutive models for the representation of bulk fines.

4. Apply the non-Newtonian LBM-DEM framework to investigate interparticle percolation and fines migration in both small and large scale models.

1.5 Document Layout

This thesis is divided into seven chapters. Following this introductory chapter, Chapter 2 discusses the implementation of the LBM in the *Elfen* finite element code. The evolution of the LBM is discussed and the basic components of the numerical model are outlined. Spatial discretisations (lattices), temporal solution schemes and existing LBM formulations are contrasted. The details of the Chapman-Enskog expansion are included, which shows how the simple kinetic formulae that comprise the LBM yield physical hydrodynamics in the macroscopic limit. Various boundary conditions and techniques for implementing fluid body forces are compared. Lastly, the performance of the LBM implementation is tested by comparing the results of simple, fluid-only analyses to analytical solutions and published benchmarks.

Chapter 3 covers aspects relating to the coupling of the LBM to the discrete element method. A brief outline of DEM is provided, and then a review of LBM-DEM coupling techniques is presented. Procedures for mapping the evolving structural field of the DEM to the static LBM grid, and the coupling of their respective explicit schemes, are discussed. The chapter is concluded with a number of tests of the LBM-DEM framework.

The coupling of closed form (i.e. circles/spheres) and discrete form (i.e. polygons/polyhedra) discrete elements is compared with empirical solutions and published results for quantities such as drag force and flow profile.

In Chapter 4 the characterisation of bulk materials (i.e. fines) as a non-Newtonian fluid is considered. The limited literature relevant to modelling dynamic flow of bulk materials is reviewed, with a focus on continuum models. The evaluation of the rate of strain tensor and non-Newtonian constitutive models in the LBM are discussed, including the viscoelastic power law and the viscoplastic Bingham model. The implementation of a power law model is tested against analytical solutions for both shear-thinning and shear-thickening behaviour. The rheometry of bulk materials is investigated and novel approach to calibrating the fines material properties via numerical experiments is demonstrated.

Two-dimensional applications of the LBM-DEM framework are presented in Chapter 5. The inter-particle percolation analysis conducted by Pierce [105] is replicated using both circular and polygonal discrete elements, and the migratory behaviour of the fines phase is observed. A mine-scale analysis of a three-bell block cave is also undertaken and the migration of fines under an arbitrary draw sequence is monitored.

Similarly, Chapter 6 includes three-dimensional applications of the coupled framework. A scaled version of the DEM percolation analysis is presented along with a mine-scale simulation of a partial block. The percolation simulations investigate sensitivity to material properties while the partial block cave analyses investigate the influence of draw strategy The effect of three-dimensional void space on the mechanisms of fines migration is also considered.

Finally, Chapter 7 discusses the results of the fines migration analyses and offers concluding remarks on the coupled LBM-DEM framework. Avenues for additional research, improvement and further development are also delineated.

CHAPTER 2

THE LATTICE BOLTZMANN METHOD FOR FLUID FLOWS

The lattice Boltzmann method (LBM) [90, 18, 19] has emerged as a promising numerical method for the simulation of fluid flows. It stands as an alternative to the more established computational fluid dynamics (CFD) approaches which involve the discretisation and solution of classical macroscopic equations such as Navier-Stokes. The underlying premise of the LBM is to construct a simplified kinetic model that incorporates mesoscopic[1] processes but exhibits identical behaviour to the classical hydrodynamic equations at the macroscopic level [19]. The justification of this approach stems from the observation that the macrodynamics of a fluid is the result of the collective behaviour of many particles in the system, however the details of these microscopic interactions are not essential [66].

The solution of the discrete lattice Boltzmann equation (LBE) involves the explicit evolution of particle distribution functions which reside at each lattice node. These functions are real variables and they relate the probable amount of fluid 'particles' moving with a discrete speed in a discrete direction at each node at each time increment. The LBM solution progresses via a two stage process at each time step. Collision (also known as relaxation) redistributes the functions that arrive at each node and then streaming (also known as convection) propagates the redistributed functions to their nearest

---

[1] The length at which one can reasonably discuss the properties of a material or phenomenon without having to discuss the behaviour of individual atoms which for solids and liquids is typically $1 \sim 10$ nanometres.

neighbour nodes.

By developing a simplified version of the kinetic equation, one avoids solving the full Boltzmann equation due to the reduction of the continuous phase space to a few discrete directions and thus the movement of each particle does not have to be calculated as in molecular dynamics simulations. The kinetic nature of the lattice Boltzmann method introduces three features that distinguish it from other numerical methods for fluid dynamics, namely [19];

1. The LBM utilises a limited velocity set in phase space as opposed to a complete functional space as in traditional kinetic theory using the Maxwell-Boltzmann equilibrium distribution,

2. The streaming operation of the LBM in velocity space, which has been borrowed from kinetic theory, is linear as opposed to the nonlinear convection terms in macroscopic continuum approaches. When combined with the collision operation the simplified convection allows recovery of nonlinear macroscopic advection via multiscale analysis such as the Chapman-Enskog expansion (see Section 2.5),

3. The macroscopic Navier-Stokes equations can be obtained from the LBM in the near-incompressible limit and the pressure can be calculated using an equation of state that is velocity independent.

When compared to continuum based CFD approaches the lattice Boltzmann method offers a number of advantages. First, the LBM is traditionally implemented on a regular, orthogonal grid although this is not mandatory (see Section 2.3). Second, the collision operator is a local process meaning that each lattice node only requires information from its own location to be relaxed. These first two features facilitate straightforward distribution of the LBM on massively parallel systems [113]. Third, in their most basic fashion boundary conditions can be implemented using another local nodal procedure (see Section 2.6), however other conditions of improved accuracy and increased complexity are available. This feature allows the LBM to be employed in simulations where boundaries are complex, moving, or interacting or a combination of all three. In such simulations macroscopic partial differential equations can become inadequate due to the complicated dynamics and associated thresholds and discontinuities. The lattice Boltzmann method also offers high space-time resolution and greatly reduced solution times in certain classes of problems [44].

As a consequence of these and other positive aspects, the LBM has found application in a vast array of fluid flow problems including magnetohydrodynamics, multiphase and multicomponent flows, flow in porous media, turbulent flows and particle suspensions.

2.1 Evolution from Lattice Gas Automata

The lattice Boltzmann method originated as an extension of lattice gas automata (LGA). Its development was motivated by the characteristic shortcomings of LGA such as the large noise-signal ratio, non-Galilean invariance and the unphysical dependence of the pressure on the velocity field. Another limitation of LGA is that the transport coefficients (i.e. viscosity) that emerge from the microscopic collision operators are of a very limited range [119].

A lattice gas automaton which first employed both discretised space and time was proposed by Hardy et al. [55]. The HPP model is the simplest arrangement of LGA as it uses an orthogonal grid with only four velocities. By using only four velocity directions, the lattice symmetry is insufficient to ensure the isotropy of the fourth degree tensor relating momentum flux to quadratic terms in the velocity (see Section 2.5). To overcome this problem, Frisch et al. [41] proposed the FHP-I, FHP-II and FHP-III hexagonal lattice gas (HLG) models, offering improvement of the collision operator to include deterministic and non-deterministic rules. This work was very important in the development of LGA as it recognised the importance of lattice symmetry in the recovery of the the Navier-Stokes equations. From these hexagonal lattice models, the continuous Navier-Stokes equations were derived for the first time.

Contemporary with this work was the description of a cellular automaton [139] that could be used to simulate macroscopic fluid dynamics and the simulation of 3D hydrodynamics using a lattice gas model in [29]. In the latter, the simulations are undertaken using two different lattice geometries. The first is a cubic lattice with speeds of 0, 1 and $\sqrt{2}$ and the second is a projection of the lattice gas implementation of the 4D Navier-Stokes equations on a face-centred hypercubic (FCHC) lattice.

The lattice gas automaton is constructed as a simplified, molecular dynamic model in which space is discretised by a symmetric lattice, time is discretised by an explicit time-stepping scheme and velocity is discretised by a small number of lattice-dependent particle speeds. A set of Boolean variables, $n_i(\mathbf{x}, t)$, is defined which describes the location, $\mathbf{x}$, of the particles on the domain lattice. From the initialised occupancy state, the location of particles is updated at each time step by two sequential processes, namely streaming and collision. During streaming, the particles move to the nearest-neighbour lattice node in their velocity direction, and in collision the particles arriving at a node interact and change velocity according to a set of scattering rules. The stream-collide evolution of these particle occupation variables is written as,

$$n_i(\mathbf{x}+\mathbf{c}_\mathrm{i},t+1) = n_i(\mathbf{x},t) + \Omega_i(n(\mathbf{x},t)) \qquad (i=0,1,2,\ldots,M), \qquad (2.1)$$

in which $\mathbf{x}$ is the position of the lattice node, $\mathbf{c}_\mathrm{i}$ is the velocity of the particle, Ω_i is the collision operator or scattering rules, and M is the number of velocity directions at each lattice node. Note that the zeroth velocity which is present on some models indicates a 'rest' particle which is not moving. The collision process in LGA can be deterministic or non-deterministic and is controlled by a table of scattering rules that conserve mass and linear momentum for every possible input combination. The exclusion principle is imposed which allows only one particle to exist at each velocity at each lattice node at any time [40].

Some advantages of lattice gas automata include intrinsic stability due to the presence of a Boltzmann H-theorem, straightforward implementation of boundary conditions via the bounce-back method and natural parallelisation due to the regular spatial discretisation and local collision operator. As already mentioned, limitations to the method do exist. As well as non-Galilean invariance and velocity dependent pressure, LGA simulations require an undesirable level of computational resources to overcome the technique's intrinsic noise at the microscopic scale. To obtain reasonably resolved densities (i.e. macroscopic, hydrodynamic variables) this noise is overcome by averaging the microscopic dynamic behaviour over a combination of large sub-regions of the lattice, long times, and numerous initial conditions [90].

2.2 Founding Principles of the LBM

Scientific phenomena in fluids and solids can be studied at different spatial and temporal scales. For example, at the microscopic level a fluid can be viewed as a system of a large number of molecular particles interacting in a complicated way whereas at the macroscopic level it is described in terms of continuous hydrodynamic quantities such as density and velocity fields. In general, the macroscopic behaviour depends very little on the interaction details at the microscopic [22] level. The link between the two is statistical physics (i.e. the Boltzmann equation) and this is where the averaged mesoscopic scale of the lattice Boltzmann method is exploited.

The primary feature of the extension of lattice gas automata to the lattice Boltzmann method is to replace the Boolean particle occupation variables, $n_i(\mathbf{x},t)$, with real-valued particle distribution functions, $f_i(\mathbf{x},t) = \langle n_i(\mathbf{x},t)\rangle$

[90], in which $\langle\rangle$ denotes an ensemble average. In contrast to macroscopic fluid dynamics, the primary variables in the LBM are not velocity or density but these particle distribution functions, which exist at each of the grid nodes that make up the fluid domain. These functions relate the probable amount of fluid 'particles' moving with a discrete speed in a discrete direction at each lattice node at each time increment. The particle distribution functions are analogous to the continuous, microscopic density function of the Boltzmann equation. In this way individual particle motion is averaged and the inherent statistical noise of LGA can be overcome [19]. The improved lattice Boltzmann model preserves a number of the advantages of LGA such as the efficiency of local operations, discrete structure and ease of parallelisation, but relative to LGA it requires far fewer lattice sites [18].

With the Boolean occupation variables of LGA replaced with the real-valued particle distribution functions the lattice Boltzmann equation can written as,

$$f_i\left(\mathbf{x}+\mathbf{c}_i\Delta t, t+\Delta t\right) = f_i\left(\mathbf{x}, t\right) + \Omega_i\left(f\left(\mathbf{x}, t\right)\right) \tag{2.2}$$

where Δx is the lattice spacing, Δt is the explicit time step, $c = |\Delta x/\Delta t|$ is the lattice speed and $\Omega_i\left(f\left(\mathbf{x}, t\right)\right)$ is the collision operator which controls the rate of relaxation of the particle distribution functions that meet at a node. The bounds of the index i vary depending on the spatial lattice used and are not included in (2.2). Note that in the LBM the discretisation of space is usually undertaken in a fashion that is consistent with the kinetic equation, so that the particle distribution function velocities are parallel to the locations of the neighbouring nodes. Therefore, the neighbours to node $\mathbf{x}$ can be defined as $\mathbf{x}+\mathbf{c}_i\Delta t$. The discretisation of a simple fluid domain and the location of the particle distribution functions are illustrated schematically in Figure 2.1.

The LBE (2.2) is evolved by the collision and streaming processes at each node at each time step. Collision (also known as relaxation) redistributes the functions that arrive at each node and then streaming (also known as convection) propagates the redistributed functions to their nearest neighbour nodes. Over a number of time steps the ordering of the streaming and collision operations is irrelevant.

It is sometimes convenient to rewrite the lattice Boltzmann equation in terms of the post-collision distribution function,

$$f_i^+\left(\mathbf{x}, t\right) = f_i\left(\mathbf{x}, t\right) + \Omega_i\left(f\left(\mathbf{x}, t\right)\right), \tag{2.3}$$

then (2.2) can be simplified as,

$$f_i\left(\mathbf{x}+\mathbf{c}_i\Delta t, t+\Delta t\right) = f_i^+\left(\mathbf{x}, t\right). \tag{2.4}$$

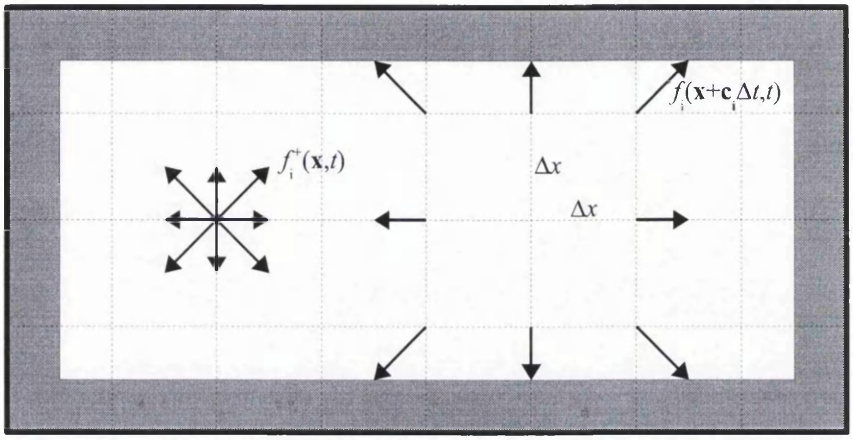

Figure 2.1: A simple enclosed domain discretised by the lattice Boltzmann method showing (left) the particle distribution functions after collision which are (right) then streamed to their respective neighbouring nodes.

This highlights the fact that no calculations are required in the streaming process as the post collision distribution function is simply shifted to its relevant neighbouring node.

The macroscopic fluid variables, density ρ, and momentum flux, $\rho\mathbf{u}$,

$$\rho = \sum_i f_i \tag{2.5}$$

$$\rho\mathbf{u} = \sum_i f_i \mathbf{c}_\text{i} \tag{2.6}$$

can be calculated at each lattice node as velocity moments of the particle distribution functions. The pressure is calculated directly from the density using an isothermal equation of state,

$$p = c_s^2 \rho, \tag{2.7}$$

in which $c_s = c/\sqrt{3}$ is lattice speed of sound (see Section 2.5 for more details).

It has been shown how the lattice Boltzmann equation has evolved from the microdynamical models of LGA. However it should be mentioned that the LBE can be derived directly from the continuous Boltzmann equation with a Bhatnagar-Gross-Krook (BGK) collision operator [4],

$$\frac{\partial g}{\partial t} + \xi \cdot \nabla g = -\frac{1}{\varepsilon\tau}\left(g - g^{eq}\right), \tag{2.8}$$

and a Maxwell-Boltzmann equilibrium distribution function. This is done using a discrete velocity set and a small Mach number expansion as detailed by He and Luo [58] or by discretising (2.8) using first order spatial and temporal finite differences [17, 15]. Although this discretisation only has first order convergence in space and time, it has been shown that the discretisation error has a special form which can be included in viscous terms, resulting in second order accuracy in both space and time.

2.3 Spatial Discretisation and Lattice Geometries

It was shown for lattice gas models [41] that a minimum lattice symmetry is necessary to ensure isotropy of the velocity tensors and recover the Navier-Stokes equations from the kinetic model. The same symmetry requirement applies to the lattice Boltzmann method. Historically, lattices have been based on periodic arrays of polyhedra, but as discussed in Section 2.3.3 this is not mandatory.

A choice of lattices is available in two and three dimensions with increasing number of velocities and therefore symmetry. However, the benefits of increased symmetry can be offset by the associated computational cost, especially in 3D.

2.3.1 2D: D2Q6, D2Q9

Options for spatial discretisation in two dimensions include six and seven velocity models based on a hexagonal arrangement known as D2Q6 and D2Q7, respectively. These lattices differ by the presence of a rest function with null velocity in the latter. The rest particle distribution function acts as a mass reservoir at each node allowing the pressure to be evaluated independently from the velocity [17]. Five velocity (D2Q5) and and nine velocity (D2Q9) models based on a regular orthogonal arrangement, both with a rest function, are also available. However, the D2Q5 is rarely used due to its limited lattice symmetry.

The velocity vectors of the D2Q6 lattice are included in (2.9) and shown schematically in Figure 2.2a.

$$\mathbf{c}_i = c\left(\cos\left(\frac{\pi\,(i-1)}{3}\right), \sin\left(\frac{\pi\,(i-1)}{3}\right)\right) \quad (i = 1, 2, 3, 4, 5, 6) \tag{2.9}$$

The velocity vectors of the D2Q9 lattice are included in (2.10) and shown schematically in Figure 2.2b. It should be noted that in the literature (e.g. [19]) the numbering of the D2Q9 velocities is often listed as continuous in an anticlockwise fashion, as opposed to the hierarchical numbering of orthogonal

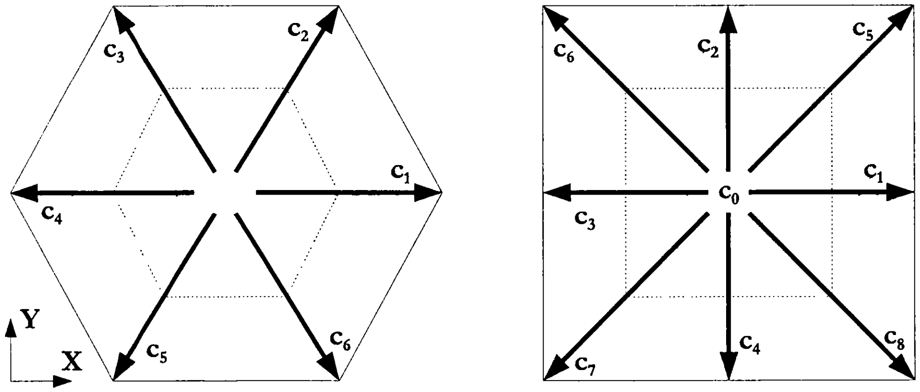

(a) (b)

Figure 2.2: Examples of LBM domain discretisations in 2D: (a) D2Q6 and (b) D2Q9.

followed by diagonal velocities as shown here.

$$\mathbf{c_i} = \begin{cases} 0 & (i = 0) \\ c\left(\cos\left(\frac{\pi(i-1)}{2}\right), \sin\left(\frac{\pi(i-1)}{2}\right)\right) & (i = 1, 2, 3, 4) \\ \sqrt{2}c\left(\cos\left(\frac{\pi(i-5)}{2} + \frac{\pi}{4}\right), \sin\left(\frac{\pi(i-5)}{2} + \frac{\pi}{4}\right)\right) & (i = 5, 6, 7, 8) \end{cases} \tag{2.10}$$

The D2Q9 lattice has been shown [118] to be significantly more accurate than the D2Q7 lattice, and as such the use of orthogonal lattices is more prevalent in the literature.

2.3.2 3D: D3Q15, D3Q18

The presence of orthogonal neighbours (distance of 1), diagonal neighbours (distance of $\sqrt{2}$), and bi-diagonal neighbours (distance of $\sqrt{3}$) on orthogonal lattices, in conjunction with the option of rest functions, allows a number of lattice options in 3D. Available lattices without a rest function include D3Q14 and D3Q18, and examples of those with a rest function include D3Q15 and D3Q27.

The components of the D3Q15 lattice are listed in matrix form as,

$$\mathbf{c_i} = c\begin{bmatrix} 0 & 1 & -1 & 0 & 0 & 0 & 0 & 1 & -1 & 1 & -1 & 1 & -1 & 1 & -1 \\ 0 & 0 & 0 & 1 & -1 & 0 & 0 & 1 & -1 & 1 & -1 & -1 & 1 & -1 & 1 \\ 0 & 0 & 0 & 0 & 0 & 1 & -1 & 1 & -1 & -1 & 1 & 1 & -1 & -1 & 1 \end{bmatrix}, \tag{2.11}$$

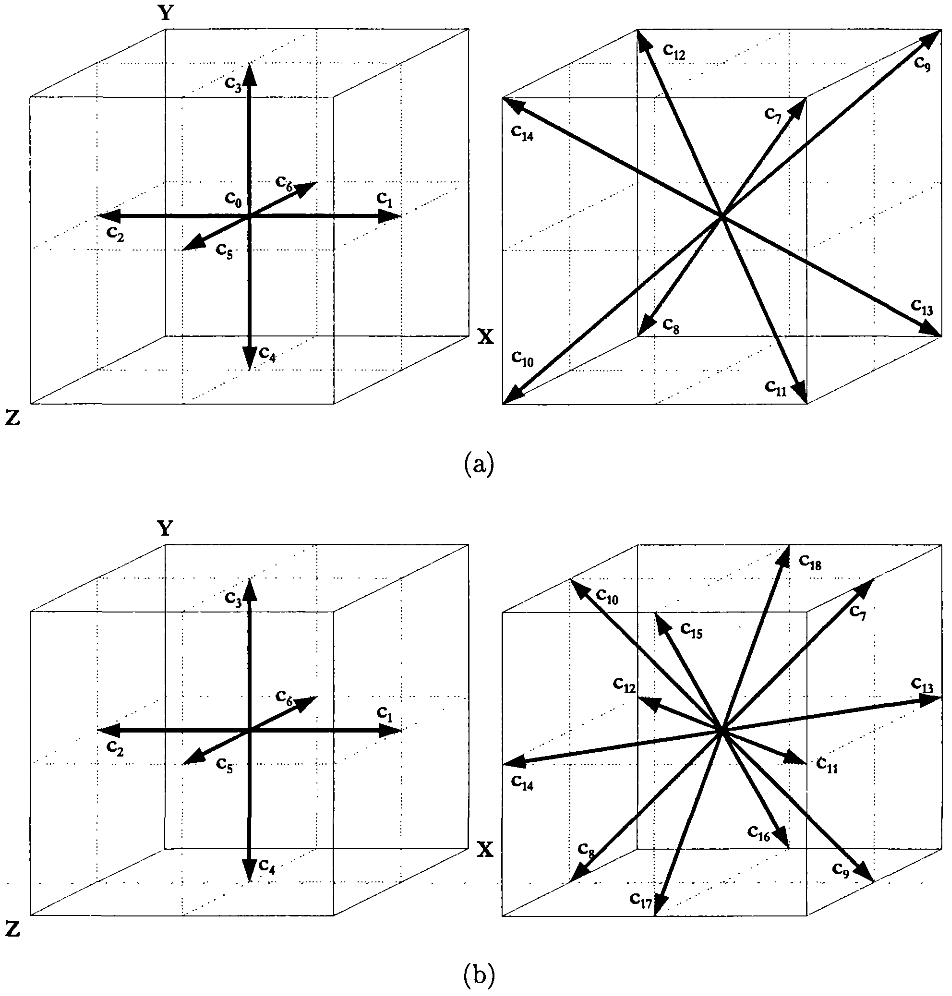

Figure 2.3: Examples of LBM domain discretisations in 3D decomposed to their orthogonal and diagonal components: (a) D3Q15 and (b) D3Q18.

and shown schematically in Figure 2.3a while the components of the D3Q18 lattice in matrix form are,

$$
\begin{aligned}
\mathbf{c_i} = c & \left[\begin{array}{ccccccccc} 1 & -1 & 0 & 0 & 0 & 0 & 1 & -1 & 1 \\ 0 & 0 & 1 & -1 & 0 & 0 & 1 & -1 & -1 \\ 0 & 0 & 0 & 0 & 1 & -1 & 0 & 0 & 0 \end{array}\right. \\
& \left.\begin{array}{ccccccccc} -1 & 0 & 0 & 0 & 0 & 1 & -1 & 1 & -1 \\ 1 & 1 & -1 & 1 & -1 & 0 & 0 & 0 & 0 \\ 0 & 1 & -1 & -1 & 1 & 1 & -1 & -1 & 1 \end{array}\right], \qquad (2.12)
\end{aligned}
$$

which are shown in Figure 2.3b.

As in 2D, an increased number of lattice directions generally improves the accuracy of the method. Maier et al. [86] compared the accuracy of the the D3Q15 and D3Q18 lattices in duct flow and found that the latter is slightly more accurate at predicting the maximum velocity in the channel. This comes at an increased computational expense. This is an extremely important consideration in 3D simulations where the total number of nodes increases as $(\Delta x)^{-3}$ and consequently the number of grid nodes required to discretise even modest physical domains can be considerable.

2.3.3 Irregular Grids

The spatial and temporal discretisations traditionally employed in the lattice Boltzmann method are not exclusive. They are in fact a legacy of the evolution of the LBM from lattice gas models [20] in which the discretisation of physical space is coupled to the discretisation of momentum space. This is because the discrete momenta of the LGA must result in the Boolean population functions arriving exactly at neighbouring nodes for the collision process to take place.

The symmetry of the LBM is actually composed of physical symmetry and lattice symmetry [15]. Physical symmetry means the symmetry attached to the velocity space and the equilibrium distribution for velocities, including the combination of specific weights in equilibrium distribution functions for different speeds, the choice of parameters in the equilibrium distribution functions, and a sufficient number of moving velocity directions. The lattice symmetry requirements are that the number of lattice directions (in $\mathbf{x}$ space) and the number of lattice links are the same as those for the particle distribution functions. Due to the analysis of real-valued particle distribution functions in the LBM the streaming process that ties the two symmetries together is not necessary. Therefore any finite difference or finite element scheme can be used to solve the lattice Boltzmann equation.

Nannelli and Succi [94] discussed a general framework to extend the lattice Boltzmann equation to arbitrary lattice geometries and demonstrated it for the case of a two-dimensional Poiseuille flow.

He et al. [59] used a nonuniform grid to study the flow of fluid through a sudden expansion. The approach used an interpolation-supplemented lattice Boltzmann equation (ISLBE) to facilitate nonuniform grids. The ISLBE adds a third operation to the regular collide-stream process of the LBM. After the streaming step interpolation of the particle distribution functions is undertaken to reconstruct their values at the irregular lattice positions. The assumption here is that the particle distribution functions are continuous in space and time, and smooth enough to be differentiated up to the order consistent with the interpolation. The algorithm was tested by simulating two-dimensional flow through a sudden expansion on a regular grid, a uniform rectangular grid and a nonuniform rectangular grid, and the results compared to experiments. The correlation of x-direction profiles at two locations in the channel was good between all the mesh types. Slight deviations from the numerical results was attributed to the asymmetry of the experimental apparatus (influence of gravity). The profile along the centreline was plotted using linear and quadratic interpolation. In the former case the error was significant. This is due to the linear interpolation being only first order accurate in terms of grid size, in contrast to the LBM which is second order accurate. Lastly, the recirculation stream lines adjacent to the expansion were found to be less accurate using the regular rectangular grid. This is because the discretisation was insufficient in regions of high velocity gradient.

In the work of He and Doolen [56], ISLBE was again used to simulate vortex shedding behind a cylinder at varying Reynolds numbers. For matters of convenience, the interpolation grid was based on a polar coordinate system that was concentric with the cylindrical obstacle in the analysis. The correlation of predicted Strouhal numbers, drag and lift coefficients to benchmark results was very good.

Filippova and Hänel [38] proposed a local grid refinement procedure based on *a priori* reduction of the grid size. The time step is also refined to keep constant grid speed. In order to maintain consistent viscosity the relaxation parameter in the refined region was modified according to (2.66) in Section 2.5.2. The interaction of the coarse and fine grids is then realised by an interpolation of the post-collision distribution functions at the nodes of both grids at the interface. The mesh refinement technique was tested in conjunction with a fitted boundary condition in the case of flow around a circular cylinder in which the region in the vicinity of the cylinder was refined. The results were found to correlate well with benchmark results for drag and lift coefficients.

Lastly, it should be noted that semi-implicit schemes have been proposed as a possible solution method [69, 15, 136] with potential benefits in faster steady state solutions and increased stability of non-Newtonian models.

2.4 The Relaxation Process

The relaxation, or collision, process in lattice gas automata comprised tables of scattering rules that listed probabilities of every output state for each input state [41], however the computational handling of these rules was cumbersome. Higuera and Jiménez [62] were able to simplify the lattice Boltzmann method by linearising the collision operator on the assumption that the particle distribution functions are never far from their equilibrium state, even in dynamic flows. The collision operator in (2.2) could then be written as,

$$\Omega_i\left(f\left(\mathbf{x},t\right)\right) = -M_{ij}\left(f\left(\mathbf{x},t\right) - f^{eq}\left(\mathbf{x},t\right)\right), \tag{2.13}$$

in which M_{ij} is the collision matrix and $f^{eq}\left(\mathbf{x},t\right)$ is the equilibrium distribution function (see Section 2.4.2) The dimensions of the square collision matrix are the number of lattice functions, and its components depend only the angle between the colliding functions. Following this important work, Higuera et al. [64] proposed an enhanced collision operator that was linearly stable.

Note that the collision process is local, which means that only the particle distribution functions arriving at a particular node are considered in the operation. This locality is paramount to the inherently parallel nature of the LBM. The collision operator must satisfy conservation principles at each lattice node and as such (2.14) and (2.15) must hold for mass and momentum conservation, respectively.

$$\sum_i \Omega_i = 0 \tag{2.14}$$

$$\sum_i \Omega_i \mathbf{c_i} = 0 \tag{2.15}$$

It is evident in (2.13) that the relaxation process acts on the non-equilibrium part of the distribution functions at a node to drive them towards equilibrium. It will be shown in Section 2.5 that the collision operator represents the action of hydrodynamic viscosity in the lattice Boltzmann method.

2.4.1 Single-Relaxation-Time Bhatnagar-Gross-Krook Models

Prior to the advent of the lattice Boltzmann method, a single-relaxation-time collision operator was employed by Bhatnagar et al. [4] in conjunction with an appropriate Maxwellian equilibrium function to facilitate solutions to the continuous Boltzmann equation. The same assumption, that the collision operator relaxes the local particle distribution functions at a single rate, can be applied to the LBM and the linear collision matrix simplified to,

$$M_{ij} = -\frac{1}{\tau}\delta_{ij}. \tag{2.16}$$

In conjunction with an appropriate equilibrium distribution function this results in the lattice Bhatnagar-Gross-Krook model (LBGK) that was proposed by a number of authors [18, 17, 108]. The LBGK collision operator is then written as,

$$\Omega_i\left(f\left(\mathbf{x},t\right)\right) = -\frac{\Delta t}{\tau}\left(f_i\left(\mathbf{x},t\right) - f_i^{eq}\left(\mathbf{x},t\right)\right). \tag{2.17}$$

The dimensionless relaxation time τ in (2.17) controls the rate at which the particle distribution monotonically relaxes towards equilibrium by operating directly on the non-equilibrium function. The simplicity of this collision operator has lead to its widespread implementation in the literature. It should be noted that the relaxation time τ is subject to stability and accuracy constraints which are discussed in Section 2.5.2.

2.4.2 The Equilibrium Function

Application of the classical Maxwell-Boltzmann equilibrium distribution from kinetic theory in the LBM is impractical. Instead a discrete, truncated form of the Maxwellian distribution is defined as the general form of the LBM equilibrium function [22, 58]. This function is a small-velocity expansion of the Maxwell-Boltzmann distribution [78],

$$f_i^{eq}\left(\mathbf{x},t\right) = A_i + B_i\left(\mathbf{c}_i\cdot\mathbf{u}\right) + C_i\left(\mathbf{c}_i\cdot\mathbf{u}\right)^2 + D_i u^2, \tag{2.18}$$

in which A_i, B_i, C_i and D_i are adjustable coefficients.

Criteria for an appropriate equilibrium function include;

1. Dependence only on local density and velocity,
2. A form that leads to the macroscopic Navier-Stokes equations via the Chapman-Enskog analysis,
3. Admission of additional properties such as the removal of non-physical lattice effects.

By the multi-scale Chapman-Enskog analysis of the lattice Boltzmann equation the general form of the equilibrium function (2.18) can be tuned to meet the above criteria. Details of this procedure can be found in Section 2.5. The equilibrium functions for the D2Q9 and D3Q15 lattices can then be written as,

$$f_I^{eq}\left(\mathbf{x},t\right) = \rho w_I\left[1 - \frac{3}{2c^2}\left(\mathbf{u}\cdot\mathbf{u}\right)\right], \tag{2.19}$$

$$f_{II}^{eq}\left(\mathbf{x},t\right) = \rho w_{II}\left[1 + \frac{3}{c^2}\left(\mathbf{c}_i\cdot\mathbf{u}\right) + \frac{9}{2c^2}\left(\mathbf{c}_i\cdot\mathbf{u}\right)^2 - \frac{3}{2c^2}\left(\mathbf{u}\cdot\mathbf{u}\right)\right], \tag{2.20}$$

$$f_{III}^{eq}\left(\mathbf{x},t\right) = \rho w_{III}\left[1 + \frac{3}{c^2}\left(\mathbf{c}_i\cdot\mathbf{u}\right) + \frac{9}{2c^2}\left(\mathbf{c}_i\cdot\mathbf{u}\right)^2 - \frac{3}{2c^2}\left(\mathbf{u}\cdot\mathbf{u}\right)\right], \tag{2.21}$$

in which f_I^{eq}, f_{II}^{eq} and f_{III}^{eq} and w_I, w_{II} and w_{III} are the functions and weights for the three speeds of each lattice. For the D2Q9 lattice $w_I = 4/9$ for $i = 0$, $w_{II} = 1/9$ for $i = 1, 2, 3, 4$ and $w_{III} = 1/36$ for $i = 5, 6, 7, 8$. For the D3Q15 lattice $w_I = 2/9$ for $i = 0$, $w_{II} = 1/9$ for $i = 1 \rightarrow 6$ and $w_{III} = 1/72$ for $i = 7 \rightarrow 14$.

2.4.3 Multiple-Relaxation-Time Models

Generalised versions of the lattice Boltzmann equation are available as alternatives to the LBGK model. Multiple-relaxation-time (MRT) models [80, 75, 49] replace the LBGK collision operator with the relaxation of a number of moments of the particle distribution functions at different rates.

Assuming the distribution functions can be written in vector form, $|f_i(\mathbf{x}, t)\rangle$, a transformation matrix, M, is defined to convert it to a vector of velocity moments $|m(\mathbf{x}, t)\rangle$,

$$|m(\mathbf{x}, t)\rangle = \mathsf{M}\,|f_i(\mathbf{x}, t)\rangle\,, \tag{2.22}$$

in which $|m(\mathbf{x}, t)\rangle$ for the D2Q9 lattice is,

$$|m(\mathbf{x}, t)\rangle = (\rho, e, \varepsilon, j_x, q_x, j_y, q_y, p_{xx}, p_{xy})^T\,. \tag{2.23}$$

The first three terms of this vector are the scalars of density, energy and energy square. The next four terms are the vectors of directional momenta and heat fluxes, and the last two terms are the second order tensors of stress. The collision process in MRT models is then written as,

$$\Omega_i(\mathbf{x}, t) = -\mathsf{M}^{-1}\hat{\mathsf{S}}\left[|m(\mathbf{x}, t)\rangle - |m^{eq}(\mathbf{x}, t)\rangle\right], \tag{2.24}$$

in which $\hat{\mathsf{S}} = \mathrm{diag}\left[S_0, S_1, \ldots, S_n\right]$ is the diagonal collision matrix and $|m^{eq}(\mathbf{x}, t)\rangle$ is the vector of equilibrium moments (see [80] for more details). It can be seen in (2.24) that the collision matrix operates on the non-equilibrium moments, which are then converted back to distribution functions via the inverse transformation matrix. In this fashion different hydrodynamic modes can be adjusted through the components of the collision matrix.

It is understood that multiple-relaxation-time LBM models exhibit increased numerically stability over their LBGK counterparts [80]. Related benefits include the ability to tune the hydrodynamic properties such as the bulk viscosity and the shear viscosity [7] and the reduction of pressure oscillations, particularly near the stability limit.

Due to its associated benefits, the increased computational cost associated with MRT models can be considered worthwhile especially in cases involving extremely turbulent flows [75] and non-Newtonian constitutive models (see Section 4.2).

2.5 From Mesoscopic to Macroscopic: The Chapman-Enskog Expansion

This section outlines the Chapman-Enskog expansion undertaken specifically on the D2Q9 lattice [66]. This is a multi-scale analysis of the lattice Boltzmann equation that shows how the Navier-Stokes equations are recovered in the near-incompressible limit with isotropy, Galilean invariance and a velocity independent pressure. This is required as evidence that the lattice Boltzmann method is an appropriate tool for solving Newtonian and non-Newtonian fluid mechanics problems.

The analysis is started with the lattice Boltzmann equation, a lattice geometry, a general form of the equilibrium function and some assumptions on temporal and spatial scales. The aim is to show that the combination of these ingredients can recover macroscopic equations of the same form as Navier-Stokes and in the process specify the details of the generalised equilibrium function [118].

To start, the moments of the lattice velocities are calculated to show the symmetric properties of the tensor $\sum_i (c_{i\alpha}c_{i\beta}\ldots)$ for subsequent use in the multi-scale analysis. Using the D2Q9 lattice vectors listed in (2.10) the first four orders of the tensor are,

$$\sum_i c_{i\alpha} = 0, \tag{2.25}$$

$$\sum_i c_{i\alpha}c_{i\beta} = \begin{cases} 2c^2\delta_{\alpha\beta} & (i = 1,2,3,4) \\ 4c^2\delta_{\alpha\beta} & (i = 5,6,7,8) \end{cases}, \tag{2.26}$$

$$\sum_i c_{i\alpha}c_{i\beta}c_{i\gamma} = 0, \tag{2.27}$$

$$\sum_i c_{i\alpha}c_{i\beta}c_{i\gamma}c_{i\theta} = \begin{cases} 2c^4\delta_{\alpha\beta\gamma\theta} & (i = 1,2,3,4) \\ 4c^4\Delta_{\alpha\beta\gamma\theta} - 8c^4\delta_{\alpha\beta\gamma\theta} & (i = 5,6,7,8) \end{cases}, \tag{2.28}$$

in which $\delta_{\alpha\beta}$ is the Kronecker delta, $\delta_{\alpha\beta\gamma\theta}$ is the fourth order analogue of the Kronecker delta and $\Delta_{\alpha\beta\gamma\theta} = \delta_{\alpha\beta}\delta_{\gamma\theta} + \delta_{\alpha\gamma}\delta_{\beta\theta} + \delta_{\alpha\theta}\delta_{\beta\gamma}$. The details of these identities can be found in Appendix A. It is important to note that these identities will be utilised with the non-dimensionalised form of the lattice speed, $c = \Delta x/\Delta t = 1$, in order to simplify the multi-scale analysis. The relationship between physical and lattice units in the LBM is discussed in more detail in Appendix B.

The general form of the equilibrium function $f_i^{eq}(\mathbf{x},t)$ (2.18) can be written [17] for the three speeds of the D2Q9 lattice as,

$$f_i^{eq}(\mathbf{x},t) = \begin{cases} A_0 + B_0 c_{i\alpha} u_\alpha + C_0 c_{i\alpha} c_{i\beta} u_\alpha u_\beta + D_0 u_\alpha u_\alpha & (i=0) \\ A_1 + B_1 c_{i\alpha} u_\alpha + C_1 c_{i\alpha} c_{i\beta} u_\alpha u_\beta + D_1 u_\alpha u_\alpha & (i=1,2,3,4) \\ A_2 + B_2 c_{i\alpha} u_\alpha + C_2 c_{i\alpha} c_{i\beta} u_\alpha u_\beta + D_2 u_\alpha u_\alpha & (i=5,6,7,8) \end{cases}, \tag{2.29}$$

in index notation where the Einstein summation convention is used.

The general form of the equilibrium function can be considered as a small velocity expansion up to second order, and a simplified representation of the continuous Maxwell-Boltzmann equilibrium function in kinetic theory [108]. The coefficients (A_0, B_0, ... , C_2, D_2) can be progressively determined during the multi-scale analysis of the lattice Boltzmann equation so that the macroscopic continuity and momentum equations are recovered. Due to the null velocity of the rest distribution it is obvious that $B_0 = C_0 = 0$.

A continuous form of the lattice Boltzmann equation up to $\mathcal{O}(\delta^2)$ is obtained by undertaking a Taylor expansion of the LBE (2.2),

$$\begin{aligned} f_i(\mathbf{x}+\delta\mathbf{c}_i, t+\delta) &= f_i(\mathbf{x},t) + \delta\frac{\partial}{\partial\mathbf{x}} f_i(\mathbf{x},t)\,\mathbf{c}_i + \delta\frac{\partial}{\partial t} f_i(\mathbf{x},t) \\ &\quad + \frac{1}{2}\delta^2\frac{\partial^2}{\partial\mathbf{x}^2} f_i(\mathbf{x},t)\,\mathbf{c}_i\mathbf{c}_i + \frac{1}{2}\delta^2\frac{\partial^2}{\partial t^2} f_i(\mathbf{x},t) \\ &\quad + \delta^2\frac{\partial^2}{\partial\mathbf{x}\partial t} f_i(\mathbf{x},t)\,\mathbf{c}_i + \mathcal{O}(\delta^3), \end{aligned}$$

which after replacing $f_i(\mathbf{x},t)$ with f_i can be substituted into (2.2) with the BGK collision operator (2.17),

$$\begin{aligned} \delta\left(\frac{\partial f_i}{\partial t} + \mathbf{c}_i\cdot\nabla f_i\right) + \frac{1}{2}\delta^2\left(\frac{\partial^2 f_i}{\partial t^2} + \mathbf{c}_i\cdot\nabla\frac{\partial f_i}{\partial t}\right. \\ \left. + \mathbf{c}_i\mathbf{c}_i\cdot\nabla\nabla f_i\right) + \mathcal{O}(\delta^3) &= \frac{-1}{\tau}\left(f_i - f_i^{eq}\right), \end{aligned}$$

and then simplified to,

$$\delta\left(\frac{\partial}{\partial t} + (\mathbf{c}_i\cdot\nabla)\right) f_i + \frac{1}{2}\delta^2\left(\frac{\partial}{\partial t} + (\mathbf{c}_i\cdot\nabla)\right)^2 f_i + \mathcal{O}(\delta^3) = \frac{-1}{\tau}\left(f_i - f_i^{eq}\right). \tag{2.30}$$

The multi-scale Chapman-Enskog expansion is then applied to (2.30) using a smallness parameter. To find the long-time long-wavelength dynamics, a scaling parameter ϵ is introduced, defined as the ratio of the lattice spacing to a characteristic macroscopic length. The hydrodynamic limit requires

$\epsilon \ll 1$ [78]. It is suggested by Hou et al. [66] that the small physical time step, δ, can be used as the smallness parameter and thus play the role of the I

$$f_i = f_i^{eq} + \delta f_i^{neq1} + \delta^2 f_i^{neq2} + \mathcal{O}\left(\delta^3\right), \tag{2.31}$$

distr

in which f_i^{neq1} and f_i^{neq2} represent the deviation[3] in increasing order of

$$f_i = f_i^{eq} + \delta f_i^{neq1} + \delta^2 f_i^{neq2} + \mathcal{O}\left(\delta^3\right), \tag{2.31}$$

in which f_i^{neq1} and f_i^{neq2} represent the deviation[3] in increasing order of

the particle distribution functions from equilibrium. Time can then be decomposed into convective (t_0) and diffusive (t_1) time scales [19, 121] as $t = t_0 + \delta^{-1} t_1 + \delta^{-2} t_2$ which allows the differential operator,

$$\frac{\partial}{\partial t} = \frac{\partial}{\partial t_0} + \delta \frac{\partial}{\partial t_1} + \delta^2 \frac{\partial}{\partial t_2} + \ldots . \tag{2.32}$$

On the assumption that the equilibrium deviations of the particle distribution functions do not contribute to the macroscopic density or momentum the following constraints can be defined,

$$\textstyle\sum_i f_i^{eq} = \sum_i f_i = \rho, \quad \sum_i f_i^{eq} \mathbf{c_i} = \sum_i f_i \mathbf{c_i} = \rho \mathbf{u}, \tag{2.33}$$

$$\textstyle\sum_i f_i^{neq} = 0 \quad , \quad \sum_i f_i^{neq} \mathbf{c_i} = 0, \tag{2.34}$$

which can be used in the determination of the equilibrium function coefficients. Substituting the general expression for the equilibrium function (2.29) into the density summation in (2.33) gives,

$$\begin{aligned} \rho \;=\; & A_0 + D_0 u_\alpha u_\alpha \\ & +4A_1 + \sum_{i=1\to 4} \left(B_1 c_{i\alpha} u_\alpha + C_1 c_{i\alpha} c_{i\beta} u_\alpha u_\beta\right) + 4D_1 u_\alpha u_\alpha \\ & +4A_2 + \sum_{i=5\to 8} \left(B_2 c_{i\alpha} u_\alpha + C_2 c_{i\alpha} c_{i\beta} u_\alpha u_\beta\right) + 4D_2 u_\alpha u_\alpha, \end{aligned}$$

which can be simplified using the identities in (2.25), (2.26), (2.27) and (2.28) to give,

$$\rho = A_0 + 4A_1 + 4A_2 + \left(2C_1 + 4C_2 + D_0 + 4D_1 + 4D_2\right) u^2.$$

---

[2] From kinetic theory, the Knudsen number is the ratio of the molecular mean free path (the average distance a fluid molecule can move without colliding with another molecule) to a representative physical length scale (e.g. the radius of a body in a fluid). Generally, it varies from high for rarified gases to low for dense fluids. Consequently, the Knudsen number is useful for determining whether statistical mechanics or continuum mechanics should be used to represent a flow problem [4].

[3] It is an important assumption of kinetic theory that even in dynamic flows the microscopic behaviour is never far from equilibrium [41].

Equating the density and velocity terms [144] then leaves,

$$\rho = A_0 + 4A_1 + 4A_2, \tag{2.35}$$

$$0 = 2C_1 + 4C_2 + D_0 + 4D_1 + 4D_2. \tag{2.36}$$

Similarly, substituting the equilibrium function into the momentum flux summation in (2.33) gives,

$$\begin{aligned} \rho u_\alpha &= \sum_{i=1\to 4} \left(A_1 c_{i\alpha} + B_1 c_{i\alpha} c_{i\beta} u_\beta + C_1 c_{i\alpha} c_{i\beta} c_{i\gamma} u_\beta u_\gamma + D_1 c_{i\alpha} u_\beta u_\beta\right) \\ &\quad + \sum_{i=5\to 8} \left(A_2 c_{i\alpha} + B_2 c_{i\alpha} c_{i\beta} u_\beta + C_2 c_{i\alpha} c_{i\beta} c_{i\gamma} u_\beta u_\gamma + D_2 c_{i\alpha} u_\beta u_\beta\right), \end{aligned}$$

which can again be simplified using the velocity moment identities to leave,

$$\rho = 2B_1 + 4B_2. \tag{2.37}$$

The Taylor expansion of the LBE can be found to first order in δ by substituting the equilibrium (2.31) and differential time (2.32) expansions into (2.30),

$$\begin{aligned} &\left(\delta \frac{\partial}{\partial t_0} + \delta^2 \frac{\partial}{\partial t_1} + \delta\left(\mathbf{c}_i \cdot \nabla\right)\right)\left(f_i^{eq} + \delta f_i^{neq1}\right) \\ &\quad + \frac{1}{2}\left(\delta^2 \frac{\partial}{\partial t_0} + \delta^3 \frac{\partial}{\partial t_1} + \delta^2\left(\mathbf{c}_i \cdot \nabla\right)\right)^2 \\ &\qquad \left(f_i^{eq} + \delta f_i^{neq1}\right) + \mathcal{O}\left(\delta^3\right) = \frac{-\delta}{\tau} f_i^{neq1}, \end{aligned} \tag{2.38}$$

and removing all term of $\mathcal{O}\left(\delta^2\right)$ and higher,

$$\left(\frac{\partial}{\partial t_0} + \left(\mathbf{c}_i \cdot \nabla\right)\right) f_i^{eq} = \frac{-1}{\tau} f_i^{neq1}. \tag{2.39}$$

Using the second order expansions of equilibrium and differential time and removing all terms of $\mathcal{O}\left(\delta^3\right)$ and higher the LBE to second order in δ can be found,

$$\begin{aligned} &\delta\left[\left(\frac{\partial}{\partial t_0} + \left(\mathbf{c}_i \cdot \nabla\right)\right) f_i^{eq}\right] \\ &+ \delta^2\left[\frac{\partial}{\partial t_1} f_i^{eq} + \frac{\partial}{\partial t_0} f_i^{neq1} + \left(\mathbf{c}_i \cdot \nabla\right) f_i^{neq1}\right] \\ &+ \frac{\delta^2}{2}\left[\left(\frac{\partial}{\partial t_0} + \left(\mathbf{c}_i \cdot \nabla\right)\right)^2 f_i^{eq}\right] = \frac{-\delta}{\tau}\left(f_i^{neq1} + \delta f_i^{neq2}\right), \end{aligned}$$

and simplified using (2.39) to,

$$\frac{\partial}{\partial t_1} f_i^{eq} + \left(1 - \frac{1}{2\tau}\right)\left(\frac{\partial}{\partial t_0} + (\mathbf{c_i} \cdot \nabla)\right) f_i^{neq1} = \frac{-1}{\tau} f_i^{neq2}. \tag{2.40}$$

Undertaking a summation of (2.39) over all lattice directions,

$$\frac{\partial}{\partial t_0} \sum_i f_i^{eq} + \nabla \cdot \sum_i f_i^{eq} \mathbf{c_i} = \frac{-1}{\tau} \sum_i f_i^{neq1},$$

and utilising the definitions of density and momentum flux and the constraint on non-equilibrium functions results in,

$$\frac{\partial \rho}{\partial t_0} + \nabla \cdot (\rho \mathbf{u}) = 0, \tag{2.41}$$

which is the continuity equation to $\mathcal{O}(\delta)$. This shows that density fluctuations relax on the timescale t_0 via the propagation of sound waves, and therefore decouple from the t_1 timescale evolution of the viscous stresses [78]. Multiplying (2.39) by $\mathbf{c_i}$ and performing the same summation gives,

$$\frac{\partial}{\partial t_0}(\rho \mathbf{u}) + \nabla \cdot \Pi^{eq} = 0, \tag{2.42}$$

in which $\Pi^{eq} = \sum_i f_i^{eq} \mathbf{c_i} \mathbf{c_i}$ is the first order momentum flux tensor. Similarly, summing (2.40) over i,

$$\frac{\partial}{\partial t_1} \sum_i f_i^{eq} + \left(1 - \frac{1}{2\tau}\right)\left(\frac{\partial}{\partial t_0} + (\mathbf{c_i} \cdot \nabla)\right) \sum_i f_i^{neq1} = \frac{-1}{\tau} \sum_i f_i^{neq2},$$

and using the same constraints gives the continuity equation to $\mathcal{O}(\delta^2)$,

$$\frac{\partial \rho}{\partial t_1} = 0, \tag{2.43}$$

which means that there are no density fluctuations and the fluid is incompressible at the t_1 timescale. All relaxation of density fluctuations takes place on the t_0 timescale [78]. Multiplying (2.40) by $\mathbf{c_i}$ and summing gives,

$$\frac{\partial}{\partial t_1}(\rho \mathbf{u}) + \left(1 - \frac{1}{2\tau}\right) \nabla \cdot \Pi^{neq1} = 0, \tag{2.44}$$

in which Π^{neq1} is the second order momentum flux tensor.

The first order momentum flux tensor can be rewritten in index notation, after including the general form of the equilibrium distribution function and applying the identities in (2.25), (2.26), (2.27) and (2.28),

$$\begin{aligned}\Pi^{eq}_{\alpha\beta} &= 2A_1\delta_{\alpha\beta} + 2C_1\delta_{\alpha\beta\gamma\theta}u_\gamma u_\theta + 2D_1\delta_{\alpha\beta}u_\gamma u_\gamma \\ &\quad +4A_2\delta_{\alpha\beta} + C_2\left(4\Delta_{\alpha\beta\gamma\theta} - 8\delta_{\alpha\beta\gamma\theta}\right)u_\gamma u_\theta + 2D_2\delta_{\alpha\beta}u_\gamma u_\gamma,\end{aligned}$$

which reduces to,

$$\begin{aligned}\Pi^{eq}_{\alpha\beta} &= \left[2A_1 + 4A_2 + \left(4C_2 + 2D_1 + 4D_2\right)u^2\right]\delta_{\alpha\beta} \\ &\quad +8C_2 u_\alpha u_\beta + \left(2C_1 - 8C_2\right)u_\alpha u_\beta \delta_{\alpha\beta}.\end{aligned} \tag{2.45}$$

In the absence of body forces, the momentum flux tensor for an incompressible fluid is,

$$\Pi_{\alpha\beta} = \rho u_\alpha u_\beta + p\delta_{\alpha\beta} - \mu\left(\frac{\partial u_\alpha}{\partial x_\beta} + \frac{\partial u_\beta}{\partial x_\alpha}\right). \tag{2.46}$$

In considering the form of (2.45) it can be seen that the first term is similar to the pressure term in the the Navier-Stokes equations as in (2.46). Therefore, to ensure a velocity independent pressure in the LBM the velocity component within the pressure term in (2.45) is forced to vanish via its coefficient,

$$4C_2 + 2D_1 + 4D_2 = 0. \tag{2.47}$$

Galilean invariance is ensured by removing the anisotropic $u_\alpha u_\beta \delta_{\alpha\beta}$ term,

$$2C_1 - 8C_2 = 0, \tag{2.48}$$

and by direct comparison of (2.45) and (2.46) it can be assumed that,

$$8C_2 = \rho. \tag{2.49}$$

At this stage an isothermal equation of state for the pressure is introduced such that,

$$p = c_s^2\rho = 2A_1 + 4A_2, \tag{2.50}$$

in which c_s is the speed of sound on the D2Q9 lattice. Applying (2.47), (2.48), (2.49) and (2.50) to (2.45) gives the momentum flux tensor to $\mathcal{O}(\delta)$,

$$\Pi^{eq}_{\alpha\beta} = \rho u_\alpha u_\beta + c_s^2\rho\delta_{\alpha\beta}, \tag{2.51}$$

which can then be placed in the first order momentum equation (2.42) to yield,

$$\frac{\partial}{\partial t_0}(\rho\mathbf{u}) + \nabla\cdot(\rho\mathbf{u}\mathbf{u}) + \nabla\left(c_s^2\rho\right) = 0. \tag{2.52}$$

Equations (2.41) and (2.52) are the inviscid Euler equations which have been derived from the LBE by a first order expansion in the smallness parameter δ. It is subsequently apparent that the first order expansion is insufficient for extracting the viscous terms of the Navier-Stokes equations.

In order to derive a higher order momentum equation from the LBE the $\mathcal{O}\left(\delta^2\right)$ momentum flux tensor must be found using the same procedure as above. Recalling that $\Pi^{neq1} = \sum_i f_i^{neq1}\mathbf{c}_i\mathbf{c}_i$ and that (2.39) can be rearranged to define f_i^{neq1} results in,

$$\begin{aligned}\Pi^{neq1}_{\alpha\beta} &= -\tau\left[-c_s^2\frac{\partial}{\partial x_\gamma}\left(\rho u_\gamma\right)\delta_{\alpha\beta} + \frac{\partial}{\partial t_0}\left(\rho u_\alpha u_\beta\right) + \left(2B_1 - 8B_2\right)\frac{\partial u_\beta}{\partial x_\alpha}\delta_{\alpha\beta}\right.\\ &\qquad \left. +4B_2\frac{\partial u_\gamma}{\partial x_\gamma}\delta_{\alpha\beta} + 4B_2\left(\frac{\partial u_\beta}{\partial x_\alpha} + \frac{\partial u_\alpha}{\partial x_\beta}\right)\right]. \qquad (2.53)\end{aligned}$$

The details of this derivation can be found in Appendix C. To maintain isotropy the third term of (2.53) is removed by,

$$2B_1 - 8B_2 = 0, \qquad (2.54)$$

which when combined with (2.37) gives,

$$B_1 = \frac{\rho}{3},\ \ B_2 = \frac{\rho}{12}. \qquad (2.55)$$

To remove the time derivative in (2.53) the product rule is applied,

$$\frac{\partial}{\partial t_0}\left(\rho\mathbf{u}\mathbf{u}\right) = \mathbf{u}\frac{\partial}{\partial t_0}\left(\rho\mathbf{u}\right) + \frac{\partial}{\partial t_0}\left(\rho\mathbf{u}\right)\mathbf{u}$$

and then substituting the inviscid momentum equation (2.52),

$$\frac{\partial}{\partial t_0}\left(\rho\mathbf{u}\mathbf{u}\right) = \mathbf{u}\left[-\nabla\cdot\left(\rho\mathbf{u}\mathbf{u}\right) - \nabla\left(c_s^2\rho\right)\right] + \left[-\nabla\cdot\left(\rho\mathbf{u}\mathbf{u}\right) - \nabla\left(c_s^2\rho\right)\right]\mathbf{u},$$

to give, in index notation,

$$\frac{\partial}{\partial t_0}\left(\rho u_\alpha u_\beta\right) = -\frac{\partial}{\partial x_\gamma}\left(\rho u_\alpha u_\beta u_\gamma\right) - u_\alpha\frac{\partial}{\partial x_\beta}\left(c_s^2\rho\right) - \frac{\partial}{\partial x_\alpha}\left(c_s^2\rho\right)u_\beta. \qquad (2.56)$$

Substituting (2.55) and (2.56) into (2.53) gives,

$$\begin{aligned}\Pi^{neq1}_{\alpha\beta} &= -\tau\left[\left(\frac{1}{3} - c_s^2\right)\frac{\partial}{\partial x_\gamma}\left(\rho u_\gamma\right)\delta_{\alpha\beta} - u_\alpha\frac{\partial}{\partial x_\beta}\left(c_s^2\rho\right) - u_\beta\frac{\partial}{\partial x_\alpha}\left(c_s^2\rho\right)\right.\\ &\qquad \left. +\frac{1}{3}\frac{\partial}{\partial x_\alpha}\left(\rho u_\beta\right) + \frac{1}{3}\frac{\partial}{\partial x_\beta}\left(\rho u_\alpha\right) - \frac{\partial}{\partial x_\alpha}\left(\rho u_\alpha u_\beta u_\gamma\right)\right]. \qquad (2.57)\end{aligned}$$

The fourth and fifth terms of (2.57) can be expanded using the product rule and the equation then regrouped,

$$\begin{aligned}\Pi^{neq1}_{\alpha\beta} &= -\tau\left[\left(\frac{1}{3}-c_s^2\right)\frac{\partial}{\partial x_\gamma}\left(\rho u_\gamma\right)\delta_{\alpha\beta}+\left(\frac{1}{3}-c_s^2\right)\left(u_\alpha\frac{\partial\rho}{\partial x_\beta}-u_\beta\frac{\partial\rho}{\partial x_\alpha}\right)\right.\\ &\quad\left.+\frac{\rho}{3}\left(\frac{\partial u_\beta}{\partial x_\alpha}+\frac{\partial u_\alpha}{\partial x_\beta}\right)-\frac{\partial}{\partial x_\alpha}\left(\rho u_\alpha u_\beta u_\gamma\right)\right], \qquad (2.58)\end{aligned}$$

and the placement of (2.58) in (2.44) gives the momentum equation to second order in δ.

To this point, the continuity and momentum equations have been derived to both $\mathcal{O}\left(\delta\right)$ and $\mathcal{O}\left(\delta^2\right)$ from the expanded lattice Boltzmann equation. Recalling the differential time expansion (2.32), the two continuity equations, (2.41) and (2.43)[4], can be combined to yield the macroscopic continuity equation,

$$\frac{\partial\rho}{\partial t}+\nabla\cdot\left(\rho\mathbf{u}\right)=0. \qquad (2.59)$$

The first order (2.52) and second order (2.44) momentum equations can be combined in the same fashion,

$$\frac{\partial}{\partial t}\left(\rho\mathbf{u}\right)=-\nabla\cdot\left(\rho\mathbf{u}\mathbf{u}\right)-\nabla\cdot\left(c_s^2\rho\right)-\delta\left[\nabla\cdot\left(1-\frac{1}{\tau}\right)\Pi^{neq1}\right],$$

and then the second order momentum flux tensor (2.58) introduced in index notation,

$$\begin{aligned}\frac{\partial}{\partial t}\left(\rho u_\alpha\right) &= -\frac{\partial}{\partial x_\beta}\left(\rho u_\alpha u_\beta\right)-\frac{\partial}{\partial x_\alpha}\left(c_s^2\rho\right)\\ &\quad+\delta\left[\frac{\partial}{\partial x_\beta}\left(\tau-\frac{1}{2}\right)\left(\frac{1}{3}-c_s^2\right)\frac{\partial}{\partial x_\gamma}\left(\rho u_\gamma\right)\delta_{\alpha\beta}\right.\\ &\quad+\frac{\partial}{\partial x_\beta}\left(\tau-\frac{1}{2}\right)\left\{\left(\frac{1}{3}-c_s^2\right)\left(u_\alpha\frac{\partial\rho}{\partial x_\beta}-u_\beta\frac{\partial\rho}{\partial x_\alpha}\right)\right.\\ &\quad\left.\left.+\frac{\rho}{3}\left(\frac{\partial u_\beta}{\partial x_\alpha}+\frac{\partial u_\alpha}{\partial x_\beta}\right)-\frac{\partial}{\partial x_\alpha}\left(\rho u_\alpha u_\beta u_\gamma\right)\right\}\right]. \qquad (2.60)\end{aligned}$$

In (2.60) it can be seen that,

$$\frac{\partial u_\beta}{\partial x_\alpha}+\frac{\partial u_\alpha}{\partial x_\beta}=2e_{\alpha\beta}, \qquad (2.61)$$

---

[4] Note that the first order continuity equation contains an error term of $\mathcal{O}\left(\delta^2\right)$.

in which $e_{\alpha\beta}$ is the rate of strain tensor. Also, looking back on (2.35) and (2.50) a choice can be made for the coefficients A_0, A_1 and A_2,

$$A_0 = \frac{4\rho}{9}, \;\; A_1 = \frac{\rho}{9}, \;\; A_2 = \frac{\rho}{36}, \tag{2.62}$$

which gives a solution for the sound speed, $c_s = 1/3$. It should be noted that these coefficients are not unique and another example can be found in [25]. Using (2.61) and (2.62) and ignoring the third order velocity terms on the basis that the macroscopic velocity is small compared to the lattice speed of sound,

$$\frac{\partial}{\partial t}(\rho u_\alpha) + \frac{\partial}{\partial x_\beta}(\rho u_\alpha u_\beta) = -\frac{\partial}{\partial x_\alpha}\left(c_s^2 \rho\right) + 2\frac{\partial}{\partial x_\beta}(\rho \nu e_{\alpha\beta}), \tag{2.63}$$

in which ν is the kinematic viscosity,

$$\nu = \frac{1}{3}\left(\tau - \frac{1}{2}\right)\delta, \tag{2.64}$$

which is obviously dependent on the relaxation parameter in the BGK form of the lattice Boltzmann equation.

Therefore, the Navier-Stokes equations of continuity (2.59) and momentum (2.63) for an incompressible fluid have been derived from the lattice Boltzmann equation using the multiscale Chapman-Enskog analysis. All that remains is to specify the equilibrium function coefficients D_0, D_1 and D_2. It has been shown that $A_1 = 4A_2$, $B_1 = 4B_2$ and $C_1 = 4C_2$ so from the symmetric properties of the lattice it can be assumed that $D_1 = 4D_2$ [144]. Using this information and (2.47) and then (2.36) gives,

$$D_0 = \frac{-2\rho}{3}, \;\; D_1 = \frac{-\rho}{6}, \;\; D_2 = \frac{-\rho}{24}, \tag{2.65}$$

leaving the equilibrium functions for the D2Q9 lattice fully defined as in (2.19), (2.20) and (2.21) in Section 2.4.2.

2.5.1 The Compressibility Constraint

The Chapman-Enskog analysis of the lattice Boltzmann equation has shown that it recovers the Navier-Stokes equations in the near incompressible limit. It is important to note that the pseudo-compressibility of the LBM is not related to the same phenomenon in the full Navier-Stokes equations.

In the regular LBM the density fluctuation is assumed to be negligible. Paradoxically, slight spatial density variations are required to drive flows. As the density fluctuation becomes significant, compressibility errors can become problematic in numerical simulations. More specifically, to simulate hydrodynamic flow with the regular LBM correctly, one must ensure that the Mach number is of order ϵ and the density fluctuation is of order ϵ^2 [57]. By reducing the computational Mach number information is allowed to propagate through the lattice while little convection has occurred (ratio of fluid speed to grid sound speed is very low) and the solution approaches the incompressible limit [119]. Recall that one of the starting points of the Chapman-Enskog analysis was a general form of the equilibrium function created using a *small velocity expansion* of the Maxwell-Boltzmann distribution.

Some effort has been dedicated to the removal of the pseudo-compressibility in the LBM. He and Luo [57] presented a modified version of the method for solving the incompressible Navier-Stokes equations, rather than just in the incompressible limit. In this approach, the primary LBM variables are changed from density distribution functions to pressure and the equilibrium functions are changed to include mean and fluctuating density terms. Results were presented for 2D Poiseuille flow and 2D Womersley flow. The velocity profile and pressure drop in the Poiseuille flow matched the analytical solutions very well. The Womersley flow results matched the analytical solution well also, however it was found that the error increased as the pressure frequency increased. The incompressible LBM was compared to the regular LBM, but it was found that the modified version only offered significant improvement at Mach numbers above 0.2. At Mach numbers less than 0.1 the two methods were almost indistinguishable.

2.5.2 Accuracy and Stability

The numerical accuracy of the lattice Boltzmann method is dependent on the computational Mach number, $Ma = u/c_s$. It has been shown [40][87] that at low Mach numbers the lattice Boltzmann method can solve fluid dynamics problems with second order accuracy in space and time. In space, this means that the error decreases quadratically with Δx while keeping the ratio $\nu\,(dt/dx^2)$ constant in accordance with the definition of viscosity in physical units,

$$\nu = \frac{1}{3}\left(\tau - \frac{1}{2}\right)\frac{\Delta x^2}{\Delta t}. \tag{2.66}$$

In time, this means that the error decreases quadratically with Δt while keeping Δx constant. The spatial sensitivity is dependent on suitable boundary implementation, as discussed in Section 2.6. It is also important to distinguish between discretisation errors and compressibility errors. In general, there is a discretisation limit after which the compressibility errors grow and become dominant [118].

In the LBM, an H-theorem[5] cannot be guaranteed while simultaneously using a form of the equilibrium functions that results in the correct macroscopic equations [19]. Therefore the method is not unconditionally stable.

Detailed stability analyses of the lattice Boltzmann method have been undertaken for the D2Q7 [17], D2Q9 and D3Q15 [108] lattices. They concluded that the LBM requires the mean flow velocity to be below a maximum, which is a function of several parameters including the lattice speed of sound, the relaxation time and wave number of perturbations (i.e. small Mach number constraint).

Sterling and Chen [119] undertook a linearised stability analysis of the LBM and found the linear criterion that requires the relaxation parameter, $\tau > 1/2$. This can also be determined intuitively from (2.66) and the requirement of positive viscosity. As the relaxation parameter is increased from 0.5 the maximum stable mean velocity increases monotonically to a maximum value after which further increment does not maintain stability.

2.6 Fluid Domain Boundary Conditions

The central issue in applying boundary conditions in the lattice Boltzmann method is the ability to determine a set of particle distribution functions that result in the hydrodynamic quantities desired at the boundary nodes. It is desirable that the boundary implementation procedure preserves the simplicity, and more importantly, the locality of the lattice Boltzmann equation so that solution and parallelisation procedure is not complicated.

As a consequence of the LBM's evolution from LGA, many of the techniques for boundary condition implementation have also been transferred between the methods. The primary example of this is the so called bounce-back condition (see Section 2.6.1) which is used to enforce the macroscopic no-slip condition at fluid-solid interfaces.

2.6.1 Wall Boundaries

The bounce-back technique is the simplest approach to modelling the interaction of fluid and solid in the lattice Boltzmann method. It enforces the no-slip condition at fluid-solid interfaces by reflecting particle distribution functions from the boundary nodes in the direction of incidence (i.e. 180 ° transformation). This condition can be enforced over one or two time steps,

---

[5] Boltzmann's H-theorem dictates that any initial state evolves towards a state of higher entropy thus ensuring stability.

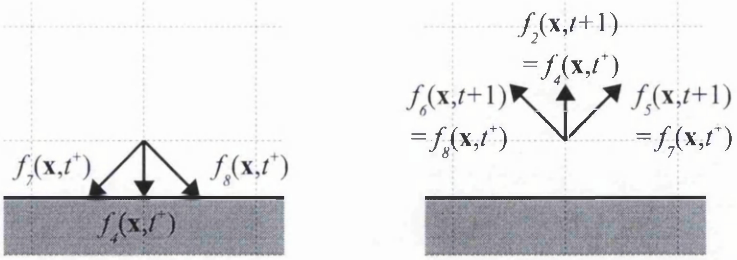

Figure 2.4: Schematic diagram of the one-step bounce-back boundary condition at (left) time t and (right) time $t+1$.

as discussed below. Two attractive features of the bounce-back condition are that the required operations are completely local and that the orientation of the boundary with respect to the grid is irrelevant. These features have historically lent the LBM to simulations involving complex boundary geometries such as porous media flows, where spatial discretisation may prove challenging for other CFD approaches. The simplicity of the bounce-back technique is at the expense of accuracy, and it has been shown that generally it is only first-order in numerical accuracy [26] as opposed to the second order accuracy of the lattice Boltzmann equation at internal fluid nodes [19]. Nevertheless, the bounce-back technique is usually suitable for simulating the fluid interaction at stationary boundaries.

One-Step Bounce-Back

The one-step bounce-back boundary condition is a direct descendant of boundary conditions in lattice gas models. In this approach (see Figure 2.4) the redirection of the post-collision distribution functions is undertaken at the fluid boundary nodes in place of the streaming operation.

Two-Step Bounce-Back

The two-step bounce-back condition (see Figure 2.5) is implemented as follows. At time t the particle distribution functions at the fluid node are relaxed resulting in, for the case of D2Q9 lattices, three particle distribution functions heading toward their respective 'wall' nodes where they are propagated during the streaming process. At time $t+1$ the wall nodes are included in the relaxation process but only in a token manner. The magnitude of the particle distribution functions is unchanged by the relaxation process. The bounce-back condition is then enforced on all wall nodes by reversing the direction of all functions at these nodes. The last task in this time step is to propagate the functions which are pointing from the wall in the direction

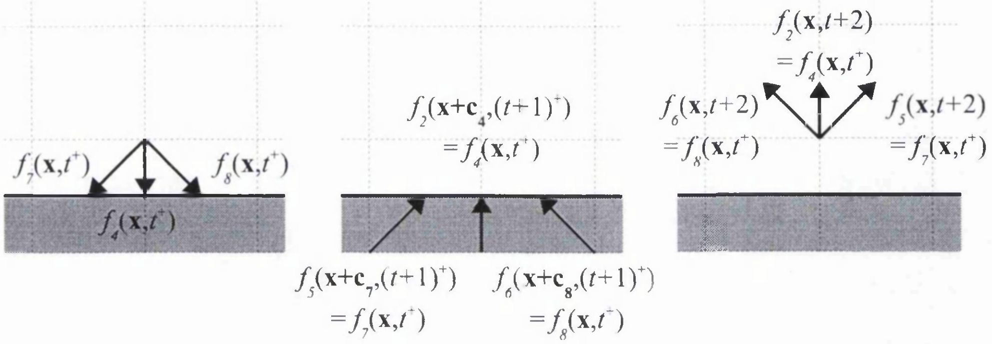

Figure 2.5: Schematic diagram of the two-step bounce-back boundary condition at (left) time t, at (middle) time $t+1$ and (right) time $t+2$.

of the fluid back to the fluid node. At the start of time $t+2$ the reflected particle distribution functions are at the node which they started (i.e. the fluid node) ready to be relaxed.

The advantage of the two-step approach is that the boundary does not require the definition of fluid boundary nodes. Also, when the physical boundary is assumed to lie halfway between the fluid node and the wall node the two-step bounce-back condition is found to be second order accurate in some cases.

Other Boundary Approaches

It has been shown that the bounce-back wall boundary transferred to the lattice Boltzmann method from lattice gas models actually results in a boundary with a finite velocity, the magnitude of which is dependent on the relaxation time. A quantitative expression for this error in Poiseuille flow is given in [147]. However, this erroneous slip velocity decreases with the simulation relaxation time [96, 67] and at appropriate values of τ (i.e. less than one) based on other simulation criteria (e.g. simulation of practical physical viscosities) the actual error is quite small.

By placing the wall location in between the last row and second last row of nodes, it was shown [146] that the bounce-back condition undertaken over two time steps (as outlined above) maintains second-order accuracy in simple geometries. This was confirmed by the results of Chen et al. [20] for Poiseuille flow at increasing grid resolution. However, for non-conforming (i.e. curved, angled) boundaries, the bounce-back wall boundary has been shown [26, 46] to be a first order representation of a no-slip interface even when the wall is assumed to lie halfway in between the wall node and the first fluid node.

Ziegler [146] considered the interpretation of the bounce-back method [26] by placing the boundary halfway between the wall nodes and first fluid nodes and then proposed a modified no-slip condition. In this approach the boundary is kept coincident with the first line of nodes and after streaming, the arriving functions are copied to their complimentary leaving functions which sets the normal velocity to zero. The remaining functions are then set to the average of the incoming directions which sets the tangential velocity to zero. The relaxation process is then applied to the fluid nodes and the boundary nodes followed by the streaming process. The results showed minor improvement over the reinterpreted bounce-back method in a Poiseuille flow test. An important drawback of this approach is that the orientation of the boundary with respect to the lattice needs to be known so that the correct distribution functions can be modified. This is obviously reduces the generality of the method.

Skordos [118] presented an alternative method for specifying initial and boundary conditions in the LBM. In this work the unknown boundary populations are calculated for the macroscopic variables specified at that location using the gradients of flow velocity. This method requires a procedure to calculate the distribution functions from the macroscopic fluid variables. An additional term based on the gradient of the velocity field is added to the collision operator to allow adjustment of the fluid viscosity independent of the relaxation parameter. The velocity gradients are calculated using finite differences. However, these finite differences introduce a cumulative error into the time evolution of the problem. This is overcome by using a hybrid method, in which the modified collision operator is used everywhere in the initialisation step and only at the boundaries thereafter. The reliance on finite differences generates some problems in this method. First, they cannot be evaluated at boundaries where the velocity is unknown. Second, irregular boundaries and coupled particles would also introduce major challenges.

Inamuro et al. [67] also recognised that diffuse particle reflection at boundaries does not generally result in a fluid velocity equal to the wall velocity at the interface. In response to this problem a non-slip boundary condition was devised that calculates the unknown (incoming) particle distribution functions as equilibrium values of the local density and the counter-slip velocity. This boundary condition was tested numerically in Poiseuille and Couette flows and found to reproduce the analytical velocity profiles to machine accuracy and to be second order with respect to grid size. However, a significant drawback of the method is that corner boundary nodes cannot be handled using the general approach. Therefore, the implementation of this boundary condition could be problematic for practical solutions that contain irregular boundaries with few segments parallel to the computational lattice.

Noble et al. [96] presented on the D2Q7 lattice a hydrodynamic boundary condition that calculates the unknown particle distribution velocities at the boundary from the known distributions at neighbouring nodes and the specified velocity components. In this method it is assumed that adjacent to the boundary nodes lies fluid nodes (in the fluid) and wall nodes (outside the fluid). The only undefined distribution functions that will propagate to the boundary node are the two from the wall nodes. The hydrodynamic density and momentum at the boundary nodes is then defined in terms of the incoming distributions from neighbouring nodes. Because the velocity components at the boundary are specified, the three unknowns (density and two incoming distributions) can be found using the three available equations. This method was tested in both Poiseuille and shear flows and found to replicate the analytical solutions excellently. The results also confirmed that the LBM is indeed spatially second order accurate provided that the boundary conditions are modelled accurately.

It is immediately apparent that this approach is not directly applicable to the more accurate D2Q9 lattice because the number of incoming unknown particle distribution functions would increase from two to three. As such, supplementary rules would be required. Also, this method has only been developed for boundaries that are parallel with one of the lattice directions and is thus not applicable to non-aligned or irregular boundaries.

Chen et al. [20] recognised that enforcing the velocity at the boundaries is not sufficient to ensure the momentum flux is correct. In response to this, and the other issues with the bounce-back scheme, they proposed a method based on the extrapolation of the distribution functions at the boundary. This techniques assumes the existence of an additional layer of nodes behind the boundary and inside the wall (i.e. exterior nodes). Before streaming is undertaken the incoming distribution functions at the exterior nodes are extrapolated from the boundary nodes and the first row of fluid nodes. Note that the distribution functions at the boundary nodes are evaluated from equilibrium of the prescribed velocity or pressure. These extrapolated functions then stream to the boundary nodes and relaxation is applied to all domain nodes except the exterior nodes. Numerical tests of the extrapolation method included Poiseuille flow, unsteady Couette flow, flow in a lid driven cavity and flow around a periodic array of cylinders. They showed second order accuracy for the density, momentum and stress at the wall boundary. An associated advantage of the extrapolation method is that the true location of the boundary can be shifted with respect to the nodes whilst maintaining second order accuracy by simply altering the finite difference approximation. This is an improvement over the bounce-back approach which is only second order when the boundary lies halfway between the wall nodes and interior

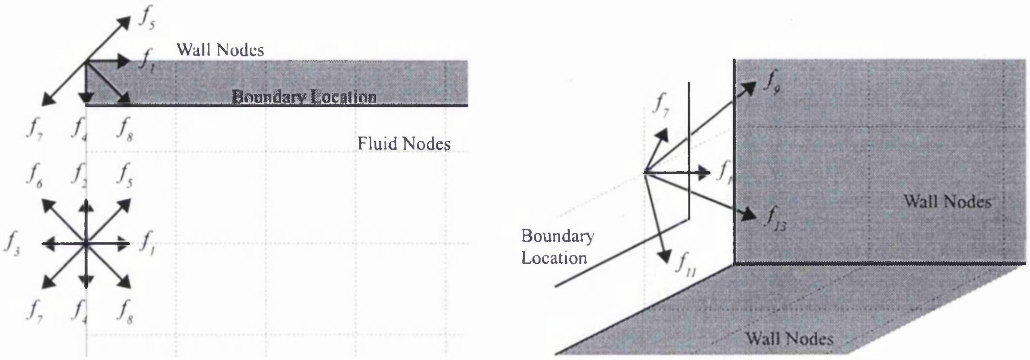

(a) (b)

Figure 2.6: Schematic of the unknown particle distribution functions on flow boundaries for (a) the D2Q9 lattice and (b) the D3Q15 lattice.

nodes and is orthogonal of the underlying lattice. However, as is the case with many of the modified boundary conditions, the extrapolation technique loses the locality of the bounce-back method by requiring information from a number[6] of internal fluid nodes.

2.6.2 Pressure and Velocity Boundaries

The application of pressure and velocity boundary conditions in the lattice Boltzmann method involves the inverse problem of assigning particle distribution functions from the prescribed macroscopic constraint. It is apparent from the equation of state for pressure (2.50) in the LBM that pressure conditions are applied by assigning the corresponding density. Figure 2.6 schematically illustrates the unknown particle distribution functions at flow boundaries for the D2Q9 and D3Q15 lattices.

Many of the bounce-back boundary condition improvements discussed in Section 2.6.1 can also be applied to velocity and pressure conditions. Zou and He [147] proposed a condition based on the bounce-back of the non-equilibrium function that can be applied to velocity, pressure and wall constraints. The most attractive feature of this boundary technique is that the required operations are local.

Consider the 2D flow boundary in Figure 2.6a. After streaming, the particle distribution functions f_1, f_5 and f_8 are unknown due to an absence of lattice sites from which information can be convected. The definition of macroscopic density (2.5) and momentum flux (2.6) provides three equations

---

[6] This number is dependent on the lattice geometry and the number of distribution functions that need to be determined.

for the solution of these unknown functions. However, depending on whether pressure or velocity is prescribed at the boundary, another macroscopic quantity is unknown. The set of unknowns, summarised as follows, therefore requires an additional equation in order to be solved.

1. Pressure boundary: Density, ρ, and tangential velocity, u_y, are specified and u_x, f_1, f_5 and f_8 are unknown.
2. Velocity boundary: Normal and tangential velocity, u_x and u_y, are specified and ρ, f_1, f_5 and f_8 are unknown.

The additional equation in this boundary technique is provided by the bounce-back of the non-equilibrium function normal to the flow boundary. With the unknowns at each boundary node determined they are included in the collision process at the next time step.

Pressure Boundaries

Assume that a pressure, $p_{in} = c_s^2 \rho_{in}$, is applied at the flow boundary in Figure 2.6a. The definition of density (2.5) in the lattice Boltzmann method allows,

$$f_1 + f_5 + f_8 = \rho_{in} - (f_0 + f_2 + f_3 + f_4 + f_6 + f_7). \qquad (2.67)$$

The normal velocity is assumed unknown and the tangential velocity is prescribed as zero at a pressure boundary so from the definition of momentum flux (2.6) in the x-direction,

$$f_1 + f_5 + f_8 = \rho_{in} u_x + f_3 + f_6 + f_7, \qquad (2.68)$$

and the y-direction,

$$f_5 - f_8 = -f_2 + f_4 - f_6 + f_7. \qquad (2.69)$$

Equating (2.67) and (2.68) and rearranging gives the normal velocity,

$$u_x = 1 - \frac{[f_0 + f_2 + f_4 + 2\,(f_3 + f_6 + f_7)]}{\rho_{in}}. \qquad (2.70)$$

The bounce-back of the non-equilibrium function is now applied normal to the boundary as,

$$f_1 - f_1^{eq} = f_3 - f_3^{eq}. \qquad (2.71)$$

The equilibrium functions f_1^{eq} and f_3^{eq} are then substituted into (2.71) to solve for f_1,

$$f_1 = f_3 + \frac{2}{3} \rho_{in} u_x. \qquad (2.72)$$

To find f_5, (2.68) is added to (2.69) and then (2.72) is substituted for f_1 which gives,

$$f_5 = \frac{1}{6}\rho_{in}u_x - \frac{1}{2}(f_2 - f_4) + f_7. \tag{2.73}$$

Finally, substituting (2.73) into (2.69) solves for f_8,

$$f_8 = \frac{1}{6}\rho_{in}u_x + \frac{1}{2}(f_2 - f_4) + f_6. \tag{2.74}$$

Application of the the same procedure on a positive[7] y-boundary allows the solution of the unknown normal velocity, u_y, and the unknown particle distribution functions, f_2, f_5 and f_6. These results are listed in (2.75), (2.76), (2.77) and (2.78), respectively.

$$u_y = 1 - \frac{[f_0 + f_1 + f_3 + 2(f_4 + f_7 + f_8)]}{\rho_{in}} \tag{2.75}$$

$$f_2 = f_4 + \frac{2}{3}\rho_{in}u_y \tag{2.76}$$

$$f_5 = \frac{1}{6}\rho_{in}u_y - \frac{1}{2}(f_1 - f_3) + f_7 \tag{2.77}$$

$$f_6 = \frac{1}{6}\rho_{in}u_y + \frac{1}{2}(f_1 - f_3) + f_8 \tag{2.78}$$

The unknown velocities and particle distribution functions at negative x-boundaries and negative y-boundaries can be found in a similar fashion.

At the corner node in Figure 2.6a only f_0, f_2, f_3 and f_6 are known after streaming but both u_x and u_y can be prescribed as zero. The reduced amount of information at this location requires a different method of processing the boundary condition. The bounce-back of the non-equilibrium function is applied normal to the flow boundary to find f_1,

$$f_1 = f_3 + (f_1^{eq} - f_3^{eq}) = f_3, \tag{2.79}$$

and normal to the wall to find ,

$$f_4 = f_2 + (f_4^{eq} - f_2^{eq}) = f_2. \tag{2.80}$$

With the knowledge that $f_1 = f_3$ the sum of momentum flux in the x-direction gives,

$$0 = f_5 - f_6 - f_7 + f_8, \tag{2.81}$$

---

[7] The boundary normal is in the positive Cartesian direction.

and using $f_4 = f_2$ the sum of momentum flux in the y-direction gives,

$$0 = f_5 + f_6 - f_7 - f_8. \tag{2.82}$$

The addition of (2.81) and (2.82) gives $f_5 = f_7$ and as a consequence $f_8 = f_6$. The remaining unknowns, f_5 and f_7, can be found from the density summation,

$$f_5 = f_7 = \frac{1}{2}\left[\rho_{in} - f_0 - 2\left(f_3 + f_2 + f_6\right)\right]. \tag{2.83}$$

The unknown particle distribution functions at other corner nodes are found in the same way.

In three dimensional analyses, when using for example the D3Q15 or D3Q18 lattices, the number of unknown particle distribution functions at boundaries can become problematic because the number of macroscopic quantities[8] available at each node is only four (one density and three momentum). Figure 2.6b shows a simple problem using the D3Q15 lattice in which a wall boundary lies in the yz-plane. It can be seen that the number of unknown particle distributions is five, which is already greater than the number of equations available even for this simple boundary geometry. To be able to specify the unknown particle distribution functions required to enforce hydrodynamic boundary conditions such as velocity or pressure, additional information is required.

Maier et al. [86] proposed a simple technique for specifying the unknown distribution functions at 3D boundaries. The first step in this approach is to apply the bounce-back condition to set provisional values for the undefined incoming particle distribution functions. This process defines the density and enforces the correct normal velocity at the boundary. These functions are then redistributed using (2.84) whilst conserving mass to achieve the desired tangential velocity at the wall. For the D3Q15 lattice $\alpha = 1/4$ while for the D3Q18 lattice $\alpha = 1/2$.

$$f_i = f_i - \alpha \mathbf{v} \cdot \mathbf{c_i} \tag{2.84}$$

The redistributions are only performed on particle distribution functions that have a component tangential to the wall (e.g. f_7, f_9, f_{11} and f_{13} in Figure 2.6b). For the case of non-zero tangential wall velocity, (2.84) is modified by substituting $\mathbf{v} = \rho\left(\mathbf{u} - \mathbf{u_w}\right)$ into the redistribution. This boundary procedure is undertaken after streaming and before collision. Non-zero normal wall velocity is accommodated by adding mass to the incoming orthogonal distribution functions (after bounce-back) to achieve the prescribed normal velocity before redistribution via (2.84).

---

[8] More importantly their respective definitions which are based on summations of the local particle distribution functions.

A similar procedure is used for applying pressure (i.e. density) boundary conditions. The unknown incoming distribution functions are first extrapolated from their corresponding outgoing distribution functions mirrored at the boundary. A provisional density can then be calculated, which is then redistributed to achieve the desired density condition. Zero tangential velocity is enforced at the boundary by applying (2.84) with $\mathbf{v} = \rho\mathbf{u} - \mathbf{c_{in}c_{in}} \cdot \rho\mathbf{u}$ in which is the incoming orthogonal distribution function (e.g. f_1 in Figure 2.6b).

Zou and He [147] applied their bounce-back boundary condition to the D3Q15 lattice and employed the tangential function redistribution discussed in [86]. Considering a 3D pressure boundary such as in Figure 2.6b, f_1, f_7, f_9, f_{11} and f_{13} are unknown, u_y and u_z can be prescribed as zero, and ρ_{in} is specified. As in the 2D case, the normal velocity, u_x, must first be found. Equating the definition of density,

$$\begin{aligned} f_1 + f_7 + f_9 + f_{11} + f_{13} &= \rho_{in} - f_0 - f_3 - f_4 - f_5 - f_6 \\ &\quad - (f_2 + f_8 + f_{10} + f_{12} + f_{14}) \,, \end{aligned} \tag{2.85}$$

and the definition of the x-direction momentum flux,

$$f_1 + f_7 + f_9 + f_{11} + f_{13} = \rho_{in} u_x + (f_2 + f_8 + f_{10} + f_{12} + f_{14}) \,, \tag{2.86}$$

gives the normal velocity after rearranging,

$$u_x = 1 - \frac{[f_0 + f_3 + f_4 + f_5 + f_6 + 2(f_2 + f_8 + f_{10} + f_{12} + f_{14})]}{\rho_{in}} . \tag{2.87}$$

Applying the non-equilibrium bounce-back in the normal direction, $f_1 - f_1^{eq} = f_2 - f_2^{eq}$, then gives,

$$f_1 = f_2 + \frac{2}{3}\rho_{in} u_x . \tag{2.88}$$

The non-equilibrium bounce-back is also applied to the diagonal distribution functions, f_7, f_9, f_{11} and f_{13}, to give in general terms,

$$f_i = f_{i+1} + \frac{1}{12}\rho_{in} u_x \quad (i = 7, 9, 11, 13) . \tag{2.89}$$

Following Maier et al. [86], f_7, f_9, f_{11} and f_{13} are further modified using (2.84) to enforce the zero tangential velocity constraint in the y and z-directions,

$$f_7 = f_8 + \frac{1}{12}\rho_{in} u_x + \frac{1}{4}\left[-(f_3 - f_4) - (f_5 - f_6)\right] , \tag{2.90}$$

$$f_9 = f_{10} + \frac{1}{12}\rho_{in} u_x + \frac{1}{4}\left[-(f_3 - f_4) + (f_5 - f_6)\right] , \tag{2.91}$$

$$f_{11} = f_{12} + \frac{1}{12}\rho_{in}u_x + \frac{1}{4}\left[(f_3 - f_4) - (f_5 - f_6)\right], \tag{2.92}$$

$$f_{13} = f_{14} + \frac{1}{12}\rho_{in}u_x + \frac{1}{4}\left[(f_3 - f_4) + (f_5 - f_6)\right]. \tag{2.93}$$

As in the 2D implementation, all operations for the 3D non-equilibrium bounce-back pressure condition are local. A further advantage of this method is that corner can nodes can be handled in an identical fashion. The same procedure can be used to determine the unknown particle distribution functions at positive and negative x, y and z-boundaries.

Velocity Boundaries

Applying velocity boundary conditions using the non-equilibrium bounce-back approach is only subtly different to applying a pressure boundary. Recall from Section 2.6 that for a 2D boundary, such as that in Figure 2.6a, u_x and u_y are prescribed and ρ, f_1, f_5 and f_8 are unknown. By equating the definition of density (2.5) and x-direction momentum flux (2.6) the nodal density can be found,

$$\rho = \frac{1}{1-u_x}\left[f_0 + f_2 + f_4 + 2\left(f_3 + f_6 + f_7\right)\right]. \tag{2.94}$$

Applying the non-equilibrium bounce-back to find f_1 gives,

$$f_1 = f_3 + \frac{2}{3}\rho_{in}u_x. \tag{2.95}$$

By adding the equations for the x-direction and y-direction momentum flux and incorporating (2.95) f_5 can be found,

$$f_5 = \frac{1}{6}\rho u_x + \frac{1}{2}\rho u_y - \frac{1}{2}\left(f_2 - f_4\right) + f_7, \tag{2.96}$$

and by subtracting the y-direction momentum flux equation from the x-direction momentum flux equation and again substituting (2.95), f_8 can be found,

$$f_8 = \frac{1}{6}\rho u_x - \frac{1}{2}\rho u_y + \frac{1}{2}\left(f_2 - f_4\right) + f_6. \tag{2.97}$$

Using the same approach for a positive y-direction boundary results in the definitions of ρ, f_2, f_5 and f_6 shown in (2.98), (2.99), (2.100) and (2.101), respectively.

$$\rho = \frac{1}{1-u_y}\left[f_0 + f_1 + f_3 + 2\left(f_4 + f_7 + f_8\right)\right] \tag{2.98}$$

$$f_2 = f_4 + \frac{2}{3}\rho_{in}u_y \tag{2.99}$$

$$f_5 = \frac{1}{2}\rho u_x + \frac{1}{6}\rho u_y - \frac{1}{2}\left(f_1 - f_3\right) + f_7 \tag{2.100}$$

$$f_6 = -\frac{1}{2}\rho u_x + \frac{1}{6}\rho u_y + \frac{1}{2}\left(f_1 - f_3\right) + f_8 \tag{2.101}$$

The application of negative x-direction and y-direction boundary conditions can be derived in the same way.

Corner nodes for 2D velocity boundaries require slightly different processing to that for pressure boundaries. Using the corner shown in Figure 2.6a as an example, ρ, f_1, f_4, f_5, f_7 and f_8 are unknown while u_x and u_y are prescribed as zero. Using the bounce-back of the non-equilibrium function normal to the flow boundary gives $f_1 = f_3$ and normal to the wall gives $f_4 = f_2$. The combination of the equations for x-direction momentum flux and y-direction momentum flux gives $f_5 = f_7$ and $f_8 = f_6$. Using the density summation and these four equalities to attempt to solve for f_5 and f_7 gives,

$$f_5 = f_7 = \frac{1}{2}\left[\rho - f_0 - 2\left(f_1 + f_2 + f_6\right)\right], \tag{2.102}$$

but the nodal density, ρ, has not yet been determined and there are no more equations available. Based on the assumption of constant density along the boundary [147], the density is borrowed from the neighbouring node (in this case, $\rho\left(x, y-1\right)$) and (2.102) can be solved.

It should be noted that Latt et al. [81] have shown that the velocity boundary condition of Zou and He is unstable for values of $\tau < 0.55$. This places constraints on the range of Reynolds numbers that can be simulated in practical applications. Also, this boundary implementation is not strictly mass conservative as it allows a gradual increase of the total mass in the fluid domain. This is not an issue as the correct particle distribution function differences are maintained. However, if a body force is implemented the additional mass will be problematic.

The 3D velocity boundary condition can be applied on the D3Q15 lattice by following the procedure for the pressure boundaries.

Curved Boundaries

It is important to note that the non-equilibrium bounce-back technique is limited to boundaries that are parallel to the orthogonal lattice directions, however other boundary-fitted approaches have been investigated.

Filippova and Hänel [38] proposed a boundary fitting concept that utilises weighted contributions from the wall node and the fluid node to evaluate the population evolution at the fluid node. The weighting is based on the position of the actual boundary with respect to the wall and fluid nodes (i.e. the ratio of distance between them). This method allows prescription of the no-slip condition at boundaries that do not conform to the underlying grid with second order accuracy. The boundary condition was tested in conjunction with a grid refinement procedure in the case of flow around a circular cylinder and found to correlate well with benchmark results for drag and lift coefficients. However, improvement over the bounce-back condition was marginal.

An improvement to the fitted boundary technique of Filippova and Hänel was offered by Mei et al. for 2D [91] and 3D [92] problems. They found the former work to be unstable in pressure driven channel flows when the boundary is closer to the fluid node than the wall node. In fact, a sensitivity analysis of the stability to the relaxation parameter and the boundary location with respect to the grid found a large instability envelope. In this work the fluid node evolution when the boundary is closer to the fluid node than than the wall node was modified which resulted in a much improved stability envelope. The accuracy of the method was comparable to that of its predecessor.

The non-conforming boundary condition of Bouzidi et al. [7] is similar to those in [38] and [91]. In this approach the ratio q is calculated as the distance of the boundary from the first internal fluid node. The boundary is handled in different ways if $q < 1/2$ or if $q > 1/2$. The first step is to identify which lattice links[9] connect to a boundary node. The incoming distributions at the first internal node are then calculated from interpolations of the first two (first order) or first three (second order) outgoing (i.e. heading to the wall node) internal post collision functions. The calculated distribution functions are then used after the streaming of all other nodes (i.e. they reenter computations after the end of the time step). Note that when $q = 1/2$ this approach reduces to the plain bounce-back approach. The method can be extended to include velocity boundaries by calculating the momentum transferred by the method.

Results were presented for Poiseuille flow in which the channel is orientated at an angle to the grid. This was done to test the performance of the boundary condition in a situation where the bounce-back method is only first order accurate. The flow was driven by a body force. The results show that the second order interpolation captures the correct result and the first order interpolation is accurate to within 5%. Despite its attractive performance, implementation of the second order interpolation would be difficult in anything other than a rectangular geometry especially if coupling of suspended

---

[9] A link is the imaginary connection from a node to its neighbour in the direction of a particular lattice velocity.

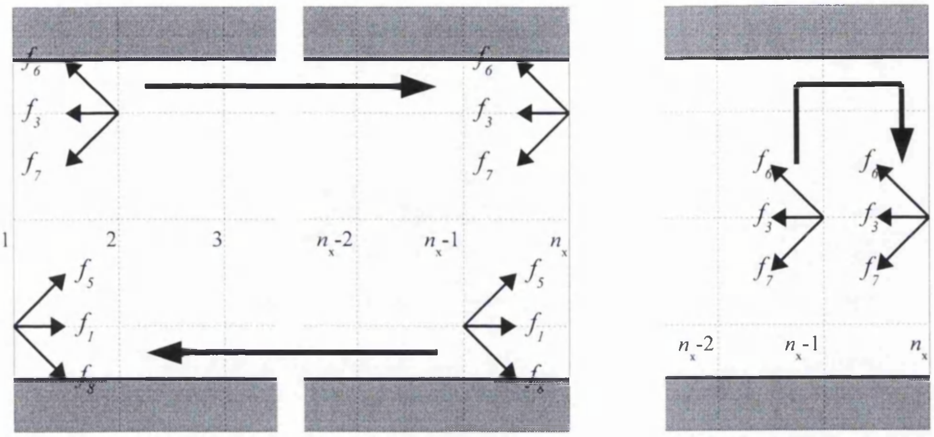

(a) (b)

Figure 2.7: Schematic of the 2D implementation procedures for (a) periodic boundaries, and (b) Neumann boundaries.

particles is required.

2.6.3 Periodic and Stress-Free Boundaries

The periodic boundary condition uses the output of the fluid domain as the input. In this way, an infinite array of the analysed fluid domain is created in the direction of the boundary normal. Pressure, and to a lesser extent, velocity boundary conditions are useful techniques for driving flow in fluid dynamics simulations because the results can be directly compared to experiments driven by a pressure gradient. However, it is a convenient feature of the lattice Boltzmann method that periodic flow boundaries can be implemented in a straightforward manner and this is evident in the much of the literature in the LBM and LGA utilising these conditions. In addition, assigning a fixed pressure to inlets and outlets to a fluid domain driven by a body force (see Section 2.7) can over-constrain the system. In this scenario periodic (or stress-free, see below) conditions are more appropriate.

The schematic diagram in Figure 2.7a shows how the periodic fluid boundaries are implemented [11] for use with a body force. As discussed in Section 2.6.2, the inward facing particle distribution functions at the left boundary, f_1, f_5 and f_8, are undefined after the streaming process. The periodic condition overcomes this problem by copying these particle distribution functions from the corresponding node on the second last column at the opposite boundary. Referring to the figure it can be seen that information from column $n_x - 1$ is passed to the undefined functions on column 1, and likewise information from column 2 (f_3, f_6 and f_7) is passed to the undefined functions on column n_x. In this way, outlet information is passed to the inlet and vice versa. It should be noted that this boundary technique implies two important requirements, namely that periodic boundaries must be defined in pairs and that these pairs must be of the same orientation and length.

As stated in [11], this periodic condition utilises information from second last column, not the last column which is more traditional. This is done to prevent the gravitational potential (see Section 2.7) of any body forces from being cancelled out by the applied boundaries.

Stress-free boundary conditions can be utilised at fluid outlets to overcome the issue of feedback [141] that is inherent in pressure and velocity boundary conditions. Enforcing either of these fluid properties to a constant value across an outlet has an effect on the flow behaviour upstream, which can be problematic in some benchmarking analyses.

Various forms of stress-free boundary conditions have been investigated in [2, 63, 109]. A simplified version of this condition involves the transfer of particle distribution functions from the column immediately before an outlet to the outlet column. Referring to the schematic in Figure 2.7b and assuming the right of the domain to be the outlet boundary, this would require the copying of the inward facing particle distribution functions (f_3, f_6 and f_7) from column $n_x - 1$ to the undefined locations on column n_x.

Yu et al. [141] proposed an outlet condition which extrapolated the particle distribution functions at column n_x from those at column $n_x - 1$ and column $n_x - 2$. With reference to Figure 2.7b, the extrapolated condition is written as,

$$f_i(n_x, y) = 2f_i\,(n_x - 1, y) - f_i\,(n_x - 2, y) \quad i = 3, 6, 7. \tag{2.103}$$

Junk and Yang [70] investigated a number of improved outflow conditions including the Neumann boundary condition, the zero normal shear stress boundary and the do-nothing boundary condition. The methods were tested in the problem of steady and unsteady flow past a cylinder in a channel and the results compared well with similar benchmarks.

2.7 Inclusion of External Forcing

In the context of simulating fines migration in a block cave adequate representation of material body forces is paramount. Gravitational effects will predominantly drive the movement of fines around larger blocks that are either stationary or moving as a result of cave draw. However, many publications on the topic of the lattice Boltzmann method ignore the weight of the fluid as the flow regime is driven by pressure or velocity gradients that are assumed to be dominant.

Buick and Greated [11] analysed the application of body forces in the lattice Boltzmann method in a detailed manner. They proposed four different methods, which used various combinations of modified equilibrium functions and macroscopic velocity definitions, and an additional operator in the LB equation that modifies the particle density functions due to the action of the body force.

The force term in the continuous Boltzmann equation can be written as $F_\alpha \partial f / \partial c_\alpha$. However the fluid particle velocity in the lattice form of the equation is constant resulting in an undefined derivative in this term. Therefore, any approach to include body forces must look to modify the fluid momentum rather than the velocity. Buick and Greated [11] used this principle to propose four methods for including fluid body forces in the lattice Boltzmann equation.

In Method 1 the equilibrium distribution function is modified to include a term for the gravitational potential, $-\rho\nabla\phi$. When this modified function is used to derive the continuum limit of the LBE the Navier-Stokes equations are found with the gravity term combined with the pressure tensor, $p \longrightarrow p + \rho\phi$. This method is applicable only when the density gradient produced by the body force is sufficiently small.

If a body force $\mathbf{G}$ is acting on a fluid then in every time increment there is a resultant change in momentum, $\Delta(\rho\mathbf{u}) = \mathbf{G}$. In Method 2 this principle is incorporated into the model by using a modified equilibrium distribution function featuring an altered equilibrium velocity, $\mathbf{u}^*$, calculated as,

$$\rho\mathbf{u}^\star = \rho\mathbf{u} + \tau\mathbf{G}. \tag{2.104}$$

The effect of this approach is to relax the particle distribution functions at each node towards an equilibrium momentum that has included the time-incremental change in momentum due to the body force. The fluid momentum for the time step is then calculated as an average of the value before and after the collision,

$$\rho\mathbf{v} = \rho\mathbf{u} + \frac{1}{2}\mathbf{G}. \tag{2.105}$$

In Method 3 an additional term is added to the lattice Boltzmann collision operator,

$$\Omega_i(\mathbf{x},t) = -\frac{1}{\tau}\left(f_i(\mathbf{x},t) - f_i^{eq}(\mathbf{x},t)\right) + \frac{D}{bc^2}\mathbf{G}\cdot\mathbf{c}_\mathrm{i}, \tag{2.106}$$

in which D is the problem dimensions and b is the number of lattice directions. The fluid momentum for each time increment is then calculated using (2.105).

In Method 4, the equilibrium function is calculated using an altered velocity,

$$\mathbf{u}^\star = \mathbf{u} + \frac{\mathbf{G}}{2\rho}, \tag{2.107}$$

and an additional term is added to the lattice Boltzmann equation,

$$f_i\left(\mathbf{x}+\mathbf{c}_\mathbf{i},t+1\right)=f_i\left(\mathbf{x},t\right)-\frac{1}{\tau}\left(f_i\left(\mathbf{x},t\right)-f_i^{eq}\left(\mathbf{x},t\right)\right)+\frac{2\tau-1}{2\tau}\frac{D}{bc^2}\mathbf{G}\cdot\mathbf{c}_\mathbf{i}. \tag{2.108}$$

This can be considered a combination of Methods 2 and 3, with the coefficients chosen to ensure the correct form of the Navier-Stokes equations in the continuum limit.

It is important to note that these methods were proposed to simulate gravity in the incompressible limit of a linearly varying density. In this limit it is required that $\mathbf{G}z \ll c_s^2$ where z is the extent of the simulation in the direction of $\mathbf{G}$ and c_s is the lattice speed of sound. These methods were tested in the cases of steady state stationary density gradient, steady state Poiseuille flow, and transient Poiseuille flow. In summary, Method 1 was found to be capable of simulating Poiseuille flow correct to computer accuracy. When a density gradient was present Method 1 performed less well than the others, even when that gradient was small. For Methods 2 and 3, if the fluid velocity was defined as in (2.107) then the models satisfied (up to second order) the continuity equation and an equation similar to the momentum equation. Within the incompressible limit, Methods 2, 3 and 4 were found to compare well with theory in situations where the nonlinear term of the Navier-Stokes equations is zero. When that nonlinear term becomes nonzero, Method 4 was an improvement over the other two methods.

Strack and Cook [120] outlined a body force method similar to Method 3 in which an additional, post-collision operator is included in the lattice Boltzmann equation. If $f_i^+\left(\mathbf{x},t\right)$ is the post collision distribution function, the post-body force distribution function $f_i^{++}\left(\mathbf{x},t\right)$ can be written as,

$$f_i^{++}\left(\mathbf{x},t\right)=f_i^+\left(\mathbf{x},t\right)+A\mathbf{G}\cdot\mathbf{c}_\mathbf{i}. \tag{2.109}$$

The streaming of the post body force distribution functions is then,

$$f_i\left(\mathbf{x}+\mathbf{c}_\mathbf{i}\Delta t,t+\Delta t\right)=f_i^{++}\left(\mathbf{x},t\right). \tag{2.110}$$

Similar body force approaches have been presented by Flekkøy and Herrmann [39] on a D2Q6 lattice and Singh and Mohanty [117] on a D3Q15 lattice.

From (2.109) the components of the body force operator in the lattice directions can be written as $F_i = A\mathbf{G}\cdot\mathbf{c}_\mathbf{i}$. In order to be mass conservative it is required that $\sum_i F_i = 0$, which defines the coefficient A as,

$$A=\frac{1}{Kc^2}, \tag{2.111}$$

where $K=6$ for the D2Q9 lattice and $K=10$ for the D3Q15 lattice.

2.8 Flow Validation Examples

The implementation of the lattice Boltzmann method in a commercial FEM-DEM code was tested via a number of simple flow validation problems. The aim of these tests was to determine the accuracy and robustness of the code and also investigate the issues discussed in the preceding sections of this chapter. These issues include the order of accuracy, compressibility errors, and the range of physical problems (i.e. fluid velocities and viscosities) that could be analysed in the employed formulation.

The D2Q9 and D3Q15 lattices were employed for two-dimensional and three-dimensional analyses, respectively. These were selected on the basis that they offer a compromise of computational efficiency and sufficient numerical accuracy.

The BGK formulation of the lattice Boltzmann equation was chosen for the collision process. Despite recent advances in multiple-relaxation-time models, the single-relaxation-time approach was selected for its proven ability in coupled DEM applications. The LBGK scheme is also less computationally intensive MRT models, which is an important consideration when dealing with large 3D problems.

Wall boundaries were enforced using the two-step bounce-back condition despite being shown to exhibit only first order accuracy at boundaries that do not conform to the underlying lattice. This method does not require information on the surface normals and it is a completely local operation. Both of these features are extremely convenient in modelling irregular domains such as those in a block cave mine. Pressure and velocity flow boundaries were implemented using the non-equilibrium bounce-back technique of Zou and He [147].

Finally, fluid body forces were included via an additional post-collision operation which alters the momenta of the particle distribution functions as outlined in Strack and Cook [120] and Buick and Greated [11].

2.8.1 Pressure Gradient from a Gravitational Body Force

The LBM body force implementation was tested using a representative gravitational force and large action direction. This was done to investigate the performance of what is the simplest implementation discussed by Buick and Greated [11] and its susceptibility to compressibility errors. A square domain with side length of $2m$ was employed with a lattice spacing of $0.05\,m$. Bounce-back boundaries were applied on the top and bottom walls which results in an effective domain height of $1.95\,m$ when the true boundary location is considered to be halfway between the wall nodes and first fluid nodes.

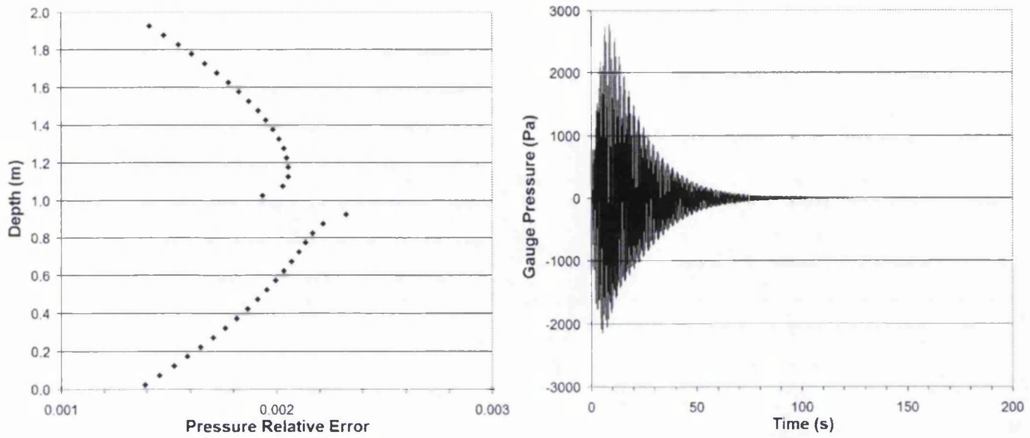

(a) (b)

Figure 2.8: Results of the 2D body force test including (a) the relative error in gravity-induced pressure throughout the depth of the domain and (b) the transient response of the pressure distribution due to the inherent compressibility of the LBM.

Periodic boundaries were employed on the left and right edges which created a domain of infinite width. Gravitational loading of -9.81m/s^2 was instantaneously applied in the vertical direction at the start of the solution. The fluid density, viscosity and relaxation parameter were 1000kg/m^3, 0.01m^2/s and 0.51, respectively.

The body force analysis was run for 200s and the steady state pressure profile in the domain was interrogated. Figure 2.8a graphs the relative error in the pressure profile against the depth in the channel. Good correlation with the analytical solution for the pressure head, $p = \rho \mathbf{G} h$, was attained.

The combination of the inherent compressibility of the LBM and the instantaneous application of the body force resulted in high frequency fluctuations in the fluid pressure. This transient behaviour can be seen in Figure 2.8b, which plots the pressure at the centre of the domain over the course of the solution. Viscous dissipation causes the decay of the pressure oscillations, but this effect could have been increased by applying no-slip walls at the left and right edge of the domain.

The input parameters for this analysis led to a lattice sound speed, $c_s = 34.64 m/s$. The applied body force and the extent of the domain result in $\mathbf{G}z = 19.13 m^2/s^2$. The ratio $\mathbf{G}z/c_s^2 = 0.016$ and therefore the compressibility constraint for the implemented body force, $\mathbf{G}z \ll c_s^2$, is obeyed.

2.8.2 2D and 3D Plane Poiseuille Flow

Poiseuille flow is commonly used as a benchmark for numerical fluid analysis as an analytical solution can be derived from the governing Navier-Stokes equations. The equation for the velocity profile across the width of the channel is,

$$u_x(y) = \frac{-1}{2\mu}\frac{\Delta p}{L}\left[\frac{h^2}{4} - \left(y - \frac{h}{2}\right)^2\right], \tag{2.112}$$

in which μ is the dynamic fluid viscosity, Δp is the pressure difference over the length of the channel, L is the length of the channel and h is the height (or width) of the channel. The origin of the transverse coordinate in (2.116) is at the bottom edge of the channel. This expression can be rewritten with the origin at the centre of the channel and the driving pressure gradient replaced by a body force, $\mathbf{G}$,

$$u_x(y) = \frac{-\mathbf{G}}{2\nu}\left[\left(\frac{h}{2}\right)^2 - |y|^2\right], \tag{2.113}$$

where ν is the kinematic viscosity.

The implemented LBM code was applied to the Poiseuille flow problem in two and three and dimensions. The model domain in 2D was a square with side length of $0.2m$ and in 3D was a cube with side length of $0.2m$. Flow was driven by an x-direction acceleration of $0.001m/s^2$ and periodic boundaries were applied on the inlet and outlet. To maintain plane flow, periodic boundaries were also applied to the front and rear walls in the 3D case. The fluid density and kinematic viscosity used were $1000\,kg/m^3$ and 1e-04m^2/s.

The 2D and 3D analyses both achieved the characteristic parabolic flow profile of the analytical solution in (2.116). The sensitivity of the solutions to both the grid size and the relaxation parameter was tested. Figure 2.9a graphs the relative error in the maximum velocity at the centre of the channel for varying relaxation parameter, τ, at a constant grid size of $0.005m$. The accuracy of the 2D and 3D results was quite similar, with both showing an increased rate of convergence for $\tau < 1$. For $\tau > 1$ the slip velocity of the bounce-back boundary condition becomes significant and the accuracy of the solution deteriorates. At the smallest analysed relaxation parameter, $\tau = 0.505$, the computational Mach number was 0.004 and relative velocity error was 6.6e-04 in both 2D and 3D. The small velocity expansion of the Chapman-Enskog analysis was maintained and the bounce-back condition yielded good results when τ is in the region required for practical physical viscosities.

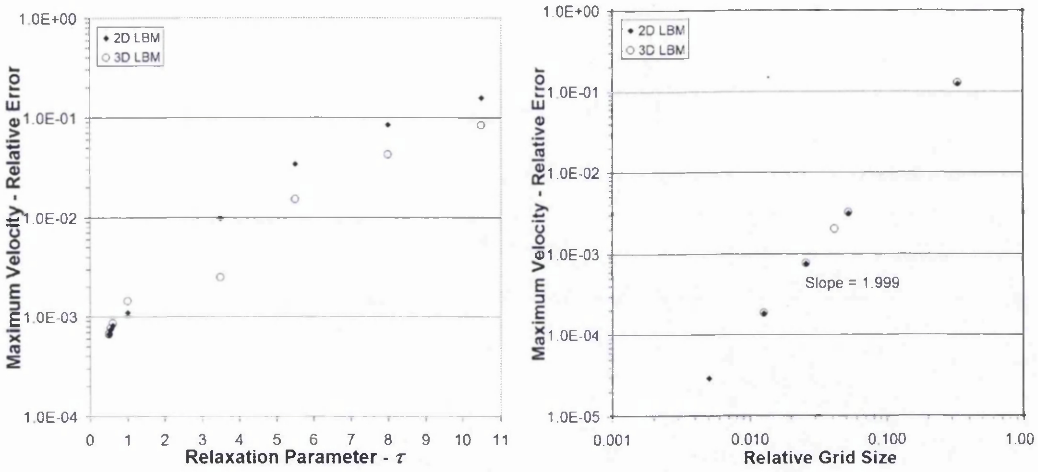

(a) (b)

Figure 2.9: Results of the 2D and 3D Poiseuille flow analyses including the relative error in the maximum velocity for (a) varying relaxation parameter, τ, and (b) varying grid size.

Figure 2.9b graphs the relative error in the maximum velocity at the centre of the channel for varying grid size and a constant relaxation parameter, $\tau = 0.55$. At a lattice spacing of $0.0025m$ the relative error was 1.8e-04 in both 2D and 3D. Both results also highlight the second order convergence of the LBM using the bounce-back boundary condition when the walls conform to the underlying lattice. This is evident in the log-log slope of 1.999 ($\approx$ 2) for both sets of data. Note that due to the assumption of the boundary existing halfway between the wall node and the first fluid node, the simulated domain dimensions are equal to the physical dimensions less one grid spacing.

2.8.3 3D Rectangular Duct Flow

To test the 3D LBM implementation in a three dimensional flow profile, the flow through a square duct was simulated. Maier et al. [86] analysed this problem extensively using the LBM with both the D3Q15 and D3Q18 lattices and a redistributed boundary condition (see Section 2.6.2). The results of this investigation showed that convergence to the analytical solution is dependent on factors such as the lattice implemented, the driving force (i.e. pressure boundaries or body force), and the Mach number. Monotonic convergence was found when using a body force with periodic boundaries and a constant

Mach number for increasing grid resolution[10]. However, when using pressure boundaries the error was found to increase with increased grid resolution for certain Mach numbers. This could be overcome for the pressure boundary case by simultaneously reducing the Mach number at the same rate as the lattice spacing and thereby ensuring the compressibility and discretisation errors were of the same order. Lastly, comparison of the D3Q15 and the D3Q18 lattices found the latter to be more accurate.

The quasi-parabolic axial velocity distribution for flow in a rectangular duct is given by the series approximation [138],

$$\begin{aligned} u_x(y,z) &= \frac{16a^2}{\rho\nu\pi^3}\left(-\frac{\partial p}{\partial x}\right)\sum_{k=1,3,5,\ldots}\left\{(-1)^{(k-1)/2}\right. \\ &\left.\left[1-\frac{\cosh(k\pi z/2a)}{\cosh(k\pi b/2a)}\right]\frac{\cos(k\pi y/2a)}{k^3}\right\}, \end{aligned} \tag{2.114}$$

in which $-a \leq y \leq a$ and $-b \leq y \leq b$. The LBM cannot reproduce this flow profile exactly because of spatial discretisation errors [120] and it has been shown [86] that the error is greatest at an aspect ratio of one. As the aspect ratio increases the flow profile tends toward two-dimensional Poiseuille flow and the agreement between (2.114) and the LBM improves.

To consider the worst-case geometry the duct flow problem was analysed for a square cross-section with height, width and length of $0.2\,m$. Flow was driven by an x-direction body force of $0.001 m/s^2$ which was kept constant for all simulations and periodic boundaries were applied on the inlet and outlet. The fluid density, kinematic viscosity and relaxation parameter used were $1000 kg/m^3$, 1e-04m^2/s and 0.51, respectively. Figure 2.10a is a contour plot of the axial velocity in the duct when a lattice spacing of $0.005\,m$ is used. The characteristic quasi-parabolic flow profile is evident.

Figure 2.10b graphs the error in the duct against lattice spacing. The relative error in the maximum velocity at the centre of duct is plotted with the L_2 norm error in the cross-sectional flow profile. This is evaluated as,

$$\varepsilon_{L_2} = \sum\sqrt{\frac{(u_{LBM}-u_A)^2}{u_A^2}}, \tag{2.115}$$

in which u_A is the solution in (2.114). The summation in (2.115) is undertaken at all cross-sectional locations that are common to each grid resolution.

---

[10] The lattice spacing is related to the relaxation parameter and the time step through (2.66). To maintain a constant Mach number at changing grid size either the relaxation parameter or the macroscopic velocity must be adjusted.

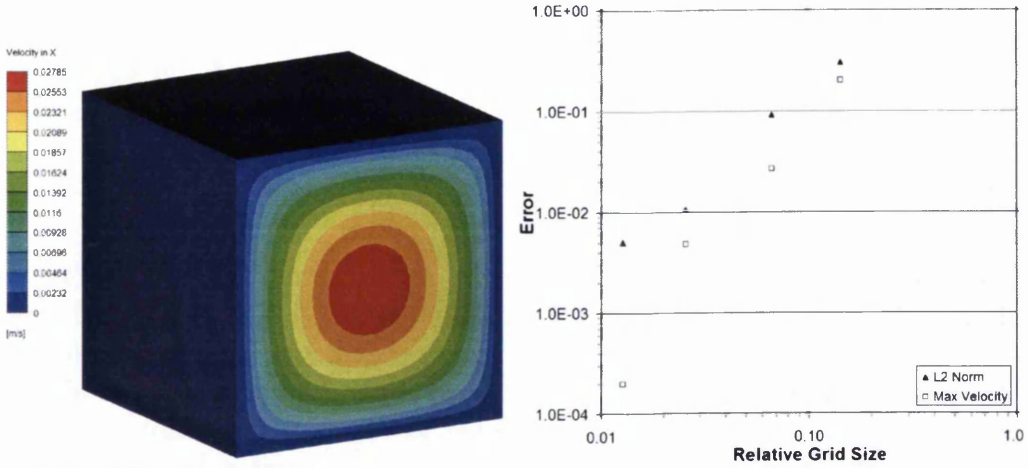

(a) (b)

Figure 2.10: Results of the 3D duct flow analysis including (a) a contour plot of the x-direction velocity and (b) a graph of the maximum velocity error and the L2Norm error of the velocity profile for varying grid size.

Approximately second order convergence can be seen in both in the maximum velocity error (slope 2.16) and the L_2 norm error (slope 1.96) with the exception of the highest resolution data points.

The combination of input parameters in this investigation resulted in a decrease in the computational Mach number, from 0.015 to 0.0024, as the lattice spacing decreased. The results of Maier et al. [86] only displayed monotonic convergence when the Mach number was held constant, which may explain convergence deviation in the present result. Also, by applying the bounce-back boundary condition and interpreting the actual wall location as halfway between the wall nodes and the first layer of fluid nodes, the actual extents of the cross-section decrease with increasing lattice spacing. This will affect the rate of convergence of the solutions.

2.8.4 3D Hagen-Poiseuille Flow

The preceding benchmark simulations have all used orthogonal boundaries which are aligned with the lattice. However the LBM implementation of the present study was written to accommodate irregular, non-orthogonal domains. The availability of such boundaries, as opposed to only those parallel to the Cartesian axes, greatly increases the applicability of the LBM-DEM framework, particularly in large-scale cave simulations presented in Chapters 5 and 6.

The slow, incompressible, viscous flow of fluid in a circular cross-section, or tube, is known as Hagen-Poiseuille flow. The analytical solution for this flow profile can be derived from the Navier-Stokes equations in a cylindrical coordinate system as,

$$u_x\left(r\right)=\frac{-\mathbf{G}}{4\nu}\left[r^2-R^2\right], \tag{2.116}$$

in which R is the radius of the tube. The flow in (2.116) is driven by a body force however this can be modified to a pressure gradient by the simple relation, $\mathbf{G}=\left(1/\rho\right)\left(\partial p/d\mathbf{x}\right)$.

The accuracy of the bounce-back boundary condition on irregular boundaries was discussed at length in Section 2.6.1. At walls that do not conform to the underlying lattice directions the accuracy deteriorates from second order to first order. To investigate this point the flow through a 3D cylindrical tube with a radius of $0.05m$ was simulated at increasing grid resolution. As in preceding examples, flow was driven by an x-direction body force of $0.001m/s^2$ which was kept constant for all simulations and periodic boundaries were applied on the inlet and outlet. The fluid density, kinematic viscosity and relaxation parameter used were $1000kg/m^3$, 1e-04m^2/s and 0.51, respectively. Figure 2.11a is a contour plot of the axial velocity in the tube when a lattice spacing of $0.001m$ is used. The characteristic parabolic flow profile is evident. Also shown in the figure is the approximation of the cylindrical boundary by the regular LBM grid at a resolution of 101 nodes across the diameter.

The relative error in velocity at the centre of the channel is graphed in Figure 2.11b for varying grid size. At a relative grid size of 0.01 the error in the maximum velocity is approximately 3%. It can be seen in this graph that the rate of convergence is not monotonic and that it is less than that in the preceding examples. From a linear fit of the data the convergence slope is approximately 0.7, which is less than first order. This can be explained by the necessary approximations of the tubular boundary. In the coupled LBM-FEM framework the circular cross-section is created using finite element facets. In this analysis the chosen finite element mesh density resulted in the circular cylinder being represented by a hexdecagonal cylinder. This geometry is then further approximated by the orthogonal structure of the D3Q15 lattice, which can be seen in the step-wise nature of the boundary in Figure 2.11a. Despite these approximations, the correlation of the analytical and numerical results is good. Improvement could be achieved by an interpolation-supplemented grid and a polar coordinate system as discussed in Section 2.3.3.

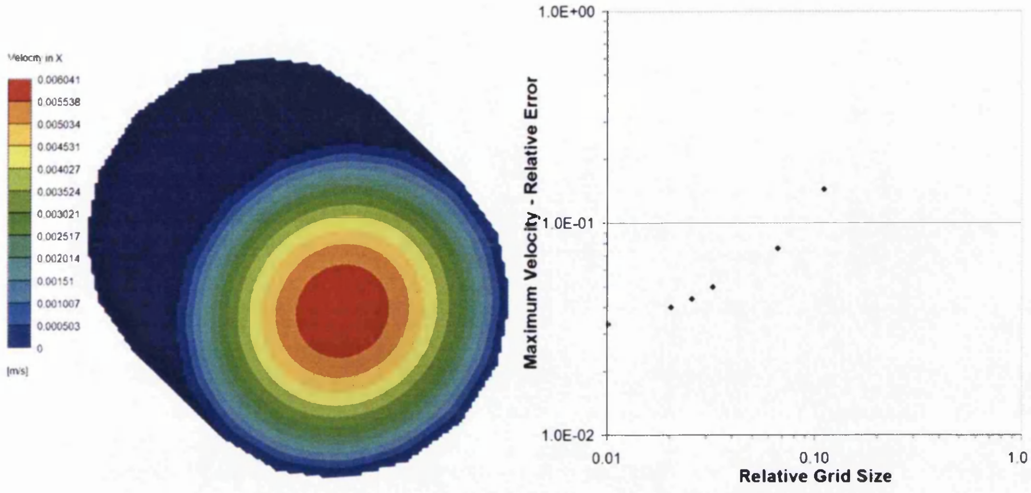

(a) (b)

Figure 2.11: Results of the 3D Hagen-Poiseuille flow analysis including (a) a contour plot of the x-direction velocity and (b) a graph of the maximum velocity error at the centre of the tube for varying grid size.

2.8.5 2D Flow Over a Backward Facing Step

The problem of flow over a backward facing step is commonly used as a benchmark [109, 59, 85] for numerical fluid analysis due to the availability of published experimental data [76], specifically the length of the recirculation eddy. This flow regime adds a degree of complexity to the Poiseuille and duct flow problems by the characteristic recirculation that occurs immediately downstream of the channel expansion (backward step).

The backward step problem was analysed using the LBM implementation. Figure 2.12 shows the characteristic velocity profile for this problem, including the related nomenclature for the step height, h, channel height, H, and recirculation length, X_r. The Reynolds number is defined as [76],

$$Re = \frac{u_{max} h}{\nu}, \tag{2.117}$$

where u_{max} is the maximum velocity at the centre of the parabolic inflow.

Pressure boundaries were employed to drive the flow over the backward step. However, due to the difference of the inlet and outlet area the pressure difference that could be applied was subject to limits. Above the limiting value the flow velocity became sufficient for transition into unsteady flow. Therefore, higher flow velocities were achieved using a prescribed parabolic velocity profile at the inlet and a stress-free outlet. The fluid density, kinematic viscosity and relaxation parameter used were $1000 kg/m^3$, 1e-05m^2/s

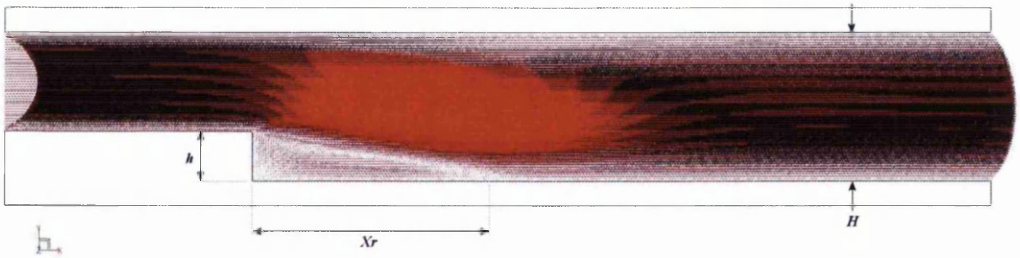

Figure 2.12: The characteristic velocity profile for flow over a backward facing step including the related nomenclature for the flow geometry.

and 0.56, respectively. Note that the stability limit of the Zou and He [147] velocity boundary requires $\tau > 0.5\dot{5}$ (see Section 2.6.2).

The length of the channel analysed was $2m$, but for $Re > 50$ the channel length was increased to $4m$ to isolate the recirculation zone from outlet boundary effects. The expanded channel height, H, was $0.3m$, and the step height, h, was $0.1m$. The resultant channel to step ratio H/h was 3.026. This value is a consequence of the lattice spacing of $0.005m$ and the bounce-back interpretation of the boundary location as halfway between the wall nodes and first fluid nodes.

Figure 2.13a is a graph of the non-dimensionalised recirculation length, X_r/h, against Reynolds number as calculated in (2.117), and Figure 2.13b is a vector plot of the recirculation zone at $Re = 26$. The results of the present 2D study are plotted against the LBM results of Qian et al. [109] and experimental results of Kueny and Binder [76]. Good correlation between both sets of LBM results can be seen. At $Re = 150$ the numerical results are approximately 8% greater than the experimental value. The numerical over-prediction of the recirculation length may be due to the absence of gravitational body forces, which will have been present in the experiments.

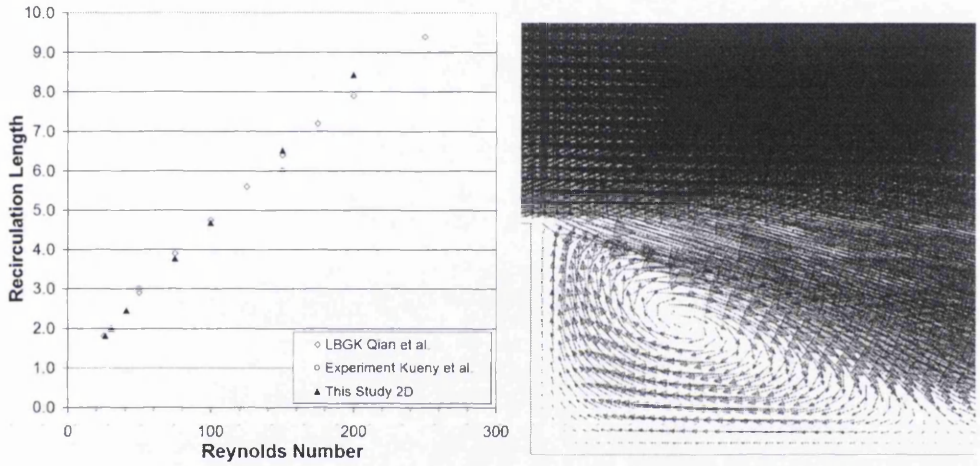

(a) (b)

Figure 2.13: Results of the 2D flow over a backward facing step including (a) a graph of the recirculation length against Re for $H/h = 3.026$ and (b) a velocity vector plot of the recirculation zone for $Re = 26$.

CHAPTER 3

MULTIBODY STRUCTURAL COUPLING WITH THE LATTICE BOLTZMANN METHOD

One of the greatest strengths of the LBM is its ability to be fully coupled to a large number of moving bodies. Furthermore, this coupling can be undertaken in both two-dimensional and three-dimensional dynamic systems where the transient nature of contacts and the tortuosity of the void spaces would make finite element discretisation for traditional CFD intractable.

The most common approach for multibody coupling with the lattice Boltzmann method is to utilise the discrete element method to govern the structural dynamics and interaction. This approach has been taken to investigate the sedimentation of particles in fluid [95, 37], fluid-induced erosion of cemented granular solids [24, 25], and the hydraulic transport of solids in turbulent flows [33]. All of these examples include multiple particle systems that are dominated by a large number of intermittent contacts, moderate to high Reynolds numbers, and representative physical properties for the fluids and solids.

In the present study a LBM-DEM framework is created to simulate the phenomenon of fines migration in a block cave during draw. The DEM is employed to govern the dynamics of rock blocks up to $1\,m$ across in caves with dimensions in the order of $10\,m$. Under the influences of gravity and draw control these physical attributes will result in large contact forces that will need to be handled in stable fashion. The coupling of the fines phase to the blocks via the LBM will be problematic if the block dynamics becomes erratic.

In this chapter, LBM coupling approaches for moving boundaries are reviewed and contrasted following a brief discussion of the basics of the DEM. Issues related to the implementation of fluid-solid coupling are discussed including boundary mapping techniques, cell coverage calculation, and hydrodynamic force evaluation. The coupling of the explicit schemes of the LBM and the DEM is investigated and a dynamic sub-cycling procedure is presented. The chapter is concluded with a number of validation examples which qualitatively and quantitatively test the performance of the LBM-DEM framework.

3.1 The Discrete Element Method

In many lattice Boltzmann simulations of particle suspensions, the inter-particle interaction is either ignored or approximately treated. However, cases where particles are densely packed and subject to large displacements, such as block cave dynamics, require accurate resolution of the contact of the distinct blocks. A rational choice is to employ the discrete element method (DEM) to account for this interaction, which necessitates a framework that efficiently couples the DEM to the LBM for application in fluid-particle interaction problems.

The discrete element method, which originated in geotechnical and granular flow applications in the 1970's [27], has become a well-established numerical tool capable of simulating problems of a discrete or discontinuous nature. In its classical form, a discrete system is considered as an assembly of individual objects which are treated as rigid and represented by simple geometric entities such as discs, spheres, ellipses and ellipsoids. Recently, more complex shaped elements such as superquadrics, polygons and polyhedra [52, 34] have also been introduced to more realistically represent objects encountered in practice.

In the context of the explicit, central difference integration scheme employed to solve the dynamic equations of the system, the major computational steps involved in the DEM at each time step consist of (global) spatial search, (local) interaction resolution, interaction force computation and solutions of element positions and velocities. The global search aims to determine for each discrete element a list of neighbouring elements that may potentially interact with it. In the second step, each potential contact-target pair is locally resolved on the basis of their kinematic relationship. In the third step, the interaction forces between each contact pair are determined according to a constitutive relationship or interaction law (e.g. linear or Hertzian). Fi-

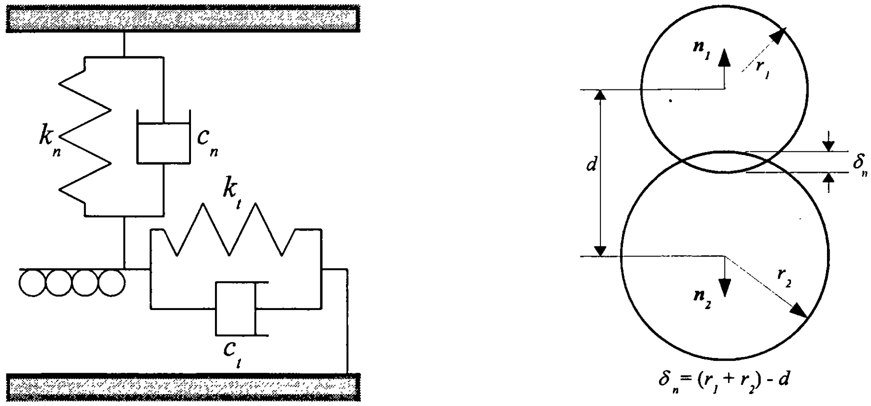

(a) (b)

Figure 3.1: Aspects of contact interaction in the discrete element method including (a) rheological representation of the soft contact model with damping and (b) the evaluation of contact overlap for two circular elements.

nally the velocities and displacements of the discrete elements are updated by the time integration scheme employed.

Figure 3.1a schematically illustrates the soft-contact model (when contact damping is employed) used to resolve interaction forces between discrete elements. It can be seen that the total contact force is composed of normal and tangential components, with both determined from the small, permissible overlap between the particles. The contact overlap, and its evaluation for the simple case of two contacting circular elements, is shown in Figure 3.1b. A range of interaction laws of varying complexity are available for the calculation of the normal contact force. Examples include linear, Hertzian, Winkler and power laws [53]. The linear and power laws are evaluated from the contact overlap[1] and can be written in a general form as,

$$F_N = \alpha K_N \delta_n^m, \tag{3.1}$$

in which $\alpha = m = 1$ for the linear model, and $\alpha = 1$ and m is a model parameter for the power law. The normal stiffness K_N is a model parameter for both interaction laws. The tangential contact component is calculated using a modified Coulomb friction model the details of which can be found in [54].

By taking into account inertial ($\mathbf{G}$), contact ($\mathbf{F_c}$) and hydrodynamic ($\mathbf{F_f}$) forces acting on a discrete element, the dynamic translational and rotational

---

[1] The Hertz and Winkler models evaluate the $F_n - \delta$ relationship by integrating the surface traction as detailed in [53].

equations can be expressed as,

$$m\mathbf{a} + c\mathbf{v} = \mathbf{F_c} + \mathbf{F_f} + m\mathbf{G}, \tag{3.2}$$

$$I\alpha + c\omega = \mathbf{T_c} + \mathbf{T_f}, \tag{3.3}$$

in which c is a damping coefficient, and the term $c\mathbf{v}$ represents a viscous force that accounts for the effect of all possible dissipation forces existing in the system.

Due to the influence of the solution time step in the lattice Boltzmann method on the physical transport properties of the fluid (i.e. viscosity), coupling with the discrete element method must be handled carefully. This is discussed further in Section 3.3.

3.2 Review of Coupling Methods

The interaction of the fluid regime with suspended particles is integral to the coupling of the lattice Boltzmann method to the discrete element method. A number of techniques which vary in complexity, accuracy and computational cost have been developed to handle this interaction including, not exclusively, bounce-back [40, 43], link bounce-back [78, 79], dry coupling methods [2] and immersed boundary methods [97, 120, 103]. In addition, slight variations of each of these interaction methods have been developed for specific applications.

Successful coupling of the DEM to the LBM first requires adequate mapping of the structural elements to the lattice Boltzmann grid. This is shown for a circular and a polygonal element in Figure 3.2. The mapping process can differ slightly between coupling methods but it generally requires a number of different classifications on the nodes underlying the element. The terminology used here, and shown in Figure 3.2, includes the the nodal classes of solid boundary nodes, fluid boundary nodes, and internal solid nodes. The solid boundary nodes lie inside the solid and define the element boundary in a step-wise fashion on the lattice. The interior solid nodes are all other nodes covered by the element. Lastly, the fluid boundary nodes are those nodes that lie outside the element which are connected to a boundary node by one or more of the lattice links.

3.2.1 Bounce-Back Method

The bounce-back condition (see Section 2.6.1) has been tested in particle coupling problems due to its simplicity and locality of operations. Its suitability was evaluated by Gallivan et al. [43] for the cases of flow past a

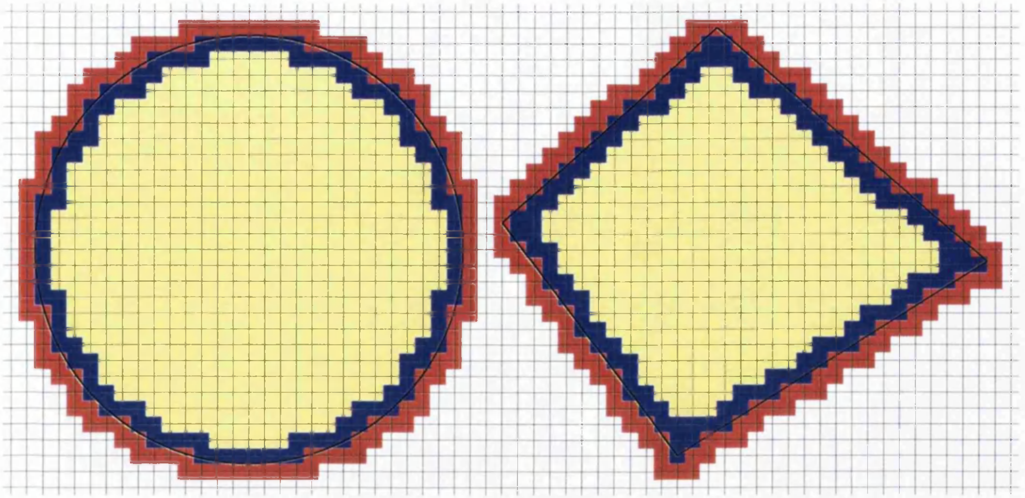

Figure 3.2: The representation of discrete elements on a regular D2Q9 lattice showing solid boundary nodes (blue), fluid boundary nodes (red) and internal solid nodes (yellow).

periodic array of circular and octagonal cylinders on a D2Q9 lattice. Due to the fact the octagonal element conformed to the underlying lattice it was expected to yield reasonable results. The benchmark solution for the octagonal cylinder was the LBM using the hydrodynamic boundary condition of Noble et al. [96] (see Section 2.6.1), while for the circular cylinder an implicit finite difference scheme was employed (because the hydrodynamic boundary condition (HBC) in [96] cannot readily handle non-aligned boundaries). In terms of computational expense it was found that the HBC consumed 25% of the solution time as opposed to 1% for the bounce-back, which is a significant increase.

With sufficient grid resolution the bounce-back condition was found to give good predictions of the velocity field and the drag force. The velocity field results for the octagonal cylinder showed sub-linear convergence with grid size at Reynolds number of 10. It was anticipated that the condition would be first order in the region adjacent the boundary but it was found that it in fact influences the entire field, degrading the second order convergence of the LBM. The convergence of drag force was also found to be sub-linear. However, the error in drag force for Reynolds numbers from 0.1 to 10 showed a constant error of 1%, which decreased with further increasing Reynolds number. Errors were found to reduce slightly with relaxation parameter.

Similar trends were found in the analysis of the circular cylinder however the maximum velocity error was considerably greater at the coarsest mesh density. The quantitative results for the bounce-back condition compared

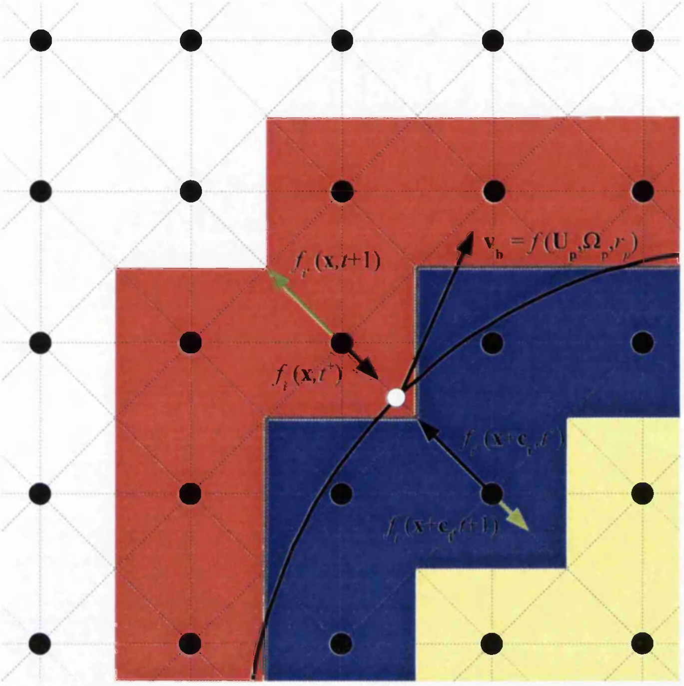

Figure 3.3: The link bounce-back method for fluid particle coupling.

very well with the benchmark solutions. However, the obstacles in these analyses did not move with respect to the lattice. This can result in undesirable force fluctuations [78, 79] on the obstacle as it is re-mapped during the solution.

3.2.2 Link Bounce-Back Method

The link bounce-back method was proposed by Ladd [78, 79] as an improvement to the bounce-back technique for modelling fluid-particle interaction with moving boundaries. As the name suggests, this method enforces the bounce-back condition on the links between fluid boundary nodes and solid boundary nodes and assumes that the solid-fluid interface exists in the middle of each link. (i.e. halfway between the fluid boundary nodes and solid boundary nodes).

Details of the link bounce-back condition can be seen in Figure 3.3. The velocity of the boundary at the approximated interface is calculated from the solid's translational and rotational velocities as,

$$\mathbf{v_b} = \mathbf{U_p} + \boldsymbol{\Omega}_\mathbf{p} \times \left[\left(\mathbf{x} + \frac{1}{2}\mathbf{c_i}\Delta t \right) - \mathbf{X_p} \right], \tag{3.4}$$

in which $\mathbf{U_p}$, $\mathbf{\Omega_p}$, and $\mathbf{X_p}$ are the translational velocity, rotational velocity and centroid of the solid particle, respectively. Using the boundary velocity at the link intersection, the bounce-back procedure for fluid boundary nodes is,

$$f_{i'}(\mathbf{x}, t + \Delta t) = f_i\left(\mathbf{x}, t^+\right) - 2w_i\rho\mathbf{v_b}\cdot\mathbf{c_i}. \tag{3.5}$$

Recall that w_i is the weighting function for for the lattice direction i (see Section 2.4.2) and note that $f_{i'}$ refers to the distribution function in the opposite direction to f_i. Similarly, the bounce-back procedure for solid boundary nodes is,

$$f_i(\mathbf{x} + \mathbf{c_i}\Delta t, t + \Delta t) = f_{i'}\left(\mathbf{x} + \mathbf{c_i}, t^+\right) + 2w_i\rho\mathbf{v_b}\cdot\mathbf{c_i}. \tag{3.6}$$

It can be seen in (3.5) and (3.6) that when the boundary velocity is zero, the link bounce-back method reduces to the one-step bounce-back technique. However, when the boundary is moving a portion of the incident particle distribution function proportional to the boundary velocity $\mathbf{v_b}$ is passed across the fluid-solid interface. The direction of momentum transfer is dependent on the node class (i.e. either fluid boundary or solid boundary) and whether the boundary is approaching or retreating from the boundary node. Obviously rearrangements of distribution functions, and subsequent momentum transfer between the fluid and the solid, can only be made among pairs of opposing velocities.

The force exerted on the solid particle as a result of the bounce-back and momentum transfer is calculated from the net change at the links,

$$\begin{aligned}\mathbf{F_{i'}}\left(\mathbf{x} + \frac{1}{2}\mathbf{c_i}\Delta t, t + \frac{1}{2}\Delta t\right) &= 2\left[f_i\left(\mathbf{x}, t^+\right)\right. \\ &\left. - f_{i'}\left(\mathbf{x} + \mathbf{c_i}\Delta t, t^+\right) - 2w_i\rho\mathbf{v_b}\cdot\mathbf{c_i}\right]\mathbf{c_i}\end{aligned} \tag{3.7}$$

and the total hydrodynamic force is found by summing over all boundary links.

Two significant drawbacks of the link bounce-back method are the disparity between the physical and simulated boundary shape and the occurrence of fluctuations in the induced hydrodynamic load. The former is usually accounted for by the definition of a hydraulic radius for the suspended particle. The latter, in which temporal discontinuity exists in the hydrodynamic force imparted on moving solid obstacles, is a feature of this and many other lattice-based fluid-solid interaction methods [143]. As a solid particle moves across the grid, boundary links are switched 'on' and 'off' in a discrete manner resulting in discontinuities in the total number of links that define the boundary and consequently the hydrodynamic force. The summation of force contributions over all boundary links does not completely attenuate this phenomenon, and the problem is exacerbated as the particle velocity becomes large. Ladd [78] mitigated this problem by applying the time average of the total force on the particle at the previous and future time steps.

From the definition of the link bounce-back technique it can be seen that lattice nodes on either side of the particle boundary are treated identically, so that fluid fills the space both inside and outside the particle. Although counterintuitive, this approach is taken on the basis of computational convenience. As a solid obstacle moves across the lattice, it will progressively cover and uncover nodes. To prevent the presence of fluid inside the moving solid would require the 'birth' and 'death' of fluid particle distribution functions at nodes that have just been uncovered and covered, respectively (see Section 3.2.3). To avoid the creation and destruction of mass, momentum is exchanged between fluid boundary and and solid boundary nodes as in (3.5) and (3.6) so that the fluid momentum at the approximated boundary matches the hydrodynamic no-slip condition. The fluid at the remaining internal solid nodes is relaxed to an equilibrium which mimics the rigid body motion of the particle. At moderate Reynolds number the internal fluid exerts a force equivalent to its inertial mass on the particle, which over short times is generally negligible [79].

As an improvement to the link bounce-back method, the continuous bounce back method [133, 134] was proposed. In it, a scalar is introduced which represents the fluid volume fraction of each cell[2]. Using this parameter, rules are constructed which relate the particle distribution function after propagation to the post collision distribution. The amount of fluid reflected and propagated is broken up proportionally with respect to the fluid volume fraction. Results show reasonable reproduction of Poiseuille flow in channels only a couple of cells across, and also in channels at an arbitrary angle to the grid. The improved boundary representation offered by the CBB reduces the cell requirements for adequate representation of curved boundaries, which in turn results in significant computational savings. However, results for drag on discs and spheres in periodic arrays showed that the CBB has not eliminated the need for a hydraulic radius. It was also found that when the lattice viscosity deviates from 1/6 the predicted drag force drifted from the theoretical solution [134].

Chun and Ladd [23] proposed an interpolated bounce-back boundary condition to correct the problems associated with LBB and CBB techniques, particularly the discrepancy between the physical and approximated boun-

---

[2] A lattice cell is the unit area that surrounds a grid node. For example, the fluid boundary node cells in Figure 3.3 are coloured red.

dary location. In the IBB, the particle distribution functions incident on a boundary travel a total distance of one grid spacing and are reflected from the true boundary location to a position inbetween grid nodes. The reflected distribution is then used, in conjunction with the nearest fluid node, to interpolate the unknown function at the fluid boundary node. Different interpolations are used if the boundary is closer to the solid boundary or the fluid boundary node. In this method , the equilibrium function is advected and interpolated rather than the particle distribution function. Provided that two nodes are present between boundary surfaces (i.e. distance greater than Δx), this approach is found to be second order accurate and independent of viscosity. One drawback of the EIBB method is that it suffers from mass leakage in certain grid orientations. This has been corrected in mass conservative interpolations but they involve greater complexity and lose second-order accuracy. However, in the incompressible limit this leakage is not significant [23].

It has been shown that interpolated bounce-back is only first order convergent for LBGK models [36] and that MRT-LBM models are required to attain second order accuracy [46, 7]. Recently, Peng and Luo [103] undertook a comparison of the IBB condition and an immersed boundary condition (IBM) in the case of flow past a circular cylinder. Analyses were run at $Re = 20$ for steady flow and $Re = 100$ for unsteady flow. The results showed that both methods were second order convergent. With the same resolution, the IBB was found to be more accurate than the IBM for drag, lift, pressure and recirculation length, however the latter still performed well compared to benchmark results. It also has the added advantage of being easier to implement.

3.2.3 Dry Particle Coupling Method

In all of the coupling methods based on bounce-back principles discussed thus far, fluid is allowed to exist inside the solid particles primarily for matters of computational convenience. Aidun et al. [2] proposed an approach in which fluid was not permitted to exist within solid obstacles. The absence of fluid nodes inside the solid obstacle, and subsequent absence of internal collisions with fluid from those nodes, means that there is no inertial force applied to the particle from the internal fluid. The forces acting on the solid obstacle are then limited to the hydrodynamic force of the particle distribution functions impacting it from the outside and its own body forces. The absence of the internal inertial force facilitates the modelling of obstacles with a solid density close to or less than the fluid density, which was previously not possible with bounce-back based coupling methods.

In the dry coupling method of Aidun et al. many of the features of the LBB are employed. The boundary links are defined in the same fashion, the fluid-solid boundary is approximated at the middle of the links, the boundary velocity is calculated as in (3.4) and the same bounce-back condition (3.5) is applied at the fluid boundary nodes. At this point it is important to note that the lack of a complementary solid boundary node on each link means that the mass at the fluid boundary node can change. The increment of momentum at fluid boundary nodes is then calculated as,

$$\delta \mathbf{p_i} = 2\mathbf{c_i}\left[f_i\left(\mathbf{x}, t+\Delta t\right) - \rho\left(\mathbf{x}, t+\Delta t\right) w_i \mathbf{v_b}\cdot\mathbf{c_i}\right], \tag{3.8}$$

if i' is a boundary link and the corresponding force exerted on the particle is,

$$\mathbf{F}^{(b)}_{\mathbf{i}}\left(\mathbf{x}+\frac{1}{2}\mathbf{c_{i'}}\Delta t, t+\frac{1}{2}\Delta t\right) = \frac{-\delta\mathbf{p_i}}{\Delta t}. \tag{3.9}$$

As the solid obstacle traverses the grid over a time step it may cover a node previously inhabited by fluid particle distribution functions. At this time, the particle assumes the momentum of the fluid node imparting a small force on the particle,

$$\mathbf{F}^{(c)}\left(\mathbf{x}, t_0+\frac{1}{2}\Delta t\right) = \sum_i f_i\left(\mathbf{x}, t_0\right) c_i, \tag{3.10}$$

and the fluid at this node is 'destroyed'. Likewise, due to translation and rotation, nodes previously mapped as part of the solid obstacle may become exposed as fluid nodes. Consequently, particle distribution functions must be 'created' at the new fluid nodes. The density of new fluid nodes is determined from an average of adjacent fluid nodes using,

$$\rho\left(\mathbf{x}, t_0\right) = \frac{1}{N_b}\sum_{N_b}\rho\left(\mathbf{x}+\mathbf{c_{i'}}\Delta t, t_0\right), \tag{3.11}$$

and the macroscopic fluid velocity is enforced to be the same as the obstacle boundary adjacent to it using (3.4). With the density and velocity of the fluid at the new node known the equilibrium distribution can then be calculated. Since the newly created fluid node is assigned a momentum of $\rho\left(\mathbf{x}, t_0\right)\mathbf{u}\left(\mathbf{x}, t_0\right)$, the equivalent amount of momentum must be removed from the particle as,

$$\mathbf{F}^{(u)}\left(\mathbf{x}, t_0+\frac{1}{2}\Delta t\right) = -\rho\left(\mathbf{x}, t_0\right)\mathbf{u}\left(\mathbf{x}, t_0\right). \tag{3.12}$$

The total force on the particle is found by the summation of forces over all fluid boundary nodes, newly covered nodes, and newly uncovered fluid nodes.

As in the LBB method the discontinuity of total force and momentum is still a problem in this method and it is handled in the same way by applying time averages of both quantities. Also, the bounce-back method applied at fluid boundary nodes means that the dry coupling method is not locally mass conservative, however it is on a global scale. Lastly, although it removes limitations on the range of solid-fluid density ratios that can be simulated, another drawback of this technique is the additional computational cost involved in the destruction and creation of fluid nodes, which is not insignificant.

3.2.4 The Immersed Moving Boundary Method

The immersed boundary method [104] is another coupling approach that has been applied to the lattice Boltzmann method [96, 36, 30] to solve fluid solid interaction problems. Historically, in immersed boundary methods the fluid domain is described by a Eulerian grid and the structural boundaries are mapped by a set of Lagrangian nodes. The regular, stationary grid of the LBM and the dynamic mapping of the structural field to the grid allows the same approach to be applied in LBM-DEM coupling. As a basic description, in immersed boundary methods the boundary conditions (i.e. no-slip) are enforced as additional body forces applied to the fluid. The hydrodynamic coupling between fluid and structure is therefore achieved by evaluating the force the flow exerts on the nodes and the reaction force the nodes exert on the flow [103].

An immersed moving boundary technique for LBM-DEM coupling was proposed by Noble and Torczynski [97]. Two objectives of the method were to overcome the momentum discontinuity of LBB-based techniques and provide adequate representation of non-conforming boundaries at lower grid resolutions. It was also important to retain two critical advantages of the LBM, namely the locality of the collision operator and the simple linear streaming operator, and thus facilitate solutions involving large numbers of irregular-shaped, moving boundaries. In this method the lattice Boltzmann equation is modified to include a term which is dependent on the proportion of the nodal cell that is covered by solid (see Figure 3.4a), thus improving the boundary representation and smoothing the hydrodynamic forces calculated at an obstacle's boundary nodes as it moves relative to the grid.

In the immersed moving boundary method the lattice Boltzmann equation is modified to include an additional collision term, Ω_i^s, and can be written

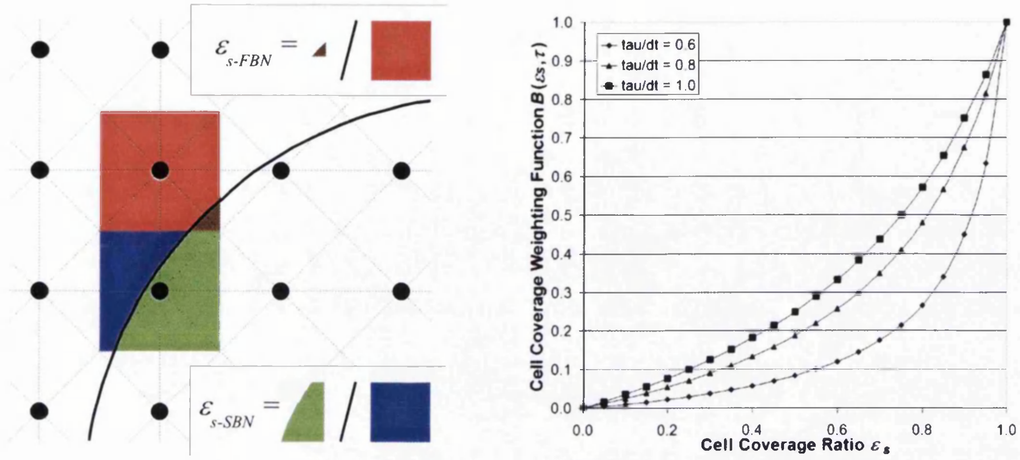

(a) (b)

Figure 3.4: Aspects of the solid coverage weighting function in the immersed moving boundary method of Noble and Torczynski [97]: (a) evaluation of the solid coverage ratio, ε_s, and (b) the viscosity dependent weighting function $B_n\left(\varepsilon_n, \tau\right)$.

including the body force term (see Section 2.7) as,

$$\begin{aligned} f_i\left(\mathbf{x}+\mathbf{c}_\mathrm{i}\Delta t, t+\Delta t\right) &= f_i\left(\mathbf{x}, t\right) - \left[1-B_n\right]\left[\frac{\Delta t}{\tau}\left(f_i\left(\mathbf{x}, t\right) - f_i^{eq}\left(\mathbf{x}, t\right)\right)\right] \\ & \quad + B_n\Omega_i^s + \left[1-B_n\right]\frac{\mathbf{G}\cdot\mathbf{c}_\mathrm{i}}{Kc^2}, \end{aligned} \tag{3.13}$$

in which B_n is a weighting function for the additional collision operator based on the total solid coverage ratio in each nodal cell, ε_n. Note that both the solid coverage ratio and the weighting function are summations of all coverage contributions from solid obstacles that intersect a nodal cell such that $\varepsilon_n = \sum_s \varepsilon_s$ and $B_n = \sum_s B_s$, where ε_s and B_s are the contributions from each obstacle. The additional collision term, Ω_i^s, modifies the momenta of mapped obstacle nodes and accounts for fluid interaction with any solid obstacles present in the nodal cell. At its limits $B_n = 0$ and $B_n = 1$, corresponding to pure fluid and pure solid existing at the node, respectively. The simplest form of the weighting function is simply $B_n = \varepsilon_n$ which gives a relationship directly proportional to the solid ratio.

Two forms of the additional collision operator, Ω_i^s, were presented in [97] for the immersed moving boundary method. The first was based on the concept of the bounce-back of the non-equilibrium part of the particle distribution function,

$$\Omega_i^s = \left[f_{i'}\left(\mathbf{x}, t\right) - f_{i'}^{eq}\left(\rho, \mathbf{u}\right)\right] - \left[f_i\left(\mathbf{x}, t\right) - f_i^{eq}\left(\rho, \mathbf{v}_\mathrm{p}\right)\right]. \tag{3.14}$$

In (3.14) the rigid body velocity of particle, $\mathbf{v_p}$, at fluid boundary nodes, solid boundary nodes and internal solid nodes is evaluated as a combination of translation and rotation as in (3.4). By rewriting the non-equilibrium bounce-back condition [147] (see Section 2.6.2) in the x-direction, $f_1 - f_1^{eq} = f_3 - f_3^{eq}$, as,

$$\Delta_{1-3}^{s} = \left[f_3 - f_3^{eq}\right] - \left[f_1 - f_1^{eq}\right], \tag{3.15}$$

it can be seen that in the limit of pure solid, $B_n = 1$, (3.14) and (3.15) are analogous. In the limit of pure fluid, $B_n = 0$, the additional collision operator vanishes and the ordinary LBE collision is processed.

The second additional collision operator was formulated from the superposition of the equilibrium distribution at the solid obstacle velocity and a term that depends on the deviation of the current distribution from its equilibrium value,

$$\Omega_i^s = f_i^{eq}(\rho, \mathbf{v_p}) - f_i(\mathbf{x}, t) + \left[1 - \frac{\Delta t}{\tau}\right]\left[f_i(\mathbf{x}, t) - f_i^{eq}(\rho, \mathbf{u})\right], \tag{3.16}$$

which can be substituted into (3.13) to give (ignoring the body force term),

$$\begin{aligned} f_i(\mathbf{x} + \mathbf{c}_i\Delta t, t + \Delta t) &= f_i(\mathbf{x}, t) - \frac{\Delta t}{\tau}\left(f_i(\mathbf{x}, t) - f_i^{eq}(\mathbf{x}, t)\right) \\ &\quad + B_n\left[f_i^{eq}(\rho, \mathbf{v_p}) - f_i^{eq}(\rho, \mathbf{u})\right]. \end{aligned} \tag{3.17}$$

From interrogation of (3.17) it can be seen that the additional collision operator again vanishes in the limit of pure fluid. In the limit of pure solid (3.17) can be rewritten as,

$$f_i(\mathbf{x} + \mathbf{c}_i\Delta t, t + \Delta t) = f_i^{eq}(\rho, \mathbf{v_p}) + \left[1 - \frac{\Delta t}{\tau}\right]\left[f_i(\mathbf{x}, t) - f_i^{eq}(\rho, \mathbf{u})\right], \tag{3.18}$$

which can be interpreted as incrementally forcing the distribution function to the equilibrium value of the solid velocity at that node.

In testing, the non-equilibrium bounce-back operator (3.14) was employed with the simple weighting function equal to the solid coverage ratio, whereas the superposition collision operator (3.16) required a more complicated weighting function,

$$B_s(\varepsilon_s, \tau) = \frac{\varepsilon_s(\tau/\Delta t - 1/2)}{(1 - \varepsilon_s) + (\tau/\Delta t - 1/2)}, \tag{3.19}$$

based on the dimensionless relaxation parameter. The weighting function in (3.19) is determined from physical intuition and empirical closure of Poiseuille flow [65] and is graphed in Figure 3.4b for different values of $\tau/\Delta t$. It should be noted that this weighting function and the presented collision operators are not exclusive.

The total hydrodynamic force acting on the solid obstacle is found by summing the change of momenta due to the additional collision operator over all lattice directions at each node and then over all fluid boundary, solid boundary and internal solid nodes,

$$\mathbf{F_p} = \sum_n B_n \left(\sum_i \Omega_i^s \mathbf{c_i} \right) . \tag{3.20}$$

The hydrodynamic torque is calculated similarly,

$$\mathbf{T_p} = \sum_n \left[(\mathbf{x_n} - \mathbf{X_p}) \times B_n \left(\sum_i \Omega_i^s \mathbf{c_i} \right) \right] , \tag{3.21}$$

in which $\mathbf{x_n} - \mathbf{X_p}$ is the vector from the centre of rotation to the coupled node. Both (3.20) and (3.21) assume coordinates and momenta are in physical units, however if they are employed in non-dimensional lattice units (which is computationally more convenient) both equations require an additional term of $(\Delta x)^D / \Delta t$ to yield physical force and torque, respectively. The exchange between physical and lattice units is discussed further in Appendix B.

Three combinations of the additional collision operator and weighting function were tested and benchmarked against a simple, binary bounce-back of the non-equilibrium part of the distribution (i.e. similar to the link bounce-back approach). The combinations were:

1. Equations (3.14) and (3.19) - non-equilibrium bounce-back with τ-dependent weighting
2. Equation (3.14) and $B_s = \varepsilon_s$ - non-equilibrium bounce-back and solid ratio weighting
3. Equation (3.16) and $B_s = \varepsilon_s$ - near-equilibrium superposition and solid ratio weighting
4. Equation (3.14) and $B_s = \mathtt{NINT}(\varepsilon_s)$ – simple, binary non-equilibrium bounce-back.

For the test case of flow past a stationary cylinder, combinations (1), (2) and (3) were all found to be an improvement over the bounce-back approach (4). Combination (1) performed the best of the immersed moving boundary approaches as it appeared to give second order convergence with grid size for the drag force whilst the others only demonstrated first order convergence.

As an extension to the immersed boundary method of Noble and Torczynski [97], Holdych [65] altered the non-equilibrium bounce-back collision operator (3.14) by replacing the fluid equilibrium in the reflected direction with the particle equilibrium,

$$\Omega_i^s = \left[f_{i'}\left(\mathbf{x},t\right) - f_{i'}^{eq}\left(\rho,\mathbf{v_p}\right)\right] - \left[f_i\left(\mathbf{x},t\right) - f_i^{eq}\left(\rho,\mathbf{v_p}\right)\right]. \tag{3.22}$$

In testing, Strack and Cook [120] found Holdych's modified collision operator increased the accuracy of force and torque on a sphere in periodic Poiseuille flow. It also has the advantage of only requiring one equilibrium function calculation to process the node, as opposed to two in the original operator.

Implementation Issues of the IMB

From the review of the IMB it can be seen that the additional collision operators only require local nodal information to enforce coupling between the fluid and solid. Information from neighbouring nodes is not required, as in IBB techniques and others, and neither is the solid surface normal. No additional data storage or organisation is necessary. The generality and locality of the IMB operations result in a coupling technique that can be applied to complex geometries as in porous media flows and also densely packed, evolving suspensions of particles.

By using three nodal classifications in the mapping of solid obstacles, namely fluid boundary nodes, solid boundary nodes and internal solid nodes, the process of calculating the solid coverage ratio can be optimised. With simple geometry it can be shown that all internal solid nodes are always entirely covered and thus have a coverage ratio of unity. The coverage ratio at the fluid boundary nodes and solid boundary nodes can then be calculated by either closed form solutions, polygonal approximations or cell decomposition as illustrated schematically in Figure 3.5. Obviously, closed form solutions (Figure 3.5a) provide an exact value for the solid coverage ratio but this can be at significant computational cost. In 2D, polygonal particles can be processed in a reasonably straightforward manner and circular elements can be processed at moderate cost as combinations of polygons and circular segments. However, in 3D attaining an exact solution, especially for spherical elements or higher order shapes such as superquadrics, is cumbersome and expensive. The cell decomposition method (Figure 3.5b) takes a brute force approach to evaluating the solid coverage ratio. In this technique, each nodal cell is decomposed into n_{sub}^2 sub-cells of side length Δx_{sub} such that $\Delta x_{sub} = \Delta x / n_{sub}$. An inside-outside check of the sub-cell vertices is then

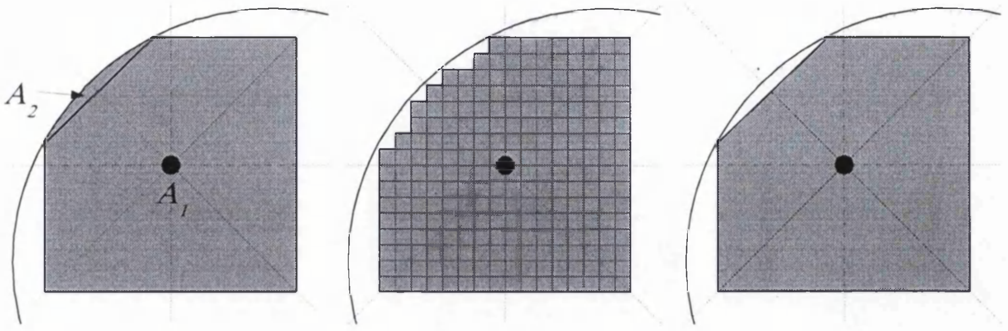

(a) (b) (c)

Figure 3.5: Techniques for evaluating the solid coverage ratio in 2D for the immersed boundary coupling method [97] including (a) an exact closed form solution, (b) cell decomposition and (c) polygonal approximation.

performed for the obstacle boundary and the solid coverage ratio calculated as the sum of the sub-cells inside the boundary. Whilst the simplest to implement, the cell decomposition method becomes prohibitively time consuming as n_{sub} is increased to improve the accuracy of the coverage ratio. Lastly, polygonal approximations (Figure 3.5c) of curved boundaries offer a compromise between the preceding techniques. In this approach the coverage area is approximated as a polygon in 2D or a combination of polyhedra in 3D. In 3D, this requires the definition of a number of generalised polyhedron combinations for spherical obstacles. These general shapes are then applied to the fluid boundary and solid boundary nodes to evaluate the solid coverage ratio.

It should be noted that as with preceding bounce-back based coupling techniques, the IMB of Noble and Torczynski [97] does not resolve detailed particle-fluid-particle interactions, such as lubrication pressure between immersed particles, once particles approach within one lattice cell of one another. This phenomenon was investigated by Feng and Michaelides [36] in another immersed boundary method, and approximated by a large repulsion force when the distance between particles becomes less than a specified threshold value. This is of particular relevance when overlap-based force such as those in the discrete element method are used to handle particle-particle and particle-wall interactions. The allowance of a small overlap, δ_n, can result in nodal classification conflicts between two or more particles, where for example a lattice node may define the boundary of both particles. Such conflicts must be treated carefully, however they can be minimised by the introduction of a contact buffer. In the DEM, this buffer employs a contact radius that is marginally greater than the physical radius so that contact interaction occurs before there is any chance of nodal conflict.

3.3 Coupling of Explicit Schemes and Sub-Cycling

The coupling of the lattice Boltzmann method and discrete element method explicit schemes necessitates matching of their respective critical time steps. Stability criteria require the DEM time step to be less than a critical value however however in the lattice Boltzmann method the time step is implicitly dependent on other solution parameters. Both time steps have the capacity to vary by a number of orders of magnitude and therefore the ratio between two time steps can be much smaller or much greater than one. Consequently, an efficient technique to handle any disparity in the time steps and couple the two explicit solution schemes is desirable.

With reference to Figure 3.1a, the contact between two discrete elements can be considered as a lumped mass-spring-damper system with a resonant frequency [53], ω_n,

$$\omega_n = \sqrt{\frac{1}{\overline{M}}\frac{dF_n}{d\delta_n}}, \tag{3.23}$$

in which $dF_n/d\delta_n$ is the instantaneous contact stiffness (which is dependent on the interaction law used) and $\overline{M}$ is the equivalent mass of the contacting elements,

$$\overline{M} = \frac{M_1 M_2}{M_1 + M_2}. \tag{3.24}$$

The resonance frequency of contact is taken into account in the evaluation of the critical time step such that,

$$\Delta t_{cr} = \begin{cases} \frac{2}{\omega_n} & \text{no damping} \\ \frac{2}{\omega_n}\left(\sqrt{1-\xi^2} - \xi\right) & \text{damping} \end{cases}, \tag{3.25}$$

where ξ is the critical damping factor [53]. However, it has been shown [142] that (3.25) is not sufficient to guarantee a stable contact solution and a critical time step factor, λ, is subsequently employed,

$$\Delta t_{DEM} = \lambda \Delta t_{cr}, \tag{3.26}$$

with the range $0 < \lambda < 1$ and recommended value [54] $\lambda = 0.1 \sim 0.3$. From (3.26) it can be seen that a stable solution of the DEM can be obtained for any time step value less than the evaluated value, $\Delta t \leqslant \Delta t_{DEM}$, but for computational expediency use of the evaluated value (i.e. largest permissible) is desirable. This is an important consideration in coupling with the LBM time step.

From the definition of the physical viscosity in the lattice Boltzmann method (2.66) it can be seen that the time step, grid size, relaxation parameter and viscosity are inter-related. By rearranging this expression the LBM time step can be written as,

$$\Delta t_{LBM} = \left(\tau - \frac{1}{2}\right) \frac{(\Delta x)^2}{3\nu}. \tag{3.27}$$

In practical applications of the LBM where the physical viscosity is known it is usually most convenient to first select a spatial discretisation Δx that adequately describes the domain boundaries and any coupled particles. A relaxation parameter can then be chosen based on accuracy and stability considerations (see Section 2.5.2) and the LBM time step calculated using (3.27). Therefore, with constraints on the other model parameters there is often little scope for adjustment of the LBM time step in coupling with the DEM.

In coupled simulations where $\Delta t_{LBM} < \Delta t_{DEM}$ the solution time step can simply be forced to equal the LBM time step, $\Delta t_{SOL} = \Delta t_{LBM}$. This conservatively reduces the DEM time step to less than that which is required and the solution can progress in time with enforced parity of increments and a one to one ratio of DEM and LBM updates.

When $\Delta t_{LBM} > \Delta t_{DEM}$ a sub-cycling approach to coupling the time steps [33] can be taken which allows the execution of a number of consecutive DEM time steps within a single LBM time step, as shown in Algorithm 3.1. In this technique, the ratio of the time steps is evaluated $R_{SUB} = \Delta t_{LBM}/\Delta t_{DEM}$ and then integerised $N_{SUB} = \texttt{CEILING}(R_{SUB})$. The new DEM time step is then calculated, $\Delta t_{DEM}^{SUB} = \Delta t_{DEM}/N_{SUB}$, and the resultant relationship between the LBM and new DEM time steps is $\Delta t_{LBM} = N_{SUB} \Delta t_{DEM}^{SUB}$.

It is important to note that during DEM sub-cycling the discrete element particle mapping and hydrodynamic force and torque are not updated. This means that the hydrodynamic force and torque applied to the discrete elements due to fluid interaction are constant over the number of sub-cycles, and that the fluid-solid interface (i.e. mapped discrete element boundary) does not move. The boundary nodes and hydrodynamic load values of the first sub-cycle are used for all sub-cycles. For these reasons, a practical limit on the sub-cycling number is required. This limit is problem dependent, but ideally should ensure that the discrete element boundary is remapped before crossing more than one grid cell and that all physical load fluctuations are captured.

In this work, the evolution of the DEM solution is optimised by dynamically adjusting the time step depending on the state of the solution. For

Algorithm 3.1 Implementation of the DEM-LBM sub-cycling procedure.

```
DO 10 I=1, NUMBER_LBM_STEPS
  ...
  Undertake LBM computations
  Update DEM-LBM sub-cycling number
  ...
  DO 20 J=1, NUMBER_OF_SUB-CYCLES
    ...
    Undertake DEM computations
    Update DEM time step
    ...
  20 CONTINUE
10 CONTINUE
```

example, the DEM time step may increase during periods where no contact pairs exist, or it may decrease when non-linear interaction laws are used and large contact forces exist. This ensures the maximum efficiency of the analysis but complicates the implementation of DEM-LBM sub-cycling. Consequently, the sub-cycling number is also dynamically calculated. The dynamic updating of the DEM time step and the sub-cycling number are shown in Algorithm 3.1. Note that in the approach presented, it is possible for the DEM time step to change within a sub-cycle which would result in the total elapsed time for that sub-cycle to differ from the intended time. Recall that the total sub-cycle time is equal to the LBM time step. However, in the DEM the maximum change in subsequent time steps is constrained for numerical stability and therefore the disparity in elapsed times would be small. Nevertheless, with reference to (2.66), the deviation of the LBM time step from its intended value over one increment can be interpreted as a small change in the simulated viscosity for that increment.

3.4 LBM-DEM Coupling Validation Examples

The extension of the LBM-FEM implementation to a fully coupled LBM-DEM framework was tested qualitatively and quantitatively via a number of simple flow validation problems. The immersed moving boundary method of Noble and Torczynski [97] and later modifications by Holdych [65] were chosen for the hydrodynamic coupling of the LBM and the discrete elements. This method offers a completely local collision operation and a cell coverage ratio that results in improved boundary representation without prohibitively high mesh resolution.

For circular and spherical discrete elements (i.e. closed form boundary expressions) a boundary tracing algorithm was used to map the particles to the LBM grid. The cell coverage ratio, ε_s, was calculated using polygonal approximations (see Section 3.2.4) as opposed to exact solutions or the cell decomposition method. Comparison of the three approaches found that polygonal approximations offered better accuracy than the cell decomposition method (at realistic lattice spacing) while being the least computationally intensive of the three. The mapping of polygonal elements in 2D used a ray-cast approach which determined the intersection point of all boundary facets with the velocity directions of the underlying lattice. With the lattice-boundary intersection locations already known the cell coverage ratios could be evaluated exactly in a straightforward manner.

The performance of the LBM-DEM coupling was validated quantitatively using results including hydrodynamic drag, torque and flow profile. The rate of convergence of the predicted results was also investigated, and qualitative observations were made where appropriate.

3.4.1 2D Flow Past a Circular Cylinder

One of the most common validation tests for the coupling of fluid and structural fields is the flow past a circular cylinder. A search of the literature related to the LBM reveals a great number of publications comparing quantities such as lift and drag coefficient [63, 134, 35, 93], velocity and pressure distribution [97], vortex shedding and Strouhal number [56].

In the present study the drag coefficient on a stationary cylindrical obstacle was investigated at varying Reynolds number. A single circular discrete element with diameter $0.02m$ was placed in the middle of a channel that was $2m$ long and $0.3m$ wide. The bounce-back wall boundary condition was applied at the top and bottom of the channel and periodic boundaries were used at the inlet and outlet. The chosen channel length kept the periodic cylinders a distance of $100D$ apart and therefore minimised any influence on the single-obstacle drag coefficient. The LBM domain was discretised with a lattice spacing of $0.002m$ and a relaxation parameter of 0.55 was employed. The fluid velocity was governed by a variable body force and the density and kinematic viscosity used were $1000kg/m^3$ and 1e-04m^2/s, respectively.

The LBM-DEM analyses were run until steady state for Reynolds numbers ranging from 0.5 to 34 and the drag coefficient on the circular element was calculated as,

$$C_D = \frac{2F_D}{\rho U_{max}^2 D}, \tag{3.28}$$

in which U_{max} is the maximum velocity at the centre of the channel. Figure

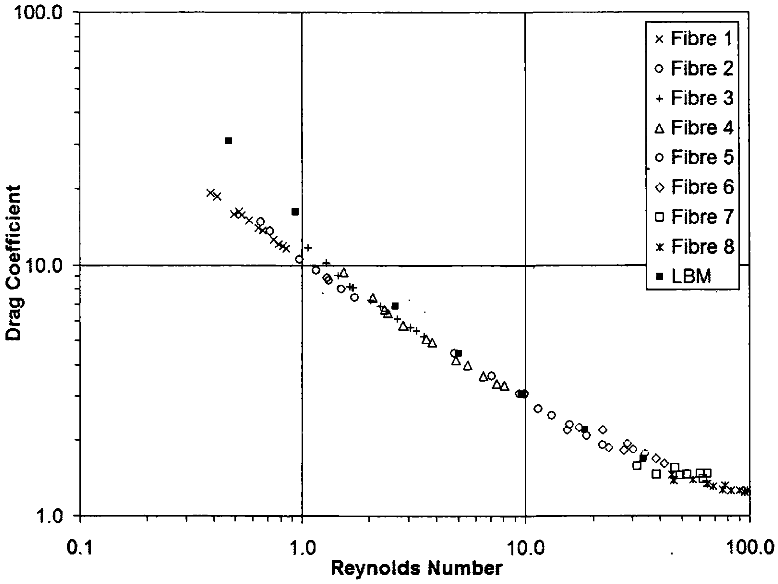

Figure 3.6: Graph of the drag coefficient, C_D, of a circular cylinder in steady, laminar flow at varying Reynolds number. The experimental results of Tritton [132] are included for comparison.

3.6 plots the numerical results against experimental data [132], which was determined by observing the bending of quartz fibres in an air stream. It can be seen that the correlation between the numerical and experimental results for inertial flows is excellent. However, when $Re < 1$ and Stokes flow is approached the numerical and experimental drag coefficient predictions deviate. In this flow range the viscous effects dominate pressure effects in the total drag coefficient, suggesting that the immersed moving boundary technique does not accurately predict the shear stress at the fluid-solid interface for very low Reynolds numbers. Similar issues with the prediction of the drag coefficient using the LBM have been found in the literature [134] in which the difference was attributed to the existence of a hydraulic radius. This hydraulic radius defines a hydrodynamic boundary that is different to the physical boundary due to the actual no-slip interface existing outside of the circular element. This issue is also discussed in Section 3.4.4.

No other publications that employ the LBM to compute the drag coefficient at very low Reynolds number could be found. Therefore, the comparison of the Stokes flow results of the present study with other numerical predictions was not possible. Nevertheless, the drag coefficient predictions in the low to moderate Reynolds number range were excellent, and this range is the focus of later applications in block cave modelling.

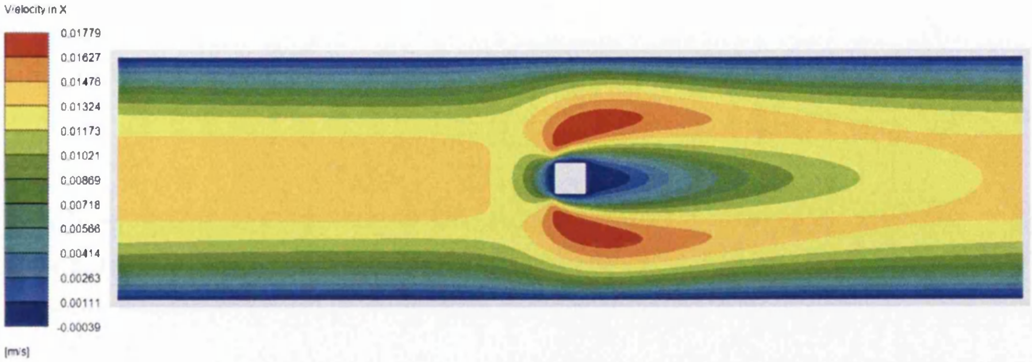

Figure 3.7: Contour plot of the x-direction velocity for the laminar flow past a square cylinder at $Re = 15.5$.

3.4.2 2D Flow Past a Square Cylinder

The use of the immersed moving boundary method to couple the LBM to irregular, polygonal obstacles has not been previously reported in the literature. Consequently, this was investigated in the present study by analysing steady, laminar flow past a square cross-section. A single square discrete element with side length $0.1025m$ was placed in the centre of a channel with length and height of $3.07m$ and $0.82m$, respectively. This resulted in a blockage ratio[3], B, of 1/8. The bounce-back wall boundary condition was applied at the top and bottom of the channel and periodic boundaries were used at the inlet and outlet. The length of the channel, $L = 30D$, was chosen to minimise the interaction of the flow around the periodic column of obstacles. The lattice spacing, fluid density, kinematic viscosity, and relaxation parameter chosen were $0.005m$, $1000kg/m^3$, 1e-04m^2/s, and 0.55, respectively. Figure 3.7 is a contour plot of the x-direction velocity in the channel when a body force of 4e-05m/s^2 was used to drive the flow, resulting in a Reynolds number of approximately 15.5. The characteristic recirculation region can be seen trailing the square obstacle.

Figure 3.8a is a graph of the drag coefficient at low to moderate Reynolds number for the present investigation. This problem was investigated also by Breuer et al. [9] using both finite volume methods (FVM) and the LBM with the bounce-back wall boundary for the fluid-solid coupling. These results are included in Figure 3.8a for comparison. The correlation between the three sets of data is excellent.

The flow profile around the square obstacle was investigated by measuring the trailing recirculation length at varying Reynolds number, as plotted in

---

[3] The blockage ratio relates the obstacle width to the channel width as $B = D/H$.

Figure 3.8b. The same interrogation was undertaken by Breuer et al. [9] and an empirical expression for the recirculation length was proposed,

$$\frac{L_r}{D} = -0.065 + 0.0554Re, \tag{3.29}$$

in which L_r is the recirculation length. This relationship is included in the graph in Figure 3.8b. The pair of symmetric vortices behind the obstacle emerge when the Reynolds number is sufficiently high for separation to occur at the trailing edges of the square cross-section. In the present study, this occurred at a Reynolds number between 3.4 and 4.7 but Breuer et al. found it a lower value of approximately 1.0. The recirculation length then gives a reasonable fit to (3.29) however the relationship in this study was found to be nonlinear. One possible reason for this anomaly is the influence of upstream and downstream obstacles that form part of the periodic domain. Another possibility is that the IMB coupling method is sensitive to one or more of the flow parameters and the true location of the hydrodynamic boundary differs from the physical boundary by an amount dependent on the Reynolds number. This is discussed further in Section 3.4.4. Unfortunately, no experimental data could be found in the literature to further evaluate the three sets of data.

As the Reynolds number is increased the trailing vortices become unstable and an unsteady wake is formed behind the square cylinder. It has been reported [73] that this occurs at a critical Reynolds number of 54, whilst Breuer et al. [9] found $Re_{crit} \approx 60$. In this study the transition from steady to unsteady flow occurred at a Reynolds number between 46.0 and 54.5, which strongly supports the validity of the IMB for coupling the LBM to immersed polygonal obstacles.

3.4.3 2D Cylindrical Couette Flow

Thus far, the validation of the LBM-DEM coupling using the immersed moving boundary method has only considered the hydrodynamic translational force exerted on the discrete elements. To test the prediction of the hydrodynamic torque on an immersed object the common benchmarking problem of cylindrical Couette flow was analysed. In this flow geometry a circular shaft rotates inside a circular cavity creating an annulus of fluid that is subject to a nonlinear shear profile. This problem, for which a schematic diagram can be seen in Figure 3.9a, is popular in the literature as an analytical solution can be derived from the Navier-Stokes equations for the tangential flow profile,

$$u_\theta(r) = \left[\frac{\omega_2 r_2^2 - \omega_1 r_1^2}{r_2^2 - r_1^2}\right] r + \left[\frac{(\omega_1 - \omega_2) r_1^2 r_2^2}{r_2^2 - r_1^2}\right] \frac{1}{r} \tag{3.30}$$

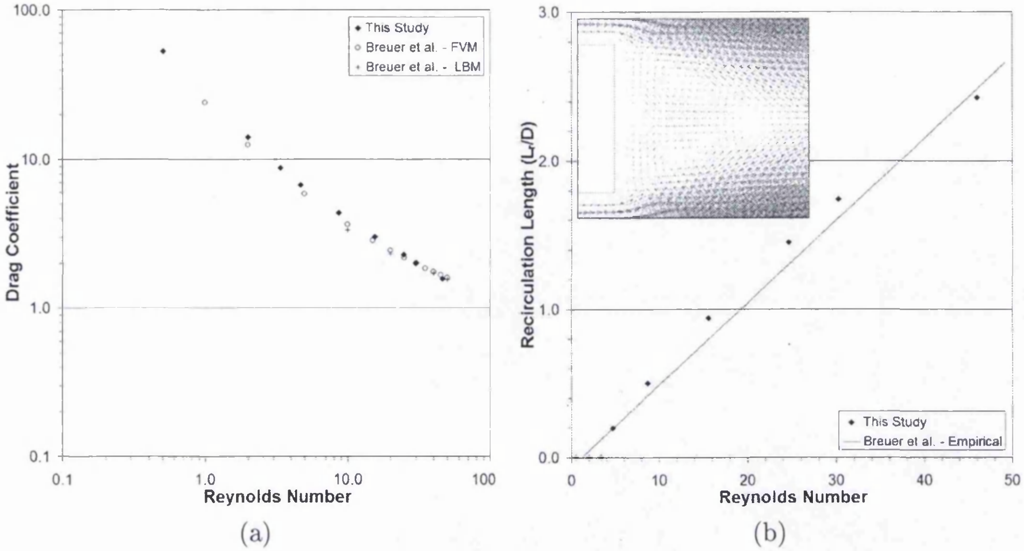

Figure 3.8: Results of the flow past a square cylinder using the IMB coupling method including graphs of (a) the drag coefficient and (b) the trailing recirculation length at low to moderate Reynolds number.

and the driving torque [25],

$$T = -4\pi\rho\nu\left[\frac{(\omega_1 - \omega_2)\, r_1^2 r_2^2}{r_2^2 - r_1^2}\right]. \tag{3.31}$$

In (3.30) and (3.31) the angular velocities and radii of the inner and outer profiles are denoted by ω_1, r_1 and ω_2, r_2, respectively.

The cylindrical Couette flow problem was analysed using an inner radius of $0.1m$ and an outer radius of $0.3m$. The internal cylinder was coupled to the LBM fluid using the IMB method and ramped to an angular velocity of $0.1 rad/s$ while the outer boundary was handled with the bounce-back boundary condition and held stationary. A fluid density of $1000 kg/m^3$ and a kinematic viscosity of 1e-04m^2/s was employed. Figure 3.9b is a contour plot of the total velocity in the annulus while Figure 3.10a graphs the analytical and numerical velocity profile for the analysed geometry and highlights the excellent correlation between the two results. The inset focuses on the region adjacent the inner cylinder and shows that the numerical velocity at the boundary ($0.00987 m/s$) does not quite reach the theoretical value ($0.01\, m/s$). This suggests the no-slip interface between the fluid and the rotating cylinder actually lies inside the physical boundary. This phenomenon has been found by other researchers [134] when coupling the LBM to moving boundaries, and is discussed in more detail in Section 3.4.4.

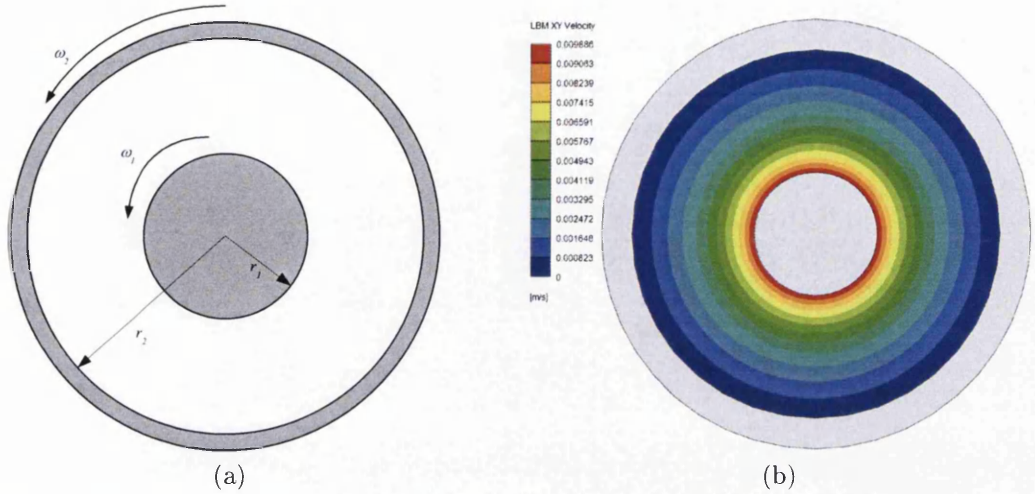

(a) (b)

Figure 3.9: The cylindrical Couette flow problem including (a) a schematic of the flow geometry and (b) a contour plot of the total velocity in the annulus at steady state.

In Chapter 4 the cylindrical Couette flow problem is extended to undertake *numerical rheometry*, which forms an integral component of the characterisation of fines as a non-Newtonian fluid. As a precursor to this work the Newtonian case of cylindrical Couette flow was examined in more detail. Specifically, the convergence of the solution with increasing grid resolution was investigated and the performance of the different IMB collision operators was compared. Figure 3.10b graphs the relative error in the predicted torque based on the analytical result of 1.414e-03$N.m$. Results are presented for two combinations of the IMB formulation, namely the superposition (SP) collision operator (3.16) with $B_n = \varepsilon_n$, and the bounce-back (BB) collision operator (3.14) with the relaxation parameter-dependent weighting function (3.19). It can be seen that the bounce-back collision operator is almost two orders of magnitude more accurate in predicting the torque than the superposition operator. Monotonic convergence can be seen for all cases except for the bounce-back operator ($\tau = 0.6$) at the highest grid resolution. For both bounce-back cases the rate of convergence is approximately 1.7, which compares well the results of Cook et al. [25] that attained nearly second-order convergence (slope 1.9) when using the IMB method at both the inner and outer surfaces. In this study the bounce-back boundary condition is employed on the outer wall, which does not conform to the underlying lattice. Consequently it could be expected to only achieve first order convergence. However, these results show that the use of the bounce-back condition on the outer wall does not dramatically deteriorate the quality of the solution.

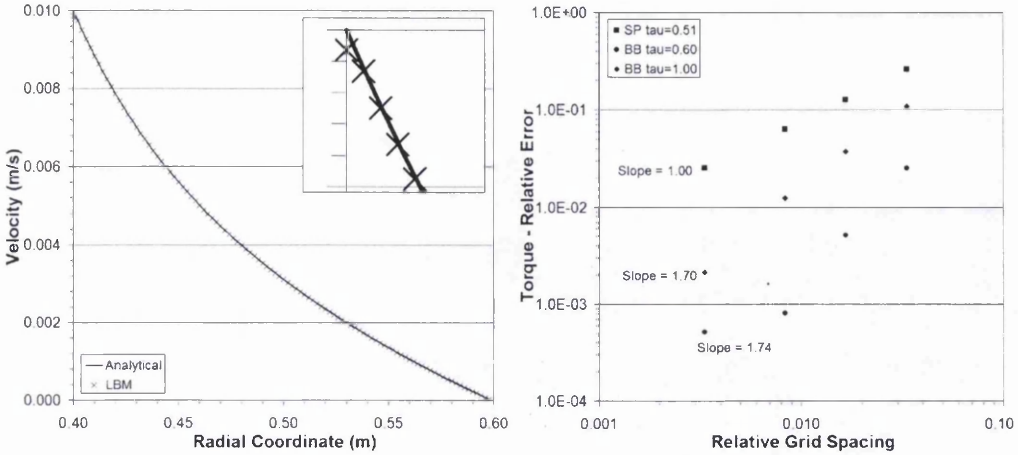

(a) (b)

Figure 3.10: Results of the cylindrical Couette flow analysis including (a) a graph of the numerical and analytical flow profile in the annulus highlighting the region adjacent the inner cylinder and (b) the convergence of the torque prediction with increasing grid resolution.

It could be seen in Figure 3.10a that fluid velocity at the surface of the inner cylinder did not reach the theoretical value. To investigate this further, Figure 3.11a plots the relative error in the maximum velocity for the IMB combinations analysed. It can be seen in this graph that the superposition collision operator is superior to both bounce-back collision operators, which is a reversal of the comparative torque prediction performance. All results display monotonic convergence however the rate, which is approximately first order, is much lower than that for the torque prediction. Nevertheless, the results of Cook et al. [25] also displayed first-order convergence for the maximum velocity and therefore the influence of the bounce-back boundary on the outer cylinder is negligible in this result.

Finally, the accuracy of the velocity profile across the annulus was investigated. Figure 3.11b graphs the L_2 norm error (2.115) for the IMB combinations analysed. The error summation was only undertaken on the nodes that were common to each lattice (i.e. those for the coarsest grid). In this result it can be seen that the superposition collision operator has reverted to being the worst performer of the analysed combinations. It displays only first-order monotonic convergence which is consistent with the torque and maximum velocity results. The results for the bounce-back collision operator compared well with those reported by Cook et al. however they did not display monotonic convergence. This could be attributed to the use of the bounce-back wall boundary at the outer cylinder and the change in the mapped geometry

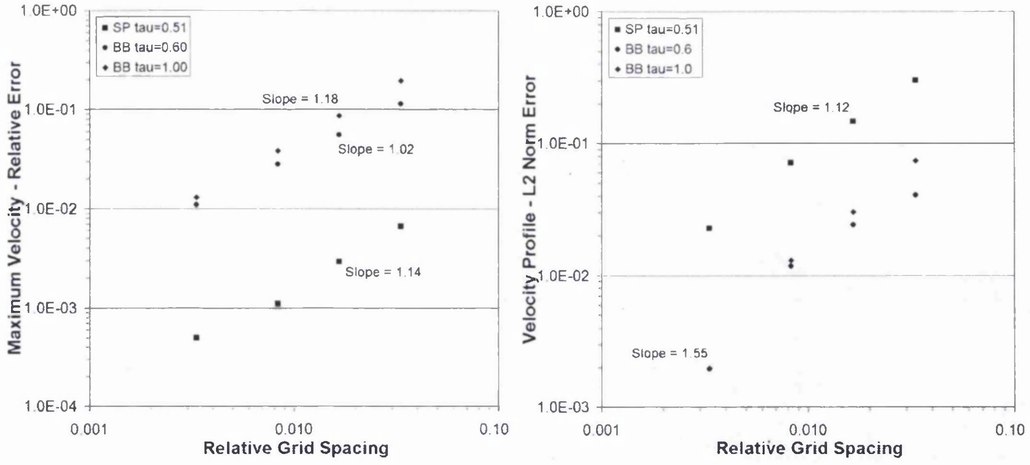

(a) (b)

Figure 3.11: Convergence of the cylindrical Couette flow results with increasing grid resolution including (a) the relative error of the maximum velocity at the surface of the inner cylinder and (b) the L_2 norm error of the velocity profile across the annulus.

as the lattice spacing is changed. Despite this, the approximate slope of 1.55 in log-log space compares well with the slope of 1.9 reported in [25].

3.4.4 3D Flow Past a Periodic Array of Spheres

The three-dimensional LBM-DEM coupling was first tested via the flow past a periodic array of spheres. This problem has been previously investigated by Verberg and Ladd [134] using link bounce-back (LBB) and continuous bounce-back (CBB) schemes (see Section 3.2.2), and Holdych [65] using a modified version of Noble and Torczynski's [97] immersed moving boundary method. An advantage of this test problem is that computational requirements can be minimised by employing periodic boundaries on all faces of the domain that surround the single spherical element.

For a face-centred-cubic (FCC) periodic arrangement of spheres the reduced drag coefficient is evaluated [145] as,

$$\hat{C}_D = \frac{F_D}{6\pi\rho\nu r U_{avg}}, \tag{3.32}$$

in which F_D is the drag force on a single sphere, r is the sphere radius, and U_{avg} is the average x-velocity in the domain. The average velocity is

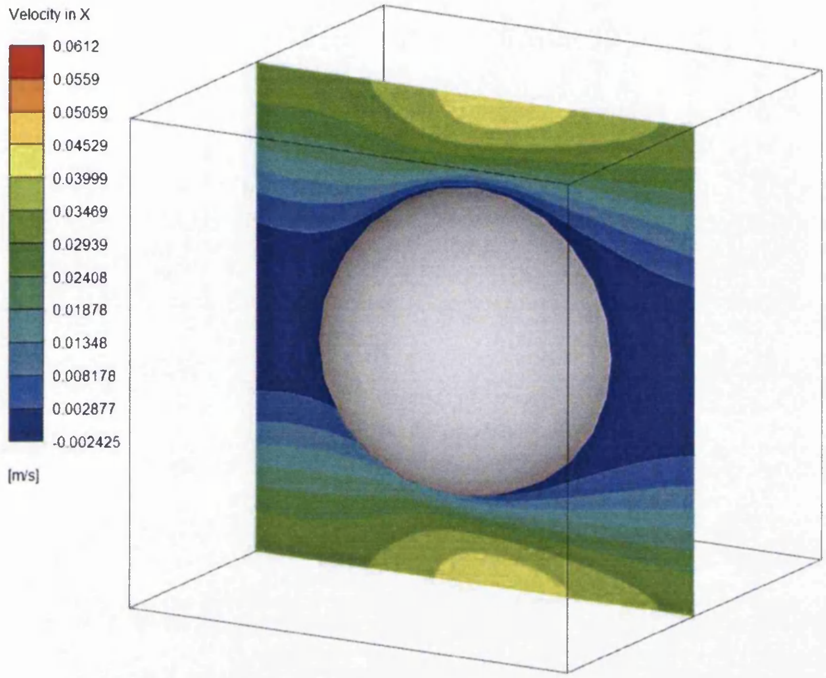

Figure 3.12: Contour plot of the x-direction velocity on the xy-plane at the centre of a sphere in a face-centred-cubic periodic array.

calculated from the uncovered cell portions in the domain,

$$U_{avg} = \frac{1}{n_x n_y n_z} \sum_{\mathbf{x}} (1 - \varepsilon_s)\, u_x, \tag{3.33}$$

where n_x, n_y and n_z are the number of nodes in each direction and ε_s is the solid coverage ratio of each nodal cell.

In this investigation a cubic domain with a side length of $0.2\,m$ was used in conjunction with a sphere radius of $0.062\,m$, giving the ratio $r/L = 0.31$ which allowed direct comparison to the results of Holdych [65] and Zick and Homsy [145]. Flow through the domain was driven by a body force, periodic boundaries were applied on all faces of the domain, and the hydrodynamic drag force, F_D, was evaluated using (3.20) in Section 3.2.4. The modified collision operator proposed by Holdych (3.22) was employed in conjunction with the relaxation-parameter-dependent weighting function (3.19). The fluid density and kinematic viscosity were $1000 kg/m^3$ and 1e-04m^2/s. Figure 3.12 is contour plot of the plot of the fluid velocity in the x-direction, showing the characteristic flow profile on the xy-plane at the centre of the sphere.

The reduced drag coefficient was calculated for varying grid size and Reynolds number and compared to the reference value, $\hat{C}_D = 4.292$, from Zick

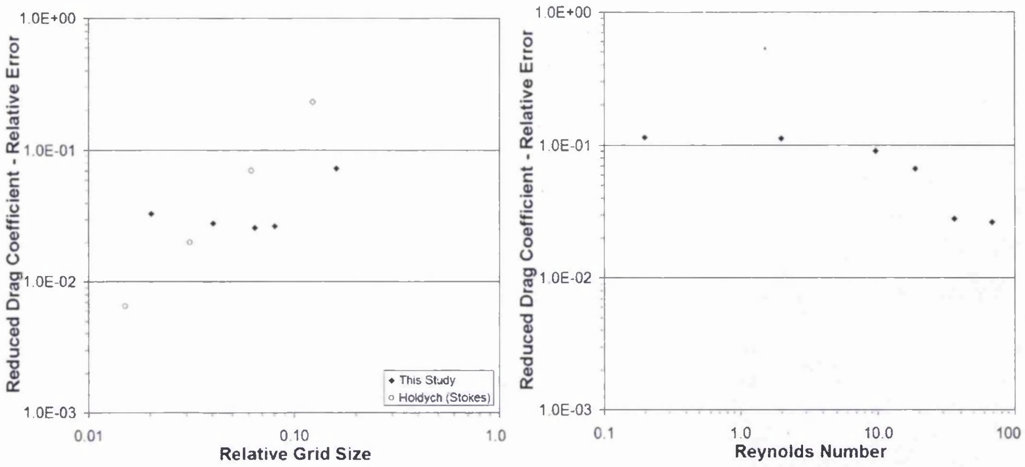

(a) (b)

Figure 3.13: Relative error in the reduced drag coefficient for flow past a sphere in a periodic, face-centred-cubic array for (a) varying grid size and (b) varying Reynolds number.

and Homsy [145]. For the grid size investigation a body force of $0.002 m/s^2$ was used, resulting in an average velocity and Reynolds number of approximately $0.03 m/s$ and 37, respectively. Figure 3.13a graphs the relative error of the reduced drag coefficient at varying grid size. The results of Holdych, which investigated Stokes flow, are included for comparison. It can be seen that the results of the present study do not display monotonic convergence and instead tend toward an error of approximately 3%. The same behaviour was found by Verberg and Ladd [134] using CBB coupling, and was explained by the fact that the physical diameter and the hydraulic diameter due to bounce-back are not equivalent. This diameter difference has been confirmed for the immersed moving boundary technique however the true location of the boundary is not easily prescribed [65].

The results of Holdych displayed super-linear convergence (slope 1.74) but this rate of convergence was found to decrease with further increase of grid resolution. The difference of these results from those of the present study can be attributed to a number of factors. Primarily, Holdych investigated Stokes flow and subsequently removed the quadratic velocity terms from the equilibrium functions to eliminate inertial contributions to the governing equations. Also, Holdych employed the D3Q19 lattice and the cell decomposition method for cell coverage calculation, as opposed to the D3Q15 lattice and polygonal approximation in this work.

Verberg and Ladd also reported a sensitivity of the predicted drag coefficient to the fluid viscosity. This was investigated by varying the simulation Reynolds number whilst maintaining a constant grid size of $0.005\,m$. Figure 3.13b plots the relative error in the reduced drag coefficient for varying Reynolds number. This result shows that the accuracy improves at higher Reynolds number with a sharp transition occurring in the range $10 < Re < 30$.

The results of this test showed reasonable prediction of the reduced drag coefficient for the analysed properties and geometry. In fact, the results are similar to those found in contemporary studies of the same problem [120]. However, the response of the immersed moving boundary method to grid resolution and Reynolds number warrants further investigation.

3.4.5 3D Flow Past a Sphere at Moderate Reynolds Number

The flow past a single sphere at low to moderate Reynolds numbers was simulated in order to further investigate the three-dimensional LBM-DEM coupling . A single sphere of diameter $0.072m$ was placed in the centre of a periodic domain that was $0.96m$ long and $0.24m$ high and wide. A lattice spacing of $0.004m$ was employed resulting in nodal dimensions of 241 long and 61 high and wide. The fluid density, kinematic viscosity and relaxation parameter were $1000kg/m^3$, 1e-04m^2/s and 0.6. This analysis follows that of Strack and Cook [120], which utilised the LBM with the D3Q19 lattice and the immersed moving boundary method. The drag coefficient was calculated as,

$$C_D = \frac{2F_D}{\rho U_{avg}^2 \pi r^2}, \tag{3.34}$$

and the results were compared with experiments [112] and the empirical correlation [138] for low to moderate Reynolds number,

$$C_D \approx \frac{24}{Re} + \frac{6}{1+\sqrt{Re}} + 0.4. \tag{3.35}$$

It has been reported [120] that at spacings greater than 30 radii the interaction of spheres in periodic flows vanishes. To completely eliminate the periodic influence on the drag of the analysed sphere the cubic domain size would require a side length of 1.08m (241 nodes) which would result in a total of 2e07 nodes. However, the serial implementation of the LBM-DEM framework in the present study is limited to approximately 4e06 nodes. This constraint required the reduction of the analysed domain dimensions and therefore the result of this investigation is only an approximation of the non-interacting case.

The drag coefficient on the sphere for Reynolds numbers ranging from approximately 22 to 108 is plotted in Figure 3.14. The results of Strack and

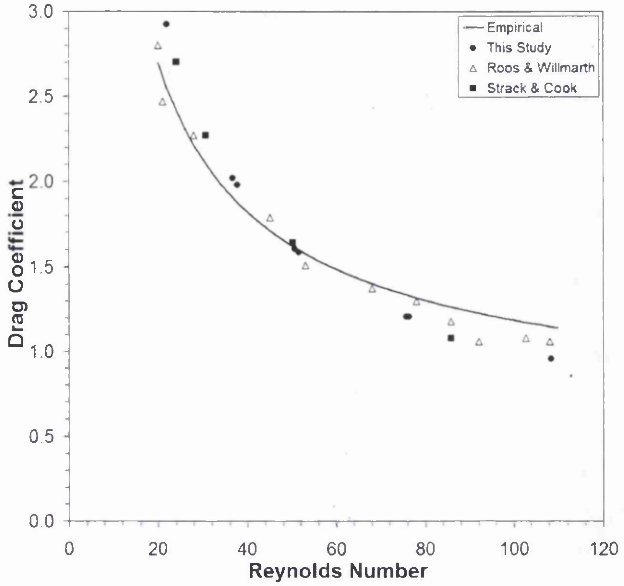

Figure 3.14: Graph of the drag coefficient on a single sphere in an approximation of a non-interacting periodic domain.

Cook [120], which used the D3Q19 lattice, are also plotted and shown to correlate very well with the present results. Both sets of numerical results also compare well with the experimental results of Roos and Willmarth [112]. Even by using an approximation of a non-interacting periodic domain, these results highlight the capability of the LBM-DEM framework to accurately predict the hydrodynamic interaction of suspended objects.

CHAPTER 4

NON-NEWTONIAN FLOWS AND CONSTITUTIVE MODELLING IN THE LATTICE BOLTZMANN METHOD

The accurate prediction of the flow behaviour of non-Newtonian fluids is of considerable interest to scientists and engineers across a number of disciplines. As an example, the lattice Boltzmann method has been applied in the oilfield industry to simulate the flow of non-Newtonian fluids through porous media [122, 123]. This work exploits the LBM's strength in representing complex structural networks in a simple and efficient manner. Additionally, many of the fluids used in oil recovery exhibit strong, non-Newtonian characteristics [102]. Many other materials such as pastes, polymers and granular suspensions can exhibit non-Newtonian characteristics such as pseudoplasticity (shear-thinning), dilatancy (shear-thickening), yield, viscoplasticity and density fluctuations [39]. In the present work the deviation from Newtonian behaviour within the LBM must be extended to capture the constitutive behaviour of a granular medium or dry bulk material.

The majority of the literature dedicated to the LBM focuses on the analysis of Newtonian fluids in which the constitutive relationship between the velocity field and the stress tensor is defined by the fluid viscosity,

$$\tau_{\alpha\beta} = 2\mu e_{\alpha\beta}, \tag{4.1}$$

where $\tau_{\alpha\beta}$ is the deviatoric component of the fluid stress tensor, μ is the dynamic viscosity of the fluid and $e_{\alpha\beta}$ is the rate of strain tensor. However, to attempt to simulate the behaviour of a bulk material with a fluid continuum approach requires a deviation from Newtonian behaviour to that in which the viscosity may be strain rate dependent or subject to discontinuities such as that which occur at yield. This is necessary to adequately simulate the movement of fines in block cave environments using the LBM-DEM framework.

The characterisation of the flow of granular materials is an area of ongoing research, with science as yet unable to provide an accepted, unified model for all regimes from quasi-static to rapid dynamic [14]. This chapter provides a brief discussion of the different approaches to this problem including kinetic models, discontinuum modelling, and continuum representations. The focus of this work is on the latter, as although the lattice Boltzmann method is built on an averaged type of (mesoscopic) kinetic model, at the macroscopic scale it has been shown to yield the continuous Navier-Stokes equations. A number of non-Newtonian continuum models are discussed including the viscoelastic power law, viscoplastic Bingham model, and other critical state and flow rule combinations. The implementation of power law and Bingham type fluids in the single-relaxation-time LBGK is investigated, including computational issues such as techniques for evaluating the rate of strain tensor in the LBM. The chapter culminates in the application of the non-Newtonian LBM-DEM framework in the replication of viscometry experiments for a dry bulk material, thereby validating the suitability of this approach in modelling block cave fines.

4.1 The Approaches to Modelling Granular Media

One of the significant issues relevant to the mathematical description of granular material is the wide range of dynamism that is encountered in physical processes, from static in storage to highly dynamic in suspension transport (and higher still). Massoudi and Phuoc [88] presented a classification scheme for the level of dynamism in granular materials, as summarised below.

- Regime A - Stationary materials in storage.
- Regime B - Quasi-static or slow, friction dominated movement.
- Regime C - The rapid flow regime in which particles are moving quickly and experiencing a large number of inter-particle contacts.
- Regime D - Suspension induced movement such as pneumatic or hydraulic conveying.

- Regime E - Chemically reactive flow regime where the particulate might be burnt or change phase due to other reactions.
- Regime F/G - Dispersed particles such as pollutants or other small-scale waste material.

During slow flows (Regimes A and B), sometimes called Coulomb flow, the dominant interaction between the particles is the surface friction as grains slide over one another during extended contact time frames. However, in rapid granular flows (Regimes C and D) the particle-particle contact time is considered to be much shorter and as such the influence of contact friction is neglected, with energy dissipation being attributed to surface inelasticity. Although the tenets of mass and momentum equation apply to both regimes, the constitutive descriptions are quite different.

Despite decades of research there is still a lack of understanding of the flow of granular materials due to the absence of an accepted constitutive description that governs flow in various regimes and geometries [88]. The predominant approaches to modelling granular materials are statistical theories, continuum approaches, and discrete element methods. In statistical theories [61, 60], one can take a particle dynamics approach or use a modified form of the kinetic theory of gases. However, Massoudi and Phuoc [88] claimed that the kinetic theory approach is plagued with many assumptions, and it is best used only in the rapid flow regime, which is not the relevant regime in the present research. Tan et al. [127] attempted to model granular materials using a lattice Boltzmann equation that had been modified to include the granular temperature [50]. Simulations of an unforced granular gas in a square periodic domain whose temperature and density are initially homogeneous and Couette flow on a square domain were undertaken with limited success.

In the continuum approach, it is assumed that the properties of the granular ensemble can be described by spatially continuous functions, and as a consequence can be divided infinitely without changing the material's properties. With respect to continuum approaches, a number of constitutive representations have been presented in the literature, including viscous, viscoelastic (i.e. power law), viscoplastic (i.e. Bingham plastic) and combinations thereof such as visco-elasto-plastic (i.e Herschel-Bulkley fluids). As the most logical approach for application in the LBM, some of these models are discussed in Section 4.1.1 and Section 4.2.

DEM is a powerful tool for simulating the dynamics of granular materials, but for the reasons of scale discussed in Section 1.3 it is not a viable option for the representation of fines in this research.

4.1.1 Continuum Models

The general principle of continuum modelling of slow flow regimes is to add a flow rule and an equation of continuity to the equilibrium equations and the yield condition of the static regime. One of the most common representations of slow soil flows is the Mohr-Coulomb critical state model, however no published material has been found on the implementation of this type of material in the lattice Boltzmann method. As an example, Karlsson et al. [72] undertook finite element simulations of bulk material flow in hoppers using an Eulerian framework, a modified fluid model and a Mohr-Coulomb yield criterion.

The yield surface used in this work was described as,

$$f = mp + g(\theta)\, q - K = 0, \tag{4.2}$$

in which p, q and θ are stress invariants,

$$p = \frac{\sigma_{\alpha\alpha}}{3}, \tag{4.3}$$

$$q = \sqrt{\frac{3}{2}\tau_{\alpha\beta}\tau_{\alpha\beta}}, \tag{4.4}$$

$$\theta = \frac{1}{3} a\cos\frac{27J_3}{2q^3}. \tag{4.5}$$

Note that $\tau_{\alpha\beta} = \sigma_{\alpha\beta} - p\delta_{\alpha\beta}$ is the tensor of deviatoric stresses and J_3 is the determinant of $\tau_{\alpha\beta}$. The function $g(\theta)$ describes the shape of the yield surface in the deviatoric plane as,

$$g(\theta) = \frac{6\cos\phi}{3-\sin\phi}\left[\frac{\sin\left(\theta+\frac{\pi}{3}\right)}{\sqrt{3}\cos\phi} - \frac{\tan\phi}{3}\cos\left(\theta+\frac{\pi}{3}\right)\right]. \tag{4.6}$$

Finally, the constants m and K are defined as,

$$m = \frac{6\sin\phi}{3-\sin\phi}, \tag{4.7}$$

$$K = \frac{m}{\tan\phi}c, \tag{4.8}$$

in which c is the material cohesion and ϕ is the internal friction angle of the material.

The yield surface only determines whether the material is subject to plastic deformation or not and consequently a plastic flow rule is also required. In this work a non-associated flow rule is used which ignores dilation (volume change during deformation) and subsequently maintains constant density of the material. The elastic behaviour of the material (i.e. when it is not deforming) is governed by a regularised model which uses an artificially high fluid viscosity to approximate the behaviour of a solid. This model was successfully applied to the simulation of flow in hoppers, capturing the transient stress behaviour at the onset of discharge and steady states of mass or funnel flow. It can be seen that in its full form the Mohr-Coulomb model is significantly complex to implement. Therefore, before attempting to implement it within the LBM, a less-detailed yield stress material model was sought.

Tardos [128] presented general equations of motion for incompressible and compressible bulk powder flows in the slow regime using a non-Newtonian fluid mechanistic approach. In this work the Coulomb powder approach is employed, where the flow regime is governed by conservation (mass, momentum) equations as in the case of fluid flow and constitutive equations are employed to describe the relationship between the stress and velocity fields (i.e. rate of deformation).

For an incompressible Coulomb powder the constitutive relationship of Schaeffer [114] defined the stress tensor $T_{\alpha\beta}$ as,

$$T_{\alpha\beta} = p\left(\delta_{\alpha\beta} - \sqrt{2}\sin\phi\frac{e_{\alpha\beta}}{\dot{e}}\right), \tag{4.9}$$

in which $e_{\alpha\beta} = \frac{1}{2}\left(\frac{\partial u_\alpha}{\partial x_\beta} + \frac{\partial u_\beta}{\partial x_\alpha}\right)$ is the rate of strain tensor and $\dot{e} = \sqrt{e_{\alpha\beta}e_{\alpha\beta}}$ is the characteristic rate of strain. Using the continuity and momentum equations for an incompressible fluid, and this constitutive relationship (4.9), Tardos [128] was able to define explicit equations of motion and stress in Cartesian, cylindrical, and spherical frames of reference. It is important to note that for this model to remain valid the domain must be in continuous flow (i.e. $\dot{e} \neq 0$) due to the presence of the characteristic rate of strain in the denominator. Also, the presence of the rate of strain tensor in the numerator and the denominator indicates that the velocity field is not uniquely defined for a given stress distribution. This constitutive equation satisfies the von Mises yield criterion and a co-axiality flow rule which states that the principal directions of the stress and the rate of deformation are parallel.

For the Coulomb powder constitutive model in (4.9) an equivalent viscosity analogous to that in the Newtonian description of fluids can be defined when the deviatoric stress tensor of the model is compared to that for a Newtonian fluid (4.1). This equivalent viscosity would be a complex function dependent on the angle of internal friction, the average principal stress and the rate of deformation. Recalling that the dimensionless LBGK viscosity is dependent on only the single relaxation time (2.66), it can be reasoned that to attempt to replicate the constitutive relationship in (4.9) with one model parameter might be optimistic. This point is discussed further in Section (4.2.2). Also, it can be seen in (4.9) that as the angle of internal friction decreases the viscous shear effects of the Coulomb powder model diminish to the limit of an inviscid fluid when $\phi = 0$ and $\sin\phi = 0$. Therefore, for friction angles less than 20° the behaviour of the Coulomb powder becomes increasingly fluid like, however this is acceptable as real powders generally exhibit friction angles greater than this [128].

The incompressible Coulomb model was compared via the calculated flow factor[1] (ff) to an analytical solution for plane flow in a wedge shaped hopper. Correlation of the results for varying hopper half angles was quite good which indicates that the postulated constitutive model adequately replicated the stress distribution. However, the comparison of the predicted and analytical solutions for flow rate differed significantly (by a factor of four for one case). This is attributed to the assumption of no wall effects in the analytical solution (wall friction angle, $\phi_w = 0$) and the incorrect imposition of the slip boundary condition at the hopper outlet.

A number of non-Newtonian compressible constitutive models were also presented and briefly discussed in this work, however it is stated that some of the assumptions in these models are controversial and not universally accepted. Regardless, this is outside the scope of the present research which employs the lattice Boltzmann method in the near incompressible limit.

Tardos et al. [129] described the rheological behaviour of powders in the intermediate regime which lies between the more commonly treated slow and rapid flow regimes. This was done by modifying the slow flow constitutive model in (4.9) for a simplified two-dimensional, Couette flow geometry. The details of the material model, which are not included here but can be found in [129], are based on the assumption that the stress field in the intermediate regime fluctuates around a mean value.

A rotational Couette device [126] was used as a benchmark for the intermediate regime model. In this experiment the material is sheared between two tall concentric cylinders and the gap between the cylinders is kept small to allow the assumption of a linear velocity profile. The applied shear rate is controlled by the angular velocity of the internal cylinder. An analytical solution of the averaged equations for the specific geometry of the Couette device is presented in Section 4.3.3. The velocity profile in the powder and the shear stress in the sheared layer was calculated and the results were compared to experimental data. It was found that the shear stress was dependent

---

[1] The flow factor is the ratio of stable arch stress to consolidating stress for a particular hopper geometry.

on shear rate (i.e. viscous) with a power law relationship and that the velocity profile decayed exponentially away from the moving wall so that flow is actually restricted to a narrow band adjacent to the wall. These results indicate a type of viscoelastic power law relationship for the material, which is discussed further in Section 4.3.3. In the experiments, it was found that shear rate dependence was only observed when the bed was confined. In the unconfined bed the powder was free to dilate and thus the torque and normal shear rate were virtually independent of shear rate. Therefore the effect of gravity cannot be ignored in the annulus.

Recently, Massoudi and Phuoc [88] proposed a non-Newtonian fluid model to study the conduction in shearing flow of granular materials between two parallel plates. In addition to the details of their complex model, the paper offers a summary of other constitutive relationships discussed in the literature. Only a small selection of continuous models for bulk materials have been presented here. A notable omission from this list is the Bingham plastic model [98], however this is discussed in the context of the lattice Boltzmann method in Section 4.2.2.

4.2 Non-Newtonian Fluid Models in the LBM

Despite the considerable amount of literature dedicated to the lattice Boltzmann method in the preceding two decades only a relatively small amount of research has investigated the incorporation of non-Newtonian fluid models. In an early work by Flekkøy and Herrmann [39], shear thinning and density waves were investigated in the simple case of gravity driven flow of a granular suspension in a vertical pipe. In the shear thinning investigation the local LB viscosity was defined as a function of the local strain rate, $\dot{e}$, and a threshold strain rate, $\dot{e}_0$, such that $\nu = \nu_1$ for $\dot{e} \leq \dot{e}_0$, and $\nu = \nu_2$ for $\dot{e} > \dot{e}_0$, with $\nu_1 > \nu_2$. Using this description of the viscosity the analysis produced a cross-sectional flow profile that was largely flat with narrow regions of steep velocity gradient (i.e. shear) adjacent to each wall, corresponding to the thinned phase. For the density wave investigation a piecewise linear representation of the viscosity was employed. It took the form $\nu = \nu_{min}$ for $\rho \leq \rho_t$ and $\nu = \nu_0 + a\,(\rho - \overline{\rho})$ for $\rho > \rho_t$, in which $\overline{\rho}$ is the average density, a is a constant and is chosen to make ν a positive continuous function of the density. In order to generate density waves a small perturbation was introduced as a 0.3% relative density difference in a small line across the pipe. It was found that the initially very weak perturbation quickly built up into a density wave of over 10% density difference.

4.2.1 Viscoelastic Power Law Fluids

The implementation of power law fluids within the lattice Boltzmann equation has been undertaken [1, 110, 6, 42, 122, 8, 123, 140, 21] to investigate both shear-thinning (pseudoplasticity) and shear-thickening (dilatant) behaviour. In a power law fluid the viscosity is defined as a continuous function of the characteristic rate of strain $\dot{e}$ (commonly referred to as the strain rate),

$$\nu = \nu_0 \dot{e}^{n-1}, \tag{4.10}$$

where ν_0 is a consistency constant ($m^2 s^{n-2}$) and n is the power law index. Clearly, an index of $n = 1$ results in a Newtonian fluid with viscosity ν_0. For a fluid with $n < 1$ the effective viscosity decreases with the strain rate and the resultant behaviour is shear-thinning. Conversely, for a fluid with $n > 1$ the effective viscosity increases with the strain rate and the resultant behaviour is shear-thickening.

The characteristic rate of strain is calculated as,

$$\dot{e} = \sqrt{e_{\alpha\beta} e_{\alpha\beta}}, \tag{4.11}$$

from the symmetric rate of strain (i.e. rate of shearing) tensor,

$$e_{\alpha\beta} = \frac{1}{2}\left(\frac{\partial u_\alpha}{\partial x_\beta} + \frac{\partial u_\beta}{\partial x_\alpha}\right). \tag{4.12}$$

It is a convenient feature of the lattice Boltzmann method that the rate of strain tensor can be obtained from the momentum flux tensor [141], $\Pi_{\alpha\beta}$, the components of which are second order moments of the non-equilibrium distribution functions at each node,

$$\Pi_{\alpha\beta} = \sum_i c_{i\alpha} c_{i\beta} \left(f_i - f_i^{eq}\right). \tag{4.13}$$

This is discussed in greater detail in Section 2.5 and Appendix C. This results in a local and explicit definition of the rate of strain tensor,

$$e_{\alpha\beta} = \frac{-3}{2\rho_0 c^2 \tau \Delta t} \sum_i c_{i\alpha} c_{i\beta} \left(f_i - f_i^{eq}\right), \tag{4.14}$$

that removes the need for finite difference calculations of the velocity gradients and the evaluation of neighbouring-node velocity components which that entails.

Recalling the relationship between the fluid viscosity and the relaxation parameter, τ, (2.66) employed in the single relaxation time LBGK model, the shear-dependent viscosity change is enforced by modifying the relaxation parameter [110, 6] to,

$$\tau = \frac{1}{2} + \left(\tau_0 - \frac{1}{2}\right) \dot{e}^{n-1}, \tag{4.15}$$

in which τ_0 is the Newtonian relaxation parameter corresponding to the viscosity consistency constant, ν_0. Therefore, equations (4.15), (4.14), (4.11) and (4.10) define the local, non-Newtonian fluid viscosity at each lattice node using only the local strain rate (which is evaluated using only the particle distribution functions) at the same location.

Aharonov and Rothman [1] implemented the power law model outlined above on a D2Q6 lattice using a collision matrix instead of the BGK collision operator. The rate of strain tensor was calculated from the hydrodynamic velocity field using finite difference approximations and the model was used to simulate the flow of shear-thinning ($n = 0.56$) and shear-thickening ($n = 3.0$) fluids through a simple porous structure. The calculated flux was compared to an analytical solution and the relationship to the driving pressure gradient was found to match within 1% for the shear-thickening case.

Rakotomalala et al. [110] used a D2Q9 lattice in conjunction with the power law model and determined the flow profile between two infinite parallel plates for indices from 0.33 to 5.0. The results were compared to the analytical solution for this problem and found to correlate well for the range of power investigated.

Boek et al. [6] repeated the porous media simulations undertaken by Aharonov and Rothman using a LBGK model and a modified relaxation parameter as shown in (4.15). Channel flow velocity profiles were reproduced to within 2% of the analytical solution and the flux-pressure gradient relationship of a generalised Darcy law was reproduced to within 3%.

From interrogation of (4.10) it can be inferred that in regions of vanishing strain the shear-thinning viscosity approaches infinity while the shear-thickening viscosity approaches zero. According to (4.15) this corresponds to the relaxation parameter approaching infinity or 0.5 for the shear-thinning and shear-thickening cases, respectively. Conversely, at regions of high strain the shear-thinning viscosity becomes very small and the relaxation parameter approaches 0.5, while in the shear-thickening case the viscosity and relaxation parameter approach infinity. Recall from the LBM stability discussion in Section 2.5.2 that stability decreases as $\tau \rightarrow 0.5$ whilst accuracy decreases for $\tau > 1.0$. Therefore, the accurate and robust simulation of power law fluids using the *continuous* relation in (4.10) and the LBGK model can become problematic at the extremes of low and high strain. Gabbanelli et al. [42] overcame this problem by introducing a *truncated* power law model which imposes lower and upper limits on the variable viscosity based on limits on the lower bound ($\dot{e}_0$) and upper bound ($\dot{e}_\infty$) of the characteristic rate of strain. The truncated power law model then modifies (4.10) as,

$$\nu = \begin{cases} \nu_0 \dot{e}_0^{n-1}, & \dot{e} < \dot{e}_0 \\ \nu_0 \dot{e}^{n-1}, & \dot{e}_0 < \dot{e} < \dot{e}_\infty \\ \nu_0 \dot{e}_\infty^{n-1}, & \dot{e} > \dot{e}_\infty \end{cases} , \tag{4.16}$$

so that the viscosity is constant in the lower and upper ranges but dependent on the rate of strain in the middle range. An analytical solution for flow in a plane channel was presented for the truncated power law model, including the locations of the transition between ranges. The correlation between the numerical results using a D3Q19 lattice and analytical results was good, and the convergence of the of the velocity profile was found to be first order. The rate of convergence was reasoned to be due to the first order finite difference scheme employed to calculate the components of the rate of strain tensor, however the wall boundary implementation used (and any associated errors) was not discussed and may have affected the rate of convergence.

Boyd et al. [8] investigated the rate convergence of the continuous power law model for the typical problem of flow in a parallel channel, and the results compared to those of Gabbanelli et al. [42]. To eliminate wall boundary effects a second order, sub-grid accurate scheme was employed and errors due to finite difference calculation of the rate of strain tensor were removed by calculating the components directly from the momentum flux tensor (4.14). The results were found to be second order convergent and subsequently highlight another benefit of calculating the rate of strain components directly from the local particle distribution functions.

Sullivan et al. [122] investigated power law fluids in the LBM within the context of non-Newtonian flow through porous media which is commonly encountered in oil recovery processes when surfactants and particle suspensions are driven through rock formations. A truncated power law model (4.16) was employed and an under-relaxation parameter, λ, was introduced to limit the change of the BGK relaxation parameter in subsequent time steps. Using the local relaxation parameter at the previous time step, τ_{t-1}, and the modified relaxation parameter for the current time step, τ_t, from (4.15) the under-relaxed relaxation time was calculated as,

$$\tau_t^* = \tau_{t-1} + \lambda \left(\tau_t - \tau_{t-1} \right) . \tag{4.17}$$

With $\lambda < 1$ excessive change in the relaxation parameter over short times is limited and the stability of the solution is subsequently increased. A sensitivity analysis of the under-relaxation parameter found that the steady state solution remained unchanged for $\lambda = 0.1 \sim 1.0$, and that a value of 0.1 was generally suitable. This power law model was tested in 2D flows through a lattice-conforming structural network and in 3D flows through a cylinder filled with spherical particles. The 2D results showed the logarithmic relationship between flux and driving gradient to be within 1% of the input power when $n = 0.5$ and $n = 0.7$. As in previous results [42] the error was found to increase with decreasing n (i.e. as the material becomes more shear thinning). This is attributed to the inability of a discrete field to accurately describe the velocity in the region of high shear adjacent the walls. The 3D results showed a significant dependence on the grid resolution. With the number of nodes across a sphere diameter at 13 the error in the logarithmic flux-force relationship was 22% for $n = 0.5$. This reduced to 0.6% for $n = 0.7$, 1.9% for $n = 0.6$ and 4.1% for $n = 0.5$ when the resolution was increased to 26 nodes across a sphere diameter. Interestingly, despite the error in the low resolution case the logarithmic relationship was still found to be linear, which can be interpreted as the simulation of a less shear-thinning fluid that that specified.

Sullivan et al. [123] continued this work by comparing the results of the lattice Boltzmann power law model with experimental results. The experimental geometry was created by filling a $46mm$ diameter cylinder with $5mm$ diameter glass beads and the numerical structural field was reconstructed from a magnetic resonance image (MRI) of the apparatus. The experimental (from MRI data) and numerical velocity fields were compared qualitatively and quantitatively and excellent agreement was found between the two. The average difference in velocity in a node-by-node comparison was found to be approximately 4% when the mesh resolution resulted in the particle diameter equalling 27 nodes.

Recently, Yoshino et al. [140] simulated power law fluids using what was termed a *lattice kinetic scheme* of the LBM. In this approach the relaxation parameter is set to unity and the fluid viscosity is controlled by including the deviatoric stress tensor in the equilibrium functions. This method was found to be more accurate than those preceding in which the non-Newtonian behaviour is included by varying the relaxation parameter. However, this benefit is offset somewhat by additional implementation complexity and the inability to calculate the rate of strain tensor components directly from the particle distribution functions. Chen et al. [21] studied porous media flow of power law fluids using a *gray* lattice Boltzmann model. In this method the structural field is not directly simulated, instead its influence is included by adding a probabilistic component of bounce-back to each lattice node. This is done to allow the simulation of larger porous structures, however it is not particularly relevant to this work as the structural field is directly simulated using the discrete element method.

4.2.2 Bingham Plastics

A popular approach in the mathematical modelling of bulk materials is to employ a viscoplastic non-Newtonian fluid [88]. In viscoplasticity, a yield stress (which in bulk materials is often related to the repose angle, friction angle and cohesion) is defined below which the material does not deform. Above the yield stress the material flows in a manner similar to viscous materials at a rate proportional to the magnitude of the post-yield stress. This is in contrast to the viscoelastic power law models discussed in Section 4.2.1 in which the material stress and strain are related by a continuous function.

The Bingham plastic [98] model is one of a class of non-Newtonian materials known as yield stress fluids, which also includes the Caisson and Herschel-Bulkley models. These materials behave as a solid below a characteristic yield stress and then deform plastically (i.e. flow) once the stress state exceeds the yield stress. In the Bingham model the plastic deformation is governed by a linear viscosity whereas in the Herschel-Bulkley fluid the viscosity can be defined as shear-thinning or shear-thickening. The most common examples of Bingham plastics are dense particulate suspensions and slurries but others include paint, silica, margarine and ketchup. Examples of Herschel-Bulkley fluids include drilling fluids and plastic propellant doughs.

As an example of bulk material classification as a Bingham plastic, Or and Ghezzehei [99] presented experimental data for the strain-stress behaviour of Millville silt loam (29% sand, 55% silt, 16% clay) in a parallel plate, rotating rheometer. A good fit to the Bingham model was found at different water contents ($0.28 kg/kg$ and $0.34 kg/kg$), however the transition from static to viscous behaviour was continuous rather than singular as in the ideal model. The experimental results also found that the yield stress decreased with increasing moisture content.

The constitutive equations for the Bingham plastic model are listed in Taylor and Wilson [130] as,

$$\tau_{\alpha\beta} = 2\left(\nu + \frac{\tau_y}{\dot{e}}\right) e_{\alpha\beta}, \quad |\tau_{\alpha\beta}| > \tau_y, \tag{4.18}$$

$$e_{\alpha\beta} = 0, \quad |\tau_{\alpha\beta}| \leq \tau_y, \tag{4.19}$$

in which τ_y is the yield stress and ν is the plastic viscosity. It can be seen in (4.19) that the rate of strain (i.e. the deformation) is zero when the stress is below the yield stress, which indicates that in this regime the material behaves as a solid. In (4.18) in can be seen that in the plastic regime the

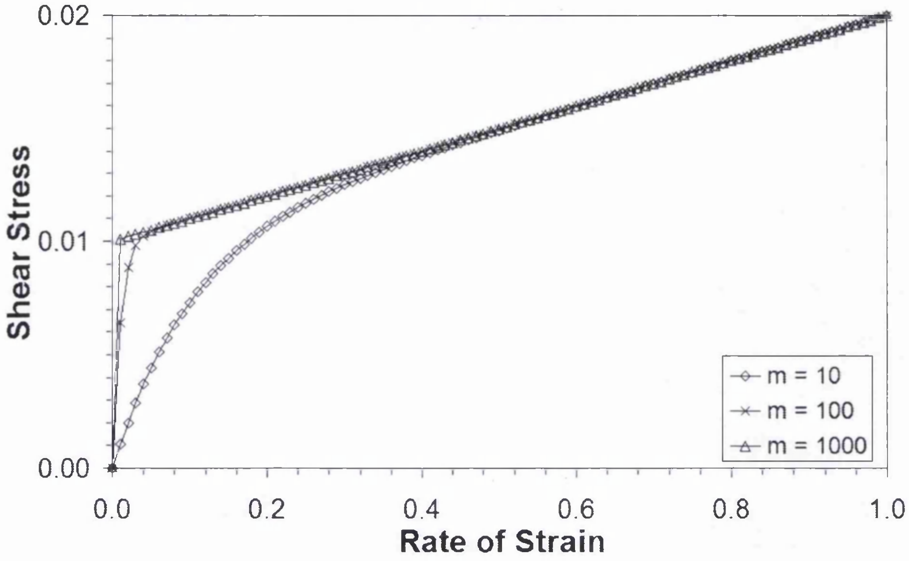

Figure 4.1: The regularised Bingham plastic model of Papanastasiou [101] for different values of regularisation parameter, m, and an arbitrary value of 0.01 for the yield stress and viscosity.

material stress increases linearly with the rate of strain. It is worth noting that the Bingham model in (4.18) is not dissimilar in form from the Coulomb powder of Schaeffer [114] in (4.9). The main differences between the two are that the yield strength of the Bingham model is constant whereas it is pressure dependent in the Coulomb powder, and the Bingham model contains a shear viscosity where the Coulomb powder does not [128].

The discontinuity in the Bingham plastic constitutive relationship means it can be difficult to solve in numerical schemes. To combat this problem, Papanastasiou [101] proposed a *regularised* version of the Bingham model,

$$\tau_{\alpha\beta} = 2\left\{\nu + \frac{\tau_y\left[1 - \exp\left(-m\dot{e}\right)\right]}{\dot{e}}\right\} e_{\alpha\beta}, \tag{4.20}$$

which allows a continuous approximation of the discontinuous model. The regularisation parameter, m, is introduced to control the exponential growth of stress. As it is increased the approximation of the regularised model converges to the ideal Bingham model, as shown in Figure 4.1. In practice the regularised model treats regions of unyielded material as a fluid with artificially high viscosity and in this fashion approximates the behaviour of a solid. Once yield has been reached the fluid viscosity is reduced to the constant plastic zone value and Newtonian flow is permitted.

Within the context of the lattice Boltzmann method only a handful of articles have been published on the implementation of Bingham plastics. Ginzburg and Steiner [?] used a Bingham plastic model in the LBM to simulate the injection of liquid metal in casting. To overcome the numerical instability of the ideal model the regularised model of Papanastasiou was employed, and the momentum flux tensor was used to calculate the rate of strain tensor directly. The relaxation parameter, τ, was then adjusted in a similar fashion to the power law model. Results were presented for 2D and 3D injection analyses, however it was found that the Bingham fluid was susceptible to numerical instability at the threshold change of viscosity, even with the regularisation model.

Vikhansky [136] addressed this instability by presenting an implicit scheme for solving the ideal (i.e. without regularisation) Bingham fluid in the LBM. In this work the collision process is solved iteratively so that the stress and the rate of strain satisfy the constitutive equation of the material at the same time. Results were presented for 2D channel flow and flow around a circular obstacle, however the implicit nature of this method does not fit within the explicit nature of the LBM-DEM framework in the present work and as such it is not a feasible option.

The recent work by Wang and Ho [137] implemented a regularised Bingham plastic model in the single-relaxation-time LBGK model on a D2Q9 lattice. This is the same approach as that used in the coupled LBM-DEM framework of the present study. The regularised Bingham model (4.20) was employed in a slightly different form,

$$\tau_{\alpha\beta} = \tau_y \left[1 - \exp\left(-m\dot{e}\right)\right] + \mu e_{\alpha\beta}, \tag{4.21}$$

which results in an apparent viscosity, η, for the model,

$$\eta = \mu + \kappa, \tag{4.22}$$

with the regularised component, κ, defined as,

$$\kappa = \frac{\tau_y}{\dot{e}} \left[1 - \exp\left(-m\dot{e}\right)\right]. \tag{4.23}$$

The rate of strain effects of this Bingham model were included in the lattice Boltzmann equation by direct inclusion in the equilibrium distribution functions, rather than modifying the relaxation parameter after calculating the characteristic rate of strain. Using the equilibrium functions, (2.19), (2.20) and (2.21), in Section 2.4.2 the modified equilibria for the distribution functions of the D2Q9 lattice are written as,

$$f_0^{eq}\left(\mathbf{x}, t\right) = \frac{4\rho}{9}\left[1 - \frac{3}{2c^2}\left(\mathbf{u}\cdot\mathbf{u}\right)\right], \tag{4.24}$$

$$\begin{aligned} f_{1-4}^{eq}(\mathbf{x},t) &= \frac{\rho}{9}\Bigg[1+\frac{3}{c^2}(\mathbf{c}_i\cdot\mathbf{u})+\frac{9}{2c^2}(\mathbf{c}_i\cdot\mathbf{u})^2-\frac{3}{2c^2}(\mathbf{u}\cdot\mathbf{u}) \\ &\quad +\frac{9\kappa}{2}\left(\frac{\partial u_x}{\partial x_x}-\frac{\partial u_y}{\partial x_y}\right)(c_{ix}c_{ix}-c_{iy}c_{iy})\Bigg], \end{aligned} \tag{4.25}$$

$$\begin{aligned} f_{5-8}^{eq}(\mathbf{x},t) &= \frac{\rho}{36}\Bigg[1+\frac{3}{c^2}(\mathbf{c}_i\cdot\mathbf{u})+\frac{9}{2c^2}(\mathbf{c}_i\cdot\mathbf{u})^2-\frac{3}{2c^2}(\mathbf{u}\cdot\mathbf{u}) \\ &\quad +\frac{9\kappa}{2}\left(\frac{\partial u_x}{\partial x_x}-\frac{\partial u_y}{\partial x_y}\right)(c_{ix}c_{ix}-c_{iy}c_{iy}) \\ &\quad +\frac{9\kappa}{2}\left(\frac{\partial u_x}{\partial x_y}+\frac{\partial u_y}{\partial x_x}\right)c_{ix}c_{iy}\Bigg]. \end{aligned} \tag{4.26}$$

This allows the collision process to relax the fluid towards a state that already includes information from the rate of strain tensor, and is similar to the approach taken by Yoshino et al. [140] in simulating power law fluids. In the continuum limit these equilibrium functions, via the Chapman-Enskog analysis, result in the momentum equation for a regularised Bingham plastic,

$$\frac{\partial(\rho u_\alpha)}{\partial t}+\frac{\partial(\rho u_\alpha u_\beta)}{\partial x_\beta}=-\frac{\partial p}{\partial x_\beta}+\frac{\partial}{\partial x_\beta}\left[\left(\frac{2\tau-1}{6}\right)+\kappa\right]e_{\alpha\beta}. \tag{4.27}$$

The resulting scheme is proposed to be more stable and efficient than the methods which use the alteration of the relaxation parameter to incorporate the strain rate effects. It should be noted that direct methods cannot be used to calculate the velocity gradients present in (4.25) and (4.26) from the momentum flux tensor. This is due to the presence of anti-symmetric components and more importantly, because the equilibrium functions are modified in this approach and they are required to calculate the non-equilibrium functions in the momentum flux tensor. Pressure driven channel flow and velocity driven flow through a channel expansion were presented for varying Bingham and Reynolds numbers in 2D and the results compared favourably with those in the literature.

A robust implementation of the Bingham plastic model in the LBM would facilitate the straightforward extension to a Herschel-Bulkley fluid. As in the Bingham plastic, this model behaves as a solid below the yield stress however the post-yield viscosity is nonlinear rather than Newtonian. This allows further material nonlinearity via shear-thinning or thickening in the plastic zone. Burgos et al. [13] and Burgos and Alexandrou [12] have reported the implementation of this type of yield stress fluid in finite element computations, however the only known attempt at this fluid in the context of the LBM is the implicit approach in [136].

4.2.3 The Stress Tensor in the Lattice Boltzmann Method

The accurate determination of the rate of strain tensor (4.12) is integral to the implementation of non-Newtonian fluids within the LBM and other CFD methods. The most intuitive approach to calculating the velocity gradients that form the components of this tensor is to calculate them directly from the macroscopic velocities at the grid points using a finite difference method. This technique is further simplified in the LBM due to the data existing on a regular orthogonal grid. As mentioned in Section 4.2.1 it is also possible in the LBM to extract the rate of strain tensor from the momentum flux tensor, $\Pi_{\alpha\beta}$ (4.13), the components of which are second order moments of the non-equilibrium distribution functions at each node. This results in a local and explicit definition of the rate of strain tensor, $e_{\alpha\beta}$ (4.14), that does not require information from neighbouring nodes to evaluate the velocity gradients. This is in contrast to finite difference methods which require information from one node or two nodes in each orthogonal direction for first order and second order schemes, respectively. Therefore, the locality of direct evaluation of the rate of strain tensor is particularly convenient at nodes adjacent to wall boundaries and discrete elements where the data required for finite difference methods may not exist.

The accuracy of the calculation of the rate of strain tensor using the LBM momentum flux tensor was tested in a two-dimensional Poiseuille flow problem. Errors due to compressibility and the chosen boundaries were investigated, and the results were compared to the exact evaluation of $e_{\alpha\beta}$. A y-direction body force was used to drive the flow of a Newtonian fluid through a channel $0.5m$ wide and $0.7m$ high with a lattice spacing of $0.005m$. The body force was varied between 9.81e-07m/s^2 and 9.81e-03m/s^2 to vary the computational Mach number. The bounce-back wall boundary condition was applied on the walls and periodic boundaries were used on the inlet and outlet. The fluid density and viscosity were $1000kg/m^3$ and 1e-05m^2/s, and the Mach number sensitivity analysis was run with $\tau = 0.51$ and $\tau = 0.60$. This was done to isolate the errors due to the slip velocity of the bounce-back wall boundary condition (see Section 2.6.1).

The characteristic parabolic profile for plane Poiseuille flow exhibits a maximum at the centre of the channel. At this location the rate of change of the velocity profile is zero and consequently the rate of strain is also zero.

The analysed parameter space resulted in a range of Mach numbers between 0.005 and 50 and the characteristic rate of strain (4.11) was evaluated across the channel width for each simulation. As expected, the accuracy of the strain prediction was found to deteriorate with increasing Mach number. At $Ma = 50$ the direct evaluation of strain (4.13) deviates considerably

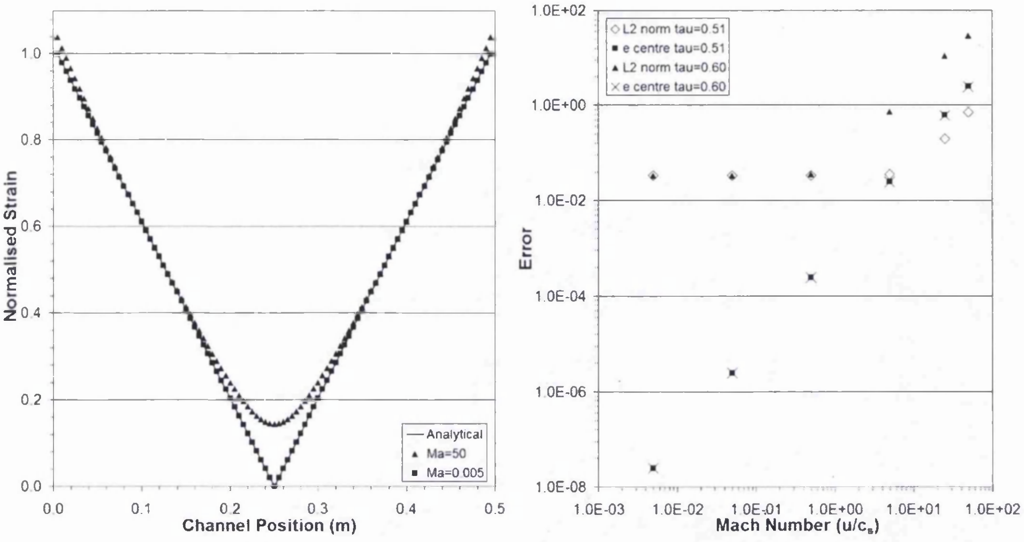

(a) (b)

Figure 4.2: The direct evaluation of the characteristic rate of strain in the LBM using the momentum flux tensor, including (a) the strain profiles across the channel at $Ma = 0.005$ and $Ma = 50$, and (b) the error at the channel centre and the L_2 norm error across the channel for varying Mach number.

from the exact result at both the channel edges and centre despite the solution still displaying good reproduction of the velocity profile. Conversely, at $Ma < 0.5$ the correlation between the direct evaluation from the LBM and the exact solution is excellent. The characteristic strain profiles for these two extremes are graphed in Figure 4.2a along with the exact solution for comparison. The consequences of breaching the compressibility constraint of the LBM ($Ma \ll 1$) are clearly evident.

Figure 4.2b graphs the strain error at the centre of the channel and the L_2 norm error across the channel for all simulations. A number of interesting points can be drawn from the plotted response. The relative error in the characteristic rate of strain at the centre of the channel was calculated by comparing the numerical results to the exact value of zero. The rate of convergence was found to be second-order with Mach number, which is consistent with the small velocity expansion of the equilibrium functions discussed in Section 2.5. It can also be seen that the error at the centre of the channel is the same for both $\tau = 0.51$ and $\tau = 0.60$. This suggests that the increased slip velocity at the bounce-back wall boundaries does not affect the strain evaluation at the centre of the channel.

The comparison of the L_2 norm error across the channel was particularly interesting. For both $\tau = 0.51$ and $\tau = 0.60$ it can be seen that the error reduces monotonically to a value of approximately 0.033 after which further reduction of Ma has no influence. This limited convergence behaviour can be explained by the reduction of the combined boundary and compressibility error (with decreasing u_{max} and consequently Ma) until the discretisation error in the channel becomes dominant. The rate of convergence (slope 1.85 for $\tau = 0.51$ and slope 1.62 for $\tau = 0.60$) is not second order due to the combination of the second order compressibility error with the boundary error which is only first order with respect to u_{max} [147]. For $\tau = 0.51$ the convergence is closer to second order (until the minimum error is reached) because of the smaller contribution from boundary slip error. This error, which is due to the presence of a slip velocity when using the bounce-back condition, is $\mathcal{O}(\tau^2)$which also explains why the magnitude of the error is significantly less for $\tau = 0.51$ at the same Mach number. This shows how the boundary error influences the strain evaluation despite not affecting the prediction at the centre of the channel.

Despite the intricacies of convergence for the calculation of the rate of strain using the direct LBM method, these results have shown that its accuracy is excellent when the compressibility constraint is obeyed.

4.3 Non-Newtonian Validation Examples

The truncated power law model [42] and the Bingham plastic model of Wang and Ho [137] discussed in this chapter were implemented in the LBM-DEM framework. These constitutive relationships formed the basis of the characterisation of fines as a non-Newtonian fluid.

The direct evaluation method (4.14) was employed to calculate the rate of strain tensor, $e_{\alpha\beta}$, from the momentum flux tensor, $\Pi_{\alpha\beta}$. A first-order finite difference scheme was also implemented to allow comparison of the two methods. The viscoelastic behaviour of the power law model was included in the LBM by adjustment of the local relaxation parameter (4.15) and an under-relaxation parameter (4.17) was added [122]. This parameter, λ, limits the change of the relaxation parameter in successive time steps and thereby increases stability and allows the solution of problems that initiate with zero strain[2] (i.e. started from rest).

The implemented power law model was tested for dilatant (shear-thickening) and pseudoplastic (shear-thinning) flows in two and three dimensions. The flow velocity and strain profiles were interrogated and compared to ana-

---

[2] Zero strain at the onset of a shear-thinning simulation would result in the prescription of a high viscosity throughout the domain which can adversely affect the result.

lytical solutions. Qualitative comments on the results were made where appropriate.

The implemented Bingham plastic model was tested for the case of plane flow in a two-dimensional channel using the finite difference method to calculate the rate of strain tensor. This was necessary because the model implementation requires the rate of strain tensor for the definition of the equilibrium function, but the equilibrium function is required for the direct method of strain evaluation. Even in this trivial flow geometry the Bingham model was found to be unstable. The response to induced strain in the domain was erratic even at small velocity gradients. This issue could possibly be overcome by initiating the solution with an initial velocity field and consequently a continuous rate of strain profile. However this approach would not be able to overcome the problem in block cave applications because the fines regime is intermittently at rest due to the nature of draw sequencing.

Consequently, the power law model was solely used to further investigate the characterisation of fines in the LBM-DEM framework. Following the validation tests, this was extended by applying the non-Newtonian LBM-DEM framework to numerical rheometry of real bulk materials and comparing the response to experimental results.

4.3.1 Viscoelastic Flow in a 2D Plane Channel

The two-dimensional validation of the viscoelastic power law model was undertaken by simulating flow through a plane channel. This flow geometry is analogous to the Newtonian case of plane Poiseuille flow.

The fluid domain analysed was $0.5m$ wide, $0.75m$ high and the lattice spacing used was $0.005m$. Flow in the channel was driven by a y-direction body force of -9.81e-04m/s^2 and periodic boundaries were used on the inlet and outlet. The bounce-back boundary condition was used on the channel walls, which were aligned with the lattice and therefore able to maintain the second-order accuracy of the solution [8].

Both pseudoplastic (shear-thinning) and dilatant (shear-thickening) flows were investigated using an index range of $0.2 < n < 3.0$. The initial viscosity and relaxation parameter were set at 1.0e-04m^2/s and 0.51, respectively. These parameters are used at the start of the analysis to calculate the LBM time step but as the solution progresses they are both overwritten by the values calculated by the power law. The truncation limits, τ_{min} and τ_{max}, were set at 0.5001 and 10.0, respectively, and the consistency constant, ν_0, was chosen as 1.0e-04m^2/s. The under-relaxation parameter, λ, was set at 0.01.

It can be shown [5] that the analytical solution for the flow of a power

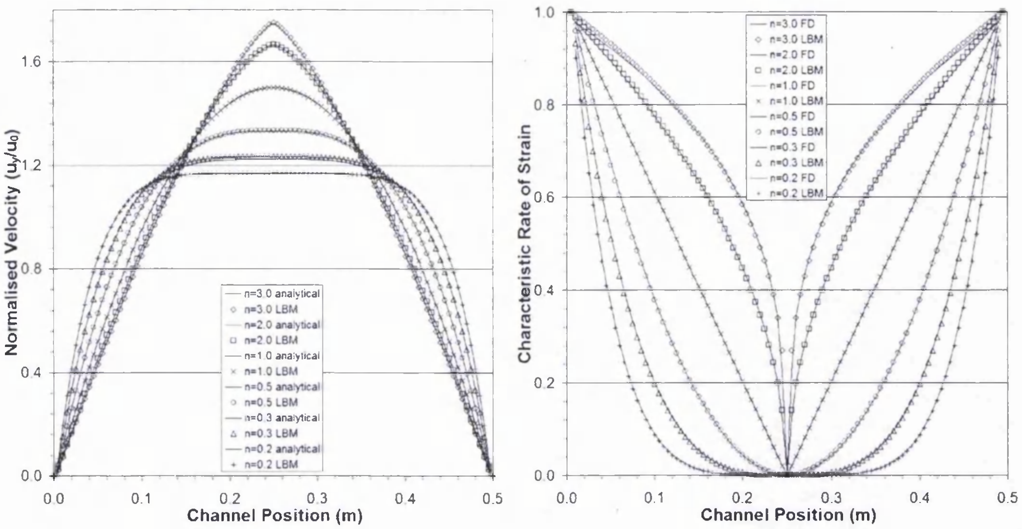

(a) (b)

Figure 4.3: The results of the viscoelastic channel flow in 2D for the power range $0.2 < n < 3.0$, including (a) the numerical and analytical velocity profiles across the channel, and (b) the normalised characteristic rate of strain across the channel as calculated using the direct method and a first-order finite difference approximation.

law fluid in a plane channel is,

$$\frac{u_y(x)}{u_0} = \frac{2n+1}{n+1}\left[1 - \left(\frac{2\,|x|}{w}\right)^{(1+1/n)}\right], \tag{4.28}$$

in which u_0 is the mean channel velocity. This is calculated as the quotient of the volumetric flow rate and the channel width, w.

Figure 4.3a graphs the velocity profiles of the validation analyses against their respective analytical solutions. It can be seen that the correlation between the numerical and analytical results is good over the power range, $0.2 < n < 3.0$. The shear-thinning results ($n < 1.0$) demonstrate a plug-type flow profile with a flat section in the channel centre where the shear strain is low and therefore the viscosity is high. Conversely, adjacent the walls the shear strain is high resulting in a low viscosity and a region of high velocity gradient. In the shear-thickening results ($n > 1.0$) the high shear regions near the channel walls result in an increase in the viscosity and the low shear at the channel centre acts to reduce the viscosity. The combination of these effects results in the sharp velocity profile evident in the graph.

The error in the velocity profile was found to be less than 1% for all cases analysed. However, it should be noted that this error was found to increase as n deviated further from the Newtonian value of 1.0, particularly in the shear-thinning regime. Recalling that the accuracy of the LBM deteriorates for $\tau > 1.0$, the increasing error in the shear-thickening simulations can be attributed to the increase in the relaxation parameter due to the power law model. The growth of errors in the shear-thinning case can be explained by the presence of compressibility errors. As the fluid becomes more shear-thinning the maximum velocity of the central plug increases. The time step, which is calculated using the initial viscosity and relaxation parameter, does not change and therefore the increasing velocity results in an increase in the computational Mach number. As n gets smaller this effect grows leading to a greater deviation from the analytical velocity profile.

In all of the analyses the influence of the truncation bounds, τ_{min} and τ_{max}, was monitored. The good correlation of the velocity profiles indicate that the bounds maintained stable solutions but at the same time did not restrict the viscoelastic tendencies of the fluid. In fact, it was found that for the range of powers analysed neither the lower or upper limit on the relaxation parameter was reached. For this reason the flow profiles could be compared solely with the viscoelastic analytical solution (4.30). If the bounds had been reached in sections of the channel the analytical profile in those locations would be Newtonian, and the solution for the width of the channel would be a combination of the two [42].

Figure 4.3b compares the normalised characteristic rate of strain in the channel as evaluated using the direct method and a first-order finite difference approximation. The correlation of the results is excellent. This and the velocity result demonstrate that a simple extension of the LBGK model can be employed to simulate fluids whose viscosity increases or decreases in regions of high shear.

4.3.2 Viscoelastic Flow in a 3D Tube

The three-dimensional validation of the viscoelastic power law model was undertaken by simulating flow through a cylindrical tube. This flow geometry is analogous to the Newtonian case of Hagen-Poiseuille flow.

The flow model geometry used in this analysis was identical to that reported in Section 2.8.4. The radius of the tube, R, was $0.1m$, the lattice spacing was $0.002m$, and the flow was driven by an x-direction body force of $0.01m/s^2$. Periodic boundaries were used on the inlet and outlet and the bounce-back boundary condition was applied to the channel walls. The viscoelastic parameters employed were the same as those in the 2D analysis in Section 4.3.1.

The analytical solution for the axial velocity profile can be derived as,

$$u_x(r) = \left(\frac{-\mathbf{G}}{2\nu_0}\right)^{\frac{1}{n}} \frac{n}{n+1}\left[r^{(1+1/n)} - R^{(1+1/n)}\right], \tag{4.29}$$

which can be normalised by the mean velocity, u_0, to,

$$\frac{u_x(r)}{u_0} = \frac{3n+1}{n+1}\left[1 - \left(\frac{r}{R}\right)^{(1+1/n)}\right]. \tag{4.30}$$

An index range of $0.3 < n < 3.0$ was analysed to investigate both pseudoplastic and dilatant flows in 3D. Figure 4.4a graphs the velocity profiles of the validation analyses against their respective analytical solutions. In this graph it can be seen that the flow profile characteristics for varying n were the same as in the 2D analyses. The shear-thickening cases result in a triangular flow profile across the tube diameter while the shear-thinning cases result in a flat, plug-flow profile. Excellent correlation between the analytical and numerical results is evident for $0.5 < n < 3.0$, with the velocity error typically less than 1%. However, for the case of $n = 0.3$, fluctuations can be seen in the velocity profile and the error increases to approximately 8%. This deviation of the numerical and analytical results can be explained by both the approximation of the cylindrical boundary, as discussed in Section 2.8.4, and the first-order accuracy of the bounce-back condition on non-aligned boundaries. Figure 4.4b is a contour plot of the x-direction velocity in the tube for $n = 0.3$. In this figure it can be seen that the boundary approximations, in combination with a highly shear-thinning fluid, result in a fluctuating, or *noisy*, flow profile.

The error in the 3D velocity profile for highly shear-thinning fluids could be reduced by decreasing the lattice spacing, using a closed-form description of the tube boundary (as opposed to a faceted approximation), or employing a interpolation-supplemented lattice. Nevertheless, the results of the investigation show how non-Newtonian, viscoelastic fluids can be simulated using an LBGK model with relatively minor modifications.

4.3.3 Cylindrical Couette Flow Rheometry

Classical soil mechanics generally focuses on the material response up to the point of failure and as such only small strains of a quasi-static nature are considered. However, the movement of fines within a block cave is intermittently dynamic and the resultant displacements and strains are large. In such a loading state, constitutive models such as Mohr-Coulomb are no longer valid and an alternative approach is required for the characterisation

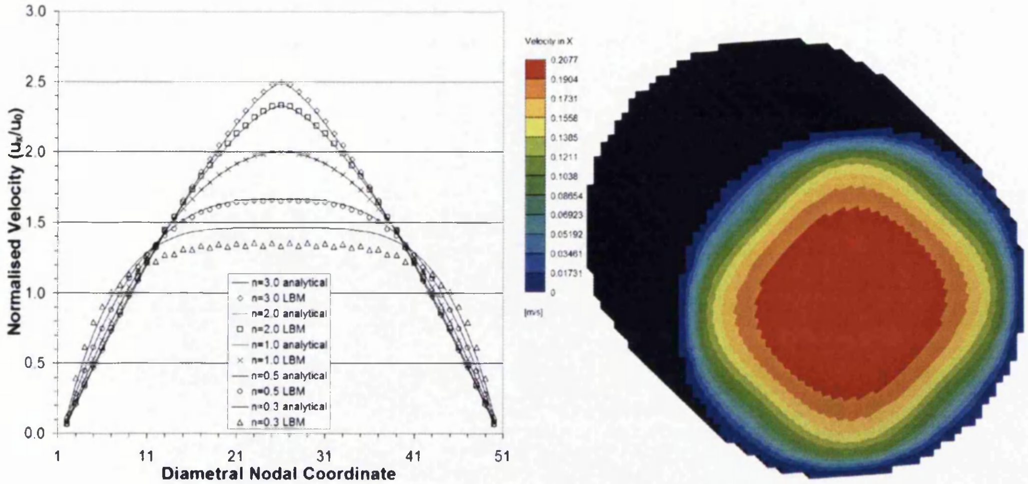

(a) (b)

Figure 4.4: The results of the viscoelastic flow in a 3D tube for the power range $0.3 < n < 3.0$, including (a) the numerical and analytical velocity profiles across the diameter, and (b) a contour plot of the x-direction velocity in the tube for $n = 0.3$, showing the *noise* induced by the boundary approximation.

of bulk materials as a continuum. Therefore, a fluid mechanistic approach has been employed in the present study to simulate block cave fines as a non-Newtonian fluid.

At the most basic level, continuum models for soils assume a linear stress-strain relationship. As an example, Tardos [128] offered evidence suggesting that granular materials exhibit quasi-Newtonian flow characteristics when the angle of internal friction is low (i.e. less than 20 degrees for powders). In reality though, a viscous component of the deformation is usually evident and consequently many studies suggest that the soil response can be assumed to be both as solid (elastic) and as fluid (viscous) depending on the loading characteristics. As discussed in Section 4.1.1, Tardos [128] presented a Coulomb powder model for the frictional flow of powders and Tardos et al. [129] used a rotational Couette rheometer to show a power-law relationship between stress and strain for granular materials. In addition, Ghezzehei and Or [45] and Or and Ghezzehei [99] carried out the rheological classification of a soil using a rotating, parallel plate apparatus. They found, for varying water contents, a viscoplastic Bingham model response for Millville silt loam (29% sand, 55% silt, 16% clay) with a well defined yield point. It should be noted that these results were presented for low strain rates ($< 0.02s^{-1}$).

A search of the literature highlights that the rheological classification of soils is a limited field. Published experimental data from rheometry is particularly lacking. However, the recent work of Davison et al. [28] presented experimental results aimed at characterising sand as a non-Newtonian fluid. The motivation for these tests was to develop a material model that could be employed in conjunction with computational fluid dynamics to simulate an auger working in sand.

The bulk material tested was well-graded Leighton Buzzard sand which exhibited 83% of the grains lying within the $300\mu m$ size range and a bulk density of $2000kg/m^3$. Direct shear box tests were undertaken and an approximate Newtonian viscosity of $3e06 Pa.s$ was determined from the induced shear stress and an assumed shear zone thickness. This corresponds to a dynamic viscosity of $1500m^2s^{-1}$, which is several orders of magnitude higher than that for the fluids discussed (to this point) in this work.

To further improve the realism of the numerical sand model the viscous component of its behaviour was considered. This was done by measuring the nonlinear deformation of the sand at different strain rates, otherwise known as rheometry. Some examples of non-Newtonian rheometry tests include the falling ball test, rotating parallel plate test, rotational vane test, and cylindrical Couette flow test. Davison et al. [28] used the latter to determine the viscous response of the sand and found distinct pseudoplastic, viscoelastic behaviour. A power law best fit of the experimental results provided a consistency constant, μ_0, of $333.6Pa.s^n$ and a power, n, of -0.14. This is clearly a highly shear-thinning response, which might be expected for a cohesionless soil such as dry sand. It is also consistent with the results of Tardos et al. [129] which tested glass beads of various size in a cylindrical Couette rheometer.

The viscoelastic sand model was applied to auger simulations using an implicit finite volume solver. To aid stability and convergence the power law viscosity was truncated to a minimum of $1 Pa.s$ and a maximum of $1000Pa.s$, which is identical to the approach taken in the present LBM formulation. The simulations were undertaken with no-slip boundaries at the auger-fluid interface and the driving force and torque was calculated by integrating the stress distribution on the external faces of the auger elements. The behaviour of the non-Newtonian and Newtonian material models was tested and the shortcomings of the latter were made apparent. Using the Newtonian model resulted in shear force predictions that were larger than the power law model by a factor of 10^5. Also, the Newtonian response lacked a velocity boundary layer, outside which the sand was minimally affected by the auger. Consequently a much greater, and unrealistic, amount of material was was raised by the auger.

The work of Davison et al.[28] and Tardos et al. [129] served as motivation for application of the non-Newtonian LBM-DEM framework to numerical rheometry of bulk materials. This novel approach allows the characterisation of particulates, such as fines, as viscoelastic fluids with a strain-rate dependent response that can be calibrated against experimental results as they become available. As in these previous studies, a cylindrical Couette rheometer was used to undertake the numerical experiments.

The cylindrical Couette rheometer is comprised of an inner cylinder (bob) which is rotated inside a larger cylinder (cup), creating an annulus inside which the test material is placed. This apparatus is shown schematically in Figure 4.5a. The interpretation of the induced radial velocity profile in the annulus is dependent on the geometry of the rheometer and the nature of material being tested. For example, if the annulus is sufficiently narrow in comparison to the radius of the bob, $(R_c - R_b) < R_b$, the velocity profile can be assumed linear and therefore the rate of strain is constant [31]. The flow is therefore approximately equivalent to linear Couette flow (Figure 4.5b) and the rate of strain is calculated as,

$$e_{r\theta} = \frac{\omega_b R_b}{R_c - R_b}, \tag{4.31}$$

in which ω_b is the angular velocity of the bob. In this fashion the strain induced in the test material is controlled by the speed at which the bob is driven.

The shear stress on the surface of the bob is independent of the nature of the material being tested and can be evaluated from the torque, T, required to drive the bob,

$$\tau_{r\theta} = \frac{T}{2\pi R_b^2 h}, \tag{4.32}$$

where h is the height of the rheometer. The instantaneous viscosity, η, can then be calculated,

$$\eta = \frac{\tau_{r\theta}}{e_{r\theta}} \tag{4.33}$$

using the shear stress and the average velocity gradient (i.e. the rate of strain).

For reasons of computational expediency, the numerical rheometry using the non-Newtonian LBM-DEM framework was undertaken in two dimensions. If the height of the rheometer is sufficiently greater than the diameter of the bob the effect of the ends on the induced strain and shear becomes negligible. Consequently, the physical flow reduces to a 2D arrangement indicating that this is a fair modelling assumption. The influence of gravity was not directly included, but the plane strain nature of the 2D analysis means

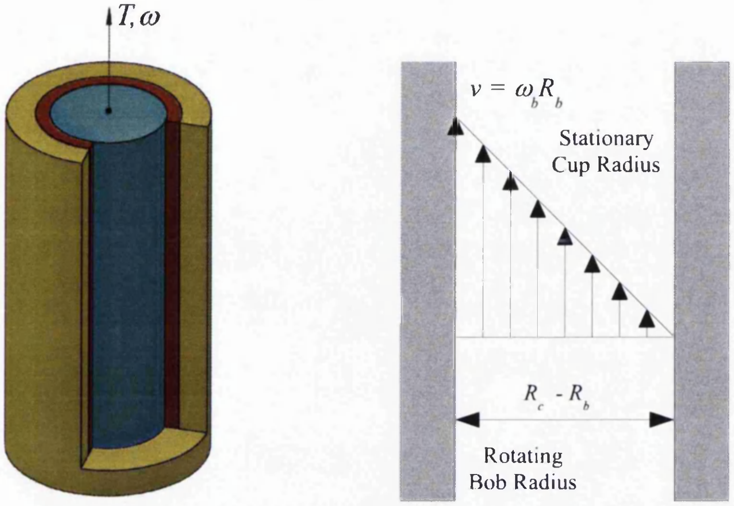

(a) (b)

Figure 4.5: Details of the cylindrical Couette rheometer, including (a) a schematic representation of the apparatus, and (b) the approximation of the velocity profile when the annulus is sufficiently narrow.

that the numerical geometry was suitably confined. This is in accordance with the results of Tardos et al. [129], which found that the experimental viscoelastic response was dependent on the prevention of dilation of the test material. The radius of the of the bob, R_b, and the radius of the cup, R_c, used in the numerical experiments was $0.04m$ and $0.05m$, respectively, as shown in Figure 4.6a. A lattice spacing of 5e-04m was employed, resulting in 21 nodes across the annulus, as can be seen in Figure 4.6b.

The numerical rheometry model was first applied in an attempt to replicate the experimental results of Davison et al. [28] for Leighton Buzzard sand. The consistency constant, ν_0, and the power law index, n, were set at $0.1668m^2s^{n-2}$ and -0.14, respectively. The density, initial viscosity and relaxation parameter used were $2000kg/m^3$, $0.005m^2/s$, and 0.6. The truncation of the power law was effected by incorporating limits on the strain-dependent relaxation parameter, $\tau_{min} = 0.51$ and $\tau_{max} = 1.5$, which corresponded to $\mu_{min} = 1Pa.s$ and $\mu_{max} = 100Pa.s$. Note that using a maximum of $1000Pa.s$ would have resulted in a large maximum relaxation parameter which could potentially deteriorate the accuracy of the solution. This point is particularly important when the slip velocity of the bounce-back wall boundary, which is $\mathcal{O}(\tau^2)$, is considered.

The numerical experiment was run for a range of strain rates between $4s^{-1}$ and $80s^{-1}$ and the instantaneous viscosity was calculated for each case using

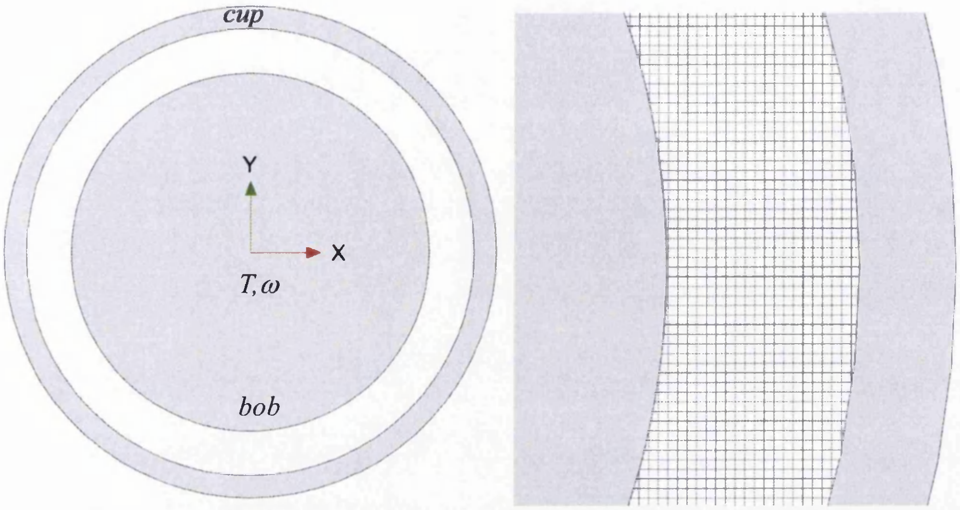

(a) (b)

Figure 4.6: The 2D numerical rheometry undertaken using the non-Newtonian LBM-DEM framework, including (a) the geometry of the bob and cup, and (b) the discretisation of the annulus with the LBM grid.

(4.31), (4.32), and (4.33). Figure 4.7 plots the results of the non-Newtonian LBM-DEM framework alongside the best fit of the experimental data [28]. The correlation of the numerical and experimental results is excellent. At higher strain rates it can be seen that the LBM marginally overestimates the viscosity. This is due to the lower truncation limit, $\tau_{min} = 0.51$, being reached in the annulus and the consequence is that the model does not quite reach the level of shear-thinning required to match the experiments. This could be addressed by further reducing the lower truncation limit but that would act to reduce the stability of the material model in asymmetrical flows.

Contour plots of the total velocity in the annulus when the bob is driven at $1rad/s$ and $15rad/s$ are included in Figures 4.8a and 4.8b, respectively. At low strain rate the velocity profile is relatively uniform but at high strain rates it can be seen that a thin shear band of high velocity material exists adjacent the bob surface. The same shear zone was observed in the experiments undertaken by Tardos et al. [129].

Following the successful replication of the Leighton Buzzard sand response, a number of other material models were tested with the numerical rheometer. A lack of suitable experimental data meant that the additional materials could not be calibrated to physical samples and therefore the response could only be discussed qualitatively. Table 4.1 summarises the viscoelastic power law properties that were used for Material A, B and C. All

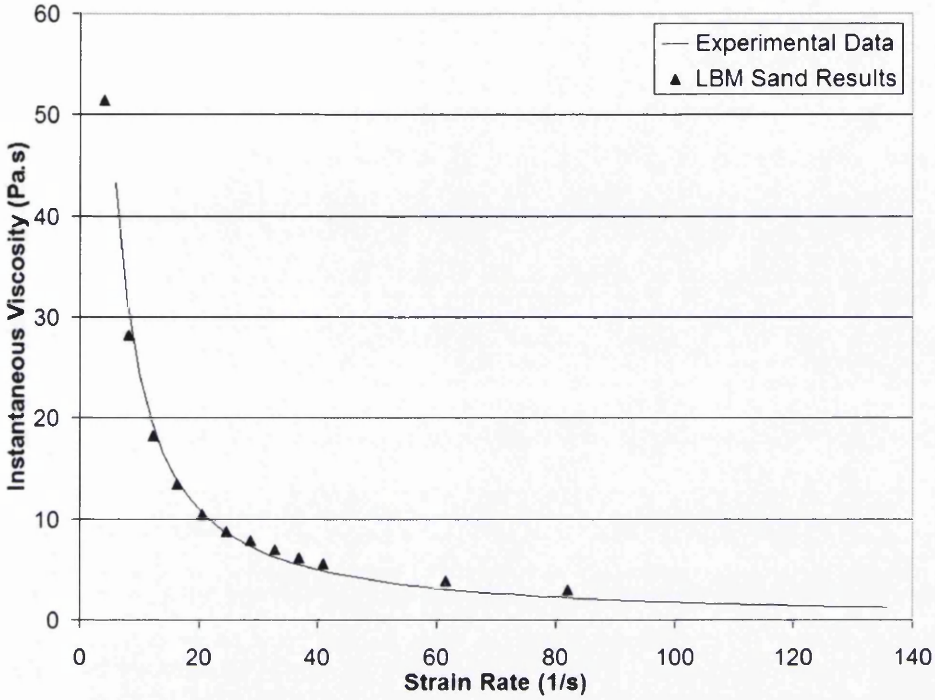

Figure 4.7: The results of the numerical rheometry of Leighton Buzzard sand undertaken using the non-Newtonian LBM-DEM framework, with the experimental results [28] included for comparison.

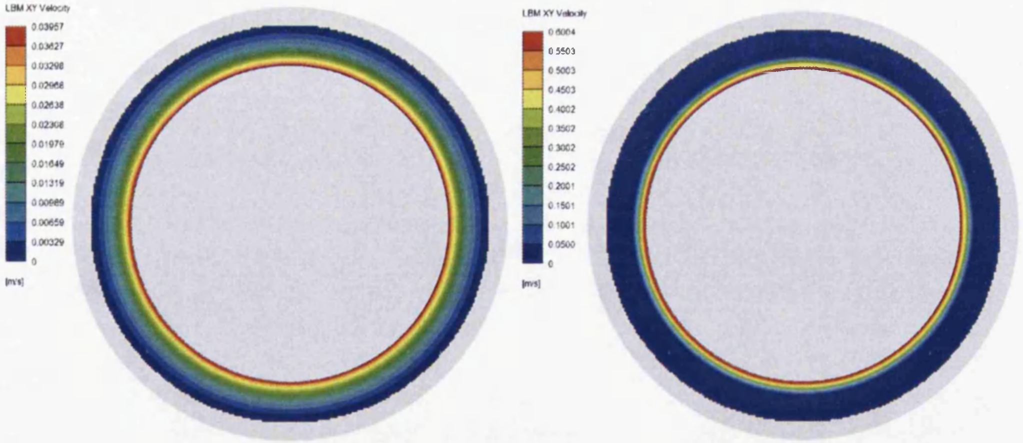

(a)

(b)

Figure 4.8: Contour plots of the total velocity in the cylindrical Couette rheometer for Leighton Buzzard sand driven at (a) $1rad/s$, and (b) $15rad/s$.

Material	n	$\nu_0\,(m^2s^{n-2})$	τ_{min}	τ_{max}	τ_{in}	$\nu_{in}\,(m^2/s)$
A	0.3	0.3336	0.51	1.7	0.60	0.0416
B	0.1	0.3336	0.51	1.7	0.60	0.0416
C	0.3	0.0833	0.505	0.6	0.51	0.0416

Table 4.1: The viscoelastic power law properties of the three materials tested in the numerical rheometer.

materials used a bulk density of $1000kg/m^3$ and an under-relaxation parameter, λ, of 0.01. The aim of these parameter combinations was to achieve a response that was less shear-thinning than the sand model and more representative of a cohesive bulk material.

Figure 4.9 graphs the instantaneous viscosity of Materials A, B and C against strain rate and the LBM sand response is included for comparison. The higher power of Material A ($n = 0.3$) results in a more gradual reduction in the viscosity as the the strain rate increases. The larger consistency constant for Materials A and B ($0.3336m^2s^{n-2}$) resulted in the high-strain viscosity being greater than that for the sand model. This can be interpreted as an increase in the cohesion of the material being tested. Material C exhibits a higher and constant viscosity than the others due to the lower truncation limit, $\tau_{min} = 0.505$, being reached even at moderate levels of strain. The result is a material response that is approximately rigid due to high viscosity at low strains and then Newtonian (i.e. constant viscosity) after a threshold value of strain is reached. The characteristics of this response are similar to those of a Bingham plastic, which behaves as a solid below its yield stress and as a Newtonian fluid above it.

The transitional behaviour of the material responses was investigated further by plotting the shear stress (4.32) against the strain rate (4.31) for the materials tested. This is shown in Figure 4.10 and, again, the sand response is included for comparison. The flat gradient of the curve for Leighton Buzzard sand is a result of the highly shear-thinning nature of the material model and the low viscosity that is achieved at high strain rate. Conversely, the gradient for Material C is much greater due to the larger high-strain viscosity. Approximate asymptotes of the stress-strain response for the four materials are also included in the graph which allow an interesting observation to be made. With the assistance of these high-strain asymptotes it can be seen that the response of the pseudoplastic material models is similar to the characteristic response of a regularised Bingham plastic (See Figure 4.1). The y-intercept of the asymptotes is equivalent to the yield stress of the ideal Bingham model (i.e. not regularised) and the gradient is equivalent to the plastic

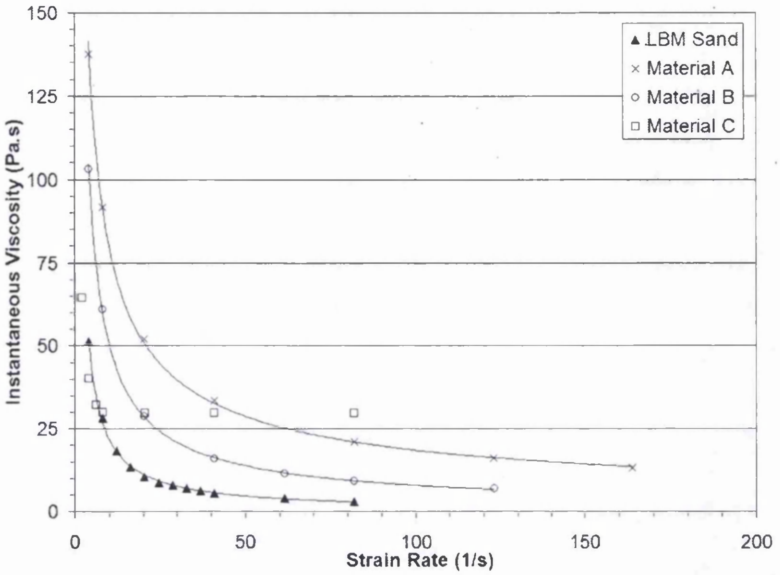

Figure 4.9: Graph of the instantaneous viscosity against strain rate for Materials A, B and C, as tested in the numerical rheometer.

viscosity. The rate at which the material response tends to the asymptote is analogous to the effect of the regularisation parameter, m, which smooths the stress-strain discontinuity at the yield point of the ideal Bingham model. As an example, Material B tends to the asymptote faster than Material A due to the lower power index, n, and therefore the corresponding Bingham interpretation is that Material B has a higher regularisation parameter than Material A. At the scale shown, Material C displays an almost ideal-Bingham response with a yield stress of just under $100Pa$ and a plastic viscosity of approximately $30Pa.s$.

The results of the numerical rheometry experiments have provided qualitative and quantitative support for the hypothesis that the LBM can be used to model bulk materials as a non-Newtonian fluid. Unfortunately, a lack of experimental data in the literature means that numerical rheometry of Materials A, B and C undertaken in this section cannot be directly compared to physical material samples. However, Or and Ghezzehei [99] presented rheometry results for Millville silt loam (29% sand, 55% silt, 16% clay) which was tested using a rotating parallel plate apparatus. At water contents of $0.28kg/kg$ and $0.34kg/kg$ a well defined yield stress was found and therefore both sets of data were interpreted as Bingham plastics. For the sample with the lower water content, the yield stress was found to be $350Pa$ and the plastic viscosity was evaluated as approximately $6e04Pa.s$. For the higher water content sample the yield stress was $800Pa$ and the plastic viscosity was

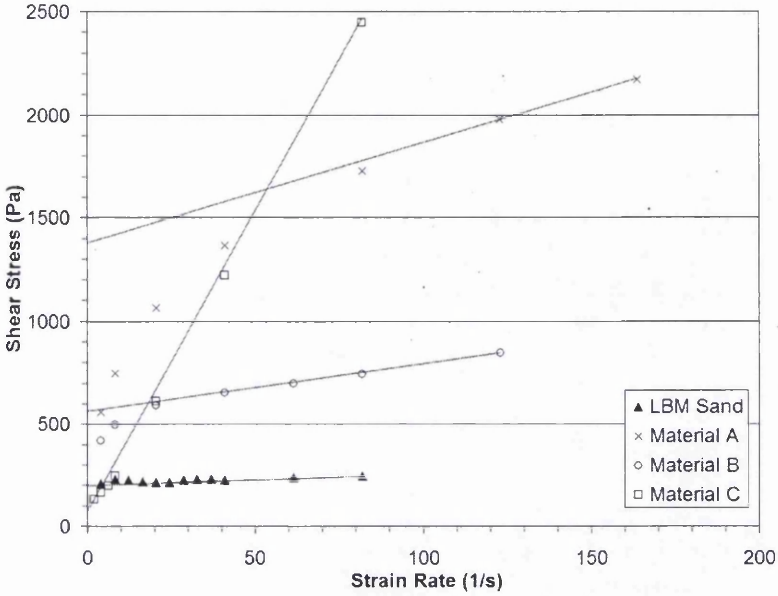

Figure 4.10: Graph of the shear stress against strain rate for Materials A, B and C, as tested in the numerical rheometer.

approximately 4e04$Pa.s$. This and other similar results [45] highlighted the sensitivity of the Bingham parameters to the amount of water in the sample. Regardless, it is apparent that viscosities determined in these experiments are several orders of magnitude larger than those found for Materials A, B and C. The reason for this is that the experiments are only undertaken up to a maximum strain rate of $0.02s^{-1}$ and in this range the gradient of the stress-strain curve is high. On closer inspection though it can be seen that at the maximum strain rate the gradient is still decreasing. It can therefore be assumed that the plastic viscosity over a test range in the order of $100s^{-1}$ would be significantly lower and, when water content is also taken into account, of similar scale to that of Materials A, B and C.

CHAPTER 5

TWO-DIMENSIONAL APPLICATIONS OF THE LBM-DEM FRAMEWORK

The preceding chapters of this thesis have outlined the incremental development of a computational framework that is capable of simulating fines migration in a block cave. Chapter 2 discussed the implementation of the lattice Boltzmann method within a commercial finite element code, with special consideration given to the accuracy and stability of the model in large scale problems. Chapter 3 then addressed the coupling of the LBM to the discrete element method, including particle mapping techniques and the matching of explicit solution schemes. Finally, Chapter 4 dealt with the extension of the framework to include non-Newtonian fluids and the characterisation of bulk materials using a complex material model. The successful amalgamation of these features then allowed the modelling of fines percolation and migration to be undertaken.

Prior to the extension of the LBM-DEM framework to three dimensions, moderate and large scale applications were undertaken in two dimensions. The use of 2D models allows large physical domains to be simulated over moderate time periods due to the comparatively low number of lattice nodes, and therefore computational resources, required. However, it also simplifies the representation of the actual cave geometry and limits the mechanics of block dynamics and fines migration to a plane. The interaction of multiple adjacent draw zones in a cave requires a 3D model layout, and it is fair to assume that the inter-particle percolation that occurs during migration is also a 3D phenomenon with fines moving in all three Cartesian directions to

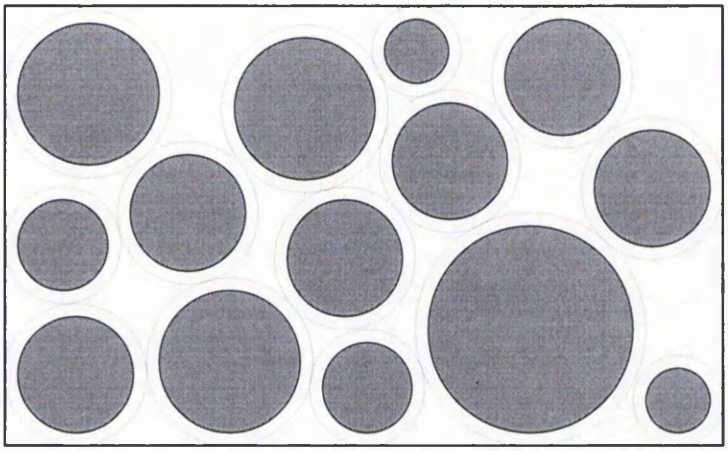

Figure 5.1: Schematic representation of the discrete element contact buffer applied to circular elements. The hashed circles represent the contact boundaries and the solid circles represent the physical boundaries.

occupy evolving voids.

Another limitation of 2D fines migration simulations is the very low permeability of the structural, discrete element field. At steady state the porosity (portion not filled with blocks) of the cave is less than 10% when circular elements are used, and the well-developed network of block-block contacts forms a barrier impermeable to fines percolation. To overcome this problem a contact *buffer* was incorporated into the discrete element contact which would allow neighbouring blocks to engage in contact before they were physically touching. The contact buffer for circular elements is introduced as a reduction of the original boundary radius, as shown schematically in Figure 5.1, while the contact radius remains unchanged. This simple modification allowed the porosity of the 2D structural field to be adjusted via a single contact parameter.

Despite the limitations of 2D modelling it can still be employed to provide insight into the kinematics of fines migration. In this chapter, the results of a moderate scale percolation analysis and a large scale cave migration analysis are presented.

5.1 Replication of DEM Percolation Tests

The two-dimensional LBM-DEM framework was first applied to replicate fines percolation analyses undertaken using the discrete element method. As discussed in Section 1.2, Pierce [105] used the commercial code *PFC3D* to investigate the percolation of small elements through large elements in both

Figure 5.2: The method of shear induction in the small scale percolation tests [105]. The strain rate was governed by the period of the angular deformation.

small scale shear tests and large scale cave draw simulations. The objective of the research was to determine the significant factors that influence percolation and to develop equations based on these trends for implementation in *REBOP*.

The small scale DEM tests were themselves a replication of experiments undertaken by Bridgewater et al. [10]. These tests measured the shear-induced percolation of spheres of various sizes in a bed subjected to angular deformation. Figure 5.2 shows the deformation induced in the bed in the DEM experiments. The top of the bed was seeded with smaller elements and the time required for them to reach the bottom was investigated for various factors including fines size distribution, shearing rate and shear orientation with respect to gravity.

The salient results of the small scale percolation tests are listed as follows.

1. The rate of percolation increased for lower strain rates. The slower rearrangement of large particles allowed more time for small particles to fall into intermittent void spaces.

2. The rate of percolation decreased as the size of the smaller particles was increased towards the size of the larger particles. The rate of percolation also decreased when using a statistical distribution for the size of the smaller particles. These are largely intuitive results.

3. The orientation of the shearing direction with respect to gravity did not have a significant effect on the rate of percolation.

Pierce also undertook a large scale cave analysis using DEM to test the hypothesis that the shear induced by draw was a primary cause of fines migration/percolation. The analysis was performed in 3D in a quarter symmetry model measuring 19.25m along each base edge and 42m high. Draw was undertaken by prescribing the exit velocity of particles at the 14m circular outlet at the bottom of the domain. The domain was filled with two-ball clumps with an equivalent radius of 0.75m. A layer of small spherical particles with a radius five times smaller than the large particles was also placed across the vertical centre of the cave. A picture of the cave model is reproduced from [105] in Figure 5.3a and the migration results after 2.9% and 4.9% of the total volume has been removed are included in Figure 5.3b. The results of the cave draw analysis showed the most significant percolation of fines inside the draw zone. However, it appears in the results that a significant amount of percolation still occurs in the domain extremities where the larger particles do not move significantly.

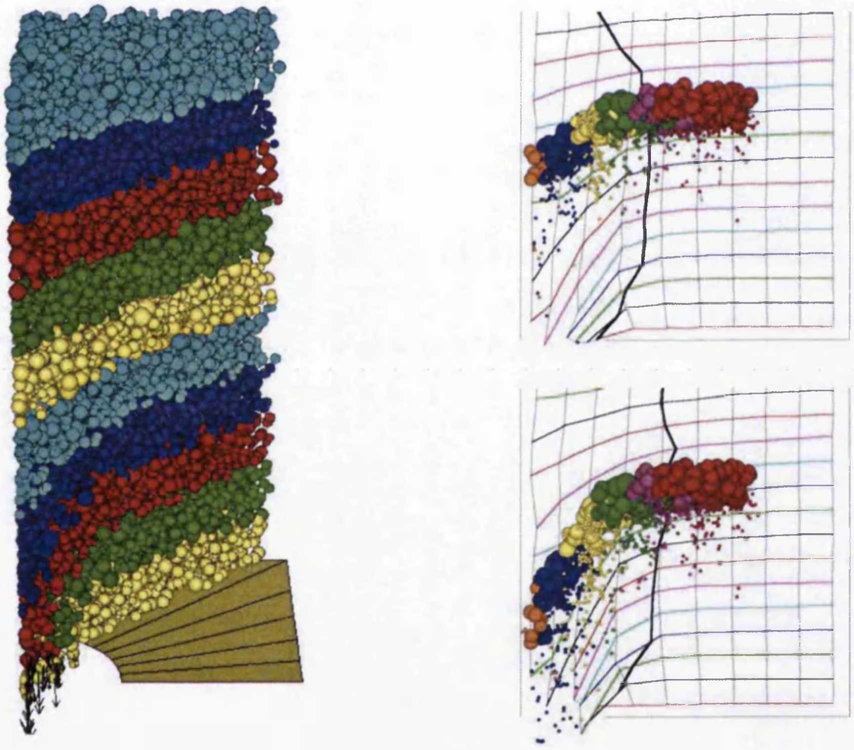

(a) (b)

Figure 5.3: Pictures reproduced from [105] showing (a) the quarter-symmetry cave draw model and (b) the relative movement of fines and their initial neighbours after (above) 2.9% of material has been drawn and (below) 4.9% of material has been drawn.

5.1.1 Percolation Through Circular Discrete Elements

After reviewing the work of Pierce, the cave draw analysis was replicated in an approximate fashion using the 2D LBM-DEM framework. The model domain, as shown in Figure 5.4a, measured $20\,m$ in width and $24m$ high and the outlet length was $7m$. The physical diameter of the 1100 discrete element blocks was normally distributed between $0.55\,m$ and $0.65m$. This is inclusive of a radial contact buffer of $0.025\,m$, meaning that the contact diameter of the particles ranged between $0.6m$ and $0.7m$. A Hertzian contact penalty was employed, in conjunction with normal, tangential and rotational contact damping ratios of 0.6, 0.3 and 0.3, respectively, and a friction coefficient of 0.2.

The fines domain was meshed with a D2Q9 lattice and a spacing of $0.05\,m$ resulting a grid size of 401×481 and approximately 1.9e05 nodes. The resolution with which the discrete elements were represented by the grid can be seen in Figure 5.4b. The LBM fines were modelled with a shear-thinning power law model and the parameters of Material C listed in Table 4.1 in Section 4.3.3. A gravitational body force of $9.81m/s^2$ was applied to the discrete elements and the fines. The draw of blocks and fines from the cave was simulated by the intermittent deactivation of discrete elements from the outlet. Atmospheric pressure boundary conditions were applied at the inlet and outlet of the LBM domain, and the walls were handled using the bounce-back condition.

The cave draw model was run for a period of seven intermittent draws and a total solution time of $20s$, during which 5% of the block material was removed from the domain. The total kinetic energy of the discrete elements was monitored to ensure that the cave was at steady state before the next draw was undertaken. Figure 5.5a is a contour plot of the y-direction displacement of the blocks at the conclusion of the simulation and Figure 5.5b highlights the deformation of the block layers. The movement of the blocks shows the emergence of a distinct draw zone which is orientated slightly to the right of vertical. Also of interest is the presence of a slip plane on the lower right side of the draw zone (see Figure 5.5a), where blocks move toward the draw point past a ridge of stationary material.

The movement of the fines phase during draw can be interrogated via the LBM velocity field. For example, Figure 5.6a plots the y-direction velocity of the fines after the first draw has taken place. The contour plot shows the movement of fines within the draw zone, which is induced by the collapse of blocky material into the draw point. Looking at the velocity distribution in more detail, Figure 5.6b is a vector plot of the fines' total velocity in the region just above the draw point. This picture highlights a *channel* of

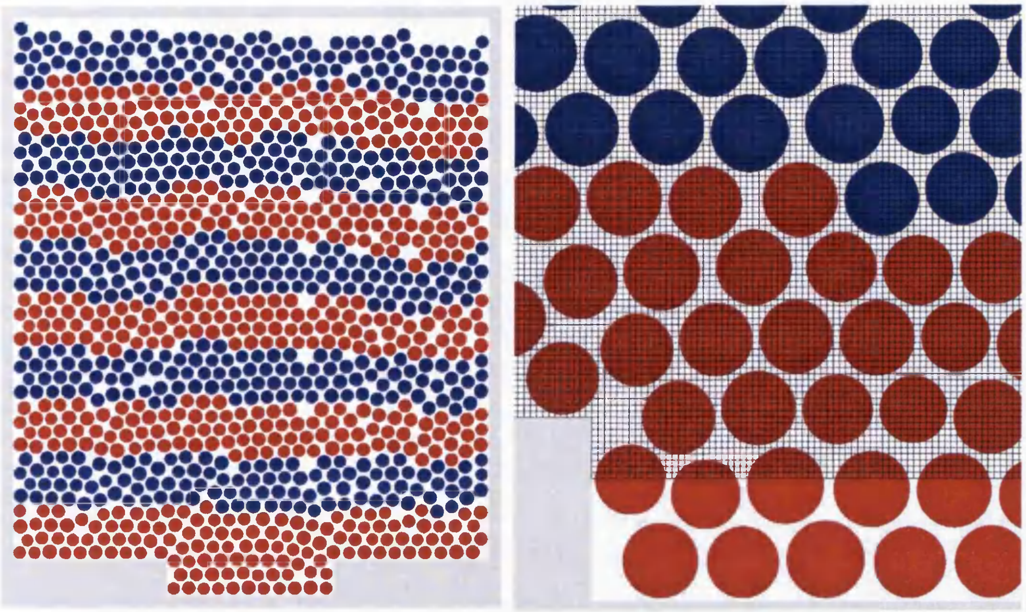
(a) (b)

Figure 5.4: The 2D LBM-DEM cave draw analysis showing (a) the analysis domain and DEM blocks and (b) the LBM grid overlaid on a section of the domain.

preferential fines flow, characterised by the consistently larger vectors, in which the material is moving faster than that adjacent to it. Interrogation of the results showed that these channels vary in location throughout the solution, as they are dependent on the movement of blocks in the region and the constant evolution of void spaces.

The rate of movement of the fines phase is indirectly governed by the rate of strain induced by draw. This is because the truncated power law model employed to characterise the fines as a non-Newtonian fluid alters the model viscosity by an amount dependent on the local rate of strain. Figures 5.7a and 5.7b plot the characteristic rate of strain in the LBM fines at two times during the first draw. The strain is induced by the relative movement of blocks as they collapse into the draw point. At $0.05\,s$ after draw the strain is localised to immediately above the draw point but at $0.15\,s$ after draw the region of strain can be seen to have branched to the left and right edges of the draw zone. The latter result indicates regions of high shear at the interface of the draw zone and the stationary blocks in the cave, which is an intuitive result. These regions of high shear lead to pseudoplastic *failure* of the fines (i.e. localised viscosity reduction) which promotes accelerated movement with respect to the adjacent blocks and fines. This result supports the hypothesis that regions of high shear lead to increased percolation of fines.

On their own, the displacement results for the blocks and the velocity results for the fines provide a good description of the draw zone but they do not quantify the amount of fines migration that occurred in the analysis. Instead, a post-processing technique that determined the relative movement of the fines and the blocks was required, which led to the development of a procedure called migration tracing. The migration trace is undertaken by first seeding the cave in its original configuration with a number of infinitesimal markers. These markers are placed in the voids between discrete elements which are filled with fines. The movement of these markers in the fines regime is then calculated by applying a finite difference scheme to integrate the fines velocity field both spatially and temporally as the solution progresses. The migration trace outputs the path of each marker over the course of the solution. This can be compared with the movement of adjacent blocks and the relative movement of the two can be quantified.

For this analysis three rows of twelve markers were placed in the cave as shown in Figure 5.8a, with Row 1 closest to the draw point, Row 2 in the middle and Row 3 at the top. The blocks that neighbour each marker in their original location are also shown. Figure 5.8b plots the results of the migration trace by showing the path of the markers and the final location of their neighbouring blocks. The contour scale indicates the y-direction displacement of the blocks in metres. In this figure, the amount of percolation that has occurred during draw is evidenced by the difference in the final location of the blocks and the markers. It can be seen that the amount of migration in Row 1 immediately above the draw point is minimal despite the movement of fines and blocks being greatest in this region. This result cannot be directly compared with the work of Pierce because migration information is only provided for the seam of fines at the middle of the domain. In the LBM-DEM analysis migration can be seen at both the middle and top rows of markers. At Row 2, the fines have moved on average 200% the distance of the blocks (i.e. twice as far) and at the top row the fines have moved approximately 150% the distance of the blocks. This compares well with the predictions of Pierce, which show the fines moving approximately 150% the distance of the blocks in the centre of the domain. On all three rows significant migration can be seen at the edge of the draw zone, in particular on the right side. This is caused by the shear thinning of the material model in the bands of high strain rate. The movement of fines outside the draw zone was found to be minimal. The results of this investigation support the hypothesis that fines migration is greatest in regions of high shear in the cave.

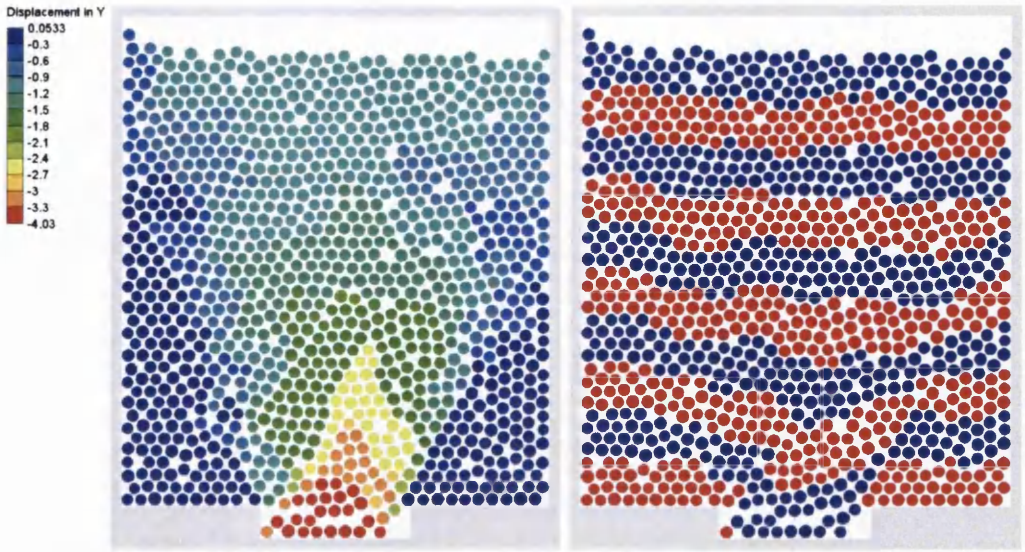

(a) (b)

Figure 5.5: The y-direction displacement of the discrete element blocks at the end of the analysis including (a) a contour plot of the vertical displacement and (b) the deformation of the original layers.

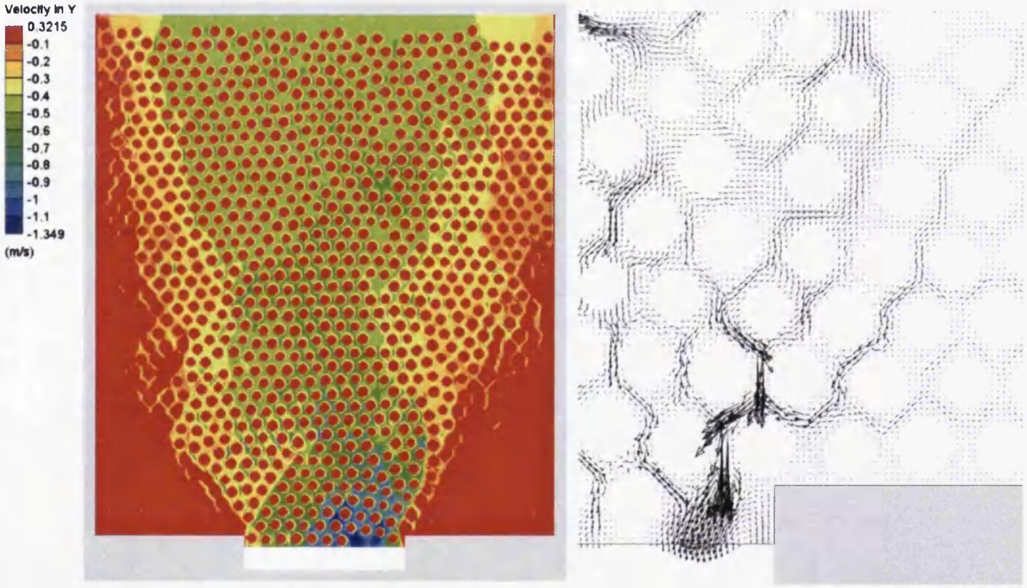

(a) (b)

Figure 5.6: The velocity of the LBM fines including (a) a contour plot of the y-direction velocity 0.2s after the first draw and (b) a vector plot of the total velocity 1.0s after the first draw.

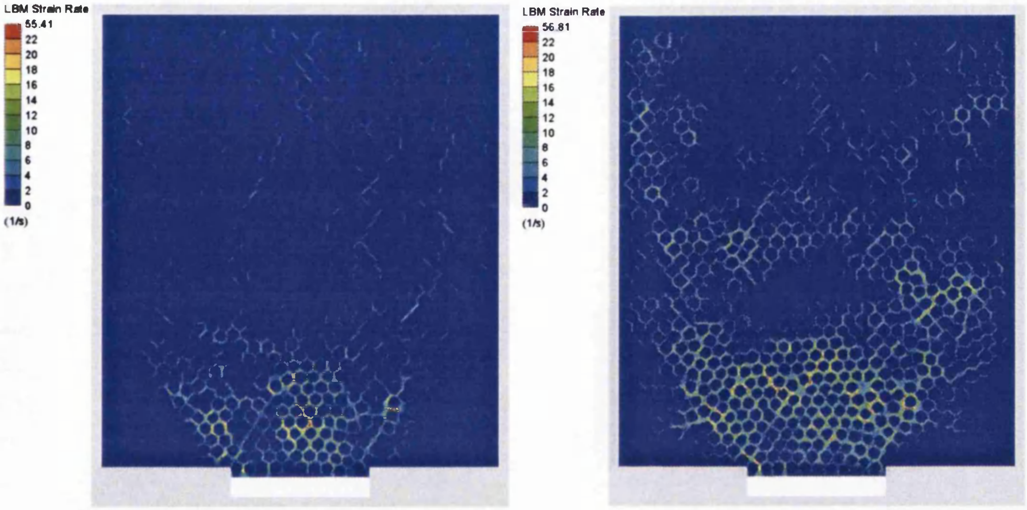

(a) (b)

Figure 5.7: Contour plot of the characteristic rate of strain in the LBM fines at (left) 0.05s after the first draw and (right) 0.15s after the first draw.

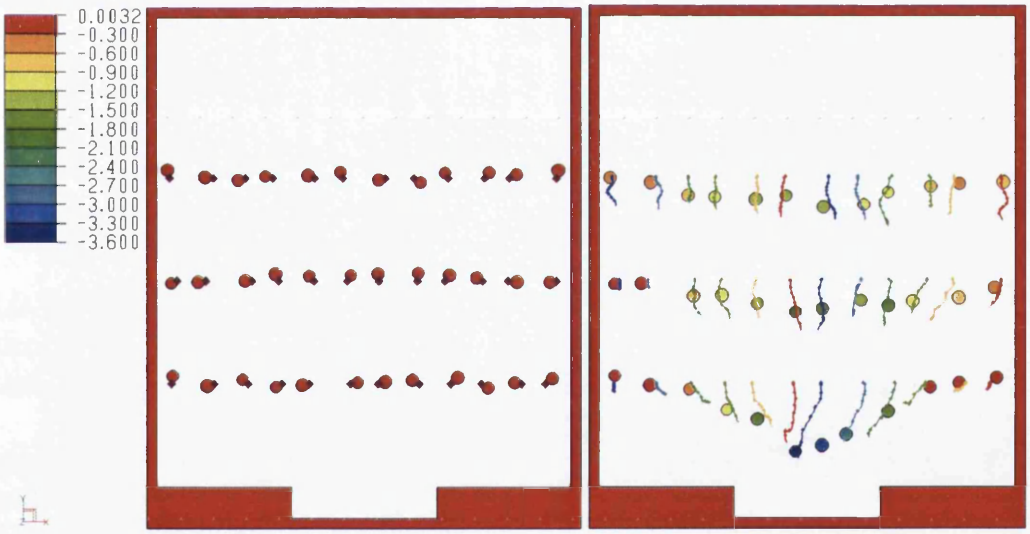

(a) (b)

Figure 5.8: Trace of the spatial fines migration throughout the 2D percolation analysis showing (a) the trace markers and their initial neighbouring blocks and (b) the relative movement of the markers and their neighbour blocks at the end of the analysis.

5.1.2 Percolation Through Polygonal Discrete Elements

To improve the representation of the cave blocks, the percolation test was then repeated using polygonal discrete elements in place of circular elements. Polygons offer angularity that cannot be achieved with single discs, however due to the added complexity in contact detection and resolution they are more computationally expensive. Four-sided elements were used in this analysis, with the size and shape normally distributed. The method of draw control was changed from instantaneous element deactivation to support relaxation over a period of one second. This provided a more realistic representation of the draw point excavation process. Also, the contact buffer was not used in this analysis because it was not implemented for polygonal elements. All other features of the simulation were identical to those described in Section 5.1.1.

The final configuration of the blocks can be seen in Figure 5.9a, which is a contour plot of their y-direction displacement. The displacement of the blocks clearly indicates the extents of the draw zone, and it can be seen that the use of polygons has resulted in a narrower draw zone than that which was predicted with circular discrete elements. The movement of the polygonal blocks was also found to be more stochastic than the circular ones and the settling time after draw was also greater for the polygonal blocks.

The fines velocity in the y-direction $0.1s$ after the completion of the seventh and last draw can be seen in Figure 5.9b. The narrower draw zone highlighted by the block displacement is also evident in the plot of fines velocity. In this figure the zone of fines movement is shown to be much narrower than that found using circular elements, and as a consequence of the block movement it is noticeably biased to the right of the domain.

Figure 5.10a is a contour plot of the characteristic rate of strain in the LBM fines $0.5s$ after the completion of the seventh and final draw. As in the circular element analysis, the regions of highest shear can clearly be seen on the left and right edges of the draw zone.

Finally, Figure 5.10b plots the results of the migration trace for the polygonal element analysis. The comparison of the final location of the markers and the blocks shows almost no percolation of the fines through the blocks. This result was not entirely unexpected as the contact buffer for increasing 2D porosity has not been used in this analysis. In fact, close inspection of the structural field revealed some regions where the blocks had packed in way that resulted in effectively zero porosity. This problem could be overcome by implementing the contact buffer for polygons, which is considerably more complex than for circular elements, but this would still not overcome the inherent limitations of 2D analyses.

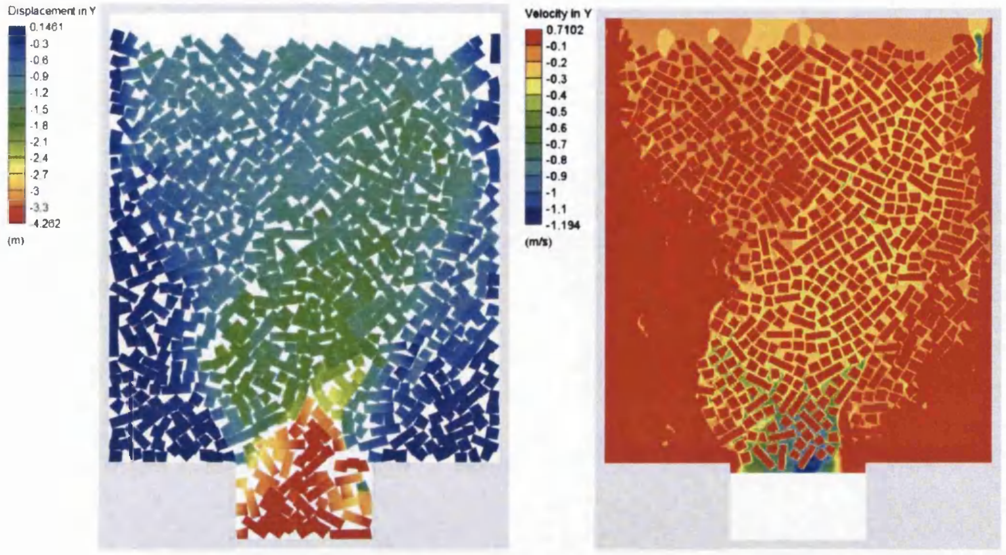

(a) (b)

Figure 5.9: Results of the 2D percolation analysis using polygonal discrete elements showing (a) a contour plot of the y-direction displacement of the blocks at the end of the analysis and (b) a contour plot of the y-direction velocity of the fines 0.1s after the completion of the last draw.

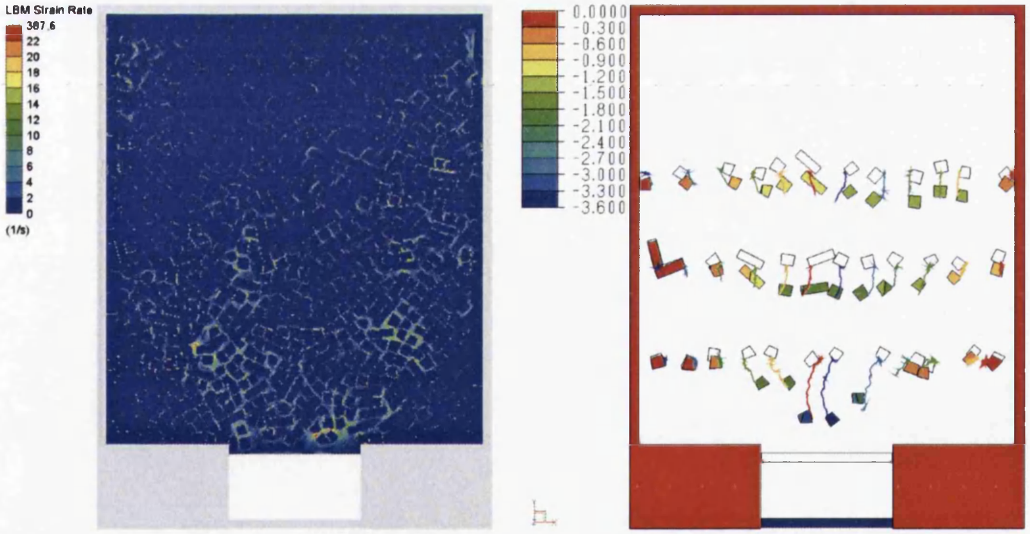

(a) (b)

Figure 5.10: Results of the 2D percolation analysis using polygonal discrete elements showing (a) a contour plot of the characteristic rate of strain in the LBM fines 0.5s after the completion of the last draw and (b) the results of the migration trace.

5.2 Field Scale Block Cave Analysis

Following the cave percolation analyses the two-dimensional LBM-DEM framework was applied in a field-scale cave simulation. A geometry was created that included some of the relevant features of an actual cave, as shown in Figure 5.11. The three-bell cave measured $35\,m$ wide and $20m$ high and the outlet draw points were $3.5\,m$ wide and spaced at $8.5m$ centres. The profile of the pillars and the rugosity of the cave walls were chosen arbitrarily. Circular discrete elements with a normally distributed diameter range between $0.46\,m$ and $0.56m$ were employed to represent the cave blocks. This is inclusive of a radial contact buffer of $0.02\,m$, meaning that the contact diameter of the particles ranged between $0.50m$ and $0.60m$. As an additional, arbitrary feature to the model, a vertical seam of smaller elements was included in the cave. These particles were assigned a physical diameter range between $0.36\,m$ and $0.46m$ and the same radial contact buffer of $0.02\,m$. The seam of smaller particles can be seen above the right pillar in Figure 5.12. The discrete element contact properties used in the analysis were identical to those in the percolation analyses.

The LBM fines grid spacing used was $0.05\,m$ resulting in a grid size of 427×711. The implementation of the LBM allowed the basic rectangular domain to be optimised so that only the nodes inside the cave boundary were processed. This *trimming* of the LBM domain resulted in a total of approximately 2.5e05 nodes. The LBM fines were again modelled with a shear-thinning power law model and the parameters of Material C in Table 4.1. A gravitational body force was applied to the discrete elements and the fines and atmospheric pressure boundary conditions were applied at the inlet and outlet of the LBM domain.

The three-bell cave analysis was run for seven draws and a total time of $20s$. The draw of blocks and fines from the cave was handled by the intermittent relaxation of the supports over a period of one second at each outlet. The draw sequencing was chosen randomly to be left, middle, right, left, middle, middle, left as shown in Figure 5.11. This resulted in three draws from both the left and middle draw points and one from the right one.

As in the percolation analyses the behaviour of the cave blocks and fines during and after draw was interrogated by displacements and velocities. Figure 5.12 is a contour plot of the y-direction displacement of the discrete element blocks at the conclusion of the simulation. Of greatest interest in this figure is the interactive zone that can be seen above the left pillar, between the left and middle draw points. This interaction has resulted in the material above the pillar descending further in the cave than that directly above the draw points, which is a common gravity flow phenomenon. The influence of the cave wall roughness is evident in the limited block movement adjacent the walls. Also, the seam of smaller blocks appears to have influenced the shape of the draw zone above the middle draw point as a discontinuity in the block displacement can be seen on the right edge of the seam.

Figures 5.13 and 5.14 are contour plots of the y-direction fines velocity at the end of the first draw and second draw, respectively. In the first plot, a relatively narrow band of fines movement can be seen extending from the draw point into the cave at an angle of approximately 45° to the right. In the second plot the draw is more evenly distributed throughout the draw zone above the draw point. However, the seam of smaller blocks can be seen to influence the movement of fines at the right hand side of the draw zone by restricting the speed of the fines in this area. This suggests that, intuitively, the migration of fines is reduced in regions of smaller blocks where the void space is smaller.

Figures 5.15 and 5.16 plot the characteristic rate of strain in the LBM fines at the end of the first and second draws, respectively. The effect of the channel of fines movement above the left pillar (see Figure 5.13) can be seen in the first plot. A band of high shear has been generated in the same location, which would promote increased migration due to the shear-thinning characteristics of the material model. The second plot shows regions of high shear in the draw zone above the middle draw point.

The migration trace of the three-bell cave analysis was undertaken using three rows of markers (24 at the top, 22 at the middle and 20 at the bottom). The results of the fines migration trace for this example can be seen in Figure 5.17. Unlike the percolation analysis reported in Section 5.1.1, minimal migration can be seen in the three-bell cave at the top and middle rows. Instead, the greatest amount of migration in this analysis can be seen in the bottom row above the left and middle draw points, which undergo the largest amount of draw. In these areas the fines moves approximately 150% the distance of the blocks. This result is again in contrast to the percolation analysis in which minimal migration was seen directly above the outlet. The differences in the qualitative results could be attributable to a number of differences in the two analyses such as cave geometry, draw technique (relaxation rather than deactivation) and material properties.

The quantitative and qualitative outcomes of the two-dimensional analyses have highlighted the potential of the coupled code for application in fines migration investigations. However, due to the three-dimensional nature of the percolation phenomenon, it is probable that 3D analyses would be better suited to capture fines migration behaviour in a block cave.

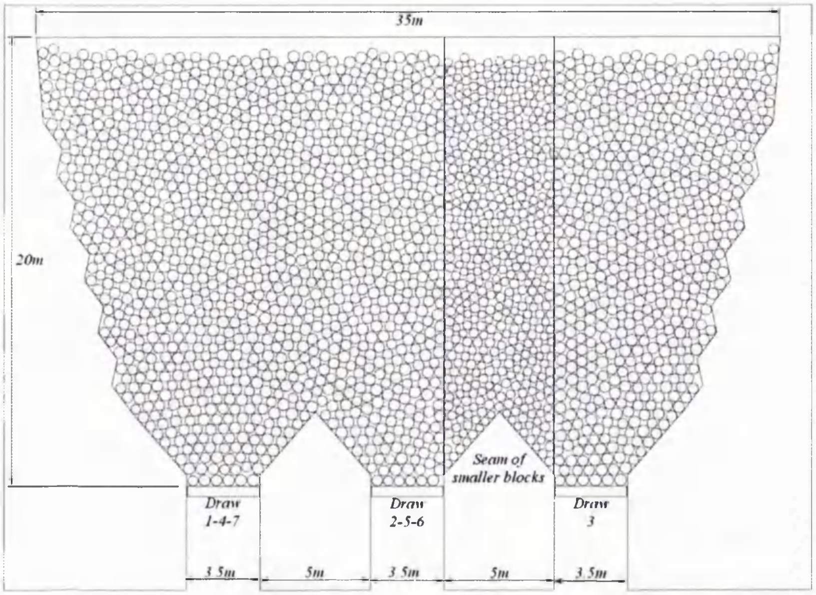

Figure 5.11: The geometry and relevant features of the three-bell cave analysed using the two-dimensional LBM-DEM framework.

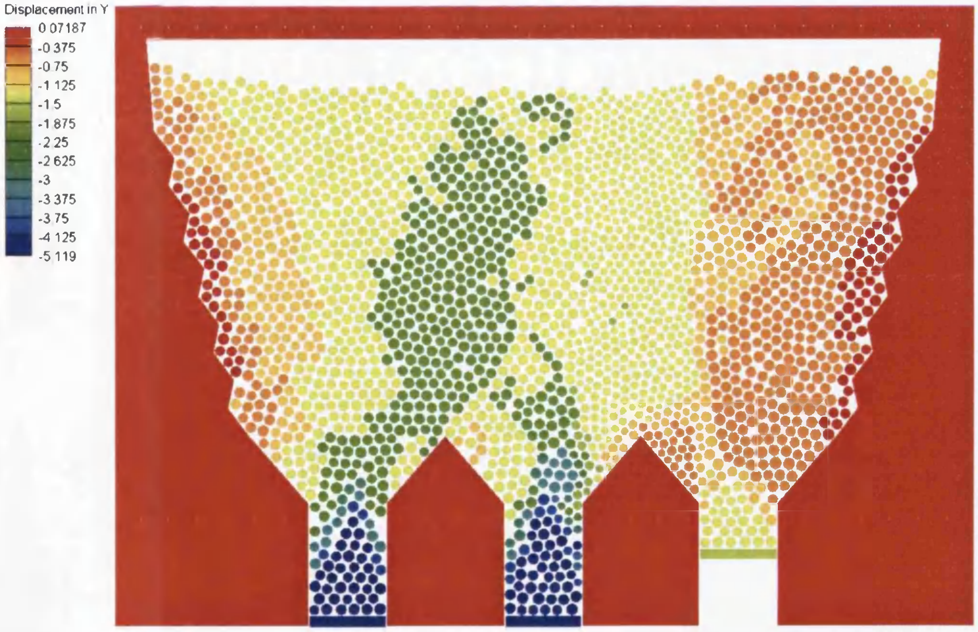

Figure 5.12: Contour plot of the y-direction displacement of the discrete element blocks at the end of the analysis. The interactive zone above the left pillar can be seen.

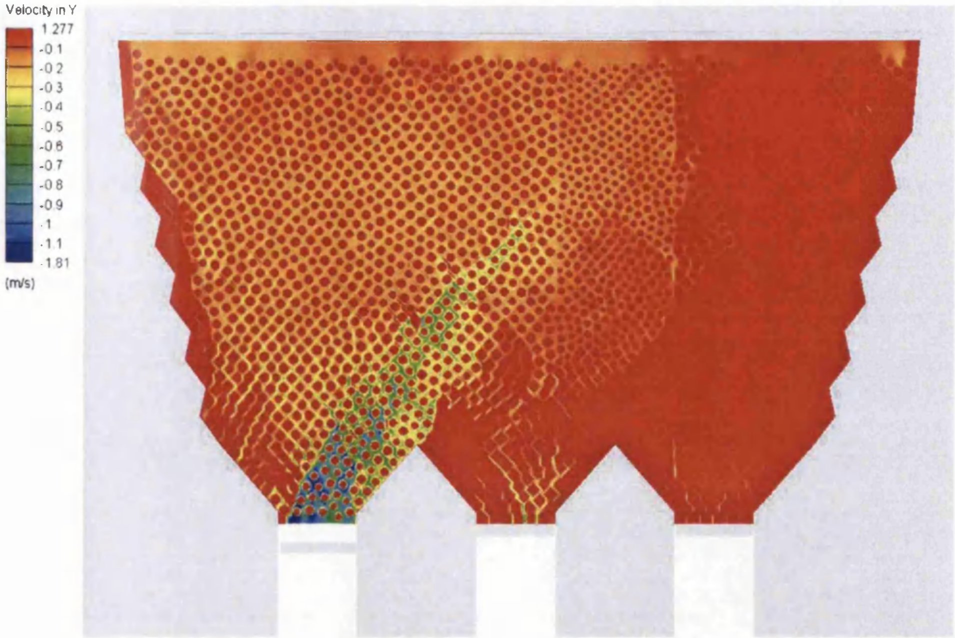

Figure 5.13: Contour plot of the y-direction velocity of the fines at the end of the first draw. The movement of fines appears to be in a band strongly biased to the right.

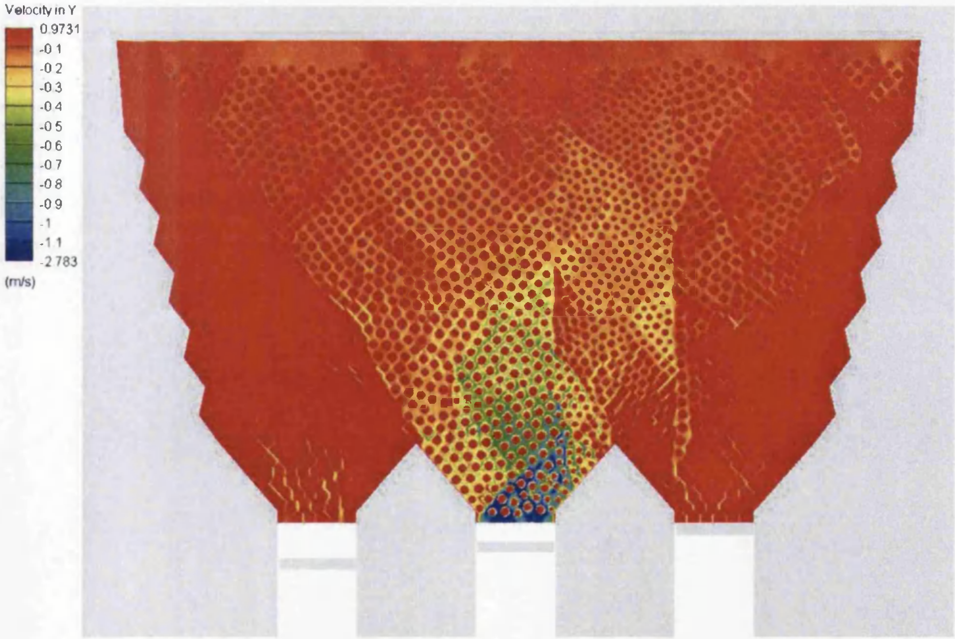

Figure 5.14: Contour plot of the y-direction fines velocity at the conclusion of the second draw, showing the restriction caused by the smaller blocks.

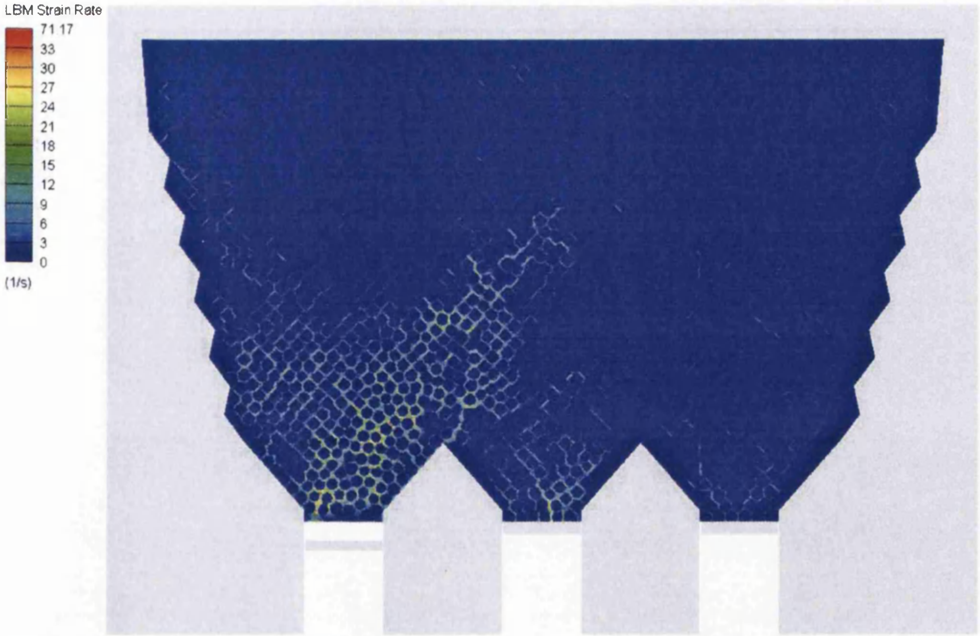

Figure 5.15: Contour plot of the characteristic rate of strain in the fines at the end of the first draw. The channel of fines movement (see Figure 5.13) has resulted in a band of high shear.

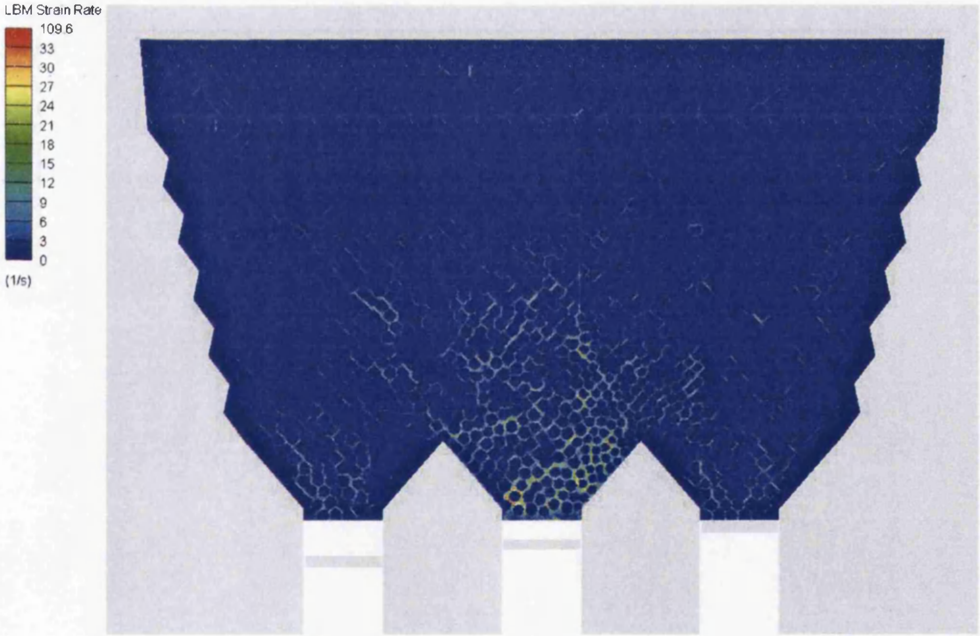

Figure 5.16: Contour plot of the characteristic rate of strain in the fines at the end of the second draw.

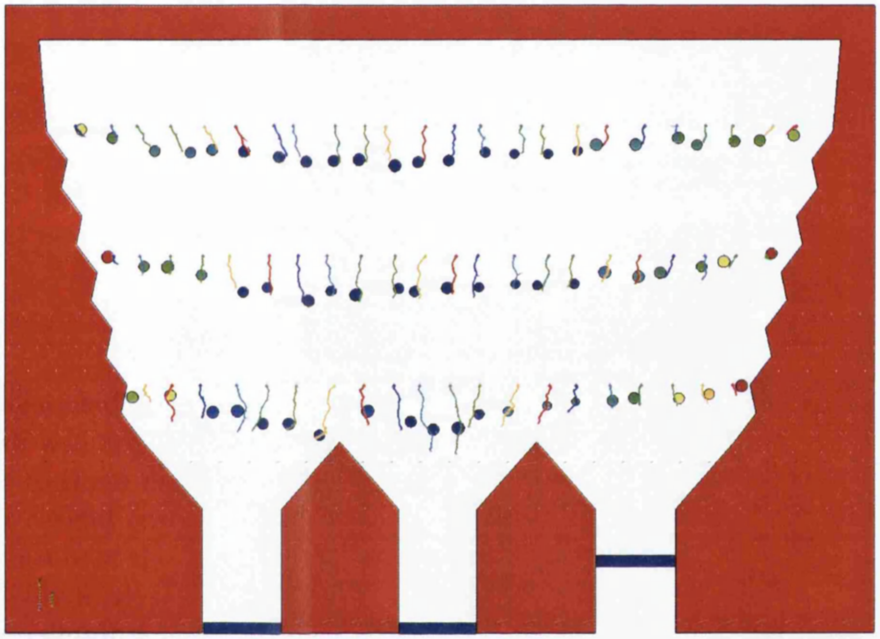

Figure 5.17: Results of the migration trace for the three-bell cave analysis.

CHAPTER 6

THREE-DIMENSIONAL APPLICATIONS OF THE LBM-DEM FRAMEWORK

Upon completion of the expansion to three dimensions the LBM-DEM framework was applied in moderate scale percolation and migration problems similar to those described in Chapter 5. The analysis of 3D problems necessitated careful consideration of the computational requirements due to the serial nature of the framework code. In general the size of problem that could be reliably analysed was constrained by memory. Whilst three-dimensional lattices contain a much greater number of nodes than their 2D counterparts, in making the transition from D2Q9 to D3Q15 they also increase the number of floating point values at each node from nine to fifteen. This limitation was partially mitigated by employing 64-bit hardware which increased the available memory from 2GB to 4GB.

The three-dimensional problems presented in this chapter include a replication of the percolation analysis undertaken by Pierce [105] and the simulation of a block cave section with two draw points. Almost all of the analysis techniques described in Chapter 5 are carried over to these problems and the results are again interpreted in terms of displacements and velocities of the blocks and the fines. The 3D nature of the results, particularly the fines phase, required some new post-processing techniques to aid the visualisation of the analysis outcomes.

6.1 Replication of DEM Percolation Tests

As in Chapter 5 the cave draw analysis undertaken by Pierce was replicated in an approximate fashion. The aforementioned memory constraints meant that the linear dimensions of the model were approximately three times smaller than the original analysis. The quarter-symmetry model domain, as shown in Figure 6.1a, measured $6m$ in width and depth and $12m$ high. The circular outlet at the bottom of the domain had a radius of $2.5m$. The domain was filled with 2000 spherical discrete element *blocks* whose diameter was normally distributed between $0.55m$ and $0.65m$. Due to the naturally occurring void space between the 3D blocks the contact buffer was not required to increase the permeability of the structural field. To govern the DEM contact between the blocks, a Hertzian penalty was employed, in conjunction with normal, tangential and rotational contact damping ratios of 0.6, 0.3 and 0.3, respectively. The block density was $2000kg/m^3$ and the friction coefficient for block-block contact was 0.1 and for block-wall contact was 0.3.

The fines domain was meshed with a D3Q15 lattice and a spacing of $0.05m$. This resulted in a grid size of $121 \times 121 \times 241$ and a total of approximately 3.5e06 nodes. Figure 6.1b plots the wire frame of the LBM grid over the discrete elements, indicating the resolution with which they were represented by the lattice. A body force of $9.81m/s^2$ was applied to the discrete elements and the fines to simulate gravity. Boundary conditions at the walls were handled using the bounce-back condition and at the inlet and outlet they were modelled using atmospheric pressure constraints.

The LBM fines were modelled with a shear-thinning power law model, and in this analysis the influence of the fines material properties was investigated. Two material types were tested and the fines migration behaviour of each was compared. The first analysis employed the parameters of Material C as listed in Table 4.1 in Section 4.3.3. The parameters of the second analysis included an initial viscosity, ν_{in}, and relaxation parameter, τ_{in}, of $0.0833m^2/s$ and 0.55, respectively. In conjunction with the lattice spacing this resulted in a LBM time step of 5e-04s. The consistency constant, ν_0, and the power law index, n, were set at $0.1668m^2s^{n-2}$ and 0.3, respectively. The power law truncation limits on the relaxation parameter were set at $\tau_{min} = 0.51$ and $\tau_{max} = 1.5$. The bulk density of both material types was $1000kg/m^3$.

The second set of fines material properties used in this investigation are from here on referred to as Material D. The objective of the parameters chosen for this material was to create a material with a plastic viscosity that was lower than the value of $30Pa.s$ for Material C, yet not as low as the almost cohesionless Leighton Buzzard sand. To enable a direct comparison of the viscoelastic response of these three materials, Material D was tested

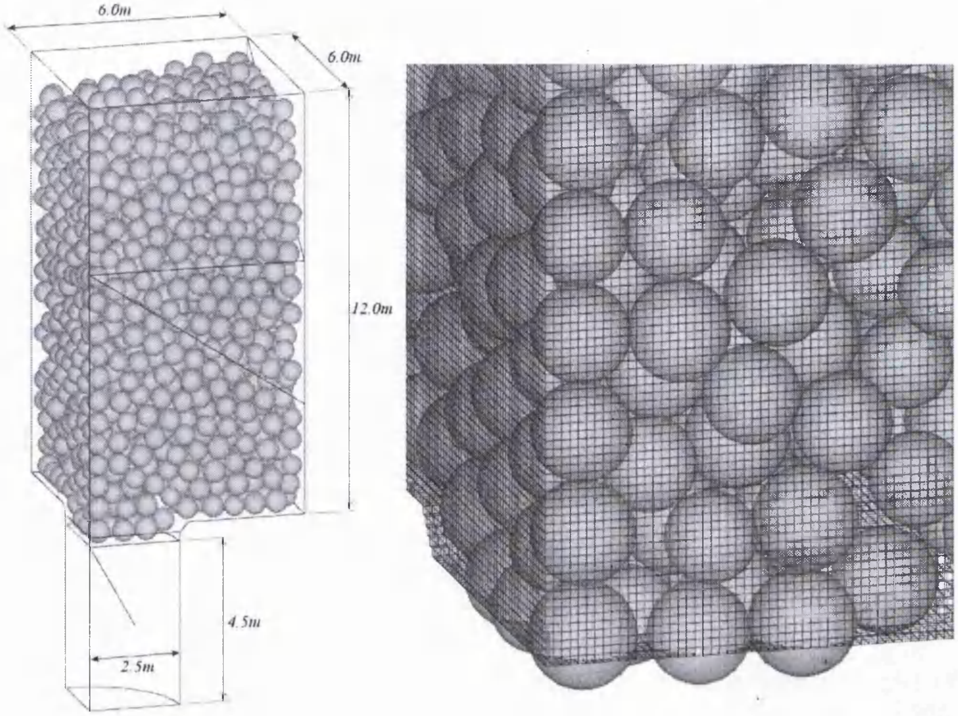

(a) (b)

Figure 6.1: The 3D LBM-DEM cave draw analysis showing (a) the domain and DEM blocks and (b) the LBM grid overlaid on a section of the domain.

in the numerical rheometer described in Section 4.3.3. Figure 6.2 graphs the instantaneous viscosity of the three materials against strain rate. In comparison to Material C, it can be seen that at high strain the viscosity of Material D is lower at approximately $23 Pa.s$. It it is also evident that the transition to the ultimate viscosity is more gradual in Material D than Material C.

As in the 2D analyses, 5% of the block volume was removed from the domain. This was achieved by lowering the support at the cave outlet a total of 4.5m over a period of $9s$ within a total solution time of $10s$. Due to differences in the initial viscosity and relaxation parameter, Material C and D required LBM time steps of 2e-04s and 5e-04s, respectively. Consequently, the explicit sub-cycling number was different for each solution, as shown in Figure 6.3. In this graph it can be seen that the larger LBM time step of Material D generally necessitates a larger sub-cycling number to maintain synchronisation with the DEM time step. The ability of the coupled framework to dynamically update the sub-cycling number, as the DEM time step changes with the state of the structural field, is also evident.

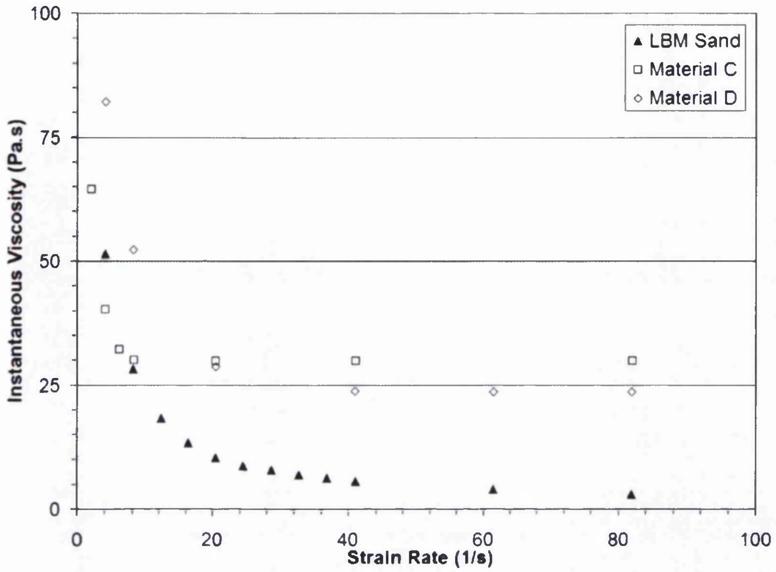

Figure 6.2: Graph of the instantaneous viscosity against strain rate for Leighton Buzzard sand, Material C, and Material D, as tested in the numerical rheometer.

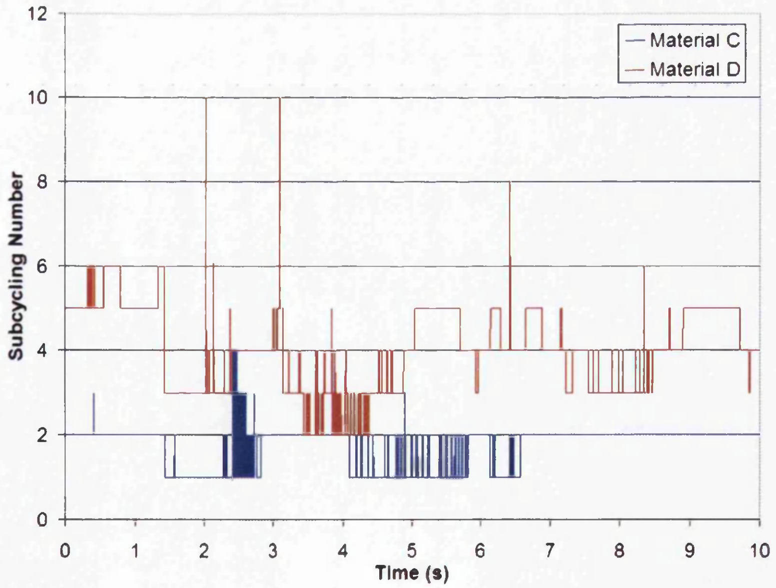

Figure 6.3: Graph of the sub-cycling number, which relates the time step of the LBM and DEM explicit schemes, throughout the solution for both Material C and D.

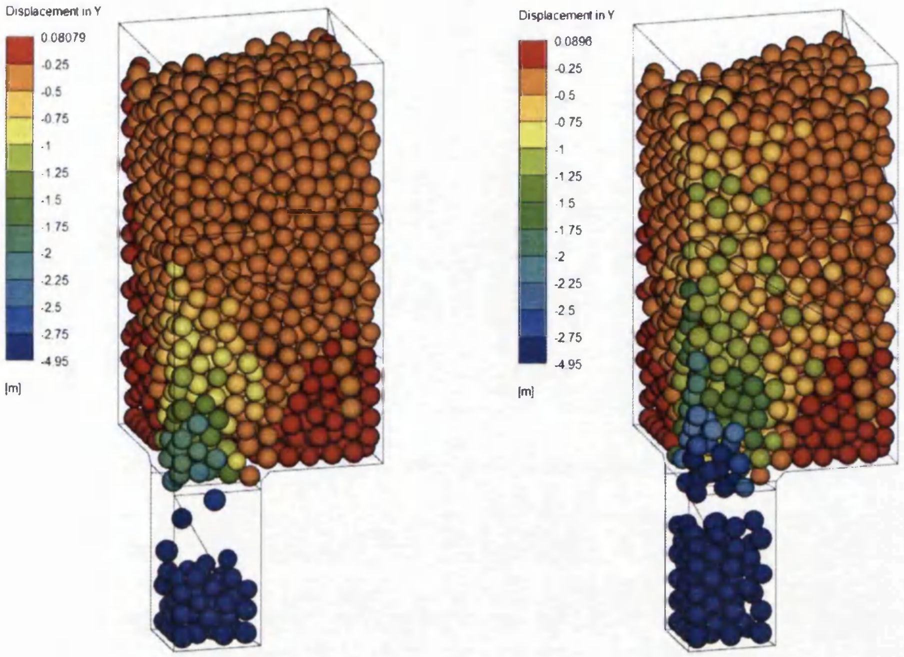

(a) (b)

Figure 6.4: Results of the 3D percolation analysis showing contours plot of the y-direction displacement of the blocks at the end of the analysis for (a) Material C and (b) Material D.

Figures 6.4a and 6.4b are contour plots of the y-direction displacement of the blocks at the end of the simulation. The draw zone, within which material is moving toward the outlet, can be seen. At the top of the domain the draw zone has reached the outer boundaries, which is a consequence of the computational limitations of the serial LBM-DEM framework. Ideally, the ratio of the domain dimensions and the block diameter would be greater, thereby allowing the draw zone to remain isolated from the domain boundaries. The most obvious observation that can be made from these figures is that neither solution is at equilibrium. At the end of both analyses blocks are continuing to collapse into the draw point, meaning that less than the intended 5% of material has been drawn from the model. This phenomenon is more pronounced for Material C than D, and can be explained by the difference in high-strain viscosity of the two. The plastic viscosity of Material C is higher than that of Material D, meaning that the resistance to block movement caused by the fines is greater. This is exacerbated in both cases by mechanical resistance to block movement at the domain outlet, which is a consequence of the outlet radius being equivalent to only five block diameters.

The interrogation of the fines velocity is more difficult in 3D than 2D and therefore post-processing techniques are required that are more complicated than basic contour plots of the visible surfaces. In fact, an array of visualisation tools, including cut planes, single and multiple isosurfaces, and moving slices, is required to adequately gain insight into the 3D movement of fines. As an example, Figures 6.5a and 6.5b plot the y-direction velocity of the fines for Material C and D, respectively, on the yz-plane. These contour plots were captured after $3.5s$ (approximately 35% of draw) with the location of the cut plane $0.3m$ from the front boundary of the domain. From comparison of these figures it can be seen that a greater amount of fines is moving, some with greater velocity, with Material D. This can be explained, like the greater movement of blocks, by the lower plastic viscosity of the material model which has undergone more thinning under shear.

The difference in fines movement for the two materials can also be highlighted by an isosurface plot, as shown in Figures 6.6a and 6.6b. The isosurfaces in these figures display the regions of material that have a y-direction velocity of $-0.3m/s$, and as expected a greater amount of fines movement can be seen for Material D. An important advantage of the isosurface plot is that it is able to highlight *channels* of preferential fines flow at an instant throughout the entire domain. This performs the same role as the total velocity vector plots in two dimensions. The regions of preferential flow are a major contributor to the percolation of fines through the blocks in the cave. The random size and distribution of these *channels*, particularly in Figure 6.6b, highlight the stochastic nature of the fines migration phenomenon.

The relative movement of the fines and blocks in the two percolation analyses was investigated using the migration tracing procedures described in Section 5.1.1. The domain was seeded with three rows of ten markers which ran diagonally from the centre to the corner furthest from the outlet. Row 1, which was closest to the draw point, was placed one quarter of the way up the domain while Row 2 and Row 3 were placed one half and three quarters of the way up, respectively. Figure 6.7a plots the migration trace results for Material C and Figure 6.7b plots the migration trace results for Material D. Both figures show the initial and final location of the blocks that neighbour each marker as well as the path of the fines markers. The y-direction displacement of the blocks in metres is shown in the contour.

From the results of the trace for Material C it can be seen that some migration exists at third and fourth markers on Row 1. In this area, which is coincident with the edge of the draw zone, the fines move approximately 150% of the distance of the blocks. There is only minimal fines movement outside the draw zone on Row 1. Significant fines percolation can be seen on Row 2 inside the draw zone, especially directly above the outlet. At

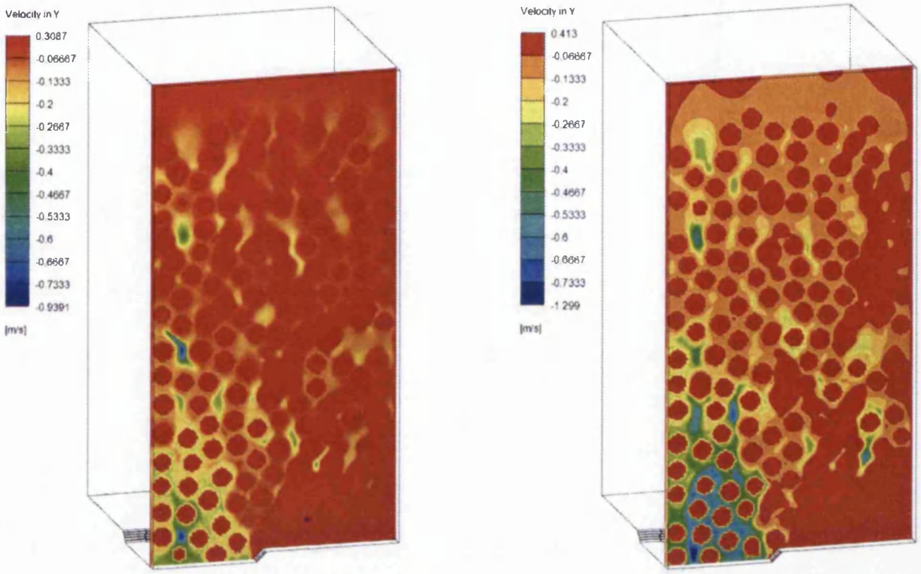

(a) (b)

Figure 6.5: Contour plot of the y-direction fines velocity midway through the cave draw for (a) Material C and (b) Material D. The slice of the fluid domain is located $0.3m$ from the front boundary.

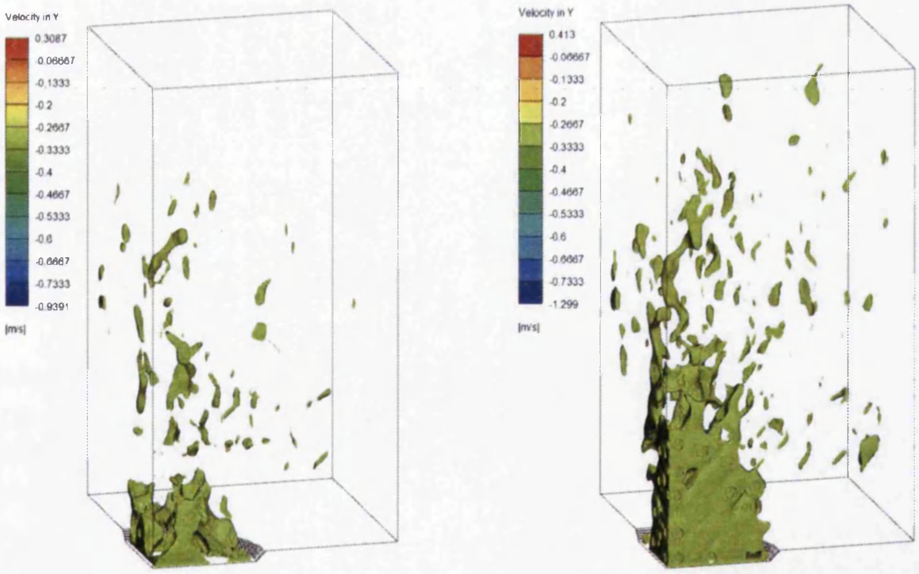

(a) (b)

Figure 6.6: Isosurface plot of the y-direction fines velocity midway through the cave draw for (a) Material C and (b) Material D. The velocity magnitude of the isosurface is -0.3m/s.

the first marker the fines has moved approximately 250% the distance of the neighbouring block which suggests that a wide *channel* of fines flow exists at this location. At the third marker the fines has descended twice as much as the block despite both moving considerably less than at the first marker. Interestingly, migration can also be seen at the eighth and ninth markers, which are well outside the draw zone. Lastly, only a small amount of migration can be seen at Row 3. This is possibly a consequence of the small amount of block movement and relatively even draw at this height.

The results of the migration trace for Material D display similar characteristics to those for Material C but the amount of percolation is generally greater. On Row 1, the first and second markers move further than for Material C due to the greater amount of draw. However, they do not move further than their neighbouring blocks and therefore there is no migration. The same percolation can be seen on the edge of the draw zone and the third and fourth markers however the *relative* movement is actually less than it is for Material C. Again, only negligible migration can be seen outside the draw zone. On Row 2, the same migration above the outlet can be seen, with the fines moving approximately 250% the distance of the blocks at the first and third markers. Although the magnitude of fines and block movement is greater for Material D the relative movement is approximately the same. At the eighth and ninth markers the percolation seen in Material C is again evident but in greater magnitude. Despite being outside the draw zone, the rearrangement of blocks and the evolution of voids has allowed a channel of fines flow to be created. This in turn has allowed significant migration to occur, which is significant because at this location the amount of block movement is minimal. At Row 3 percolation can be seen at the second and sixth markers, both of which are inside the draw zone. At these locations the fines move approximately 250% the distance of the blocks. At other locations on this row migration is negligible.

It should be noted that the analysis of Material C and D employed the same initial structural field. The similar characteristics of the migration traces for the two materials suggest that the arrangement of the discrete element blocks and voids has a strong influence on the behaviour of fines during draw. This acts in conjunction with the fines materials properties to govern the magnitude and location of migration in the cave. The results of the percolation analyses also suggest that definitive rules governing the level of migration throughout the domain do not exist. Whilst migration typically occurred inside the draw zone, a number of exceptions to this observation were found. No migration was found at some locations within the draw zone whilst migration was found at a small number of locations outside the draw zone. This suggests, perhaps intuitively, that fines migration is a

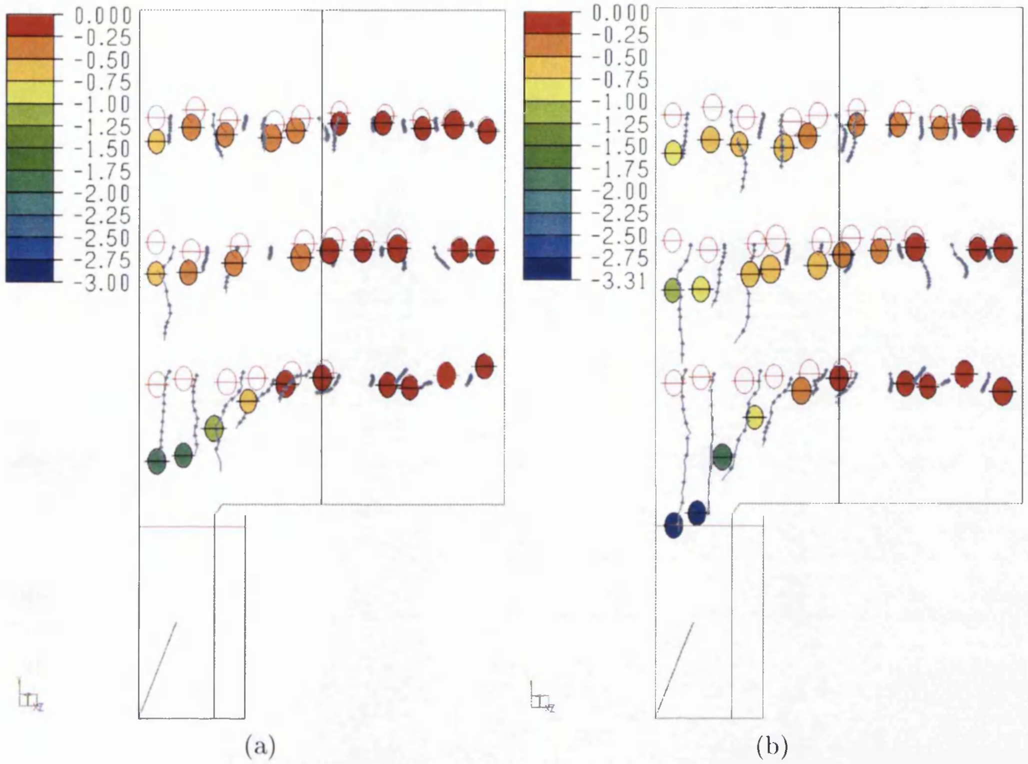

(a) (b)

Figure 6.7: The results of the migration trace for (a) Material C and (b) Material D, in the 3D percolation analysis. The y-direction displacement $[m]$ of the neighbouring blocks is shown in the contour.

highly stochastic phenomenon which is sensitive to subtle differences in the arrangement of blocks within the cave. Nevertheless, general trends can be seen in these results that are consistent with the work of Pierce [105], which showed greatest migration inside and on the fringes of the draw zone.

6.2 Partial Block Cave Analysis

Following the three-dimensional percolation analyses the LBM-DEM framework was applied in a moderate-scale cave simulation. The computational limitations of the serial code implementation were of even greater significance in this investigation due to the physical size of a fully developed block cave. Figure 6.8a is a schematic representation of a well developed block cave, showing the development and production level tunnels and the caved ore body. It is clear from this picture that the linear dimensions of the mine can be of the order of hundreds of metres and therefore, even if distributed computing is available, the model domain must be chosen carefully. In addition, the

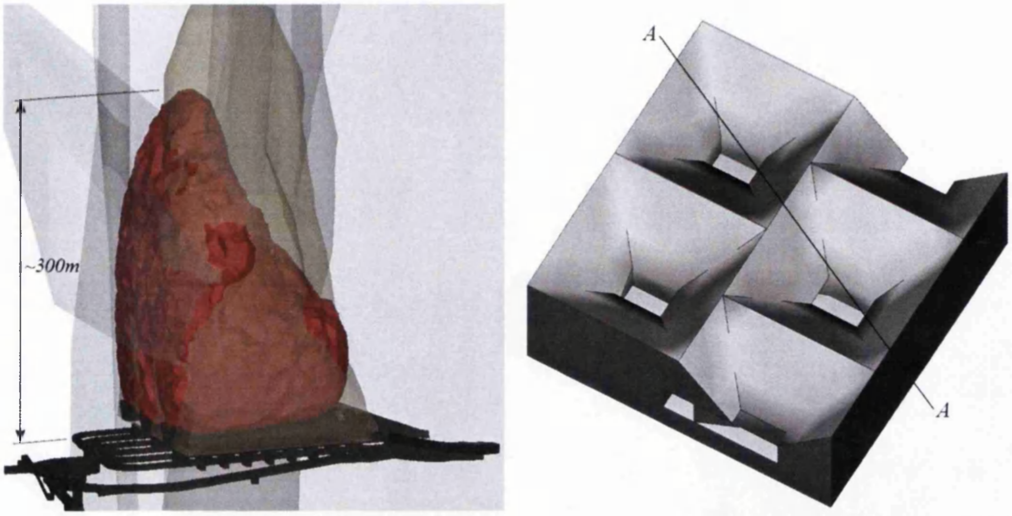

(a) (b)

Figure 6.8: Schematic representation of a block cave including (a) the extents of a well-developed mine showing the tunnel network and the caved ore body, and (b) an array of draw bells showing the section A-A that is used in the partial block cave analysis.

best location within the cave for capturing fines migration is not an automatic choice, and requires a degree of engineering judgement. Figure 6.8b is a schematic diagram of an array of draw bells at the production level. In this investigation the model domain was chosen to follow the section A-A, thereby incorporating the interaction of two adjacent draw points. By choosing a domain that includes the draw bell outlet the removal of blocks can be controlled and the region of greatest block dynamics, and therefore void evolution, is captured.

From section A-A shown in Figure 6.8b a 3D, partial block cave geometry was created. The profile of the domain was similar to that used in the the 2D cave analysis however due to computational limitations only a thick *slice* of the draw bells could be incorporated. The geometry and dimensions of the 3D model can be seen in Figure 6.9a. The two-bell cave measured $15\,m$ wide, $10m$ high and $2m$ deep and the outlet draw points were $2.5\,m$ wide and spaced $5.5m$ apart. The profile of the pillars and the rugosity of the cave walls were chosen arbitrarily. The cave blocks were modelled using circular discrete elements with a normally distributed diameter range between $0.40\,m$ and $0.50m$. The block density and discrete element contact properties used in this analysis were identical to those in the 3D percolation analyses, and the contact buffer was not employed.

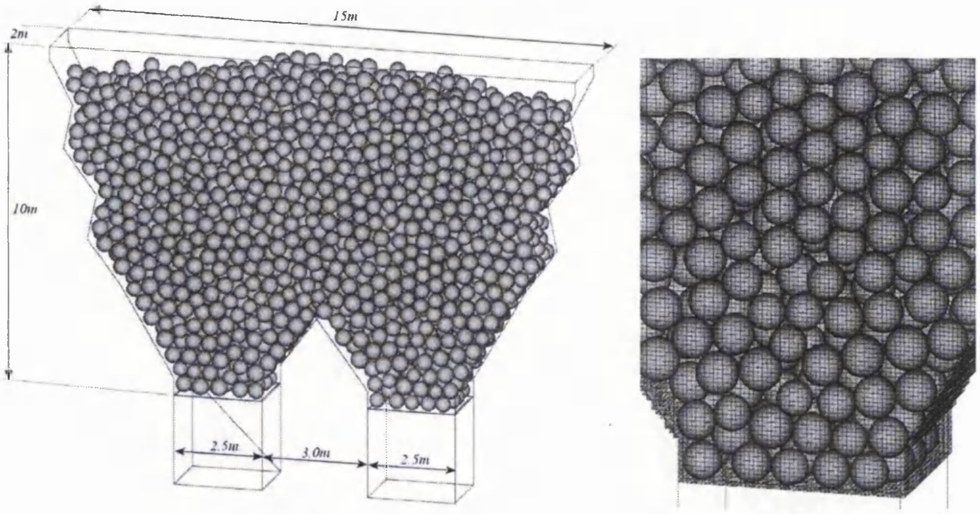

(a) (b)

Figure 6.9: The 3D LBM-DEM partial block cave analysis showing (a) the domain and DEM *blocks* and (b) the LBM grid overlaid on a section of the domain.

The fines domain was meshed with a D3Q15 lattice and a spacing of $0.05m$. This resulted in a grid size of $301\times201\times41$ and a total of approximately 2.5e06 nodes. Optimisation, or *trimming*, of the orthogonal domain reduced the number of processed nodes to 1.9e06. Figure 6.9b plots the wire frame of the LBM grid over the discrete elements, indicating the resolution with which they were represented by the lattice. A body force of $9.81m/s^2$ was applied to the discrete elements and the fines to simulate gravity. Boundary conditions at the walls were handled using the bounce-back condition and at the inlet and two outlets they were modelled using atmospheric pressure constraints.

In the 3D percolation analyses in Section 6.1 the sensitivity to fines properties was investigated by comparing the migration results of Material C and D. In this investigation, however, the fines properties are kept constant and the shear-thinning power law model is employed solely with the parameters of Material D. Instead of testing the response to different material properties, the partial block cave model was used to investigate the effect of draw strategy on percolation. Two analyses were undertaken with the first employing isolated draw and the second employing interactive draw. A total of six draws was executed in both analyses over a total solution time of $9\,s$. As in previous fines migration and percolation models the draw of blocks and fines from the cave was handled by the intermittent relaxation of the supports over a period of one second at each outlet

The draw sequencing in the isolated investigation featured three consecutive draws from the left draw point followed by three from the right draw point. This can be seen in Figure 6.10, which includes contour plots of the y-direction displacement of the blocks after the first three draws and at the end of the simulation. After the first three draws a distinct draw zone can be seen above the left draw point, and by repeatedly drawing from the same location a shear plane is created between the draw zone and the surrounding material. In the interactive investigation the material draw was alternated between the left and right draw points for a total of six draws. Figure 6.11 plots the y-direction displacement of the blocks in the interactive analysis after three draws and six draws. By alternating the draw location the relative movement between the draw zone and the surrounding material is minimised, potentially limiting the possibility of fines migration. It can be seen that for both analyses the final configuration of the structural field is similar despite utilising different draw strategies.

The shape of the draw zone in each analysis can also be interpreted from the velocity of the the fines during draw. Figure 6.12 includes two isosurface plots of the y-direction velocity of the fines in the isolated draw analysis. The images are captured at $t = 2.2s$ which is in the middle of the second draw and at $t = 6.8s$ which is in the middle of the fifth draw, and the velocity magnitude shown is at $t = -0.3m/s$. Comparison of the fines velocity at the two times in the figure shows a considerably narrower draw zone at $t = 2.2s$, which suggests that any fines percolation during this draw would be limited to a narrow band above the draw point. Figure 6.13 includes the same y-direction velocity isosurface plots for the interactive draw analysis. At $t = 2.2s$ it can be seen that the movement of fines in the draw zone is considerably less than at $t = 6.8s$. This is most probably due to the block velocity during this draw being less than is typical, and it is further evidence of the stochastic nature of block movement in the cave. At $t = 6.8s$ the fines velocity indicates the existence of an average-sized draw zone above the left draw point, however a considerable amount of fines movement can also be seen above the right draw point. This indicates that either a small number of blocks have collapsed into the right draw point or that some fines percolation is occurring, or both are occurring simultaneously.

Figures 6.14 and 6.15 plot the characteristic rate of strain in the LBM fines for the isolated and interactive draws, respectively. The two contour plots for each analysis were captured at $t = 2.2s$ and $t = 6.8s$ on a cut plane at the centre of the domain thickness. The timing of the rate of strain contour plots was chosen to correspond with the velocity isosurfaces included in Figures 6.12 and 6.13. At the instants shown the regions of highest shear in

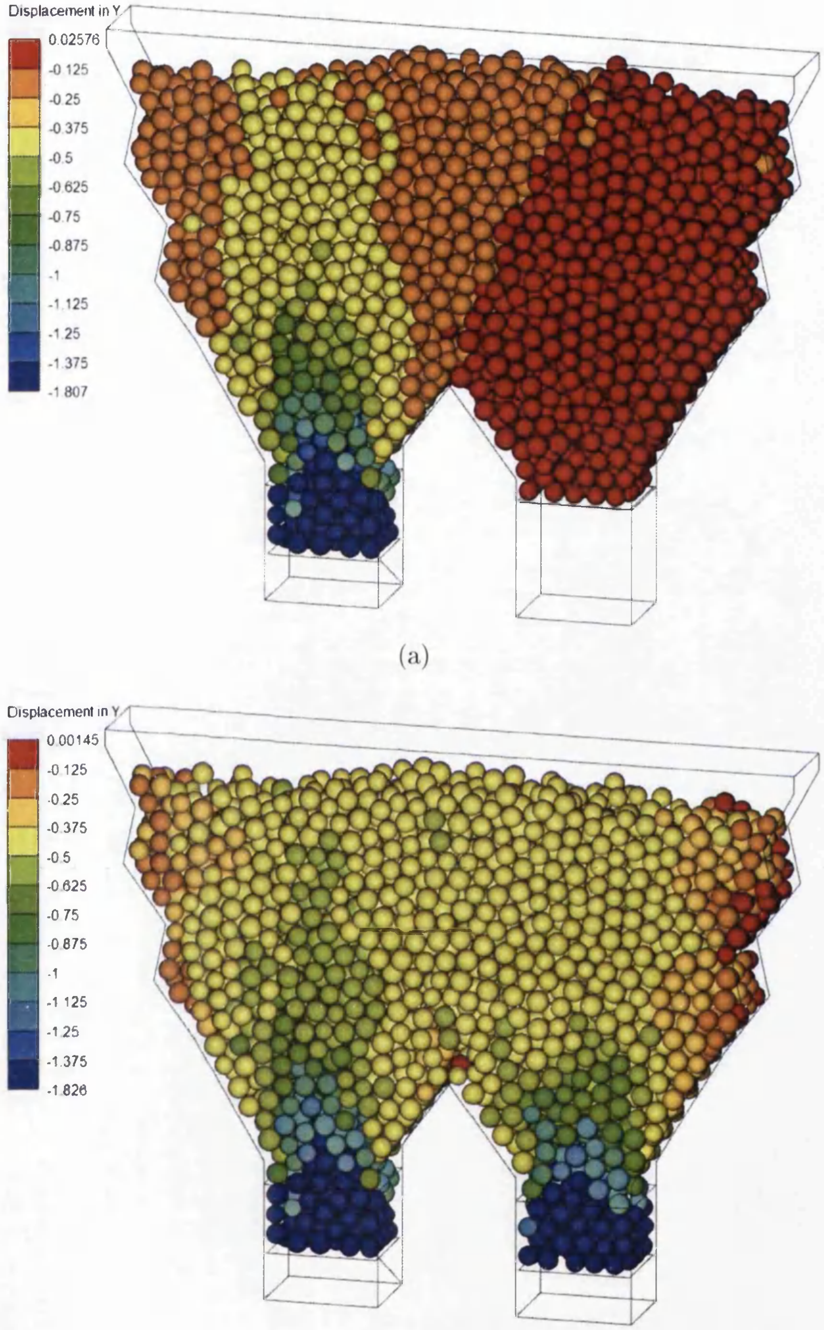

(a)

(b)

Figure 6.10: Contour plots of the y-direction displacement of the discrete element blocks in the isolated analysis after (a) three draws from the left draw point and (b) three draws from the right draw point.

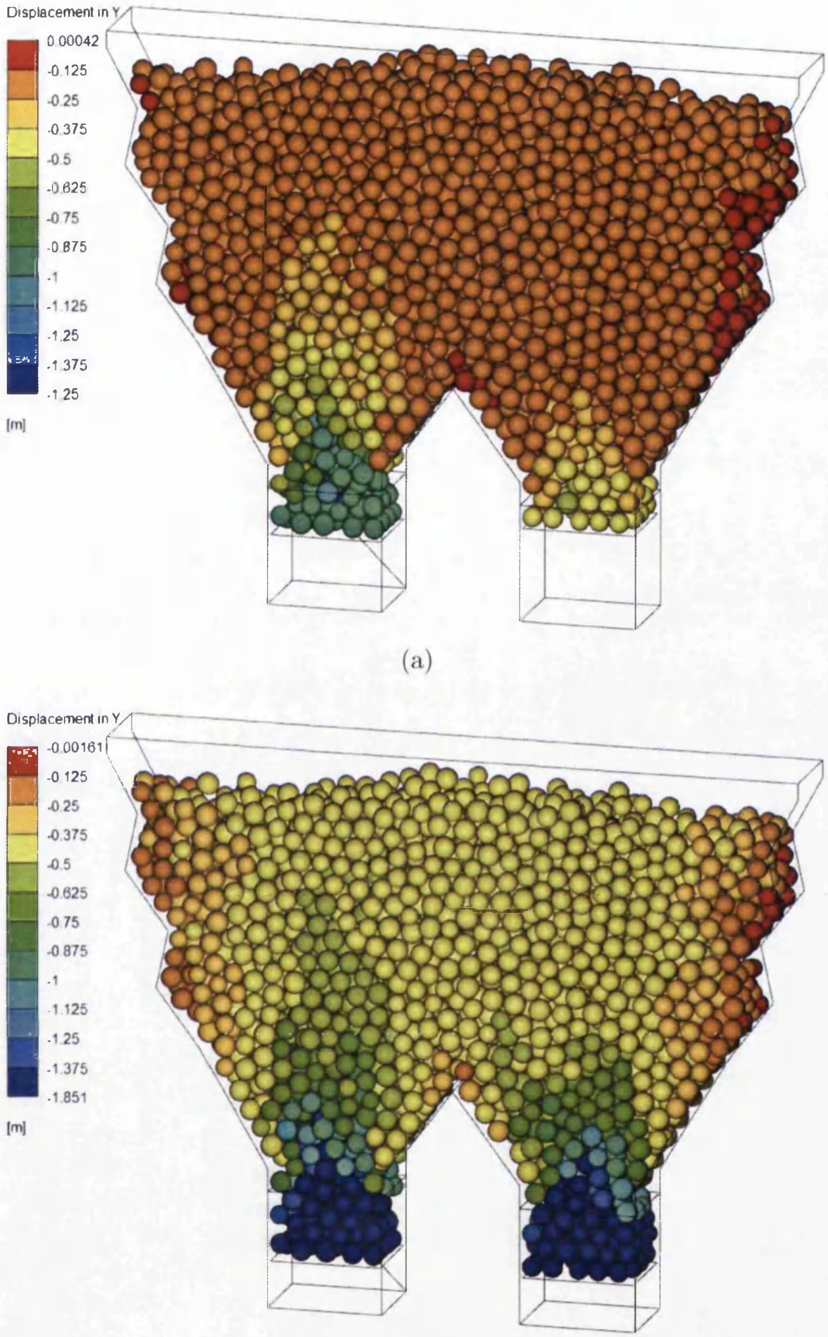

(a)

(b)

Figure 6.11: Contour plots of the y-direction displacement of the discrete element blocks in the interactive analysis after (a) three alternating draws starting from the left draw point and (b) three more alternating draws starting from the right draw point.

the fines are present within their respective draw zones. No significant shear band is evident at the interface of the draw zone and the adjacent stationary material. These results suggest that any migration of fines within the cave would be limited to within the draw zone, because the magnitude of the local strain rate directly influences the pseudoplasticity (i.e. shear-thinning and failure) of the material model.

Finally, a migration trace of the 3D partial block cave results was undertaken to investigate the relative movement of the fines and blocks under different draw strategies. The domain was seeded with a row of thirteen markers positioned $4.25m$ above the outlets and a row of fifteen markers position $6.75m$ above the outlets. Figure 6.16a plots the migration trace results for the isolated draw analysis and Figure 6.16b plots the migration trace results for the interactive draw analysis. Both figures show the initial and final location of the blocks that neighbour each marker as well as the path of the fines markers. The y-direction displacement of the blocks in metres is shown in the contour.

The fines migration results for the isolated draw analysis confirm that for this partial cave geometry the greatest amount of percolation occurs within the draw zones. On Row 1, there is limited *relative* movement above the left draw point except at the fifth marker where the fines move approximately 200% the distance of the neighbouring block. More significant percolation can be seen above the right draw point on Row 1 between the eighth and eleventh markers, with the greatest value being directly above the outlet at the tenth marker. Directly above the pillar it can be seen that the amount of percolation is negligible. This is particularly interesting as this location corresponds to the interface between moving draw zones and stationary adjacent material. It was suspected that significant migration would be seen in this area for the isolated draw analysis. The trends from Row 1 can also be seen in Row 2. Above the left draw point the migration of fines appears biased to the left of the cave, with percolation ranging from approximately 150% to 250% relative fines movement seen at the second to fifth markers. Percolation above the right draw point is evident at the ninth to thirteenth markers and appears more symmetrical with respect to the draw zone and outlet. At the eleventh marker the fines moves approximately 250% the distance of the neighbouring block. As on Row 1, no migration occurs at the seventh and eight markers above the pillar.

Comparison of Figures 6.16a and 6.16b show that the fines migration results for the interactive draw analysis are very similar to those for the isolated draw analysis. This is contrary to the intuitive assumption that the isolated draw investigation would have revealed greater fines migration. Considering the similarity of the results, it is possible that the chosen model domain was not ideal for capturing the subtle differences in block kinematics that lead to fines percolation. Also, in this example it appears that the percolation of fines is dominated by the highly dynamic collapse of blocks into the outlet. A model with greater extents in all Cartesian directions, particularly height, may have captured more significant differences in percolation at locations more remote from the outlet. Alternatively, a partial LBM domain could be placed within a much larger DEM model at a location of interest away from the draw points to investigate the migration in that area. However this approach would require free surface boundaries on the fines phase which have not been investigated in the present study.

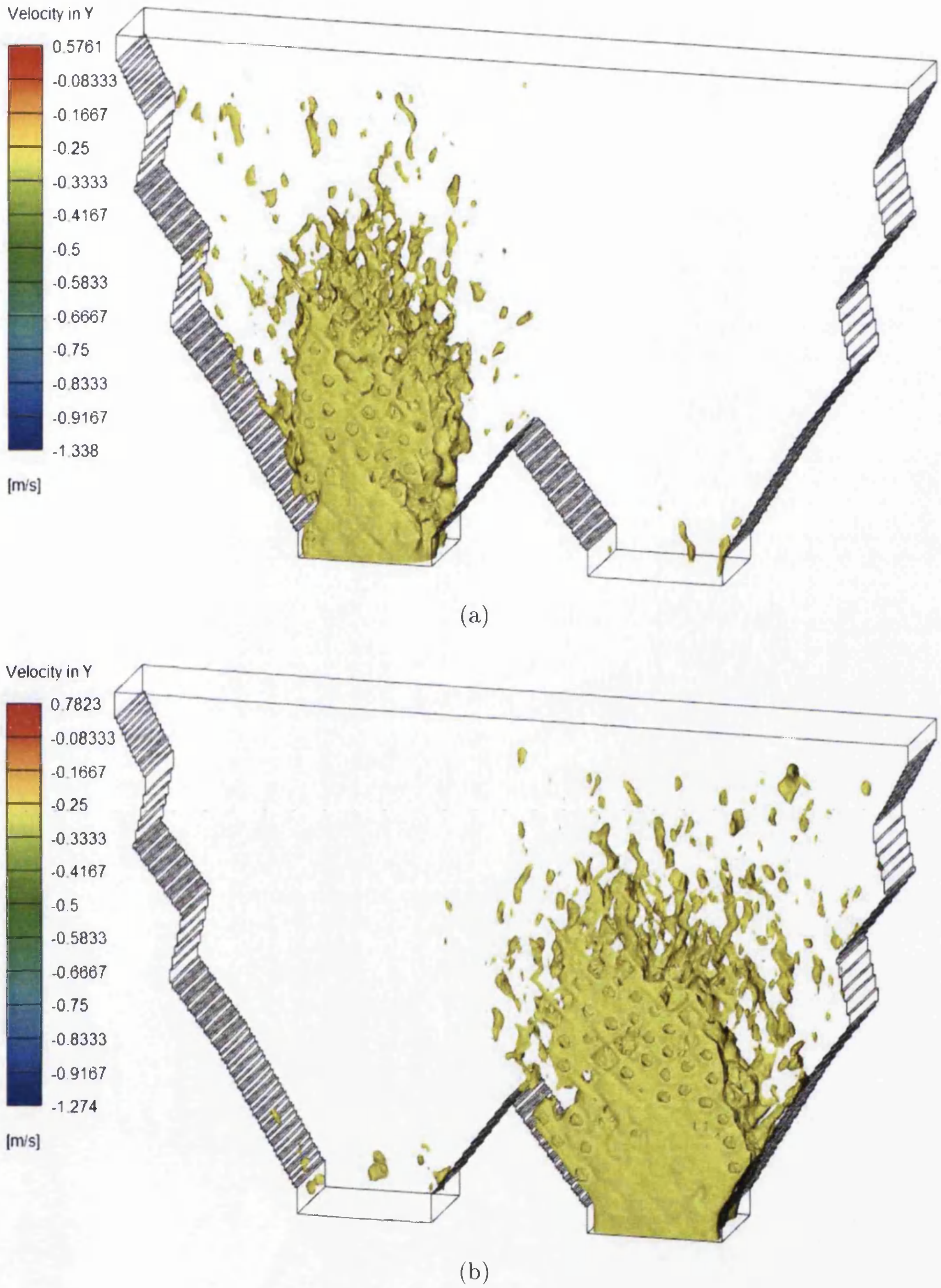

Figure 6.12: Isosurface plots of the y-direction velocity of the fines phase in the isolated analysis at (a) $t = 2.2s$ during the second draw and (b) $t = 6.8s$ during the fifth draw. The velocity magnitude of the isosurface is -0.3m/s.

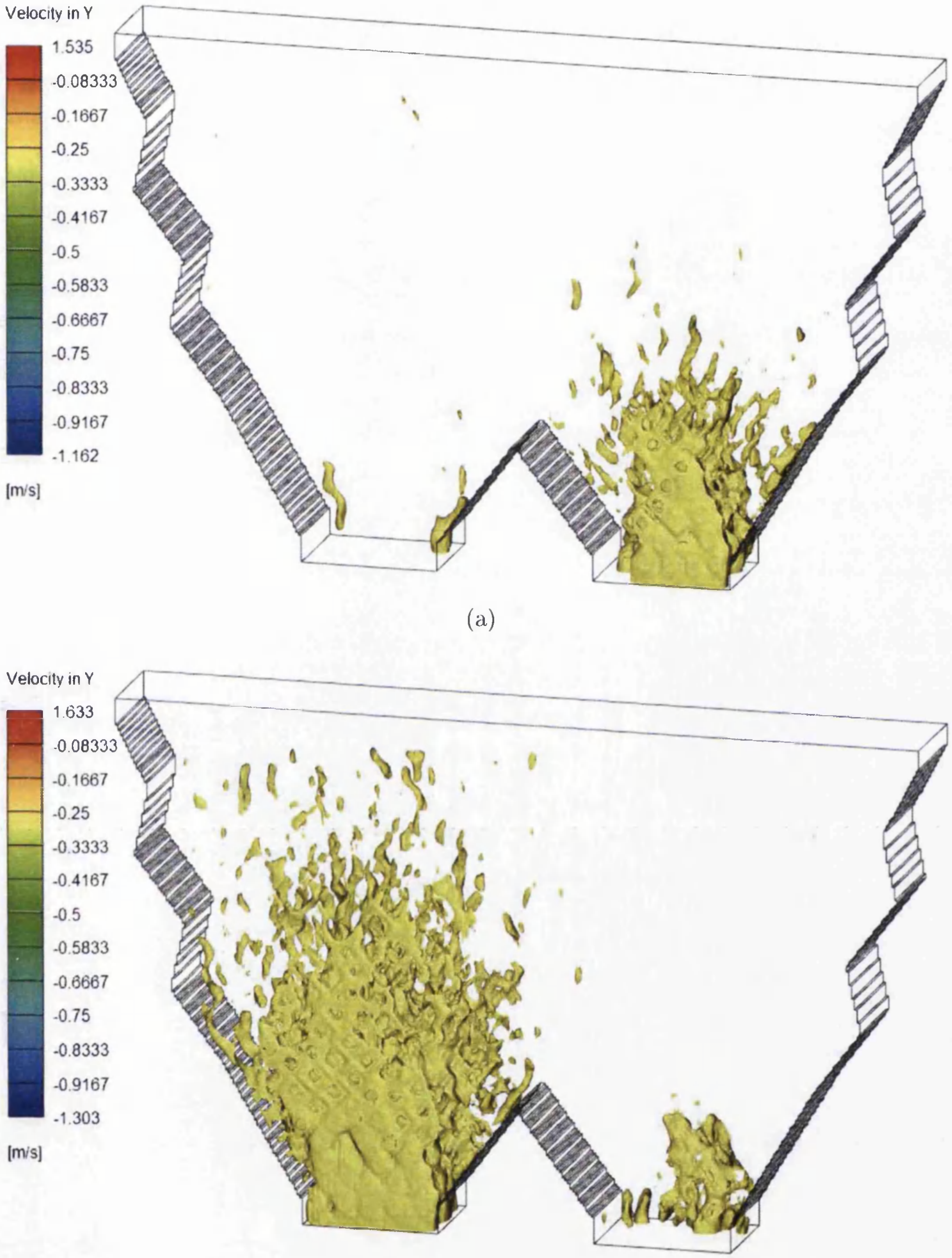

(a)

(b)

Figure 6.13: Isosurface plots of the y-direction velocity of the fines phase in the interactive analysis at (a) $t = 2.2s$ during the second draw and (b) $t = 6.8s$ during the fifth draw. The velocity magnitude of the isosurface is -0.3m/s.

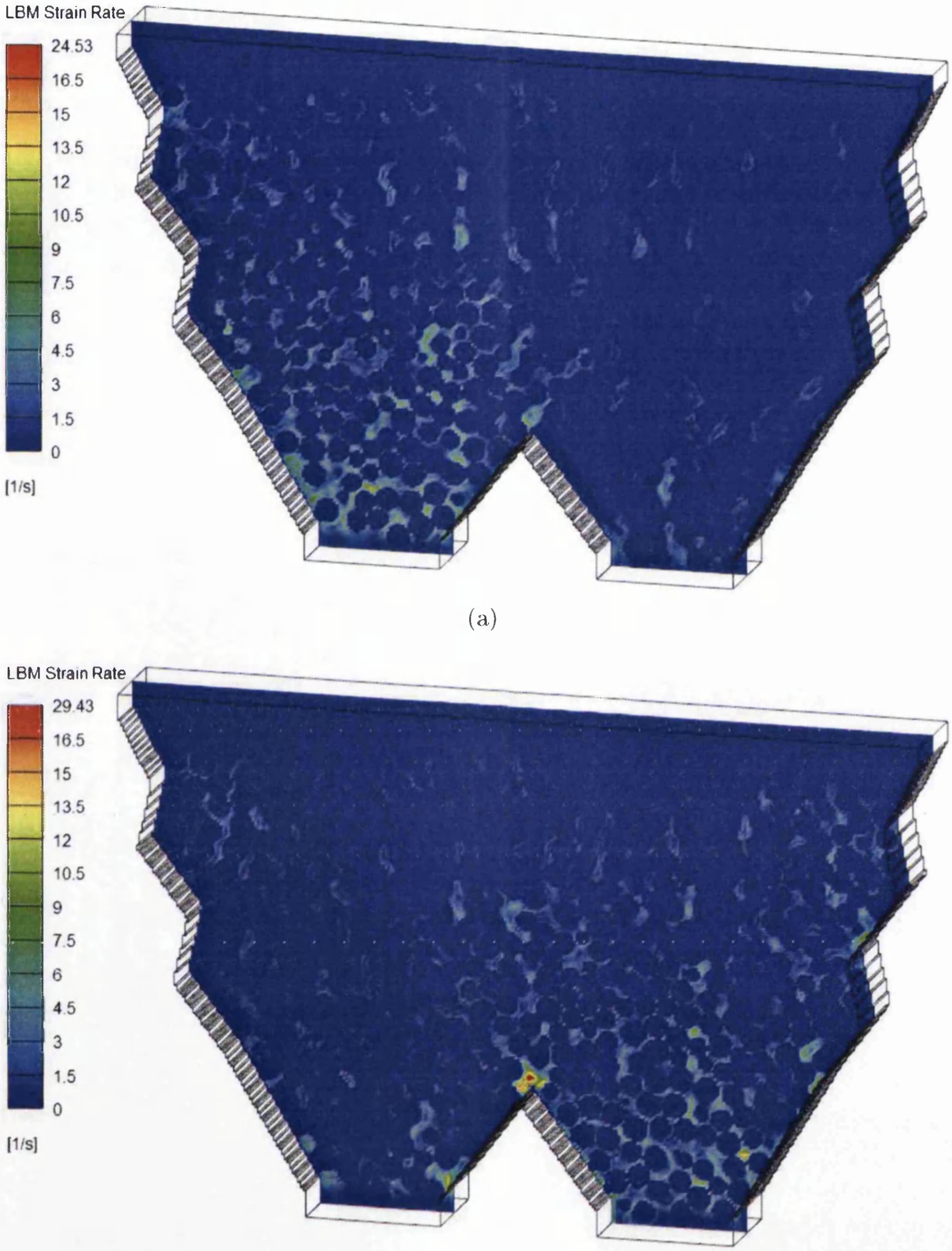

(a)

(b)

Figure 6.14: Contour plots of the characteristic rate of strain in the fines phase in the isolated analysis at (a) $t = 2.2s$ during the second draw and (b) $t = 6.8s$ during the fifth draw.

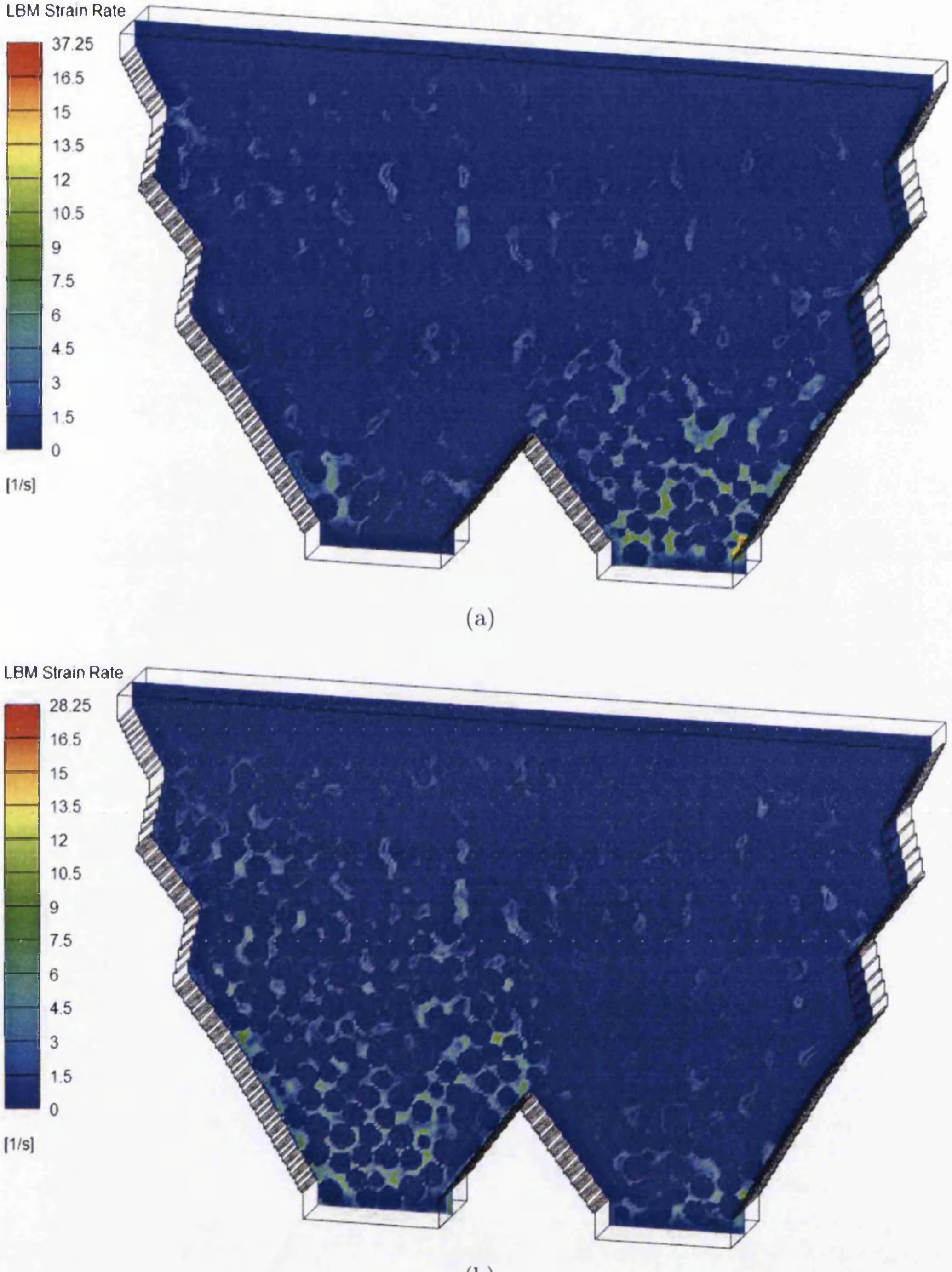

Figure 6.15: Contour plots of the characteristic rate of strain in the fines phase in the interactive analysis at (a) $t = 2.2s$ during the second draw and (b) $t = 6.8s$ during the fifth draw.

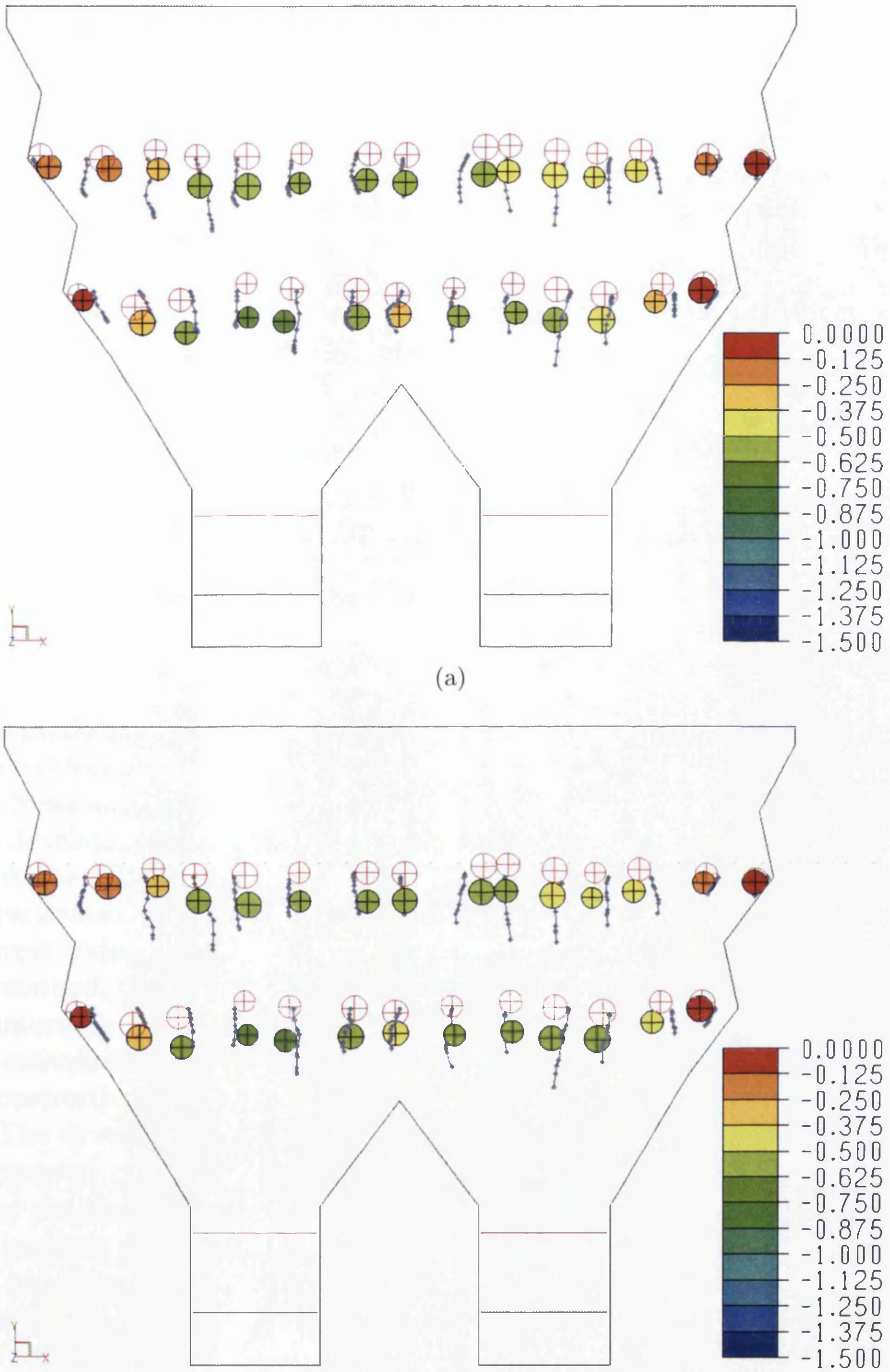

(a)

(b)

Figure 6.16: The migration trace results of the 3D partial cave investigations for (a) the isolated draw analysis and (b) the interactive draw analysis.

CHAPTER 7

CONCLUSION AND FINAL REMARKS

This thesis has presented the development and application of a novel computational framework which couples the lattice Boltzmann method (LBM) in non-Newtonian form to the discrete element method (DEM). The research and development of this framework covered a number of distinct issues related to the LBM, each of which was reviewed and tested in a detailed manner. These issues include the incorporation of the LBM within a commercial finite element code (FEM) and the investigation of the accuracy and stability of the method, the hydrodynamic coupling of the LBM to a dynamic multibody structural field (DEM) and the simultaneous solution of explicit schemes, and the extension of the fluid model to non-Newtonian flows and the calibration of constitutive models to represent the dynamic behaviour of a bulk material.

The developed LBM-DEM framework was applied in the simulation of fragmented orebody dynamics in underground block cave mines. Specifically, the phenomenon of fines migration was investigated in both 2D and 3D analyses of moderate to large scale. Fines migration is characterised by the movement of fines, which is usually waste material, at a rate that is greater than the surrounding blocks of ore. This relative movement of fines and blocks is undesirable as it results in the early presentation of waste at the draw point which in turn reduces the product grade and the efficiency of the mine. Therefore, the objective of computational simulation is to provide insight into the kinematics and interaction of blocks and fines within the cave and in doing so improve understanding of the percolation phenomenon.

The implementation and application of the non-Newtonian LBM-DEM framework were both predominantly successful. The research and implementation of the framework resulted in a computational tool that was efficient and robust in solving physical problems. Subsequently, the application of the framework to fines migration analyses allowed the investigation of real-world variables such as geometry, material properties, and mine sequencing. The simulation results could be interrogated to show features encountered in the field, such as the displacement and velocity of blocks and fines, isolated and interactive draw, and the stochastic nature of muck pile dynamics.

The results of the implementation and application undertaken in this study are presented as closing remarks to this thesis. Where appropriate, the strengths and limitations of this novel computational approach are highlighted. Finally, the aspects of this work that either deserve further investigation or present an opportunity for continued development are summarised.

7.1 Discussion of Results

The implementation of the LBM within the finite element code *Elfen* was discussed in Chapter 2. The multiscale analysis and Chapman-Enskog expansion were presented, which demonstrated how the simple kinetic formulae that comprise the LBM yield physical hydrodynamics in the macroscopic limit. This derivation also highlighted the theoretical convergence behaviour of the method along with constraints on stability and accuracy. These numerical characteristics were then tested by comparing the results of simple, fluid-only analyses to analytical solutions and published benchmarks.

The second order convergence of the LBM was demonstrated in conjunction with the convergence behaviour of the popular bounce-back boundary condition. It was shown that when the wall boundary is parallel with one of the velocity directions the bounce-back method is second order convergent, but this reduces to first order for non-aligned boundaries. The accuracy of this wall boundary technique is important as its simplicity and adaptability render it by far the most convenient (and, incidentally, popular) approach.

The inherent compressibility of the LBM was also shown by monitoring the pressure waves induced in a confined fluid domain due to an impulsive body force. However, this analysis also demonstrated the effectiveness of viscous dissipation in attenuating the transient pressure oscillations.

Chapter 3 treated the coupling of the LBM to the discrete element modelling functionality of *Elfen*. From the hydrodynamic coupling techniques reviewed, the immersed moving boundary method [97] was chosen due to the convenience offered by the locality of operations and the ability to handle partially covered cells. A number of techniques for mapping discrete elements to the LBM grid and calculating the cell coverage ratio were presented.

As the number of discrete elements in a coupled simulation increases and the porosity of the LBM domain decreases the computational cost of the mapping and coverage calculations reaches the same order of magnitude as the pure-fluid operations. Therefore, the optimisation of these processes is worthwhile, as discussed in Section 7.2.4.

Also presented in this chapter was a sub-cycling algorithm which allowed the dynamic coupling of the LBM and DEM explicit schemes. In testing and large scale applications this algorithm was shown to be robust and flexible in matching the time steps of the two numerical methods depending on their respective stability criteria. However, the appropriate limits of this coupling algorithm requires further investigation as during sub-cycling the mapping and hydrodynamic load of the discrete element field remains constant. At overly long sub-cycling intervals these approximations may become problematic, particularly when a large number of discrete element contacts are present.

In testing and validation, the coupling of closed form (i.e. circles/spheres) and discrete form (i.e. polygons) elements was compared with empirical solutions and published results. In low to moderate Reynolds number flows the drag force prediction for circles, polygons and spheres was found to be excellent. In addition, the 3D results showed that the force predictions remain good even in approximated fluid domains and at coarse grid resolution. This important result allows the reduction of computational requirements by minimising the mapping resolution required. At very low Reynolds numbers approaching the Stokes regime it was found that the drag predictions deviated slightly from experimental and analytical results, and this aspect of the IMB method deserves further investigation.

Finally, the problem of cylindrical Couette flow was employed to test the hydrodynamic torque prediction when the IMB and bounce-back methods were used on the inner and outer cylinders, respectively. The results showed super-linear convergence, and the excellent torque and velocity predictions provided a solid foundation for the application of this geometry in numerical rheometry.

The modelling of the dynamic flow of bulk materials (i.e. fines) is a limited field and an area of ongoing research, however it formed an important aspect of this study. Chapter 4 considered the characterisation of block cave fines as a continuum with non-Newtonian constitutive properties. An integral component of constitutive modelling is the rate of strain tensor and it is a convenient feature of the LBM that the deformation gradients that comprise this tensor can be calculated directly and locally from the particle distribution functions at each node. This technique was evaluated in simple flow geometries and the results highlighted the influence and relationship of compressibility, discretisation and boundary errors. This investigation also showed that when the employed LBM parameters are representative of actual simulation requirements the direct strain evaluation method performs very well.

A viscoelastic power law and a regularised, viscoplastic Bingham model was implemented in the LBM-DEM framework, however the Bingham model was found to be prohibitively unstable. Conversely, the power law model was tested in 2D and 3D validation simulations and found to be capable of reproducing the characteristics of shear-thinning and shear-thickening behaviour over a range of exponents.

The power law model was then employed to propose a novel technique for numerical rheometry which was used to calibrate the computational material model to experimental results for a specific sand. The correlation of the numerical and experimental results, both of which used the rotational Couette geometry, was excellent. Following the successful replication of a cohesionless material the numerical rheometer was then used to characterise a number of other synthetic bulk materials, however a lack of available experimental data to calibrate against meant that specific soil properties could not be attained. Instead, the synthetic materials were broadly classified by their degree of pseudoplasticity and their high-strain viscosity.

It was also found in the results of the numerical rheometry that when certain model parameters were used the stress-strain response of the power law model and the regularised Bingham model was similar. From the graph of shear stress against strain rate for the power law rheometry results, estimates of an equivalent yield stress and plastic viscosity could be made. This is particularly convenient as it facilitates the simulation of yield-stress materials in an approximate fashion without the need for an implemented Bingham model. Extension of the numerical rheometer to 3D would be a worthwhile additional exercise, as it would allow the investigation of the influence of gravity and confining pressure in the rotational Couette rheometer, which has been reported to affect the shear-thinning response of materials.

Initial applications of the non-Newtonian LBM-DEM framework were undertaken in two dimensions, the results of which were presented in Chapter 5. The DEM percolation tests conducted by Pierce [105] were replicated using both circular and polygonal discrete elements, and the migration of the fines phase between the blocks was observed. In addition, a large-scale analysis of a three-bell block cave was undertaken and the fines migration induced by an arbitrary sequence of draws was monitored. The investigation of a number of physical mine features such as block size distribution, cave geometry, and draw interactivity was undertaken. The analysis results included information on the velocity and displacement of the fines and blocks, both of which highlighted the extents of the active draw zone at all times. However, the quantification of fines migration requires data on the *relative* movement rather than absolute movement of the two phases. This information was attained via the development of a migration tracing procedure, which described the paths of fines markers and their neighbouring blocks throughout the solution.

The 2D results successfully demonstrated the existence of fines migration in the high shear regions inside and on the edge of the draw zone. Also, migration was only rarely found outside the draw zone, which is in contrast to the DEM results of Pierce that showed significant percolation in the same regions.

The polygonal element analyses provided promising results despite the low permeability of the structural field caused by the absence of the contact buffer. The dynamics of the polygons appeared to be more stochastic than that of the circular blocks, which is an intuitive outcome. The use of polyhedral elements in 3D simulations would not require a contact buffer to artificially increase the permeability of the structural field and therefore this is a recommended extension of the LBM-DEM coupling. However, known issues related to edge-edge and vertex-facet contact would need to be overcome in this scenario.

Finally, Chapter 6 included the results of three-dimensional fines migration applications of the coupled framework. A scaled version of the DEM percolation analysis was presented which investigated the effect of fines materials properties on the level of migration. A moderate scale simulation of a two draw bell section of a mine was also undertaken, and it was used to test the sensitivity of migration to different draw strategies.

The successful execution of these analyses showed that non-Newtonian fluid-solid systems could be solved robustly using a serial implementation on desktop hardware. The ability to solve 3D problems is important as fines migration is a 3D phenomenon, and the evolution of voids and movement of fines in all Cartesian directions must be captured. However, the investigation of 3D models indicated the massive computational resources that large-scale cave models would require. Even with a parallel processing implementation, the choice of domain would have to be made with a degree of care and engineering judgement.

The results of the DEM percolation replication showed, as in the 2D analyses, that migration is predominantly limited to within the draw zone. However some exceptions to this rule were found, which is indicative of fines migration being a stochastic process that is dependent on the random evolution of voids in the cave. As expected, reduction of the pseudoplastic viscosity (i.e. interpreted cohesion) of the material model resulted in a greater amount of fines migration. In addition, this investigation was used to highlight the effectiveness of the dynamic sub-cycling algorithm. The trace of the explicit time step throughout both solutions clearly showed the dynamic adjustment of the sub-cycling factor as the DEM time step changed with changes in the state of the structural field.

The draw sensitivity investigation undertaken with the two bell partial block cave analysis did not show a significant difference in the amount of migration. This is despite the two draw strategies being deliberately chosen to result in isolated and interactive draw of material. Some possible explanations for the similarity of the results include:

1. The length of the solution and the number of draws undertaken was not large enough,
2. The model domain was not large enough, as the most significant migration in both analyses was dominated by the collapse of blocks into the draw point,
3. The model domain focused on the wrong area inside the cave, and other areas would have better captured the subtle differences in fines migration between these draw sequences.

Nevertheless, the results of the 2D and 3D migration analyses highlight the potential for this novel approach to be applied in an industrial context. It has been shown that a non-Newtonian continuum model can be used to simulate the dynamic behaviour of a bulk material. Further, a technique for calibration of the fines material model to experimental data has been presented. In the context of applications, the potential to investigate physical mining influences such as cave geometry, block shape and size and draw strategy has been shown. Most importantly, the results of the 2D and 3D analyses have revealed migration trends for the geometries, material properties and operational sequences analysed. By executing an extensive programme of numerical experiments the influence of these and other relevant block cave factors on the migration of fines could be isolated.

7.2 Opportunities for Further Research

Notwithstanding the demonstrated potential of the LBM-DEM framework in fines migration applications, some issues with this approach have been identified. Therefore, scope exists for further research and development in this field, as outlined below.

7.2.1 Simulation of a Partially Filled Fines Phase

In the percolation analyses undertaken in this research the model domain is initiated with all of the void space between the blocks filled with fines. In practice this is not always the case, particularly at the onset of caving when primary fragmentation results in predominantly large blocks being present in the cave. As draw proceeds the amount of fines at a location within the muck pile changes and is governed by many factors including the proximity of external sources and the generation of fines by secondary fragmentation. The latter is dependent on the rock mass properties and the stress distribution in the muck pile and is particularly difficult to quantify.

The simulation of empty voids could be investigated by using a multicomponent lattice Boltzmann model or a single component model that is bounded by a free-surface constraint. Multiphase and multicomponent lattice Boltzmann models have been reported in the literature [19], however the additional inclusion of a moving structural field has not been undertaken to date. The work of Pan et al. [100], which investigated two-phase flow through a static porous medium, could form the basis for this approach but extending it to include moving elements would be more complex.

The use of a single fines phase that is bounded by a free surface would be more efficient than a multiphase or multicomponent approach as it would not require LBM computations for the empty voids that are occupied only by air. Some examples of free-surface applications in the LBM include in the simulation of injection moulding [47], metal casting [48] and liquid foaming [74]. The greatest challenge in applying this approach to fines migration problems would be the robust handling of the free surface interactions with the discrete element field. With this challenge overcome, the LBM-DEM framework could be used to solve problems in which only *pockets* of fines exist at specified locations in the cave.

7.2.2 Parallelisation of LBM Computations

The size of the cave domain that can be modelled with the LBM-DEM framework is limited by the serial processing architecture employed in implementation. This was particularly evident in the 3D fines migration applications presented in Chapter 6. The extension of the framework to distributed processing [71, 113], taking advantage of the inherently parallel nature of the LBM, would increase the size of the domain that could be modelled. The parallelisation of the moving structural field would not be necessary as it was found in the 2D and 3D applications that the computational requirements of the DEM were significantly less than that of the LBM. It should be noted that the simulation of significantly larger domains would transfer the computational *bottleneck* to the post-processing of results, but this could be overcome by utilising distributed visualisation techniques.

7.2.3 Non-Newtonian Fluids with MRT-LBM Models

The single-relaxation-time LBGK collision process, in conjunction with a viscoelastic power law model, was successfully applied to characterise the dynamic behaviour of fines. However, the relationship between the relaxation parameter, τ, and the lattice spacing, time step, and non-Newtonian material properties could make parameter selection difficult for certain applications. The use of multiple-relaxation-time models [80], particularly in the context of non-Newtonian constitutive modelling [47], offers a greater number of model parameters which can be used to tune the hydrodynamic behaviour in isolation from the spatial and temporal discretisation. This avenue of research, with the objective of robustly implementing additional non-Newtonian models such as Bingham and Herschel-Bulkley, would be worthwhile.

7.2.4 Novel Approaches to DEM Mapping

In the fines migration applications of the LBM-DEM framework the LBM domain is almost entirely filled with blocks. In this scenario, the computational expense of mapping the discrete elements to the grid becomes significant and of approximately the same order of magnitude as the LBM computations. This presents an opportunity for improved efficiency via a novel mapping technique using graphics hardware. In fact, GPU algorithms have been employed to perform image-based solutions of the LBM [83], and the extension image-based mapping and area calculation is a viable option.

7.3 Other Applications of the LBM-DEM Framework

As a final remark, it should be mentioned that the LBM-DEM framework developed in this study has the potential for application in other problems related to block caving. For example, water seepage and mush rush could be investigated with only minor modifications to the existing code. Also, the implementation of a turbulence model [141] would act as a basis for the investigation of air movement in the development and production tunnels, with emphasis on the phenomenon of air-blast.

References

[1] E. Aharonov and D. H. Rothman. Non-newtonian flow (through porous media): A lattice-boltzmann method. *Geophysical Research Letters*, 20(8):679–682, 1993.

[2] C. K. Aidun, Y. Lu, and E.-J. Ding. Direct analysis of particulate suspensions with inertia using the discrete boltzmann equation. *Journal of Fluid Mechanics*, 373(-1):287–311, 2000.

[3] M. Alfaro and J. Saavedra. Predictive models for gravitational flow. In *Proceedings of MassMin 2004*, pages 179–184, 2004.

[4] P. L. Bhatnagar, E. P. Gross, and M. Krook. A model for collision processes in gases. i. small amplitude processes in charged and neutral one-component systems. *Physical Review*, 94(3):511–525, 1954.

[5] R. B. Bird, W. E. Stewart, and E. N. Lightfoot. *Transport Phenomena*. John Wiley & Sons, 2nd edition, 2006.

[6] E. S. Boek, J. Chin, and P. V. Coveny. Lattice boltzmann simulation of the flow of non-newtonian fluids in porous media. *International Journal of Modern Physics B*, 17(1/2):99–102, 2003.

[7] M. Bouzidi, M. Firdaouss, and P. Lallemand. Momentum transfer of a boltzmann-lattice fluid with boundaries. *Physics of Fluids*, 13(11):3452–3459, 2001.

[8] J. Boyd, J. Buick, and S. Green. A second-order accurate lattice boltzmann non-newtonian flow model. *Journal of Physics A: Mathematical and General*, 39(46):14241–14247, 2006.

[9] M. Breuer, J. Bernsdorf, T. Zeiser, and F. Durst. Accurate computations of the laminar flow past a square cylinder based on two different methods: lattice-boltzmann and finite-volume. *International Journal of Heat and Fluid Flow*, 21(2):186–196, 2000.

[10] J. Bridgewater, M. H. Cooke, and A. M. Scott. Inter-particle percolation: Equipment development and mean percolation velocities. *Transactions of the Institution of Chemical Engineers*, 56:157–, 1978.

[11] J. M. Buick and C. A. Greated. Gravity in a lattice boltzmann model. *Physical Review E*, 61(5):5307–5320, 2000.

[12] G. R. Burgos and A. N. Alexandrou. Flow development of herschel-bulkley fluids in a sudden three-dimensional square expansion. *Journal of Rheology*, 43(3):485–498, 1999.

[13] G. R. Burgos, A. N. Alexandrou, and V. Entov. On the determination of yield surfaces in herschel–bulkley fluids. *Journal of Rheology*, 43(3):463–483, 1999.

[14] C. S. Campbell. Granular material flows - an overview. *Powder Technology*, 162(3):208–229, 2006.

[15] N. Cao, S. Chen, S. Jin, and D. Martínez. Physical symmetry and lattice symmetry in the lattice boltzmann method. *Physical Review E*, 55(1):R21–R24, 1997.

[16] G. Carlson, D. Tyler, C. De Wolfe, and L. Lorig. Understanding gravity flow for mix and dilution modeling at henderson mine. In *Proceedings of MassMin 2004*, pages 231–237, 2004.

[17] H. Chen, S. Chen, and W. H. Matthaeus. Recovery of the navier-stokes equations using a lattice-gas boltzmann method. *Physical Review A*, 45(8):R5339–R5342, 1992.

[18] S. Chen, H. Chen, D. Martinez, and W. Matthaeus. Lattice boltzmann model for simulation of magnetohydrodynamics. *Physical Review Letters*, 67(27):3776–3779, 1991.

[19] S. Chen and G. D. Doolen. Lattice boltzmann method for fluid flows. *Annual Review of Fluid Mechanics*, 30(1):329–364, 1998.

[20] S. Chen, D. Martinez, and R. Mei. On boundary conditions in lattice boltzmann methods. *Physics of Fluids*, 8(9):2527–2536, 1996.

[21] Y-L Chen, X-D Cao, and K-Q Zhu. A gray lattice boltzmann model for power-law fluid and its application in the study of slip velocity at porous interface. *Journal of Non-Newtonian Fluid Mechanics*, 159(1-3):130–136, 2009.

[22] B. Chopard and A. Masselot. Cellular automata and lattice boltzmann methods: a new approach to computational fluid dynamics and particle transport. *Future Generation Computer Systems*, 16(2-3):249–257, 1999.

[23] B. Chun and A. J. C. Ladd. Interpolated boundary condition for lattice boltzmann simulations of flows in narrow gaps. *Physical Review E*, 75(6):066705–12, 2007.

[24] B. K. Cook. *A numerical framework for the direct simulation of solid-fluid systems*. PhD thesis, Massachusetts Institute of Technology, 2001.

[25] B. K. Cook, D. R. Noble, and J. R. Williams. A direct simulation method for particle-fluid systems. *Engineering Computations*, 21(2/3/4):151–168, 2004.

[26] R. Cornubert, D. d'Humières, and D. Levermore. A knudsen layer theory for lattice gases. *Physica D: Nonlinear Phenomena*, 47(1-2):241–259, 1991.

[27] P. A. Cundall and O. D. L. Strack. Discrete numerical-model for granular assemblies. *Geotechnique*, 29(1):47–65, 1979.

[28] J. B. Davison, R. K. Çalay, and T. B. Sands. Computational simulation of rheologically classified soil over augers. *Journal of Marine Engineering and Technology*, A6:23–31, 2005.

[29] D. d'Humieres, P. Lallemand, and U. Frisch. Lattice gas models for 3d hydrodynamics. *Europhysics Letters*, 2(4):291–297, 1986.

[30] A. Dupuis, P. Chatelain, and P. Koumoutsakos. An immersed boundary-lattice-boltzmann method for the simulation of the flow past an impulsively started cylinder. *Journal of Computational Physics*, 227(9):4486–4498, 2008.

[31] P. Estellé, C. Lanos, and A. Perrot. Processing the couette viscometry data using a bingham approximation in shear rate calculation. *Journal of Non-Newtonian Fluid Mechanics*, 154(1):31–38, 2008.

[32] G. S. Esterhuizen, L. Rachmad, A. V. Potapov, and L. K. Nordell. Investigation of swell factor in a block cave draw column. In *Proceedings of MassMin 2004*, pages 215–219, 2004.

[33] Y. T. Feng, K. Han, and D. R. J. Owen. Coupled lattice boltzmann method and discrete element modelling of particle transport in turbulent fluid flows: Computational issues. *International Journal for Numerical Methods in Engineering*, 72(9):1111–1134, 2007.

[34] Y. T. Feng and D. R. J. Owen. A 2d polygon/polygon contact model: algorithmic aspects. *Engineering Computations*, 21(2/3/4):265–277, 2004.

[35] Z.-G. Feng and E. E. Michaelides. Hydrodynamic force on spheres in cylindrical and prismatic enclosures. *International Journal of Multiphase Flow*, 28(3):479–496, 2002.

[36] Z.-G. Feng and E. E. Michaelides. The immersed boundary-lattice boltzmann method for solving fluid-particles interaction problems. *Journal of Computational Physics*, 195(2):602–628, 2004.

[37] Z.-G. Feng and E. E. Michaelides. Proteus: a direct forcing method in the simulations of particulate flows. *Journal of Computational Physics*, 202(1):20–51, 2005.

[38] O. Filippova and D. Hänel. Grid refinement for lattice-bgk models. *Journal of Computational Physics*, 147(1):219–228, 1998.

[39] E. G. Flekkøy and H. J. Herrmann. Lattice boltzmann models for complex fluids. *Physica A: Statistical Mechanics and its Applications*, 199(1):1–11, 1993.

[40] U. Frisch, D. d'Humières, B. Hasslacher, P. Lallemand, Y. Pomeau, and J.-P. Rivet. Lattice gas hydrodynamics in two and three dimensions. *Complex Systems*, 1:649–707, 1987.

[41] U. Frisch, B. Hasslacher, and Y. Pomeau. Lattice-gas automata for the navier-stokes equation. *Physical Review Letters*, 56(14):1505–1508, 1986.

[42] S. Gabbanelli, G. Drazer, and J. Koplik. Lattice boltzmann method for non-newtonian (power-law) fluids. *Physical Review E*, 72(4):046312–7, 2005.

[43] M. A. Gallivan, D. R. Noble, J. G. Georgiadis, and R. O. Buckius. An evaluation of the bounce-back boundary condition for lattice boltzmann simulations. *International Journal for Numerical Methods in Fluids*, 25(3):249–263, 1997.

[44] S. Geller, M. Krafczyk, J. Tölke, S. Turek, and J. Hron. Benchmark computations based on lattice-boltzmann, finite element and finite volume methods for laminar flows. *Computers and Fluids*, 35(8-9):888–897, 2006.

[45] T. A. Ghezzehei and D. Or. Rheological properties of wet soils and clays under steady and oscillatory stresses. *Soil Science Society of America Journal*, 65(3):624–637, 2001.

[46] I. Ginzbourg and P. M. Adler. Boundary flow condition analysis for the three-dimensional lattice boltzmann model. *Journal de Physique II*, 4(2):191–214, 1994.

[47] I. Ginzburg and K. Steiner. A free-surface lattice boltzmann method for modelling the filling of expanding cavities by bingham fluids. *Philosophical Transactions of the Royal Society A: Mathematical, Physical and Engineering Sciences*, 360(1792):453–466, 2002.

[48] I Ginzburg and K Steiner. Lattice boltzmann model for free-surface flow and its application to filling process in casting. *Journal of Computational Physics*, 185(1):61–99, 2003.

[49] L. Giraud, D. d'Humières, and P. Lallemand. A lattice boltzmann model for jeffreys viscoelastic fluid. *Europhysics Letters*, 42(6):625–630, 1998.

[50] I. Goldhirsch. Introduction to granular temperature. *Powder Technology*, 182(2):130–136, 2008.

[51] A. R. Guest. The difference between interaction and interactive draw. In *Proceedings of the 1st International Symposium on Block and Sub-Level Caving*, pages 123–132, 2007.

[52] K. Han, Y. T. Feng, and D. R. J. Owen. Polygon-based contact resolution for superquadrics. *International Journal for Numerical Methods in Engineering*, 66(3):485–501, 2006.

[53] K. Han, D. Peric, A. J. L. Crook, and D. R. J. Owen. A combined finite/discrete element simulation of shot peening processes - part i: studies on 2d interaction laws. *Engineering Computations*, 17(5):593–619, 2000.

[54] K. Han, D. Peric, D. R. J. Owen, and J. Yu. A combined finite/discrete element simulation of shot peening processes - part ii: 3d interaction laws. *Engineering Computations*, 17(6):680–702, 2000.

[55] J. Hardy, O. de Pazzis, and Y. Pomeau. Molecular dynamics of a classical lattice gas: Transport properties and time correlation functions. *Physical Review A*, 13(5):1949–1961, 1976.

[56] X. He and G. D. Doolen. Lattice boltzmann method on a curvilinear coordinate system: Vortex shedding behind a circular cylinder. *Physical Review E*, 56(1):434–440, 1997.

[57] X. He and L.-S. Luo. Lattice boltzmann model for the incompressible navier-stokes equation. *Journal of Statistical Physics*, 88(3):927–944, 1997.

[58] X. He and L.-S. Luo. Theory of the lattice boltzmann method: From the boltzmann equation to the lattice boltzmann equation. *Physical Review E*, 56(6):6811–6817, 1997.

[59] X. He, L.-S. Luo, and M. Dembo. Some progress in lattice boltzmann method. part i. nonuniform mesh grids. *Journal of Computational Physics*, 129(2):357–363, 1996.

[60] H. J. Herrmann. Statistical models for granular materials. *Physica A: Statistical Mechanics and its Applications*, 263(1-4):51–62, 1999.

[61] H. J. Herrmann and S. Luding. Modeling granular media on the computer. *Continuum Mechanics and Thermodynamics*, 10(4):189–231, 1998.

[62] F. J. Higuera and J. Jimenez. Boltzmann approach to lattice gas simulations. *Europhysics Letters*, 9(7):663–668, 1989.

[63] F. J. Higuera and S. Succi. Simulating the flow around a circular cylinder with a lattice boltzmann equation. *Europhysics Letters*, 8(6):517–521, 1989.

[64] F. J. Higuera, S. Succi, and R. Benzi. Lattice gas dynamics with enhanced collisions. *Europhysics Letters*, 9(4):345–349, 1989.

[65] D. J. Holdych. *Lattice Boltzmann methods for diffuse and mobile interfaces.* PhD thesis, University of Illinois at Urbana-Champaign, 2003.

[66] S. Hou, Q. Zou, S. Chen, G. Doolen, and A. C. Cogley. Simulation of cavity flow by the lattice boltzmann method. *Journal of Computational Physics*, 118(2):329–347, 1995.

[67] T. Inamuro, M. Yoshino, and F. Ogino. A non-slip boundary condition for lattice boltzmann simulations. *Physics of Fluids*, 7(12):2928–2930, 1995.

[68] JKMRC Itasca. *International Caving Study*, 2004.

[69] M. Junk and A. Klar. Discretizations for the incompressible navier-stokes equations based on the lattice boltzmann method. *SIAM Journal on Scientific Computing*, 22(1):1–19, 2000.

[70] M. Junk and Z. Yang. Outflow boundary conditions for the lattice boltzmann method. *Progress in Computational Fluid Dynamics*, 8(1-4):38–48, 2008.

[71] D. Kandhai, A. Koponen, A.G. Hoekstra, M. Kataja, J. Timonen, and P.M.A. Sloot. Lattice-boltzmann hydrodynamics on parallel systems. *Computer Physics Communications*, 111(1-3):14–26, 1998.

[72] T. Karlsson, M. Klisinski, and K. Runesson. Finite element simulation of granular material flow in plane silos with complicated geometry. *Powder Technology*, 99(1):29–39, 1998.

[73] K. M. Kelkar and S. V. Patankar. Numerical prediction of vortex shedding behind a square cylinder. *International Journal for Numerical Methods in Fluids*, 14(3):327–341, 1992.

[74] C. Korner, M. Thies, T. Hofmann, N. Thurey, and U. Rude. Lattice boltzmann model for free surface flow for modeling foaming. *Journal of Statistical Physics*, 121(1):179–196, 2005.

[75] M. Krafczyk, J. Tolke, and L.-S. Luo. Large-eddy simulations with a multiple-relaxation-time lbe model. *International Journal of Modern Physics B*, 17(1/2):33–39, 2003.

[76] J. L. Kueny and G. Binder. Viscous flow over backward facing steps - an experimental investigation. In *Analysis of laminar flow over a backward facing step*, pages 32–47, 1983.

[77] R. Kvapil. *Gravity flow in sublevel and panel caving - a common sense approach*, 2004.

[78] A. J. C. Ladd. Numerical simulations of particulate suspensions via a discretized boltzmann equation. part 1. theoretical foundation. *Journal of Fluid Mechanics*, 271:285–309, 1994.

[79] A. J. C. Ladd. Numerical simulations of particulate suspensions via a discretized boltzmann equation. part 2. numerical results. *Journal of Fluid Mechanics*, 271:311–339, 1994.

[80] P. Lallemand and L.-S. Luo. Theory of the lattice boltzmann method: Dispersion, dissipation, isotropy, galilean invariance, and stability. *Physical Review E*, 61(6):6546–6562, 2000.

[81] J. Latt, B. Chopard, O. Malaspinas, M. Deville, and A. Michler. Straight velocity boundaries in the lattice boltzmann method. *Physical Review E*, 77(5):056703–16, 2008.

[82] D. Laubscher. *A practical manual on block caving.* JKMRC, 2000.

[83] W. Li, Z. Fan, X. Wei, and A. Kaufman. Flow simulation with complex boundaries. *GPU Gems*, 2:747–764, 2005.

[84] L. J. Lorig and P. A. Cundall. A rapid gravity flow simulator. Technical report, International Caving Study, 2000.

[85] L.-S. Luo. Symmetry breaking of flow in 2d symmetric channels: Simulations by lattice boltzmann method. *International Journal of Modern Physics C*, 8(4):859–867, 1997.

[86] R. S. Maier, R. S. Bernard, and D. W. Grunau. Boundary conditions for the lattice boltzmann method. *Physics of Fluids*, 8(7):1788–1801, 1996.

[87] D. O. Martinez, W. H. Matthaeus, S. Chen, and D. C. Montgomery. Comparison of spectral method and lattice boltzmann simulations of two-dimensional hydrodynamics. *Physics of Fluids*, 6(3):1285–1298, 1994.

[88] M. Massoudi and T. X. Phuoc. Conduction and dissipation in the shearing flow of granular materials modeled as non-newtonian fluids. *Powder Technology*, 175(3):146–162, 2007.

[89] J. McMinn. Identifying soils by a triangle based on unified soil classification system. *ASTM International*, 1960.

[90] G. R. McNamara and G. Zanetti. Use of the boltzmann equation to simulate lattice-gas automata. *Physical Review Letters*, 61(20):2332–2335, 1988.

[91] R. Mei, L.-S. Luo, and W. Shyy. An accurate curved boundary treatment in the lattice boltzmann method. *Journal of Computational Physics*, 155(2):307–330, 1999.

[92] R. Mei, W. Shyy, D. Yu, and L.-S. Luo. Lattice boltzmann method for 3-d flows with curved boundary. *Journal of Computational Physics*, 161(2):680–699, 2000.

[93] R. Mei, D. Yu, W. Shyy, and L.-S. Luo. Force evaluation in the lattice boltzmann method involving curved geometry. *Physical Review E*, 65(4):1–14, 2002.

[94] F. Nannelli and S. Succi. The lattice boltzmann equation on irregular lattices. *Journal of Statistical Physics*, 68(3):401–407, 1992.

[95] N.-Q. Nguyen and A. J. C. Ladd. Sedimentation of hard-sphere suspensions at low reynolds number. *Journal of Fluid Mechanics*, 525:73–104, 2005.

[96] D. R. Noble, S. Chen, J. G. Georgiadis, and R. O. Buckius. A consistent hydrodynamic boundary condition for the lattice boltzmann method. *Phyics of Fluids*, 7(1):203–209, 1995.

[97] D. R. Noble and J. R. Torczynski. A lattice-boltzmann method for partially saturated computational cells. *International Journal of Modern Physics C*, 9(8):1189–1201, 1998.

[98] J. G. Oldroyd. An approach to non-newtonian fluid mechanics. *Journal of Non-Newtonian Fluid Mechanics*, 14:9–46, 1984.

[99] D. Or and T. A. Ghezzehei. Modeling post-tillage soil structural dynamics: a review. *Soil and Tillage Research*, 64(1-2):41–59, 2002.

[100] C. Pan, M. Hilpert, and C.T. Miller. Lattice-boltzmann simulation of two-phase flow in porous media. *Water Resources Research*, 40:W01501, 2004.

[101] T. C. Papanastasiou. Flows of materials with yield. *Journal of Rheology*, 31(5):385–404, 1987.

[102] J. R. A. Pearson and P. M. J. Tardy. Models for flow of non-newtonian and complex fluids through porous media. *Journal of Non-Newtonian Fluid Mechanics*, 102(2):447–473, 2002.

[103] Y. Peng and L.-S. Luo. A comparative study of immersed boundary and interpolated bounce-back methods in lbe. *Progress in Computational Fluid Mechanics*, 8(1-4):156–167, 2008.

[104] C. S. Peskin. Numerical analysis of blood flow in the heart. *Journal of Computational Physics*, 25(3):220–252, 1977.

[105] M.E. Pierce. Pfc3d modeling of inter-particle percolation in caved rock under draw. In *Proceedings of the 2nd International PFC Symposium*, pages 149–156, 2004.

[106] G. R. Power. Full scale slc draw trials at ridgeway gold mine. In *Proceedings of MassMin 2004*, pages 225–230, 2004.

[107] G. R. Power. *Modelling granular flow in caving mines: large scale physical modelling and full scale experiments.* PhD thesis, University of Queensland, 2004.

[108] Y. H. Qian, D. D'Humieres, and P. Lallemand. Lattice bgk models for navier-stokes equation. *Europhysics Letters*, 17(6):479–484, 1992.

[109] Y.H. Qian, S. Succi, F. Massaioli, and S.A. Orszag. A benchmark for lattice bgk model: Flow over a backward facing step. *Fields Institute Communications*, 6:207–215, 1996.

[110] N. Rakotomalala, D. Salin, and P. Watzky. Simulations of viscous flows of complex fluids with a bhatnagar, gross, and krook lattice gas. *Physics of Fluids*, 8(11):3200–3202, 1996.

[111] J. M. Rance, A. van As, D. R. J. Owen, Y. T. Feng, and R. J. Pine. Computational modeling of multiple fragmentation in rock masses with application to block caving. In *1st Canada - US Rock Mechanics Symposium*, 2007.

[112] F. W. Roos and W. W. Willmarth. Some experimental results on sphere and disk drag. *AIAA Journal*, 9(2):285–291, 1971.

[113] N. Satofuka and T. Nishioka. Parallelization of lattice boltzmann method for incompressible flow computations. *Computational Mechanics*, 23(2):164–171, 1999.

[114] D. G. Schaeffer. Instability in the evolution equations describing incompressible granular flow. *Journal of Differential Equations*, 66(1):19–50, 1987.

[115] H. Sellden and M. Pierce. Pfc3d modelling of flow behaviour in sublevel caving. In *Proceedings of MassMin 2004*, pages 201–214, 2004.

[116] G. Sharrock, D. Beck, G. Booth, and M. Sandy. Simulating gravity flow in sub-level caving with cellular automata. In *Proceedings of MassMin 2004*, pages 189–194, 2004.

[117] M. Singh and K. K. Mohanty. Permeability of spatially correlated porous media. *Chemical Engineering Science*, 55(22):5393–5403, 2000.

[118] P. A. Skordos. Initial and boundary conditions for the lattice boltzmann method. *Physical Review E*, 48(6):4823–4842, 1993.

[119] J. D. Sterling and S. Chen. Stability analysis of lattice boltzmann methods. *Journal of Computational Physics*, 123(1):196–206, 1996.

[120] O. E. Strack and B. K. Cook. Three-dimensional immersed boundary conditions for moving solids in the lattice-boltzmann method. *International Journal for Numerical Methods in Fluids*, 55(2):103–125, 2007.

[121] S. Succi. *The lattice Boltzmann equation for fluid dynamics and beyond.* Oxford University Press, 1st edition, 2001.

[122] S. P. Sullivan, L. F. Gladden, and M. L. Johns. Simulation of power-law fluid flow through porous media using lattice boltzmann techniques. *Journal of Non-Newtonian Fluid Mechanics*, 133(2-3):91–98, 2006.

[123] S. P. Sullivan, A. J. Sederman, M. L. Johns, and L. F. Gladden. Verification of shear-thinning lb simulations in complex geometries. *Journal of Non-Newtonian Fluid Mechanics*, 143(2-3):59–63, 2007.

[124] A. Susaeta. Theory of gravity flow (part 1). In *Proceedings of MassMin 2004*, pages 167–172, 2004.

[125] A. Susaeta. Theory of gravity flow (part 2). In *Proceedings of MassMin 2004*, pages 173–178, 2004.

[126] I. Talu, G. I. Tardos, and J. Ruud van Ommen. Use of stress fluctuations to monitor wet granulation of powders. *Powder Technology*, 117(1-2):149–162, 2001.

[127] M. Tan, Y. Qian, I. Goldhirsch, and S. Orszag. Lattice-bgk approach to simulating granular flows. *Journal of Statistical Physics*, 81(1):87–103, 1995.

[128] G. I. Tardos. A fluid mechanistic approach to slow, frictional flow of powders. *Powder Technology*, 92(1):61–74, 1997.

[129] G. I. Tardos, S. McNamara, and I. Talu. Slow and intermediate flow of a frictional bulk powder in the couette geometry. *Powder Technology*, 131(1):23–39, 2003.

[130] A. J. Taylor and S. D. R. Wilson. Conduit flow of an incompressible, yield-stress fluid. *Journal of Rheology*, 41(1):93–102, 1997.

[131] T. Tezduyar. Finite element methods for flow problems with moving boundaries and interfaces. *Archives of Computational Methods in Engineering*, 8(2):83–130, 2001.

[132] D. J. Tritton. Experiments on the flow past a circular cylinder at low reynolds numbers. *Journal of Fluid Mechanics*, 6:547–567, 1959.

[133] R. Verberg and A. J. C. Ladd. Lattice-boltzmann model with sub-grid-scale boundary conditions. *Physical Review Letters*, 84(10):2148–2151, 2000.

[134] R. Verberg and A. J. C. Ladd. Accuracy and stability of a lattice-boltzmann model with subgrid scale boundary conditions. *Physical Review E*, 65(1):1–16, 2001.

[135] R. Verdugo and J. Ubilla. Geotechnical analysis of gravity flow during block caving. In *Proceedings of MassMin 2004*, pages 195–200, 2004.

[136] A. Vikhansky. Lattice-boltzmann method for yield-stress liquids. *Journal of Non-Newtonian Fluid Mechanics*, 155(3):95–100, 2008.

[137] C.-H. Wang and J.-R. Ho. Lattice boltzmann modeling of bingham plastics. *Physica A: Statistical Mechanics and its Applications*, 387(19-20):4740–4748, 2008.

[138] F. M. White. *Viscous fluid flow.* McGraw-Hill, 2 edition, 1991.

[139] S. Wolfram. Cellular automaton fluids 1: Basic theory. *Journal of Statistical Physics*, 45(3):471–526, 1986.

[140] M. Yoshino, Y. Hotta, T. Hirozane, and M. Endo. A numerical method for incompressible non-newtonian fluid flows based on the lattice boltzmann method. *Journal of Non-Newtonian Fluid Mechanics*, 147(1-2):69–78, 2007.

[141] H. Yu, S. S. Girimaji, and L.-S. Luo. Dns and les of decaying isotropic turbulence with and without frame rotation using lattice boltzmann method. *Journal of Computational Physics*, 209(2):599–616, 2005.

[142] J. Yu. *A contact interaction framework for numerical simulation of multi-body problems and aspects of damage and fracture for brittle materials.* PhD thesis, University of Wales, Swansea, 1999.

[143] G. Zanetti. Hydrodynamics of lattice-gas automata. *Physical Review A*, 40(3):1539–1548, 1989.

[144] J. G. Zhou. *Lattice Boltzmann methods for shallow water flows.* Springer-Verlag Berlin, 1st edition, 2004.

[145] A. A. Zick and G. M. Homsy. Stokes flow through periodic arrays of spheres. *Journal of Fluid Mechanics*, 115:13–26, 1982.

[146] D. P. Ziegler. Boundary conditions for lattice boltzmann simulations. *Journal of Statistical Physics*, 71(5):1171–1177, 1993.

[147] Q. Zou and X. He. On pressure and velocity boundary conditions for the lattice boltzmann bgk model. *Physics of Fluids*, 9(6):1591–1598, 1997.

APPENDIX A

CALCULATION OF VELOCITY MOMENT TENSORS FOR THE D2Q9 LATTICE

The velocity moment tensors of the lattice used in the lattice Boltzmann method have the form $\sum_i (c_{i\alpha} c_{i\beta} \ldots)$ and are used extensively in the multi-scale Chapman-Enskog analysis of the lattice Boltzmann equation. Here, the velocity moment tensors for the D2Q9 lattice are derived using the following non-dimensional lattice velocities,

$$\bar{\mathbf{c}}_{\mathrm{i}} = \begin{cases} 0 & (i = 0) \\ \left(\cos\left(\frac{\pi(i-1)}{2}\right), \sin\left(\frac{\pi(i-1)}{2}\right)\right) & (i = 1, 2, 3, 4) \\ \sqrt{2}\left(\cos\left(\frac{\pi(i-5)}{2} + \frac{\pi}{4}\right), \sin\left(\frac{\pi(i-5)}{2} + \frac{\pi}{4}\right)\right) & (i = 5, 6, 7, 8) \end{cases}, \tag{A.1}$$

which are listed in component form in Table A.1 for ease of reference in the following calculations.

Ignoring the null velocities of the rest particle distribution function, the

	$\bar{c}_0$	$\bar{c}_1$	$\bar{c}_2$	$\bar{c}_3$	$\bar{c}_4$	$\bar{c}_5$	$\bar{c}_6$	$\bar{c}_7$	$\bar{c}_8$
$\bar{c}_{1x}$	0	1	0	-1	0	1	-1	-1	1
$\bar{c}_{1y}$	0	0	1	0	-1	1	1	-1	-1

Table A.1: The non-dimensional velocity vectors of the D2Q9 lattice.

first order tensor is calculated as,

$$\begin{aligned}\sum_i \bar{c}_{i\alpha} &= \bar{c}_{1x}+\bar{c}_{1y}+\bar{c}_{2x}+\bar{c}_{2y}+\bar{c}_{3x}+\bar{c}_{3y}+\bar{c}_{4x}+\bar{c}_{4y}\\ &\quad +\bar{c}_{5x}+\bar{c}_{5y}+\bar{c}_{6x}+\bar{c}_{6y}+\bar{c}_{7x}+\bar{c}_{7y}+\bar{c}_{8x}+\bar{c}_{8y}\\ &= 0+0+1+0+0+1-1+0+0-1+1+1-1+1\\ &\quad -1-1+1-1\\ &= 0. \end{aligned} \tag{A.2}$$

The second order tensor can be calculated in two stages as,

$$\begin{aligned}\sum_{i=1\to4} \bar{c}_{i\alpha}\bar{c}_{i\beta} &= \bar{c}_{1x}\bar{c}_{1x}+\bar{c}_{1x}\bar{c}_{1y}+\bar{c}_{1y}\bar{c}_{1x}+\bar{c}_{1y}\bar{c}_{1y}+\bar{c}_{2x}\bar{c}_{2x}+\bar{c}_{2x}\bar{c}_{2y}\\ &\quad +\bar{c}_{2y}\bar{c}_{2x}+\bar{c}_{2y}\bar{c}_{2y}+\bar{c}_{3x}\bar{c}_{3x}+\bar{c}_{3x}\bar{c}_{3y}+\bar{c}_{3y}\bar{c}_{3x}+\bar{c}_{3y}\bar{c}_{3y}\\ &\quad +\bar{c}_{4x}\bar{c}_{4x}+\bar{c}_{4x}\bar{c}_{4y}+\bar{c}_{4y}\bar{c}_{4x}+\bar{c}_{4y}\bar{c}_{4y}\\ &= (1)(1)+(1)(0)+(0)(1)+(0)(0)+(0)(0)+(0)(1)\\ &\quad +(1)(0)+(1)(1)+(-1)(-1)+(-1)(0)+(0)(-1)\\ &\quad +(0)(0)+(0)(0)+(0)(-1)+(-1)(0)+(-1)(-1)\\ &= 4. \end{aligned} \tag{A.3}$$

$$\begin{aligned}\sum_{i=5\to8} \bar{c}_{i\alpha}\bar{c}_{i\beta} &= \bar{c}_{5x}\bar{c}_{5x}+\bar{c}_{5x}\bar{c}_{5y}+\bar{c}_{5y}\bar{c}_{5x}+\bar{c}_{5y}\bar{c}_{5y}+\bar{c}_{6x}\bar{c}_{6x}+\bar{c}_{6x}\bar{c}_{6y}\\ &\quad +\bar{c}_{6y}\bar{c}_{6x}+\bar{c}_{6y}\bar{c}_{6y}+\bar{c}_{7x}\bar{c}_{7x}+\bar{c}_{7x}\bar{c}_{7y}+\bar{c}_{7y}\bar{c}_{7x}+\bar{c}_{7y}\bar{c}_{7y}\\ &\quad +\bar{c}_{8x}\bar{c}_{8x}+\bar{c}_{8x}\bar{c}_{8y}+\bar{c}_{8y}\bar{c}_{8x}+\bar{c}_{8y}\bar{c}_{8y}\\ &= (1)(1)+(1)(1)+(1)(1)+(1)(1)+(-1)(-1)+(-1)(1)\\ &\quad +(1)(-1)+(1)(1)+(-1)(-1)+(-1)(-1)+(-1)(-1)\\ &\quad +(-1)(-1)+(1)(1)+(1)(-1)+(-1)(1)+(-1)(-1)\\ &= 8. \end{aligned} \tag{A.4}$$

Looking at (A.3) it can be seen that the only contributions to the tensor occur when $\alpha=\beta$. In addition, looking at (A.4) it can be seen that four contributions are made to the components of the tensor when $\alpha=\beta$. When $\alpha\neq\beta$ the net contribution to the components of the tensor is zero. With this information the two equations can be generalised as (with the non-dimensional grid velocity reintroduced as $\bar{c}$),

$$\sum_i \bar{c}_{i\alpha}\bar{c}_{i\beta} = \begin{cases} 2\bar{c}^2\delta_{\alpha\beta} & (i=1,2,3,4)\\ 4\bar{c}^2\delta_{\alpha\beta} & (i=5,6,7,8)\end{cases} \tag{A.5}$$

To list all of the components of the third order tensor,

$$\begin{aligned}\sum_{i=1\rightarrow 4} \bar{c}_{i\alpha}\bar{c}_{i\beta}\bar{c}_{i\gamma} &= \bar{c}_{1x}\bar{c}_{1x}\bar{c}_{1x} + \bar{c}_{1x}\bar{c}_{1x}\bar{c}_{1y} + \bar{c}_{1x}\bar{c}_{1y}\bar{c}_{1x} + \dots \\ &\quad + \bar{c}_{4y}\bar{c}_{4x}\bar{c}_{4y} + \bar{c}_{4y}\bar{c}_{4y}\bar{c}_{4x} + \bar{c}_{4y}\bar{c}_{4y}\bar{c}_{4y}, \end{aligned} \qquad (A.6)$$

$$\sum_{i=5\rightarrow 8} c_{i\alpha}c_{i\beta}c_{i\gamma}c_{i\theta} = \bar{c}_{5x}\bar{c}_{5x}\bar{c}_{5x}\bar{c}_{5x} + \bar{c}_{5x}\bar{c}_{5x}\bar{c}_{5x}\bar{c}_{5y} + \bar{c}_{5x}\bar{c}_{5x}\bar{c}_{5y}\bar{c}_{5x} + \dots$$

$$\begin{aligned}\sum_{i=5\rightarrow 8} \bar{c}_{i\alpha}\bar{c}_{i\beta}\bar{c}_{i\gamma} &= \bar{c}_{5x}\bar{c}_{5x}\bar{c}_{5x} + \bar{c}_{5x}\bar{c}_{5x}\bar{c}_{5y} + \bar{c}_{5x}\bar{c}_{5y}\bar{c}_{5x} + \dots \\ &\quad + \bar{c}_{8y}\bar{c}_{8x}\bar{c}_{8y} + \bar{c}_{8y}\bar{c}_{8y}\bar{c}_{8x} + \bar{c}_{8y}\bar{c}_{8y}\bar{c}_{8y}, \end{aligned} \qquad (A.7)$$

would be cumbersome. Instead, the tensor components can be derived by reasoning. In (A.9) the only nonzero terms occur when $\alpha = \beta = \gamma$ however their sum is zero for each component. For example, $\bar{c}_{1x}\bar{c}_{1x}\bar{c}_{1x} + \bar{c}_{2x}\bar{c}_{2x}\bar{c}_{2x} + \bar{c}_{3x}\bar{c}_{3x}\bar{c}_{3x} + \bar{c}_{4x}\bar{c}_{4x}\bar{c}_{4x} = 1+0+0-1 = 0$. Therefore, the total tensor components in (A.10) are zero when $\alpha = \beta = \gamma$. When the indices are not equal, the sum of the component contributions is also zero. Therefore, the third order tensor of velocity moments is zero,

$$\sum_{i} \bar{c}_{i\alpha}\bar{c}_{i\beta}\bar{c}_{i\gamma} = 0. \qquad (A.8)$$

Lastly, the fourth order tensor,

$$\begin{aligned}\sum_{i=1\rightarrow 4} \bar{c}_{i\alpha}\bar{c}_{i\beta}\bar{c}_{i\gamma}\bar{c}_{i\theta} &= \bar{c}_{1x}\bar{c}_{1x}\bar{c}_{1x}\bar{c}_{1x} + \bar{c}_{1x}\bar{c}_{1x}\bar{c}_{1x}\bar{c}_{1y} + \bar{c}_{1x}\bar{c}_{1x}\bar{c}_{1y}\bar{c}_{1x} + \dots \\ &\quad + \bar{c}_{4y}\bar{c}_{4y}\bar{c}_{4x}\bar{c}_{4y} + \bar{c}_{4y}\bar{c}_{4y}\bar{c}_{4y}\bar{c}_{4x} + \bar{c}_{4y}\bar{c}_{4y}\bar{c}_{4y}\bar{c}_{4y}, \qquad (A.9) \\ &\quad + \bar{c}_{4y}\bar{c}_{4y}\bar{c}_{4x}\bar{c}_{4y} + \bar{c}_{4y}\bar{c}_{4y}\bar{c}_{4y}\bar{c}_{4x} + \bar{c}_{4y}\bar{c}_{4y}\bar{c}_{4y}\bar{c}_{4y}, \end{aligned}$$

$$\begin{aligned}\sum_{i=5\rightarrow 8} c_{i\alpha}c_{i\beta}c_{i\gamma}c_{i\theta} &= \bar{c}_{5x}\bar{c}_{5x}\bar{c}_{5x}\bar{c}_{5x} + \bar{c}_{5x}\bar{c}_{5x}\bar{c}_{5x}\bar{c}_{5y} + \bar{c}_{5x}\bar{c}_{5x}\bar{c}_{5y}\bar{c}_{5x} + \dots \\ &\quad + \bar{c}_{8y}\bar{c}_{8y}\bar{c}_{8x}\bar{c}_{8y} + \bar{c}_{8y}\bar{c}_{8y}\bar{c}_{8y}\bar{c}_{8x} + \bar{c}_{8y}\bar{c}_{8y}\bar{c}_{8y}\bar{c}_{8y}, \end{aligned} \qquad (A.10)$$

is obviously the most laborious to write in component form. It can be reasoned that the only contributions to the tensor from (A.9) occur when $\alpha = \beta = \gamma = \theta$. The contributions from (A.10) are more difficult to determine from direct interrogation, and therefore they have been summarised in a 2D matrix with their tensor index in subscript,

$$\sum_{i=5\rightarrow 8} \bar{c}_{i\alpha}\bar{c}_{i\beta}\bar{c}_{i\gamma}\bar{c}_{i\theta} = \begin{bmatrix} 4_{1111} & 0_{1112} & 0_{1121} & 4_{1122} \\ 0_{1211} & 4_{1212} & 4_{1221} & 0_{1222} \\ 0_{2111} & 4_{2112} & 4_{2121} & 0_{2122} \\ 4_{2211} & 0_{2212} & 0_{2221} & 4_{2222} \end{bmatrix}, \qquad (A.11)$$

which is clearly symmetric. At this point the generalised isotropic fourth order tensor is introduced,

$$\Delta_{\alpha\beta\gamma\theta} = a_1\delta_{\alpha\beta}\delta_{\gamma\theta} + a_2\delta_{\alpha\gamma}\delta_{\beta\theta} + a_3\delta_{\alpha\theta}\delta_{\beta\gamma}, \tag{A.12}$$

in which a_1, a_2 and a_3 are constants. Applying (A.12) with $a_1 = a_2 = a_3 = 4$ gives,

$$4\left(\delta_{\alpha\beta}\delta_{\gamma\theta} + \delta_{\alpha\gamma}\delta_{\beta\theta} + \delta_{\alpha\theta}\delta_{\beta\gamma}\right) = \begin{bmatrix} 12_{1111} & 0_{1112} & 0_{1121} & 4_{1122} \\ 0_{1211} & 4_{1212} & 4_{1221} & 0_{1222} \\ 0_{2111} & 4_{2112} & 4_{2121} & 0_{2122} \\ 4_{2211} & 0_{2212} & 0_{2221} & 12_{2222} \end{bmatrix}, \tag{A.13}$$

which only differs from (A.13) by the term $-8\bar{c}^4\delta_{\alpha\beta\gamma\theta}$. With this information, the components of the fourth order tensor can be summarised as (with the non-dimensional grid velocity reintroduced as c),

$$\sum_i \bar{c}_{i\alpha}\bar{c}_{i\beta}\bar{c}_{i\gamma}\bar{c}_{i\theta} = \left\{ \begin{array}{cc} 2\bar{c}^4\delta_{\alpha\beta\gamma\theta} & (i = 1, 2, 3, 4) \\ 4\bar{c}^4\Delta_{\alpha\beta\gamma\theta} - 8\bar{c}^4\delta_{\alpha\beta\gamma\theta} & (i = 5, 6, 7, 8) \end{array} \right., \tag{A.14}$$

These results show that odd orders of the tensor are zero and that the second and fourth order tensors are symmetric. Sufficient symmetry of the chosen lattice is essential for the LBE to be able to capture the viscous terms of the Navier-Stokes equations [41].

APPENDIX B

THE RELATIONSHIP BETWEEN LATTICE AND PHYSICAL UNITS IN THE LBM

When coding the lattice Boltzmann method the variables are often reduced to a non-dimensionalised lattice system of units. This is done for reasons of computational convenience, as the spatial discretisation can be reduced to an integer array and the temporal counter reduced to an algebraic count. The equations and variables in this document are predominantly listed in physical units, however the relationship between the two systems is summarised in Table B.1.

Variable	Physical Units	Lattice Units	Relationship
Density	$\rho \approx \rho_0$	$\bar{\rho} \approx 1$	$\rho = \rho_0 \bar{\rho}$
Density Function	$f_i = \frac{\rho}{w_i}$	$\bar{f}_i = \frac{1}{w_i}$	$f_i = \rho_0 \bar{f}_i$
Relaxation Time	τ	$\bar{\tau}$	$\tau = \bar{\tau}\Delta t$
Lattice Spacing	Δx	$\bar{\Delta} x = 1$	-
Time Step	Δt	$\bar{\Delta} t = 1$	-
Lattice Speed	$c = \frac{\Delta x}{\Delta t}$	$\bar{c} = 1$	-
Viscosity	$\nu = \frac{1}{3}\left(\bar{\tau} - \frac{1}{2}\right)\frac{h^2}{\Delta t}$	$\bar{\nu} = \frac{1}{3}\left(\bar{\tau} - \frac{1}{2}\right)$	$\nu = \bar{\nu}\frac{h^2}{\Delta t}$
Displacement	$\mathbf{x}$	$\bar{\mathbf{x}}$	$\mathbf{x} = \Delta x \bar{\mathbf{x}}$
Velocity	$\mathbf{v} = \frac{d\mathbf{x}}{dt}$	$\bar{\mathbf{v}} = \frac{d\bar{\mathbf{x}}}{dt}$	$\mathbf{v} = c\bar{\mathbf{v}}$
Acceleration	$\mathbf{a} = \frac{d^2\mathbf{x}}{dt^2}$	$\bar{\mathbf{a}} = \frac{d^2\bar{\mathbf{x}}}{dt^2}$	$\mathbf{a} = \frac{c}{\Delta t}\bar{\mathbf{a}}$
IMB Force	$\mathbf{F} = \sum_n B_n \left(\sum_i \Omega_i^s \mathbf{c}_i\right) \frac{(\Delta x)^D}{\Delta t}$	$\mathbf{F} = \sum_n B_n \left(\sum_i \Omega_i^s \mathbf{c}_i\right)$	$\mathbf{F} = \bar{\mathbf{F}}\frac{(\Delta x)^D}{\Delta t}$
Nodal Mass	$m = \rho\left(\Delta x\right)^D$	$\bar{m} \approx 1$	$m = \rho_0 \left(\Delta x\right)^D \bar{m}$

Table B.1: The conversion factors between physical and lattice unit for relevant quantities in the LBM.

APPENDIX C

DERIVATION OF THE MOMENTUM FLUX TENSOR TO $\mathcal{O}\left(\delta^2\right)$ IN THE CHAPMAN-ENSKOG ANALYSIS

The momentum flux tensor to $\mathcal{O}(\delta^2)$, Π^{neq1}, is evaluated in the Chapman-Enskog analysis of the lattice Boltzmann equation,

$$\Pi^{neq1} = \sum_i f_i^{neq1}\mathbf{c}_i\mathbf{c}_i \tag{C.1}$$

using the definition of the non-equilibrium distribution from (2.39),

$$f_i^{neq1} = -\tau\left(\frac{\partial}{\partial t_0} + (\mathbf{c}_i\cdot\nabla)\right) f_i^{eq}, \tag{C.2}$$

and the generalised equilibrium functions (2.29),

$$f_i^{eq}(\mathbf{x},t) = \begin{cases} A_0 + B_0 c_{i\alpha}u_\alpha + C_0 c_{i\alpha}c_{i\beta}u_\alpha u_\beta + D_0 u_\alpha u_\alpha & (i=0) \\ A_1 + B_1 c_{i\alpha}u_\alpha + C_1 c_{i\alpha}c_{i\beta}u_\alpha u_\beta + D_1 u_\alpha u_\alpha & (i=1,2,3,4) \\ A_2 + B_2 c_{i\alpha}u_\alpha + C_2 c_{i\alpha}c_{i\beta}u_\alpha u_\beta + D_2 u_\alpha u_\alpha & (i=5,6,7,8) \end{cases}. \tag{C.3}$$

listed in Section 2.5. Noting that intuitively $B_0 = C_0 = 0$, (C.3) can be substituted into (C.2) which is in turn substituted into (C.1),

$$\Pi_{\alpha\beta}^{neq1} \quad = \quad -\tau\sum_i c_{i\alpha}c_{i\beta}\left(\frac{\partial}{\partial t_0} + \frac{\partial}{\partial x_\gamma}c_{i\gamma}\right)(A_0 + D_0 u_\theta u_\theta$$

$$
\begin{aligned}
&+A_1 + B_1 c_{i\theta} u_\theta + C_1 c_{i\gamma} u_\gamma c_{i\theta} u_\theta + D_1 u_\theta u_\theta \\
&+A_2 + B_2 c_{i\theta} u_\theta + C_2 c_{i\gamma} u_\gamma c_{i\theta} u_\theta + D_2 u_\theta u_\theta) ,
\end{aligned}
$$

and then expanded remembering that $c_{0\alpha} = 0$,

$$
\begin{aligned}
\Pi^{neq1}_{\alpha\beta} = -\tau \Bigg[& \sum_{i=1\rightarrow 4} \left(A_1 \frac{\partial}{\partial t_0} c_{i\alpha} c_{i\beta} + A_1 \frac{\partial}{\partial x_\gamma} c_{i\alpha} c_{i\beta} c_{i\gamma} + B_1 \frac{\partial}{\partial t_0} c_{i\alpha} c_{i\beta} c_{i\theta} u_\theta \right. \\
& + B_1 \frac{\partial}{\partial x_\gamma} c_{i\alpha} c_{i\beta} c_{i\gamma} c_{i\theta} u_\theta + C_1 \frac{\partial}{\partial t_0} c_{i\alpha} c_{i\beta} c_{i\gamma} u_\gamma c_{i\theta} u_\theta \\
& + C_1 \frac{\partial}{\partial x_\gamma} c_{i\alpha} c_{i\beta} c_{i\gamma} c_{i\theta} u_\theta c_{i\phi} u_\phi + D_1 \frac{\partial}{\partial t_0} c_{i\alpha} c_{i\beta} u_\theta u_\theta \\
& \left. + D_1 \frac{\partial}{\partial x_\gamma} c_{i\alpha} c_{i\beta} c_{i\gamma} u_\theta u_\theta \right) + \sum_{i=5\rightarrow 8} \left(A_2 \frac{\partial}{\partial t_0} c_{i\alpha} c_{i\beta} + A_2 \frac{\partial}{\partial x_\gamma} c_{i\alpha} c_{i\beta} c_{i\gamma} \right. \\
& + B_2 \frac{\partial}{\partial t_0} c_{i\alpha} c_{i\beta} c_{i\theta} u_\theta + B_2 \frac{\partial}{\partial x_\gamma} c_{i\alpha} c_{i\beta} c_{i\gamma} c_{i\theta} u_\theta \\
& + C_2 \frac{\partial}{\partial t_0} c_{i\alpha} c_{i\beta} c_{i\gamma} u_\gamma c_{i\theta} u_\theta + C_2 \frac{\partial}{\partial x_\gamma} c_{i\alpha} c_{i\beta} c_{i\gamma} c_{i\theta} u_\theta c_{i\phi} u_\phi \\
& \left. \left. + D_2 \frac{\partial}{\partial t_0} c_{i\alpha} c_{i\beta} u_\theta u_\theta + D_2 \frac{\partial}{\partial x_\gamma} c_{i\alpha} c_{i\beta} c_{i\gamma} u_\theta u_\theta \right) \right] . \qquad \text{(C.4)}
\end{aligned}
$$

The lattice identities derived in Appendix A can then be applied to (C.4),

$$
\begin{aligned}
\Pi^{neq1}_{\alpha\beta} = -\tau \Bigg[& 2A_1 \frac{\partial}{\partial t_0} \delta_{\alpha\beta} + 2B_1 \frac{\partial}{\partial x_\gamma} \delta_{\alpha\beta\gamma\theta} u_\theta + 2C_1 \frac{\partial}{\partial t_0} \delta_{\alpha\beta\gamma\theta} u_\gamma u_\theta \\
& + 2D_1 \frac{\partial}{\partial t_0} \delta_{\alpha\beta} u_\theta u_\theta + 4A_2 \frac{\partial}{\partial t_0} \delta_{\alpha\beta} + B_2 \frac{\partial}{\partial x_\gamma} u_\theta \left(4\Delta_{\alpha\beta\gamma\theta} - 8\delta_{\alpha\beta\gamma\theta} \right) \\
& + C_2 \frac{\partial}{\partial t_0} u_\gamma u_\theta \left(4\Delta_{\alpha\beta\gamma\theta} - 8\delta_{\alpha\beta\gamma\theta} \right) + 4D_2 \frac{\partial}{\partial t_0} \delta_{\alpha\beta} u_\theta u_\theta \Bigg] ,
\end{aligned}
$$

which can be expanded and regrouped,

$$
\begin{aligned}
\Pi^{neq1}_{\alpha\beta} = -\tau \Bigg[& \left(2A_1 + 4A_2 \right) \frac{\partial}{\partial t_0} \delta_{\alpha\beta} + \left(2B_1 - 8B_2 \right) \frac{\partial}{\partial x_\gamma} \delta_{\alpha\beta\gamma\theta} u_\theta \\
& + \left(2C_1 - 8C_2 \right) \frac{\partial}{\partial t_0} \delta_{\alpha\beta\gamma\theta} u_\gamma u_\theta + 4B_2 \frac{\partial}{\partial x_\gamma} u_\theta \delta_{\alpha\beta} \delta_{\gamma\theta} + 4B_2 \frac{\partial}{\partial x_\gamma} u_\theta \delta_{\alpha\gamma} \delta_{\beta\theta} \\
& + 4B_2 \frac{\partial}{\partial x_\gamma} u_\theta \delta_{\alpha\gamma} \delta_{\beta\theta} + 4B_2 \frac{\partial}{\partial x_\gamma} u_\theta \delta_{\alpha\theta} \delta_{\beta\gamma} + 4C_2 \frac{\partial}{\partial t_0} u_\gamma u_\theta \delta_{\alpha\beta} \delta_{\gamma\theta} \\
& + 4C_2 \frac{\partial}{\partial t_0} u_\gamma u_\theta \delta_{\alpha\gamma} \delta_{\beta\theta} + 4C_2 \frac{\partial}{\partial t_0} u_\gamma u_\theta \delta_{\alpha\theta} \delta_{\beta\gamma} \\
& + \left(2D_1 + 4D_2 \right) \frac{\partial}{\partial t_0} \delta_{\alpha\beta} u_\theta u_\theta \Bigg] . \qquad \text{(C.5)}
\end{aligned}
$$

It has been shown in (2.50) and (2.48) in Section 2.5 that $2A_1 + 4A_2 = c_s^2$ and $2C_1 - 8C_2 = 0$. Using this information along with Kronecker delta index changes, (C.5) can be simplified to,

$$\begin{aligned}
\Pi^{neq1}_{\alpha\beta} &= -\tau\left[\frac{\partial}{\partial t_0}\left(c_s^2\rho\right)\delta_{\alpha\beta} + (2B_1 - 8B_2)\frac{\partial u_\beta}{\partial x_\alpha}\delta_{\alpha\beta} + 4B_2\frac{\partial u_\gamma}{\partial x_\gamma}\delta_{\alpha\beta} + 4B_2\frac{\partial u_\beta}{\partial x_\alpha}\right. \\
&\quad +4B_2\frac{\partial u_\alpha}{\partial x_\beta} + 4C_2\frac{\partial}{\partial t_0}u_\theta u_\theta\delta_{\alpha\beta} + 4C_2\frac{\partial}{\partial t_0}u_\alpha u_\beta + 4C_2\frac{\partial}{\partial t_0}u_\beta u_\alpha \\
&\quad \left. + (2D_1 + 4D_2)\frac{\partial}{\partial t_0}\delta_{\alpha\beta}u_\theta u_\theta\right] \\
&= -\tau\left[\frac{\partial}{\partial t_0}\left(c_s^2\rho\right)\delta_{\alpha\beta} + (2B_1 - 8B_2)\frac{\partial u_\beta}{\partial x_\alpha}\delta_{\alpha\beta} + 4B_2\left(\frac{\partial u_\beta}{\partial x_\alpha} + \frac{\partial u_\alpha}{\partial x_\beta}\right)\right. \\
&\quad \left. +4B_2\frac{\partial u_\gamma}{\partial x_\gamma}\delta_{\alpha\beta} + 8C_2\frac{\partial}{\partial t_0}u_\alpha u_\beta + (2D_1 + 4D_2 + 4C_2)\frac{\partial}{\partial t_0}\delta_{\alpha\beta}u_\theta u_\theta\right],
\end{aligned}$$

and again using $2D_1 + 4D_2 + 4C_2 = 0$ from (2.47) and $8C_2 = \rho$ from (2.49) in Section 2.5,

$$\begin{aligned}
\Pi^{neq1}_{\alpha\beta} &= -\tau\left[\frac{\partial}{\partial t_0}\left(c_s^2\rho\right)\delta_{\alpha\beta} + \frac{\partial}{\partial t_0}\left(\rho u_\alpha u_\beta\right) + (2B_1 - 8B_2)\frac{\partial u_\beta}{\partial x_\alpha}\delta_{\alpha\beta} + 4B_2\frac{\partial u_\gamma}{\partial x_\gamma}\delta_{\alpha\beta}\right. \\
&\quad \left. +4B_2\left(\frac{\partial u_\beta}{\partial x_\alpha} + \frac{\partial u_\alpha}{\partial x_\beta}\right)\right].
\end{aligned} \tag{C.6}$$

Finally, the time derivative in the first term of (C.6) can be removed by rearranging (2.41) in Section 2.5,

$$\frac{\partial\rho}{\partial t_0} = -\frac{\partial}{\partial x_\alpha}\left(\rho u_\alpha\right),$$

which leaves,

$$\begin{aligned}
\Pi^{neq1}_{\alpha\beta} &= -\tau\left[-c_s^2\frac{\partial}{\partial x_\gamma}\left(\rho u_\gamma\right)\delta_{\alpha\beta} + \frac{\partial}{\partial t_0}\left(\rho u_\alpha u_\beta\right) + (2B_1 - 8B_2)\frac{\partial u_\beta}{\partial x_\alpha}\delta_{\alpha\beta} + 4B_2\frac{\partial u_\gamma}{\partial x_\gamma}\delta_{\alpha\beta}\right. \\
&\quad \left. +4B_2\left(\frac{\partial u_\beta}{\partial x_\alpha} + \frac{\partial u_\alpha}{\partial x_\beta}\right)\right].
\end{aligned} \tag{C.7}$$